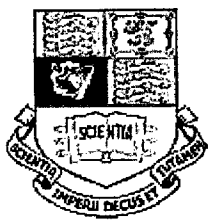
Imperial College
OF SCIENCE, TECHNOLOGY AND MEDICINE



STUDIES OF DISTILLATION TRAY HYDRODYNAMICS AND MASS TRANSFER

Hsun-min Yang
MEng, ACGI

A thesis submitted in partial fulfilment of the requirements for the degree of
Doctor of Philosophy of the University of London

Department of Chemical Engineering and Chemical Technology
Imperial College of Science, Technology and Medicine
London SW7 2BY

January 2002

Abstract

This thesis reports an experimental and computational investigation of the two-phase flows above distillation plates. The chaotic nature of such a gas-liquid flow system makes it difficult to establish a scientific theory on the subject; instead, empiricism dominates the predictions of the tray performance. The objective of the present study is to (1) reveal the structure of the two-phase flows using an advanced experimental technique and (2) produce a tray performance prediction methodology which has stronger scientific basis.

Experimental results from an air-water sieve tray simulator on the hydrodynamic parameters (such as void fraction, clear liquid height, Sauter mean bubble diameter profile and pressure drop) showed good agreement with some previously published work. These hydrodynamic results were also used in validating the Computational Fluid Dynamics (CFD) studies carried out at Bristol University and good agreement was found between the data and the CFD predictions.

A novel measuring technique, named the "Flying Optical Probe System", has been developed to analyse the detailed froth structure. During experiments, gas and liquid chord lengths were measured and these were successfully converted to bubble and droplet size distributions, assuming that the bubbles and drops are spherical. These distributions gave good qualitative and quantitative descriptions of the two-phase froth structure.

Confirmation of many of the phenomena in gas-liquid flow occurring on a distillation tray has been achieved by a liquid-liquid flow simulation. The pair of liquids has the same refractive index to overcome the optical aberration and an UV-activated photochromic dye was dissolved in the lighter phase (simulating the gas phase in the real situation) in order to track its trajectory. The interactions between drops were clearly seen and most importantly, the transition between the froth and spray regimes was clearly observed.

A new CFD-based methodology has been developed to predict the tray performance. A CFD model has been used to generate the residence time distribution of the froth above the tray. Diffusional mass transfer relationships between the gas-liquid interfaces have been included to convert the residence time distribution into product compositions leaving the tray. Validations of this methodology against the data from *Fractionation Research Inc* (1957) and *American Institute of Chemical Engineer* (1958) showed excellent agreement between the prediction and the experimental results. Compared to the traditional point/tray efficiency correlations on predicting the tray performance, this methodology has a stronger scientific basis.

Acknowledgement

It is my greatest honour to perform research work under the supervisions of Professor G.F. Hewitt, FRS and Dr. M.A. Mendes-Tatsis. This work can never be completed without their excellent guidance and most valuable comments which I will not forget for the rest of my life. Thank you very much!

I am grateful to all members of the ASID Consortium who kindly provided the sponsorship for this programme. My special thanks go to Dr. K. Krishnamurthy and Dr. R. Thorogood of B.O.C. for their many valuable advises and enormous support during my research period.

There are also various individuals who I would like to express my gratitude for the assistance I received from them: Professor G. L. Quarini for his encouragement and some brain-storming conversations throughout the course of this study. Messrs. Malcolm Dix and Peter Arnold for their helps on the construction of the flying optical probe system. Mr. Bob King for his valuable advises on various designs and constructions of the experimental rig throughout my study. Dr. Charlie Fischer for his friendship and the helps on the CFD work. Also many thanks to all the colleagues of the Multiphase Fluids System Group in particular Lukito Lau, Colin Hale, Jader Barbosa, Shay Badie, Utomi Odozi, Priscilla Ujang, Ka-wai Lee, Prashant Valluri, Tzuu-shing Ng, Leslie Yeo and Pooi-ling Cheung.

Last but not least, I would like to express my most sincere gratitude to my family for their continuous supports throughout my study in the UK and to my fiancée, Pei-Ni, for her countless helps and encouragement which made the completion of this work possible.

Love to my parents and Pei-Ni to whom this thesis is dedicated.

Table of Contents

Abstract **1**

Acknowledgement **3**

Table of Contents **4**

Chapter 1 : Introduction

1.1. General 10

1.2. Aims of Present Work 12

1.3. Outline of Thesis 12

Chapter 2 : Literature Review

2.1. Introduction 14

2.2. Sieve Tray Operation 15

2.2.1. Bubble Formation from an Orifice 17

2.2.2. Common Operational Flow Regimes on a Sieve Tray 20

2.2.3. Flow Regime Transition on a Sieve Tray 25

2.3. Hydrodynamics 30

2.3.1. Dispersion Density 30

2.3.2. Clear Liquid Height 36

2.3.3. Pressure Drop across a Sieve Tray 42

2.3.4. Characterisation of the Two-Phase Froth 50

2.4. Vapour-Liquid Equilibrium in Distillation 52

2.4.1. Fundamentals 53

2.4.2. Thermophysical Property Models for Predictions of VLE 54

2.4.3. Equation of State 55

2.4.4. Activity Coefficient Models 57

2.5. Mass Transfer in Distillation 59

2.5.1. Mass Transfer Coefficients 59

2.5.2. Diffusion Coefficients in Gas Mixtures 62

2.5.3. Diffusion Coefficients in Liquid Mixtures 70
2.5.4. Interfacial Area 76
2.6. Efficiency of a Distillation Tray 78
2.6.1. Overall Column Efficiency and Tray Efficiency 78
2.6.2. Point Efficiency 80
2.6.3. Relationship between Point Efficiency and Tray Efficiency 88
2.6.4. Calculation Procedure 95
2.7. CFD Challenges 96
2.8. Objectives of Present Work 99

Chapter 3 : Gas-Liquid Simulation Experiment (1) - CRODIS Facility

3.1. Introduction 101
3.2. The CRODIS Facility 102
3.2.1. Modifications on Air Circulation Loop 106
3.2.2. Modifications to the Air-Water Separator 107
3.2.3. Modifications to the Test Tray Inlet Downcomer 111
3.3. Measuring Techniques 112
3.3.1. Gamma Densitometry 112
3.3.2. Multiple Light Scattering Technique 117
3.3.3. Paraffin Manometer 122
3.3.4. Error Analysis 122
3.4. Results and Discussions 124
3.4.1. CRODIS Flow Visualisation 124
3.4.2. Dispersion Density Profile and Clear Liquid Height 126
3.4.3. Tray Pressure Drop 130
3.4.4. Sauter Mean Bubble Diameter 134
3.4.5. Partial Bubbling/Moving Froth Phenomenon 135
3.5. Summary 136

Chapter 4 : Gas-Liquid Simulation Experiment (2) - Flying Optical Probe System

4.1. Introduction 137
4.2. Optical Probes Measurements in Two-Phase Flows 138

4.2.1. Principle 138
4.2.2. Applications 139
4.3. Design of the Flying Optical Probes System 141
4.3.1. Background Theory 141
4.3.2. The Optical Fibre Probes 144
4.3.3. Probes Testing 147
4.3.4. The Actuation Mechanism 160
4.3.5. The Electronics System 167
4.4. Experiments and Probes Signal Processing 168
4.4.1. Experimental Raw Data 169
4.4.2. Chord Length Distributions 170
4.4.3. Bubble / Droplet Size Distributions 174
4.5. Results Analysis and Discussions 179
4.5.1. The Effect of Flow Regimes on Distribution Results 179
4.5.2. Sauter Mean Size Distributions 181
4.5.3. Limitations on the Clark & Turton's (1988) Method 185
4.5.4. Multiple Region Experiment 185
4.6. Summary 188

Chapter 5 : Liquid-Liquid Crossflow Simulation

5.1. Introduction 189
5.2. Photochromic Dye Tracing Technique 190
5.2.1. Background Theory 190
5.2.2. Literature Survey 191
5.3. Experimental Fluids System 193
5.3.1. Photochromic Dye - TNSB 193
5.3.2. Refractive Index Matching Fluids 195
5.3.3. Fluid Preparation Procedures 196
5.4. Liquid-Liquid Experimental Rig 197
5.4.1. Flowsheet 197
5.4.2. Proposed Experiments 203
5.5. Observations and Discussions 204
5.5.1. Single-hole Bubbling Experiment 204

5.5.2. Full Simulation (Multiple-hole Bubbling) Experiment....208
5.5.3. Liquid-Liquid System vs. Gas-Liquid System....216
5.6. Summary....217

Chapter 6 : Application of Computational Fluid Dynamics to Distillation Hydrodynamics

6.1. Introduction....218
6.2. CFD Fundamentals....220
6.2.1. Governing Equations....220
6.2.2. Scalar Quantity....221
6.2.3. Commercial CFD Code....222
6.3. Multiphase Modelling using the Heterogeneous Model....222
6.3.1. Heterogeneous Model....223
6.3.2. Interphase Drag Law....224
6.3.3. The MUSIG Model....227
6.4. Homogeneous Model....233
6.5. CFD Application – Fluid Age Distribution....235
6.6. Summary....236

Chapter 7 : Prediction of Distillation Tray Performance - A New Approach based on CFD Studies

7.1. Introduction....238
7.2. Estimation of Diffusion Coefficients....240
7.2.1. Diffusion Coefficients in Gas Mixtures....240
7.2.2. Diffusion Coefficients in Liquid Mixtures....241
7.3. Vapour-Liquid Equilibrium and Transport Property....241
7.3.1. Recommendations on VLE Relationships....242
7.3.2. Transport Property Models....242
7.4. Recommendations on Mass Transfer Relationships....244
7.4.1. Mass Transfer Coefficients....244
7.4.2. Interfacial Area....245
7.4.3. Mass Transfer in a Fluid Element....245

7.5. CFD Studies: Flow Distribution and Residence Time 249
7.5.1. Model Input Information 250
7.5.2. Simulation Results 250
7.5.3. Relationships between CFD Results and Outlet Composition 252
7.6. Summary 253

Chapter 8 : Validation and Application of the New Methodology

8.1. Introduction 255
8.2. Methodology Validation with Experimental Data 256
8.2.1. AIChE Data 257
8.2.2. FRI Distillation Data 268
8.3. Sensitivity Studies and Discussions 276
8.4. Applications of the New Methodology 279
8.4.1. Tray Scale-up 280
8.4.2. Improved Flow Distribution 282
8.5. Summary 284

Chapter 9 : Conclusions and Recommendations

9.1. General 285
9.2. Conclusions 285
9.2.1. General Distillation Hydrodynamics 285
9.2.2. Results from Flying Optical Probe Measurements 287
9.2.3. Liquid-liquid Simulation Rig 287
9.2.4. Computational Fluid Dynamics Predictions 288
9.3. Recommendations to Future Work 289

Nomenclature 292
References 296

Appendix A. Le Bas (1915) Additive Volumes Method **304**

Appendix B. Dispersion Density Profile **305**

Appendix C. Sauter Mean Bubble/Droplet Diameter Profile **312**

Appendix D. Computer Codes **316**

List of Figures **350**

List of Tables **356**

CD-ROM 1. Detailed results obtained from the flying optical probe system (Chapter 4)

CD-ROM 2. Full results from the liquid-liquid simulations experiments (Chapter 5)

Nomenclature

All parameters are in S.I. units, unless specified elsewhere.

A_f Fractional free area of a sieve tray

A_s Active (or bubbling) area of a sieve tray, m^2

a Constant defined in Jet Penetration model by Lockett (1981), Eq.(2.6)

a Interfacial area per unit volume of two-phase dispersion, $m^2 m^{-3}$

$\bar{a}$ Interfacial area per unit volume of liquid, $m^2 m^{-3}$

a_1 Constant defined in Biddulph's correlation (1995), Eq.(2.56)

a_2 Constant defined in Biddulph's correlation (1995), Eq.(2.56)

a_3 Constant defined in Biddulph's correlation (1995), Eq.(2.56)

Bo Bond number, $\dfrac{(\rho_L - \rho_G) g d_h^2}{\sigma}$

b Intercept of equilibrium line (binary)

C Constant defined in Bennett's correlation (1983), Eq.(2.27)

C_d Constant defined in Francis equation (1983), Eq.(2.21)

CF Capacity factor based on A_s, $u_s\left(\dfrac{\rho_G}{\rho_L - \rho_G}\right)^{0.5}$, $m\ s^{-1}$

C_v Discharge coefficient for an orifice

c Concentration

D_B Diameter of a rising bubble defined in Bennett's correlation (1983), Figure 2.19, m

D_{Bmax} Maximum diameter of a rising bubble defined in Bennett's correlation (1983), Eq.(2.50), m

D_G Diffusion coefficient in vapour phase, $m^2 s^{-1}$

D_L Diffusion coefficient in liquid phase, $m^2 s^{-1}$

d Diameter (general), m

d_b Bubble diameter, m

d_G Parameter defined in Bekassy-Molnar & Mustafa (1991), Eq.(2.33), m

d_h Hole diameter, m

d_p Droplet diameter, m

E_0 Section / overall efficiency

E_m liquid entrainment rate, kg s^{-1}

E_{ML} Murphree liquid phase tray efficiency

E_{MV} Murphree vapour phase tray efficiency

E_{OG} Murphree vapour phase point efficiency

e Liquid entrainment rate ÷ vapour rate (molar flowrate)

e_m Liquid entrainment rate ÷ vapour rate (mass flowrate)

$\mathcal{F}_i$ Poynting Factor

F_0 Parameter to be found for h_σ prediction, Eq.(2.57)

F_h Hole F-factor, $u_h \rho_G^{0.5}$, $kg^{0.5}\, m^{-0.5}\, s^{-1}$

FP Flow parameter, $\frac{M_L}{M_G}\left(\frac{\rho_G}{\rho_L}\right)^{0.5}$

Fr Froude number, u_s^2 / gh_L

Fr^* Modified Froude number, $\left[\rho_G u_h^2 / (\rho_L - \rho_G) g d_h\right]^{0.5}$

F_s Superficial F-factor, $u_s \rho_G^{0.5}$, $kg^{0.5} m^{-0.5} s^{-1}$

f Fanning friction factor, Eq.(2.42)

f Fugacity (in Section 2.4)

G Vapour flowrate, kg-mol s^{-1}

G' Vapour flowrate per unit bubbling area, kg-mol $s^{-1}\, m^{-2}$

g Acceleration due to gravity, m s^{-2}

h_D Dry tray pressure drop (equivalent height of liquid), m

h_f Froth height above tray, m

h_{fl} Clear liquid layer thickness on the tray, m

h_{hg} Hydraulic gradient on the tray, m

h_L Clear liquid height, m

$h_{L,ow}$ Clear liquid height over weir, Eq.(2.24), m

h'_L Pressure loss defined in Eq.(2.35), m

h_{ow} Height of froth flowing over the weir, m

h_T Total pressure drop across a wet tray (equivalent height of liquid), m

h_σ Residual pressure drop (equivalent height of liquid), m

h_w Weir height, m

J	Flux
K	Vapourisation equilibrium ratio
K_{OG}	Overall mass transfer coefficient based on vapour, kg-mol s^{-1} m^{-2}
K'_{OG}	Overall mass transfer coefficient based on vapour, m s^{-1}
K_{OL}	Overall mass transfer coefficient based on liquid, kg-mol s^{-1} m^{-2}
K_w	Constant defined in Smith and Van Winkle (1958), Eq.(2.43)
k	Dry-plate coefficient defined in McAllister (1958), Eq.(2.42)
k_B	Boltzman constant
k_G, k_L	Vapour and liquid phase mass transfer coefficient, kg-mol s^{-1} m^{-2}
k'_G, k'_G	Vapour and liquid phase mass transfer coefficient, m s^{-1}
L	Liquid flowrate, kg-mol s^{-1}
L'	Liquid flowrate per unit tray area, kg-mol s^{-1} m^{-2}
L'_w	Weeping rate per unit tray area, kg-mol s^{-1} m^{-2}
M_G	Gas mass flowrate, kg s^{-1}
M_L	Liquid mass flowrate, kg s^{-1}
m	Slope of equilibrium line (binary)
N	Number of completely mixed liquid pools
N_A	Molar flux of component A, kg-mol s^{-1} m^{-2}
N_{Actual}	Number of actual trays
N_G	Number of binary vapour phase transfer units
N_L, N'_L	Number of binary liquid phase transfer units (different definitions!)
N_{OG}	Number of overall binary vapour phase transfer units
N_p	Number of liquid passes per tray
N_{Theo}	Number of theoretical trays
n	Constant defined in Jet Penetration model by Lockett (1981), Eq.(2.6)
Pe	Peclet number
p	Hole pitch of a sieve tray, m
ΔP_0	Pressure drop defined in Bekassy-Molnar & Mustafa (1991), N m^{-2}
ΔP_{dry}	Dry tray pressure drop, N m^{-2}
Q_h	Gas volumetric flowrate through hole, $m^3 s^{-1}$
Q_G	Gas volumetric flowrate, $m^3 s^{-1}$
Q_L	Liquid volumetric flowrate, $m^3 s^{-1}$
r	Separation ditance for L-J potential, Eq.(2.77)

r_0 Orifice radius, m

r_b Bubble departure radius, m

Re_h Hole Reynolds number

T_s Tray spacing, m

t Tray thickness, m

t_c Contact time of the interface, s

t_G Vapour residence time, s

t_L Liquid residence time, s

u_b Velocity defined in Stichlmair's correlation (1978), m s^{-1}

u_h Hole velocity, m s^{-1}

u_L Average liquid velocity on the tray, m s^{-1}

u_s Superficial velocity, m s^{-1}

u_t Large drop terminal velocity, Eq.(2.4), m s^{-1}

V_0 Volume of a bubble with the orifice diameter, Eq.(2.55), m^3

W Weir length, m

w Distance from centre line measured parallel to weir, m

x_n Liquid mole fraction leaving elemental strip n

$\bar{x}_n$ Mean mole fraction in liquid leaving tray n via downcomer

x'_n Mole fraction in liquid weeping or entrained from a point on tray n

x^*_n Mole fraction of liquid in equilibrium with mean vapour concentration leaving tray n

y Vertical position, m

y_0 Inlet vapour mole fraction

y_n Mole fraction in vapour at a point on tray n ; vapour mole fraction leaving elemental strip n

$\bar{y}_n$ Mean mole fraction in vapour leaving tray n

y^*_n Mole fraction of vapour in equilibrium with mean liquid concentration leaving tray n via downcomer ; vapour mole fraction in equilibrium with mean liquid concentration leaving elemental strip n

Z Liquid flow path length, m

z Distance from inlet weir, m

z' position on the tray; z' changes from unity to zero as the liquid flows from the inlet weir to the outlet weir

Greek Symbols

α Liquid holdup fraction

α' Constant defined in Eq.(2.34)

α_p A parameter defined in Eq.(2.1)

α_r Residual volume ratio in Eq.(2.55)

β Aeration factor, Eq.(2.36)

β' Constant defined in Eq.(2.34)

γ Activity coefficient

γ' Constant defined in Eq.(2.34)

δ' Constant defined in Eq.(2.34)

ε Gas holdup fraction

ε Characteristic L-J energy, Eq.(2.77)

ε_s Value of ε in the spray body

ε_w Value of ε in the froth flowing over outlet wier

θ Contact angle

λ Stripping factor or ratio of slope of equilibrium line to slope of operating line, mG/L

ξ Orifice coefficient

ξ_0 Parameter defined in Stichlmair & Mersmann's correlation (1978), Eq.(2.44)

σ Surface tension, kg m^{-3}

σ Characteristic L-J length, Eq.(2.77)

ρ_L, ρ_G Liquid and vapour density, kg m^{-3}

ρ'_L, ρ'_G Liquid and vapour density, kg-mol m^{-3}

τ 1 ÷ (bubbling frequency), Eq.(2.55), s^{-1}

ϕ Fugacity coefficient

ϕ_e Parameter defined in Bennett's correlation (1983), Eq.(2.27)

ψ Defined by Hofhuis & Zuiderweg (1979), Eq.(2.24), m

ψ Intermolecular potential, Eq.(2.77)

Ω_D Dimensionless collision intergral, Eq.(2.75)

Subscripts

i	Interface
j	Leaving elemental strip j
n	Leaving tray n
G	In vapour or gas phase
L	In liquid phase

Superscripts

0	Local value at the exit weir
-	Mean value

Chapter 1

Introduction

1.1. General

Distillation is a process of physically separating a mixture into two or more products that have different boiling points. This is done by preferentially boiling the more volatile components out of the mixture. When a liquid mixture of two volatile materials is heated, the vapour that comes off will have a higher concentration of the more volatile material than the liquid from which it was evolved. Conversely, if a vapour is cooled, the less volatile material has a tendency to condense in a greater proportion than the more volatile material.

Primitive forms of distillation can be traced back to more than two thousand years ago when the Chinese first used it to produce distilled liquors. The secret of the technique slowly spread out, first to India, then Arabia and finally reached Britain before AD 500, and was used in the production of mead. The technology remained very much the same for the next 1000 years. Indeed, the original technology is still used in the production of whiskey which started in Scotland about AD 1500. These early applications were generally associated with concentrating the alcoholic content of beverages by using crude vaporisation and condensation equipment.

Although distillation is an ancient unit operation, the theory was not thoroughly studied until the work of Sorel (1893). In the 1920's, some preliminary concepts and design procedures began to be published. Since then, the development of the technique really took off and began to cause a great impact in industry; one of the very important applications was the separation of crude oil into various products. Distillation has now

become the most well known and the dominant technique for separation in the petroleum and chemical industries.

Distillation operations are usually performed in cylindrical columns. These columns come in a wide range of sizes, their diameter ranges from 0.05 m (for a typical laboratory scale column) to about 10 to 12 m (for the largest industrial columns) and their height ranges from about 0.5 m to about 100 m (Wijn, 2000). Trays or packings (or both) are introduced in a column to aid the gas-liquid contact and hence the mass transfer. Both trays and packings can each be further divided into two major types. i.e. conventional or high performance trays and random or structured packings. Trays have a long history of being an efficient gas-liquid contacting device although packings have been introduced as the column internals for energy-saving revamps since the 1980's. However, trays still continue to offer specific advantages over packings in many areas of considerable industrial interest. For example, trays generally have lower capital costs, especially in larger columns; trays are also more resistant to blockage or dirty feeds. Sometimes, both trays and packings may appear to be equally suitable for a particular application and it may be advantageous that both types of internals are applied in a single column. Selection considerations for column internals have been given by Bravo (1997) and optimal column internals can be chosen according to the properties of the fluid system and the process where distillation is to be used.

In recent years, more and more alternative methods to distillation have been applied in separation processes (e.g. membrane separations). This may be due to the fact that the weaknesses of the ancient technology have not been properly investigated and rectified. Distillation consumes enormous amounts of energy, both in terms of cooling and heating requirements and it can contribute to more than 50% of plant operating costs. The best way to reduce operating costs of distillation columns is to improve their efficiency. In the past, the complexity of the situations within the column internals made empirical correlations a predominant feature of the subject but these have little physical meaning. In order to achieve a significant improvement, a thorough understanding of hydrodynamics and mass transfers in distillation is essential.

1.2. Aims of Present Work

The present work has been part of a collaborative effort industry and academia since the early 1990's. It was felt that there was a need to improve on the empirical nature of the present knowledge on the design and operation of distillation trays. The industrial consortium, Advanced Studies In Distillation (ASID), was setup to carry out research, following a strong scientific approach, in the area of distillation sieve trays. Participating research institutes are Bristol University, Aston Universities and Imperial College. The aims of the present study are to provide validations of the predictions from CFD (Computational Fluid Dynamics) models developed at Bristol University and, at the same time, to extend CFD modelling by incorporating mass transfer relationships to form a new, residence time based methodology for estimating tray performance. The new methodology can be used in predictions associated with revamping existing facilities and also in new designs of distillation equipment.

1.3. Outline of Thesis

The thesis is divided into nine chapters, including the present one. Chapter 2 reviews work from the published literature on the two-phase hydrodynamic aspects and associated mass transfer relationships of distillation trays. A detailed list of objectives of the present work is given at the end of Chapter 2.

The experimental aspects of the present work are covered in Chapter 3 to Chapter 5. Chapter 3 describes the experimental work carried out in an air-water distillation simulator. The traditional two-phase flow measuring techniques used in the experiments are fully described and experimental results on various tray configurations are also given. Chapter 4 presents a new experimental measuring technique which involves local measurements using moving optical fibre probes and the results are interpreted into bubble and droplet sizes distributions under appropriate transformations of the raw data. Chapter 5 describes a visualisation method for examining gas-liquid flows by a liquid-liquid system where photographic images of the flows were taken from a high speed video camera.

The analytical parts of the present work are covered in Chapters 6 to 8. Chapter 6 deals with the modelling work on Computational Fluid Dynamics (CFD) and describes the available methods developed so far by the ASID consortium. In Chapter 7, a new methodology based on "liquid residence time" for estimating tray performances is introduced. This method has been specifically developed as an application tool for interpreting the CFD results on liquid residence time. Two sets of distillation tray efficiency databanks have been used to validate the predictions given by the new methodology. The validation results with analysis are given in Chapter 8 and some potential applications of the methodology are also briefly described.

The conclusions of the present study and recommendations to any future work on the subject are given in Chapter 9.

Chapter 2

Literature Review

2.1. Introduction

Research in distillation has a longer history than any other major separation processes in the chemical industry. However, most of the design procedures which exist in distillation handbooks are still empirical in nature. In a paper published by Porter (1995), it is stated that

> *"After more than fifty years of research, many people consider distillation as a mature technology where little is to be gained by further research. The present state of the art is based on the empirical correlations of past. The lack of a scientific basis for predicting the performance of new equipment in larger diameter columns slows down both the development and the acceptance of new equipment."*

Due to the extensive amount of literature published on the sieve tray operations, this chapter divides the subject into six sections. Section 2.2 describes the fundamentals of two-phase flows on sieve trays, i.e. how the tray behaves and the nature of the flows. A more detailed description of the sieve tray hydrodynamics is presented in Section 2.3 and stressing the manner in which the information is used to provide quantitative analysis of the two-phase flows. Vapour-liquid equilibrium governs distillation processes and Section 2.4 provides information on predicting such equilibrium relationships by applying modern thermophysical property models. The mass transfer aspects of distillation processes are discussed in Section 2.5 which includes a review of prediction of diffusion coefficients. Diffusion coefficient data is vital in describing the

diffusional mass transfer process. Section 2.6 presents the most traditional methods used to determine the performance of sieve trays, i.e. point efficiency, tray efficiency and overall efficiency. More recently, the technique of Computational Fluid Dynamics (CFD) has been successfully used to predict the flow behaviours of a sieve tray and this is introduced in Section 2.7.

Section 2.8 summarises the literature discussed in all previous six sections and identifies the areas that still require further research. Some of these areas have been addressed in the present work and the chapter closes with a presentation of the objectives of this work.

Although this chapter tries to cover a wide range of topics relevant to sieve tray processes, the subject is wide and details cannot be given (for reasons of space) in some areas. More detailed reviews of sieve tray distillation can be found in Lockett (1986), Kister (1990, 1992) and Stichlmair & Fair (1998).

2.2. Sieve Tray Operation

The sieve tray is the most common type of tray used in industrial distillations. It is made of a thin sheet of metal with holes punched or drilled through it. These holes are arranged either in triangular or square patterns and Figure 2.1 below shows the geometry of a typical sieve tray.

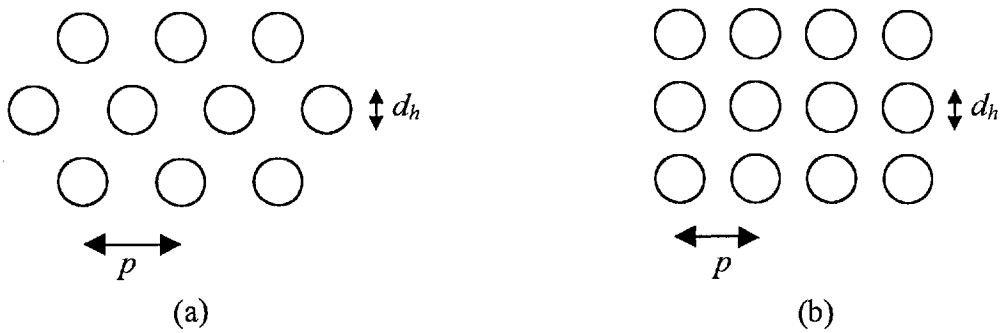


Figure 2.1. Sieve tray pitch layout: (a) triangular (b) square

The pitch (p) is the distance between the centres of adjacent holes. The open area fraction of the tray (A_f) can be calculated as follows:

$$A_f = \alpha_p \left(d_h / p \right)^2 \tag{2.1}$$

where $\alpha_p = \frac{\pi(3)^{0.5}}{6}$ for triangular pitch; $\alpha_p = \frac{\pi}{4}$ for square pitch

d_h = hole diameter

Commercial scale sieve trays have open area fractions from 5% to 15% with the most common being 8% to 12% (Lockett, 1986). For the same hole diameter to pitch ratio (d_h/p), trays with triangular pitch offer more open area than ones with square pitch. The thickness of the tray usually depends on the type of construction material and general guidelines are listed in "Distillation Operation" by Kister (1990).

The two-phase flows on a sieve tray present a typical example of chaotic flow behaviour in multiphase flow systems. Figure 2.2 gives an illustration of a typical two-phase flow structure on a sieve tray.

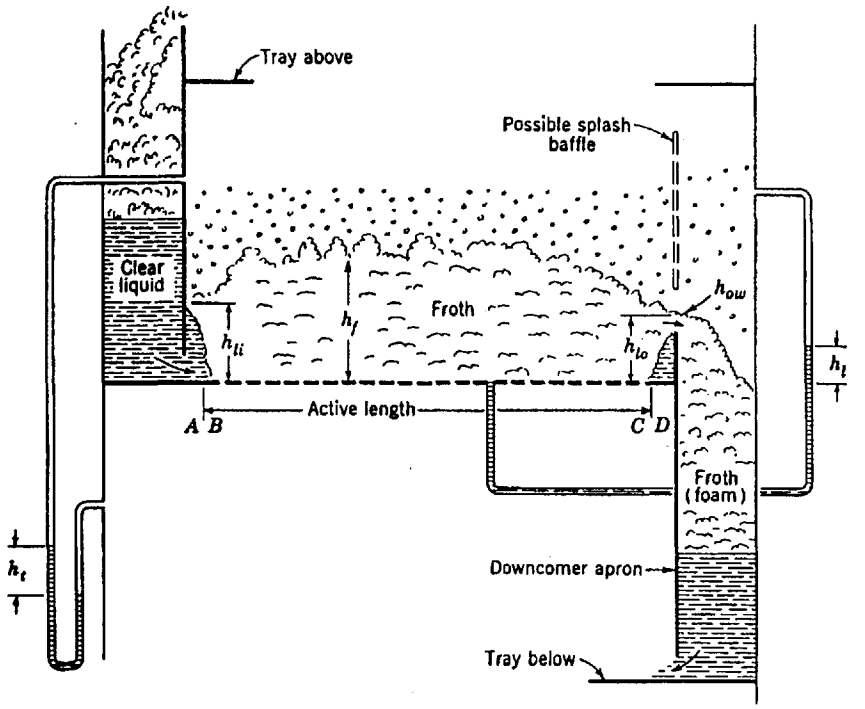


Figure 2.2. Tray dynamics schematic diagram (Smith, 1963)

2.2.1. Bubble Formation from an Orifice

Over the years, the study of flow patterns above a sieve tray has been based on the knowledge of those from an orifice plate. There has been a great deal of research both on bubble formation from orifices and on bubbly flows in vertical bubble columns. Kumar *et al* (1970) and Clift *et al* (1978) gave extensive reviews both on quantitative and qualitative aspects of bubble formation at a single orifice. More recently, Ponter and Surati (1997) published a review on bubble emission from submerged orifices; these authors reported that more than five hundred papers had been published and at least twenty predictive models had been developed over the past three decades. Discrepancies between experimental results obtained by different researchers (under similar conditions) have been pointed out in the paper and general guidelines have been given for future experimental work in the area.

2.2.1.1. Descriptions of the Bubbling Process

Among the numerous descriptions given to the bubble formation process, Kupferberg and Jameson (1969) divided the "idealised" (i.e. occurs at low gas flowrate) bubble growing process into three stages as shown in Figure 2.3.

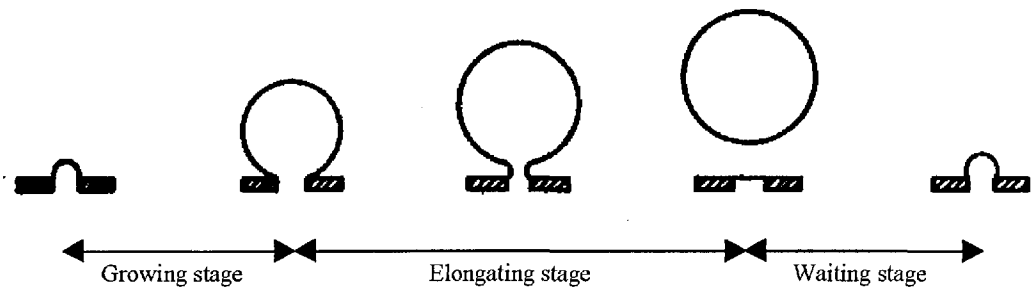


Figure 2.3. Idealised stages in bubble formation (Kupferberg and Jameson, 1969)

Growing stage:

As the bubble grows, the buoyancy is insufficient to overcome the inertial reaction of the surrounding liquid, with a resulting nett reactive force on the plate. This stage terminates when the equilibrium between the upward and downward forces is reached and the bubble starts to rise.

Elongating stage:

When the bubble rises, a small tail is developed to connect between the bubble body and the orifice. This tail is elongated up to a point when it finally breaks off and the bubble detaches from the orifice.

Waiting stage:

The formation of a bubble causes pressure fluctuation in the gas chamber below the orifice (a slight increase followed by a sharp fall). In this stage, the chamber pressure is built up to overcome the hydrostatic pressure, and then a new bubble will begin to grow. During this stage, some liquid can weep through the hole due to the lower chamber pressure.

The above descriptions only explain what happens near to the orifice and also, the "idealised" condition only occurs when the gas flowrate is low. Therefore, when considering the bubble formation process in a wider context (e.g. including the motion of bubbles after departing from an orifice), Davidson and Amick (1956) suggested that the process could be categorised into six stages in order of increasing gas flowrate:

1. *Static bubbling*

   The individual bubble volume remains more or less constant and the bubbling frequency is proportional to the gas flowrate. For the same orifice, the centre-to-centre spacing between the rising bubbles is inversely proportional to their frequency.

2. *Transition*

   An increase in gas flowrate produces a decrease in the spacing between bubbles and the frequency levels off due to the sharp increase in bubble volume. The interaction between two consecutive bubbles can be observed and perhaps explained by the formation of a liquid vortex ring at the orifice.

3. *Incipient coalescence*

   For a higher gas flowrate, bubbles begin to form in pairs although they are not physically attached. The phenomenon is known as the "doublet formation" where the upper part of the doublet is a hemi-spherical shape and the lower part is vertically elongated. This "mushroom-shape" doublet is similar to the behaviour of rising balls of explosion fires.

4. *Coalescence*

   With a further increase on gas flowrate, the two bubbles finally combine, and in most cases form a larger irregular bubble. However, there exist examples of different behaviour such as the lower bubble shooting completely through the upper one or the upper bubble absorbing the lower one incompletely and leaving a small residue. The experimental results showed that the frequency reached a maximum at this point.

5. *Coalescence at the orifice*

   Coalescence takes place closer and closer to the orifice as the gas flowrate increases, finally reaching the orifice level, which is when the first bubble has no time to rise before the second one merges. There is a noticeable drop on the bubbling frequency (the authors claimed 50% lower).

6. *Double coalescence*

   This phenomenon occurs when the large coalesced bubbles (as described in 5 above) undergo further coalescence themselves. The gas seems to be "jetting" instead of bubbling from the orifice and both phases are highly turbulent and erratic. This is a condition of particular interest to industry, however, turbulent flow measurements can be extremely difficult.

2.2.1.2. Modelling Aspects

The modelling of the bubbling process really began to take off after the pioneering work by Davidson and Schuler (1960). Their approach becomes the backbone of the later modelling work in the 1960's and the major assumptions on this type of approach were:

1. Spherical bubbles at all times
2. Negligible effects from liquid circulation
3. Negligible effect from the proceeding bubbles
4. The momentum of the gas is negligible

More recently, potential flow theory has been introduced as a common method of modelling the bubble formation under the condition of low gas velocity. The work by Kupferberg and Jameson (1969) and by McCann and Prince (1969, 1971) showed reasonably good agreement between the experimental results and the theory. Marshall *et al* (1990, 1993) and Rigby *et al* (1995) both carried out experiments on bubble

formation from an orifice with liquid cross-flow and the authors also presented their models based on the theory of potential flow which gave realistic simulation of primary bubble growth.

Although some success had been achieved on modelling the bubble formation process, these results are not usually applicable in turbulent flows where most of industrial applications are involved. In turbulent regions, the research relies very much on experimental observations and the results obtained by Muller and Prince (1972) and by Pinczewski *et al* (1973) are particularly useful. These authors developed a flow map which categorises the bubbly flow into different flow regimes and this is shown in Figure 2.4. Although this is a case dependent map, the general trends of the transition lines are still similar when the condition changes. These results are considered to be critical to the later development of the flow regime on a sieve plate.

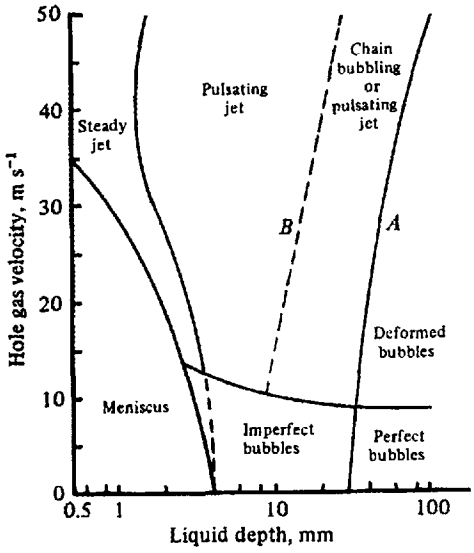


Figure 2.4.

Bubbling and jetting from single holes. d_h=6.4mm (Muller and Prince, 1972), modified by Pinczewski *et al*, 1973; picture extracted from Lockett, 1986)

2.2.2. Common Operational Flow Regimes on a Sieve Tray

The sieve tray flow pattern has been studied for more than thirty years and it combines the results of two complex situations: single-hole bubble formation and bubble interactions from neighbouring-holes. In addition, the flow conditions on sieve trays are usually more turbulent (i.e. beyond *Double coalescence*, described in the previous section) than those studied on single-hole cases. Therefore, it is more difficult to study the flow structures above sieve plates. Over the years, researchers have tended to use

different names for each regime; however, the most widely accepted ones are depicted in Figure 2.5 and can be described as follows:

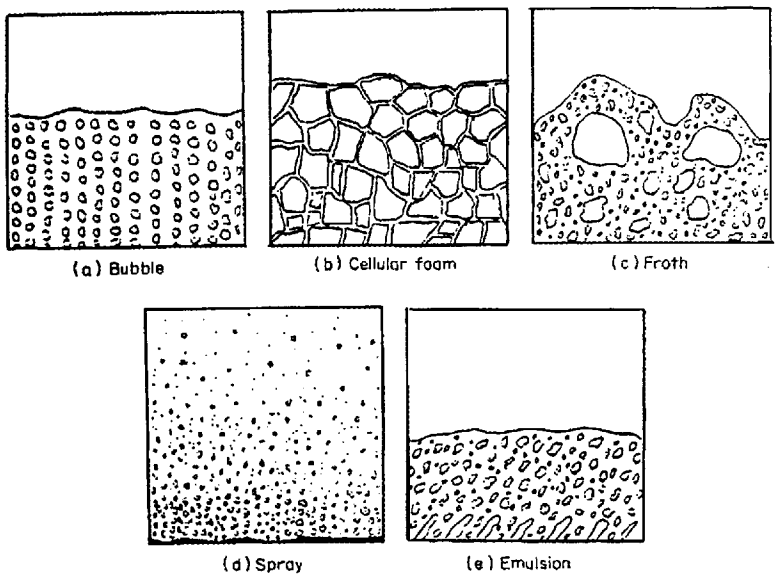


Figure 2.5. Common flow regimes on distillation trays (Kister, 1992)

Bubble Regime

This regime can be observed at very low gas and liquid flowrates. Bubbles are formed and detach periodically from all perforations; they grow and develop without interference from other bubbles from neighbouring holes or from later bubbles from the same hole. This regime has very limited importance on industrial practice.

Emulsion Regime

This regime occurs under similar conditions to the bubble regime, but at a comparatively higher liquid flowrate. Bubbles are said to be "emulsified" in the liquid phase as a result of its higher horizontal momentum. i.e. bubbles are sheared off before they can grow to their normal sizes. This regime is usually found in high-pressure distillation processes.

Foam Regime

Under certain conditions bubbles are difficult to coalesce and foam begins to occur, e.g. in more viscous or higher surface tension fluids. In distillation, this occurs at both low gas and liquid flowrates. Foams result either from the presence of mixtures, impurities or heat and mass transfer, which convey to bubbles the ability to resist coalescence

either with each other or at the upper surface of the dispersion (Lockett 1986). Cellular foam which consists of large dodecahedral bubbles is one of the common type of foams observed at low gas and liquid flow.

Froth Regime

The main characteristic of this regime is the existence of more frequent bubble coalescence, causing more vigorous interactions between the phases. The bubbles circulate rapidly through the liquid with a wide range of sizes and non-uniform shapes and they travel at different velocities. The degree of mixing is increased and therefore the heat and mass transfer is also enhanced. The froth regime can be observed at moderate gas flowrates and is commonly found in most atmospheric pressure distillation trays.

Spray Regime

At higher gas flowrates with low liquid depth, gas starts jetting through the holes. This is a gas continuous flow regime and liquid droplets of various sizes are lifted by the gas jets; both gas and liquid motions are highly turbulent. It has been concluded that the spray regime represents a stable regime of operation at high column throughput (Jeronimo and Sawistowski, 1973). This is also one of the most common regimes found in columns nowadays, especially ones operating in sub-atmospheric or vacuum conditions.

Summarising the descriptions above, the flow regime is determined by the following parameters:

- Flowrates of gas and liquid phase and their relative magnitude.
- Physical properties of the system, such as density, surface tension.
- Tray geometry, such as open fraction, hole size.
- Column operating condition, e.g. pressure.

A generalised flow map representing all the above-mentioned regimes is shown in Figure 2.6 (Lockett, 1986); this was plotted in terms of "Capacity Factor", CF $(=u_s[\rho_G/(\rho_L-\rho_G)]^{0.5}$ where u_s is the gas superficial velocity) and "Flow Parameter", FP $(=M_L\rho_G^{0.5}/M_G\rho_L^{0.5}$ where M_L and M_G are the liquid and gas flowrates, kg/s).

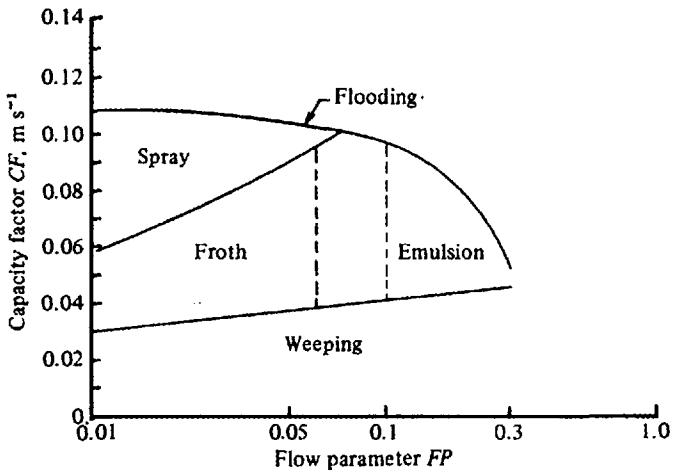


Figure 2.6. Capacity factor (based on bubbling area) vs. flow parameter showing flow regimes. (Lockett, 1986)

Generally speaking, for a constant gas flowrate (i.e. constant *CF*), as the Flow Parameter increases (representing an increase in liquid flowrate under constant *CF*), the regime will move from froth to emulsion. This is due to an increasing shearing force exerted from the liquid flow and also the slight increase on the liquid holdup on the tray, which causes greater resistance for the gas to pass through. For a fixed liquid flowrate, an increase in gas flowrate (which will give an increase in *CF* but a decrease in *FP*) will move the regime into spray, where vapour is the continuous phase.

The flow regime has significant effects on tray operation and therefore it is important to operate in the desired regime so that the required separation can be achieved. Another well-known flow regime map, similar to Figure 2.6, was developed by Hofhuis and Zuiderweg (1979) based on experimental data from different fluids in various systems, including toluene/toluene-vapour data from a 0.45-metre distillation column. This is shown in Figure 2.7 below.

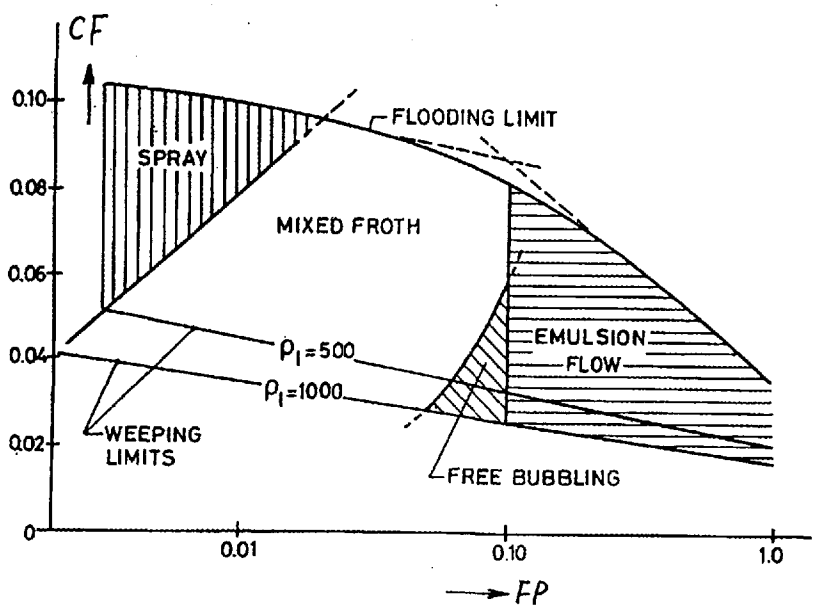


Figure 2.7. Flow regime map: capacity factor vs. flow parameter (Hofhuis and Zuiderweg, 1979)

Typically, each tray design is characterised by two operational limitations: *flooding* and *weeping* and these two limits can be seen in both Figures 2.6 and 2.7. The upper boundary of all the flow regimes is called flooding and it occurs when excessive liquid accumulates inside the column. There are two possible causes: (1) excessive liquid entrainment from the tray below and (2) liquid backup in the downcomer. Flooding can be explained by the high gas flowrate providing greater momentum to the liquid droplets which are then lifted up to the tray above. The high gas flow also gives higher resistance for the liquid to enter the tray deck from the downcomer and hence the liquid level builds up in the downcomer to cause a "backup" situation. A correlation developed by Fair (1961) predicts the conditions when flooding occurs under a given flow parameter and tray spacing. This is given in Figure 2.8 below.

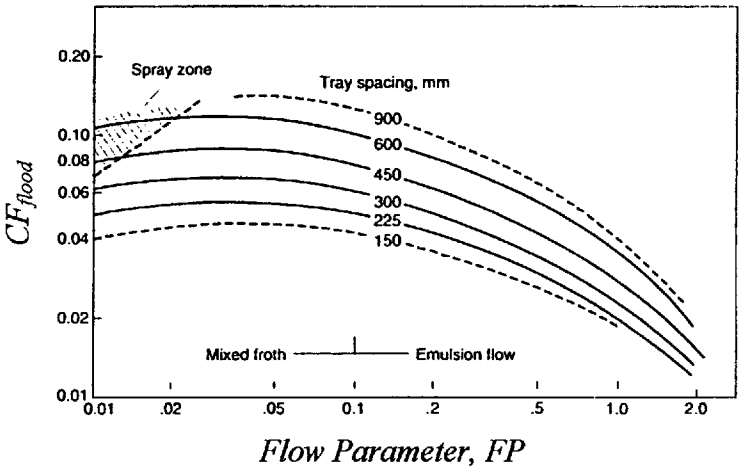


Figure 2.8. Flooding correlation for columns with crossflow trays (Fair, 1961)

where $CF_{flood} = u_{s,flood}[\rho_G/(\rho_L - \rho_G)]^{0.5}(20/\sigma)^{0.2}$

The lower boundary of all regimes is called weeping and it is caused by insufficient vapour flow, which does not provide enough pressure underneath the tray floor to hold the liquid. Instead of liquid flowing over the outlet weir, some of the liquid weeps through the perforations to the tray below. The limiting factors for weeping are the surface tension of the liquid and the vapour flowrate.

2.2.3. Flow Regime Transition on a Sieve Tray

From the previous section, descriptions for each flow pattern on a sieve tray have been defined and they can be easily demonstrated experimentally. However, the physics behind the transitions between these flow patterns is not well understood. Both semi-empirical and empirical relationships for flow regime transitions are available and it is important to note that although, mathematically, these relationships represent sharp changes, the actual transitions are nevertheless found to be more gradual.

2.3.3.1. Emulsion-Froth Flow Regime Transition

Existing correlations for emulsion-froth transition are mostly based on a simple condition: the transition takes place when the horizontal momentum of liquid phase is comparatively larger than the vertical momentum for the vapour phase. This is mathematically described by:

$$\left(\frac{Q_L}{Wh_L}\right)^2 \rho_L > u_h^2 \rho_G \tag{2.2}$$

where Q_L is volumetric liquid flowrate, W is the width of outlet weir, h_L is the clear liquid height on the tray (see Section 2.3.2 later) and u_h is the hole velocity.

Hofhuis and Zuiderweg (1979), proposed the following correlation for the transition based on the condition stated in Eq.(2.2) together with their experimental data:

$$\frac{Q_L}{Wu_s}\left(\frac{\rho_L}{\rho_G}\right)^{0.5} > 0.2 \tag{2.3}$$

where u_h is the superficial velocity based on the tray active area.

Later, Zuiderweg (1984, 1986) proposed further correlations based on a wider experimental database and these are similar to Eq.(2.3).

2.3.3.2. Froth-Spray Flow Regime Transition

There has been a great deal of research into the froth-spray transition since both are the dominant flow regimes occurred in the industrial distillation columns. The available prediction methods are either of empirical or semi-empirical nature and they can be divided into three categories: (1) semi-empirical correlations related to the "Terminal Velocity Model", (2) semi-empirical correlations which have similar form to the "Jet Penetration Model", (3) other empirical correlations.

- **Terminal Velocity Model**

The concept of the Terminal Velocity Model which describes the flow transition from spray to bubbling was first developed by Porter and Wong in 1969. It relates the terminal velocity of a single drop of liquid falling in gas to the rate of change of gas velocity above the plate (i.e. from the hole velocity, u_h, to the superficial velocity, u_s).

Porter and Wong stated that for liquid drops diameters greater than 5mm, the terminal velocity of a droplet is found to be independent of drop size, and it is called "the large drop terminal velocity" (u_t) defined as:

$$u_t = 1.04\left(\frac{\rho_L}{\rho_G}\right)^{0.5} \qquad \text{for } d_p > 5\text{mm} \tag{2.4}$$

where d_p is the drop diameter.

When liquid begins to be added onto a dry tray, drop coalescence occurs and becomes more frequent as more liquid is added. The transition is said to take place at a plane (parallel to the plate) where the gas velocity is equal to the large drop terminal velocity. At this plane, multiple drop coalescence occurs and this represents the lower limit of the gas continuous region. The authors' experimental results revealed the following relationship:

$$\frac{h_L}{d_h} = 4.0(1-\varepsilon) + 9(1-\varepsilon)\left[\frac{(u_h - u_t)}{(u_h - u_s)}\right] \tag{2.5}$$

$$\text{for} \qquad 0 < \left[\frac{(u_h - u_t)}{(u_h - u_s)}\right] < 0.8$$

where ε is the gas fraction.

This equation predicts the height (h_L) above the tray where the plane of large drop terminal velocity exists as a function of gas velocity, hole size, average void fraction and the density of the gas and liquid. However, later researchers argued that this correlation is only accurate for predicting the transition for trays with about 5% open area as the data used to develop this correlation were obtained solely from a 5% open area tray. Subsequent works following this theory include the correlations by Wong and Kwan (1979), Chen *et al* (1982) and Kwan *et al* (1992).

- **Jet Penetration Model (Lockett, 1981)**

The Jet Penetration Model (Lockett, 1981) for the froth-spray transition assumes uniform pressure from the tray floor to the top of the jet. The transition point is reached when the gas jet is momentarily brought to rest by a "liquid bridge". The force underside of the liquid bridge is due to gas momentum and on the upper surface of the liquid bridge, the force comes from the liquid head above it. This is illustrated in the Figure 2.9.

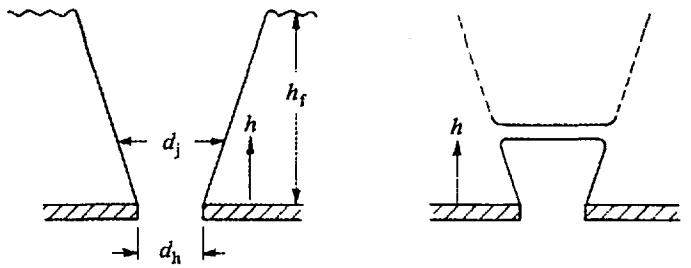


Figure 2.9. (a) Gas jet penetrating the froth ;
(b) bridging of gas jet by liquid (Lockett, 1981)

After solving the force balance on the liquid bridge, the following relationship can be obtained:

$$\frac{h_L}{d_h} = \frac{(4+n)/n}{(4/n)^{4/(4+n)}}\left(\frac{\rho_G}{\rho_L}\right)^{n/(4+n)} \frac{u_h^{2n/(4+n)}}{a^{4/(4+n)}} \frac{(1-\varepsilon)^{4/(4+n)}}{(gd_h)^{n/(4+n)}} - \frac{(1-\varepsilon)}{a} \tag{2.6}$$

where n and a are unknown parameters defined as

$$\left(\frac{d_j}{d_h}\right)^n = a\left(\frac{h}{d_h}\right) + 1 \tag{2.7}$$

and d_j and h are the parameters given in Figure 2.9.

Although Lockett derived this theoretical relationship in 1981, however, several earlier correlations already bear some resemblance to Eq.(2.6). These methods represent some particular cases of this model and they are listed below.

Payne and Prince (1977) developed the following relationship at the transition

$$\frac{h_L}{d_h} = 1.5\left(\frac{\rho_G}{\rho_L}\right)^{0.5} \frac{u_h(1-\varepsilon)^{0.5}}{(gd_h)^{0.5}} \tag{2.8}$$

This is similar to Eq. (2.6) with n=4, i.e.

$$\frac{h_L}{d_h} = 2\left(\frac{\rho_G}{\rho_L}\right)^{0.5} \frac{u_h(1-\varepsilon)^{0.5}}{a^{0.5}(gd_h)^{0.5}} - \frac{(1-\varepsilon)}{a} \tag{2.9}$$

Barber and Wijn (1979) proposed the following relationship for the transition:

$$\frac{h_L}{d_h}=1.35\left(\frac{\rho_G}{\rho_L}\right)^{0.25}\frac{u_h^{0.4}}{(gd_h)^{0.2}}\left(\frac{p}{d_h}\right)^{0.33}-0.59\left(\frac{p}{d_h}\right)^{0.33} \tag{2.10}$$

This is similar to Eq.(2.6) with n=1, i.e.

$$\frac{h_L}{d_h}=1.65\left(\frac{\rho_G}{\rho_L}\right)^{0.2}\frac{u_h^{0.4}}{a^{0.8}}\frac{(1-\varepsilon)^{0.8}}{(gd_h)^{0.2}}-\frac{(1-\varepsilon)}{a} \tag{2.11}$$

Hofhuis and Zuiderweg (1979) proposed the following empirical correlation for the transition:

$$\frac{h_L}{d_h}=1.07\left(\frac{\rho_G}{\rho_L}\right)^{0.33}\frac{u_h^{0.66}}{(gd_h)^{0.33}} \tag{2.12}$$

This is similar to Eq.(2.6) with n=2, i.e.

$$\frac{h_L}{d_h}=1.89\left(\frac{\rho_G}{\rho_L}\right)^{0.33}\frac{u_h^{0.66}}{a^{0.66}}\frac{(1-\varepsilon)^{0.66}}{(gd_h)^{0.33}}-\frac{(1-\varepsilon)}{a} \tag{2.13}$$

Lockett (1981) compared the above three relationships and found none of them is completely satisfactory.

- **Other Empirical Correlations**

There are some other empirical flow regime transition correlations which were solely based on experimental data. Two of the common ones are described below:

Lockett (1981)

Although Lockett presented the Jet Penetration Model in his 1981 paper and examined other correlations mentioned in previous section, no new relationship based on this model was given. Instead, it was found that a simple, empirical correlation could fit all the available experimental data much better (compared to Eqs.(2.8), (2.10) and (2.12) in the previous section). This equation is given as:

$$\frac{h_L}{d_h}=2.78\left(\frac{\rho_G}{\rho_L}\right)^{0.5}u_h \tag{2.14}$$

Fell and Pinczewski (1982)

The Fell and Pinczewski (1982) correlation predicts the transition in terms of the gas and liquid flowrates only, in contrast to most of other relationships where the clear liquid height (h_L) at transition is needed. The authors found that the major factors affecting the transition on sieve trays are gas and liquid loading, tray open area, hole diameter, and system gas and liquid densities. Surface tension was said to have an insignificant effect. This correlation has a maximum error of less than 10% when compared against the air/water experimental data of Pinczewski and Fell (1972).

$$u_s \rho_G^{0.5} = 2.75 \left(\frac{Q_L}{W} \rho_L^{0.5} \right)^n \tag{2.15}$$

where $n = 0.91 \left(d_h / A_f \right)$

2.3. Hydrodynamics

In the previous section, the two-phase flow behaviour above a tray has been described qualitatively. However, merely knowing the flow pattern is insufficient for the purposes of plant operation and design. In addition to the qualitative description, it is important to provide more quantitative details of the flow conditions. In this section, various hydrodynamic parameters are introduced for this purpose and some available prediction methods for these parameters are also included.

2.3.1. Dispersion Density

An important parameter in sieve tray operation is the dispersion density which can either be expressed as gas or liquid fraction. The average liquid fraction can be defined as the ratio of the clear liquid height (h_L) to the froth height (h_f), i.e.

$$\alpha = h_L / h_f \tag{2.16}$$

Clear liquid height is the level to which the liquid were collapsed on the tray in the absence of the gas and froth height is the highest point which a drop of liquid can travel in the vertical direction.

An indirect, but common, experimental technique to determine the average liquid fraction on the tray is to use a floor-mounted manometer (shown in Figure 2.10) which measures the clear liquid height. The froth height is usually determined by either visual observation, γ-radiation or a light transmission technique.

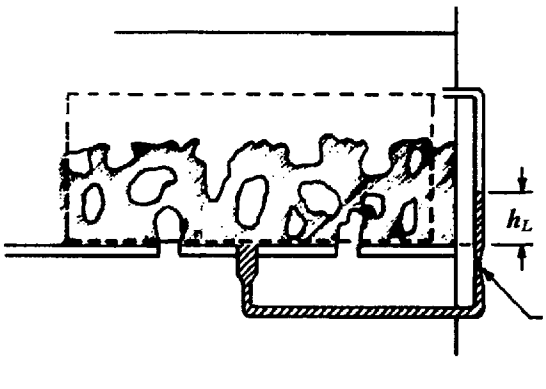


Figure 2.10.

Measurement of clear liquid height by floor mounted manometer (Lockett, 1986)

An alternative method is γ-ray attenuation where γ-radiation is used to scan through the column to obtain the local time-averaged liquid fraction (shown in Figure 2.11). This will give a full profile of the dispersion density above the tray and the clear liquid height can be calculated by integrating the profile along the vertical direction. The froth height is simply the location where a low arbitrary liquid fraction (e.g. $\alpha = 0.01$ used by Hofhuis and Zuiderweg, 1979; $\alpha = 0.05$ used by Tezock, 1994) has been reached.

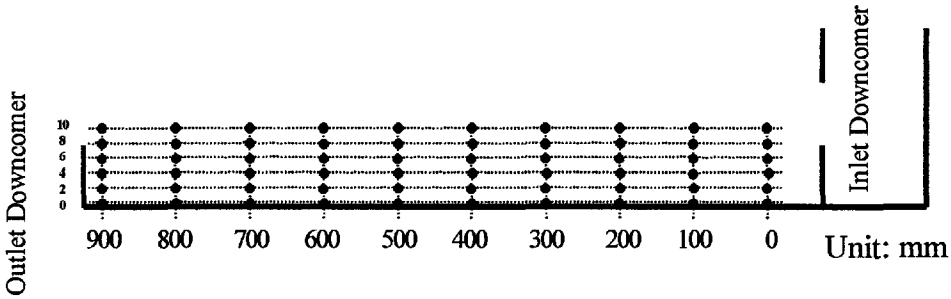


Figure 2.11. Positions for local dispersion density measurement above a sieve tray. The dots represent measuring positions.

Figure 2.12 below shows typical froth density profiles above a sieve tray and it can be observed that the profile depends strongly on the operating flow regime.

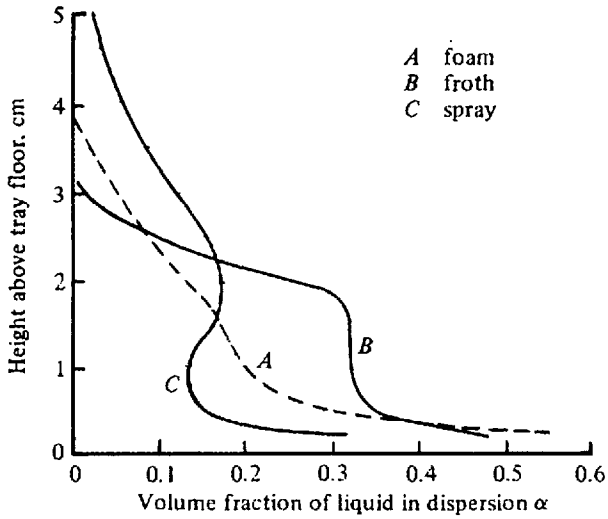


Figure 2.12. Dependence of dispersion density profile on regime (Lockett, 1986)

The relationships available for the prediction of tray dispersion density are both theoretical and empirical. Azbel (1963) first developed a theoretical expression of the average dispersion density relating solely to the dimensionless Froude number. He considered the energy balance in a discrete elementary layer in a two-phase system. It was assumed that the total energy of the layer is equal to the sum of the potential energy of the liquid, the kinetic energy of the layer and the surface energy arising from surface tension. The total energy of the froth can be obtained by integrating the elementary layer expression over the dispersion height. The steady-state distribution of the liquid content, α, sets in when the total energy of the whole two-phase dispersion is at minimum (this is also the criteria for all other theoretical studies on average dispersion density). The author proposed the following expressions for the local and average liquid fraction:

Local: $$\alpha(y) = 1 - \sqrt{\frac{Fr/4}{\left(1+\sqrt{Fr/4}\right)^2 - \frac{y}{h_L}}} \qquad (2.17)$$

Average: $$\alpha = \frac{1}{1+\sqrt{Fr}} \qquad (2.18)$$

where the Froude number, Fr, is defined as $Fr = u_s^2 / g\, h_L$

It was concluded that the dispersion density does not depend on the physical properties of the gas and liquid and the bubbling apparatus geometry.

Kim (1966) took a step further by considering the energy balance on a three dimensional differential control volume. The bubbles were assumed to be elliptical and the average gas holdup fraction was determined by limiting the value of total energy. The new equations for local and average liquid fraction are more complex than the previous ones by Azbel (1963) and depend on the cubic root of Froude number.

Local: $$\alpha(y) = 1 - \sqrt[3]{\frac{u_s^2}{2yg}} \tag{2.19}$$

Average: $$\alpha = \frac{1}{1 + \sqrt[3]{\frac{\rho_L^2 Fr}{2\rho_M^2}}} \tag{2.20}$$

where $$\rho_M = \rho_L \left(\begin{array}{l} 1 + \frac{Fr}{6} + \sqrt[3]{\frac{Fr/2 + Fr^2/6 + Fr^3/108 + \sqrt{Fr^2/4 + Fr^3/54}}{2}} \\ + \sqrt[3]{\frac{Fr/2 + Fr^2/6 + Fr^3/108 - \sqrt{Fr^2/4 + Fr^3/54}}{2}} \end{array} \right)^{-1}$$

Other theoretical relationships for the local and average liquid fraction are based on the similar theory of minimising the total energy of the two-phase dispersion and these are listed in Table 2.1.

Authors	Liquid fraction (α) models
Kolar *et al.* (1969, 1971, 1973)	Local: $\frac{y}{h_L} = \left(\frac{\varepsilon_0 \varepsilon_{h_f}}{\varepsilon_{h_f} - \varepsilon_0}\right)\left\{\left(\frac{\varepsilon - \varepsilon_0}{\varepsilon \varepsilon_0}\right) + \ln\left[\frac{(1-\varepsilon_0)\varepsilon}{(1-\varepsilon)\varepsilon_0}\right]\right\}$ & $\alpha = 1 - \varepsilon$ For ε_0 & ε_{h_f} : (1) maximum values, take $\varepsilon_0 = A_f$ & $\varepsilon_{h_f} = 1$ (2) use correlation, $\varepsilon_0 = 0.824 \exp\left(-3.6 h_L^{0.5} u_s^{-0.25}\right)$ & ε_{h_f} = arbitrary specified value
Takahashi *et al.* (1973)	Local: $\alpha(y) = 1 - \left[1 + \frac{2\rho_L g(h_f - y)}{\left(\rho_G + \frac{43}{5}\rho_L\right) u_s^2}\right]^{-0.5}$ Average: $\alpha = \frac{1}{1 + \sqrt{\frac{86}{5} Fr}}$
Unno & Inoue (1976)	Local: $\alpha(y) = 1 - \left[1 + \frac{g\left(h_w + \sqrt{\frac{Q_L}{W}} - y\right)}{\alpha_0 u_s^2}\right]^{-0.5}$ where $u_s > 0.63$ m/s: $\alpha_0 = 24/(100 u_s - 40)$ $u_s \leq 0.63$ m/s: $\alpha_0 = 1$

Table 2.1. Theoretical relationships for liquid holdup

Some literature (e.g. Colwell, 1981) reported that theoretical expressions for the two-phase dispersion density tend to give large errors when compared to experimental data and better accuracy can be achieved by using empirical correlations. Some commonly used empirical correlations are listed below in Table 2.2.

Authors	Liquid fraction (α) correlation
Gardner and McLean (1969)	$\alpha = 1 - 0.205F_s + \frac{8.7\sigma\rho_L}{\rho_{water}} - 0.55$ for $0.49 < F_s < 1.1$
Kawagoe *et al.* (1976)	*Bubble flow:* $\alpha = 1 - \frac{100u_s}{55(100d_h)^{1/3}}$ *Cellular-foam flow:* Estimates to be around $0.7 \sim 0.9$ *Froth flow:* $\alpha = \left(1 + 1.6Fr^{1/3} + 0.22Fr\right)^{-1}$ for $h_L < 0.5$ m $\alpha = 1 - \frac{100u_s}{170u_s + 36}$ for $h_L > 0.5$ m
Stichlmair (1978)	$\alpha = 1 - \left(\frac{F_s}{F_{s\max}}\right)^{0.28}$ for $0.03 < \frac{F_s}{F_{s\max}} < 0.9$ where $F_s = u_s\rho_G^{0.5}$ and $F_{s\max} = 2.5\left[A_f^2\sigma(\rho_L - \rho_G)g\right]^{0.25}$
Takahashi *et al.* (1979)	For $d_h \le 2$ mm, $u_s < 0.4$ m/s $\alpha = \left(1. + 8.5Fr^{1/2}\right)^{-1}$ for $Fr \le 4.68\times10^{-4}A_f^{-0.56}$ $\alpha = \left(1. + 1.25A_f^{-0.14}Fr^{1/4}\right)^{-1}$ for $Fr > 4.68\times10^{-4}A_f^{-0.56}$
Colwell (1981)	For froth regime conditions: $\alpha = \left[1 + 12.6\left(\frac{Fr\rho_G}{\rho_L - \rho_G}\right)^{0.4} A_f^{-0.25}\right]^{-1}$

Table 2.2. Commonly used correlations for the calculation of liquid holdup

Empirical correlations are normally based on limited amount of data and therefore, they are very sensitive to the actual operating conditions. Colwell's correlation (1981) is probably the only exception since the theoretical effect of Froude number was included in the correlation (Lockett, 1986). Stichlmair's correlation (1978) is also recommended since it has some theoretical basis, namely a fluidisation model.

2.3.2. Clear Liquid Height

Clear liquid height (i.e. the level to which the liquid were collapsed on the tray in the absence of the gas) is probably one of the most important parameter in distillation operation. It is not only required to predict the total pressure loss (see Section 2.3.3 below), it is also related to flow regime, entrainment and efficiency (see later sections). In laboratory experiments, tray floor-mounted manometers or gamma densitometer (to obtain the liquid fraction profile above the tray) were used to measure the clear liquid height; in an industrial scale operation, manometers are used. Research on this topic has been carried out over the past few decades and there exist a considerable number correlations for predictions of clear liquid height. These can be separated into three major categories: (1) semi-empirical correlations based on the Francis (1883) weir equation, (2) empirical correlations and (3) aeration factor methods.

2.3.2.1. Francis-Equation Based Correlations

Civil engineers first established the Francis weir equation from open channel flow and it was modified according to the geometry of the outlet weir to obtain the so-called the Francis's equation for flow over the exit weir of a distillation tray:

$$h_L = (1-\varepsilon)\left[h_w + \frac{0.49}{C_d^{2/3}}\left(\frac{Q_L}{(1-\varepsilon_w)W}\right)^{2/3}\right] \tag{2.21}$$

where h_w is the outlet weir height, C_d is the discharge coefficient, Q_L is the volumetric liquid flowrate and W is the width of the weir.

The above relationship was derived from first principles (Bernoulli's equation) but it has a disadvantage: the gas fraction of froth over the outlet weir, ε_w, is rather difficult to obtain in practice, so it is usually assumed to be equal to the average gas fraction above the tray floor, ε. This is the assumption which some of the later researchers modified to develop new correlations.

- **Stichlmair (1978)**

Stichlmair (1978) argued that most of the published correlations for froth height (i.e. therefore clear liquid height) are often neither dimensionally correct nor do they

adequately represent the limiting conditions. The backbone of Stichlmair's own correlation is Francis equation which assumed a continuous layer of flowing liquid over the outlet weir under which the condition is close to that of froth regime. If there are a significant number of projected liquid droplets over the weir, the relationship will no longer be valid. Therefore, the author resolved the problem by adding an extra term to account for these spraying liquid droplets.

$$h_L = (1-\varepsilon)\left[h_w + \frac{1.45}{g^{1/3}}\left(\frac{Q_L}{(1-\varepsilon)W}\right)^{2/3} + \frac{125}{g(\rho_L-\rho_G)}\left(\frac{F_s - 0.2\sqrt{\rho_G}}{\varepsilon}\right)^2\right] \tag{2.22}$$

where F_s is the F-factor based on superficial velocity, $F_s = u_s\sqrt{\rho_G}$

The last term is only considered when $F_s - 0.2\sqrt{\rho_G} > 0$. For trays with an exit calming zone before the outlet weir, the following equation should be used instead of Eq.(2.22):

$$h_L = (1-\varepsilon)\left[h_w + \frac{1.45}{g^{1/3}}\left(\frac{Q_L}{W}\right)^{2/3}\right] \tag{2.23}$$

- **Hofhuis and Zuiderweg (1979)**

The correlation of Hofhuis and Zuiderweg (1979) predicts the "clear liquid height over the weir", $h_{L,ow}$ rather than the clear liquid height (h_L) itself. This correlation also emphasises the influence of projected liquid droplets on h_L. According to the authors, the specified regimes suitable for using this correlation are spray and mixed-froth regimes which can be distinguished by the flow parameter ψ. The clear liquid height is given as the sum of $h_{L,ow}$ and h_w (the weir height):

$$h_L = h_w + h_{L,ow}$$

The relationship for $h_{L,ow}$ are given as follows:

For $0.006 < \psi < 0.2$: $$h_{L,ow} = 0.26\psi^{-0.37}\left(\frac{Q_L}{W}\right)^{0.67} \tag{2.24}$$

For $0.2 < \psi < 1.0$: $$h_{L,ow} = 0.48\left(\frac{Q_L}{W}\right)^{0.67} \tag{2.25}$$

where the parameter ψ is defined as $\psi = \frac{Q_L}{Wu_s}\sqrt{\frac{\rho_L}{\rho_G}}$

- **Colwell (1981)**

Colwell (1981) took the original form of the Francis equation and assumed $\varepsilon_w=\varepsilon$. The value of the weir coefficient C_d was established from the studies of single-phase flow (Daily & Harleman, 1966). Due to the fact that the assumption of continuous liquid flow over the weir still remains, the correlation should be applied in the froth regime (the condition stated by the author was u_s<2.0 m/s). The Colwell correlation is as follow:

$$h_L = (1-\varepsilon)\left[h_w + \frac{0.49k}{C_d^{2/3}}\left(\frac{Q_L}{(1-\varepsilon)W}\right)^{2/3}\right] \tag{2.26}$$

where $k = 1.49$ and $C_d = 0.61 + 0.08\frac{h_{ow}}{h_w}$ when $\frac{h_{ow}}{h_w} \le 8.14$

$$C_d = 1.06\left(1+\frac{h_w}{h_{ow}}\right)^{1.5} \text{ when } \frac{h_{ow}}{h_w} > 8.14$$

and $h_{ow} = \frac{h_L}{1-\varepsilon} - h_w$

- **Bennett *et al* (1983)**

Bennett *et al* (1983) collected data on distillation tray pressure drop from a number of sources and their proposed correlation gave a mean absolute error of 6.0% and an average error of –0.6% based on their data bank. Their proposed correlation is as follows:

$$h_L = \phi_e\left[h_w + C\left(\frac{Q_L}{W\phi_e}\right)^{2/3}\right] \tag{2.27}$$

where $C = 0.5 + 0.438\exp(-137.8h_w)$ and $\phi_e = \exp\left[-12.55\left(u_s\left(\frac{\rho_G}{\rho_L-\rho_G}\right)^{0.5}\right)^{0.91}\right]$

The correlation was assumed to be of the form of the Francis equation and the constants in the expressions of C and ϕ_e were tested from various choices until the standard deviation relative to the data bank was minimised.

2.3.2.2. Empirical Correlations

Empirical correlations for predicting the clear liquid height were developed solely on the basis of experimental data and they generally lack of physical basis relative to the actual fluid mechanics on the tray. Therefore, they should be used with care as they may be only valid for the range of flow conditions under which the data were collected.

- **Hofhuis and Zuiderweg (1979)**

In addition to publishing their correlation based on the Francis equation (see Section 2.3.2.1 above), Hofhuis and Zuiderweg (1979) also proposed an empirical correlation based on their data from air-water simulators and from a toluene-toluene vapour system in a small distillation column. The correlation is valid for both froth and spray regime:

$$h_L = 0.6\psi^{0.25} h_w^{0.5} p^{0.25} \tag{2.28}$$

for h_w=0.025-0.10m; p=0.012-0.04m; A_f=3.7-7.2%; d_h=0.003-0.01m.

- **Dhulesia (1984)**

Dhulesia (1984) suggested that different correlations should be applied for different flow regimes and the use of only one single equation by Hofhuis and Zuiderweg (1979) was considered inappropriate. A modified version of Hofhuis and Zuiderweg correlation which describes the clear liquid height in the froth regime was given by Dhulesia as follows:

$$h_L = 0.5\psi^{0.35} h_w^{0.5} p^{0.17} \tag{2.29}$$

for the following ranges of parameters: h_w=0.025-0.075 m; p=0.010-0.04 m; A_f=10.2%; d_h=0.0032-0.0127 m; Q_L/W=0.0055-0.028 m^3/(ms); F_s=1.30-2.85 m(kg/m^3)$^{0.5}$/s.

- **Bekassy-Molnar and Mustafa (1991)**

The correlation of Bekassy-Molnar and Mustafa (1991) is also a flow regime dependent relationship and on the basis of the froth-spray transition correlation given by Chen *et al* (1982), the appropriate clean liquid height equation for each regime is given as:

Froth regime $$h_L = 0.084 A_f^{-0.36} h_w^{0.64} d_h^{-0.19} \psi^{0.35} - d_G \tag{2.30}$$

Mixed regime $$h_L = 0.091 A_f^{-0.70} h_w^{0.63} \psi^{0.33} - d_G \tag{2.31}$$

Spray regime $$h_L = 0.015 A_f^{-1.61} h_w^{0.5} d_h^{0.33} - d_G \tag{2.32}$$

The ranges covered by the correlation are as follows: h_w=0.025-0.075 m; A_f =4.5-14.4%; d_h=0.003-0.0127 m; Q_L/W=0.0003-0.016 $m^3/(ms)$; F_s=0.41-3.8 $m(kg/m^3)^{0.5}/s$.

An important point to note in this correlation (Eqs. 2.30 to 2.32) is the term d_G. This parameter takes account of the dynamic effect due to the gas stream (in another word, the slow down of gas stream when passing through the tray) which is usually not negligible on sieve plates with small free cross section. This extra term (d_G) is given as follows:

$$d_G = \frac{M_G}{A_s(u_h - u_s)\rho_L g} \tag{2.33}$$

- **Other correlations**

There are also a number of empirical correlations given in the form of the following equation:

$$h_L = \alpha' h_w - \beta' F_s + \gamma' \frac{Q_L}{W} + \delta' + \left[\frac{u_s \rho_G (u_h - u_s)}{\rho_L g}\right] \tag{2.34}$$

where the last term takes account of the momentum head for the vapour leaving the holes. This term is included because of the use of floor mounted manometer for the measurement of clear liquid height. The values for the four constants in Eq.(2.34) for the respective correlations are given in Table 2.3.

Correlation	α'	β'	γ'	δ'
Barker & Self (1962)	0.637	0.012	1.78	0.024
Harris & Roper (1962)	0.58	$0.23h_w$	3.68	0.006
Gerster (1963)	0.725	$0.238h_w$	1.23	0.006
Finch & Van Winkle (1964)	0.22	0.012	4.54	0.025
Thomas & Campbell (1969)	0.19	0.0083	1.59	0.04
Brambilla (1969)	0.72	0.025	2.16	0.003
Thomas & Haq (1976)*	0.42	0.0096	3.93	0.031

* Exclude the vapour momentum term when calculating h_L

Table 2.3. Other empirical correaltions for clear liquid height

However, all of these correlations were based on authors' own data banks which were obtained from different experimental apparatus and the fluid systems. Thus, the correlations are case dependent and extra care should be taken when using them in order

to obtain a satisfactory prediction. Table 2.4 shows the conditions for using these correlations.

Correlation	Conditions
Barker & Self (1962)	d_h=4.8mm, p=19.1mm, t=4.8mm, 5% opening, air/water system
Harris & Roper (1962)	d_h=4.8mm, p=14.3mm, t=3.2mm, 4.37% opening, 38mm calming zones at both ends, air/water system
Gerster (1963)	N/A (not specified)
Finch & Van Winkle (1964)	d_h=1.6-7.9mm, 7% opening, air/water-methanol system
Thomas & Campbell (1969)	d_h=4.8mm, p=9.6mm, t=4.8mm, 5% opening, 114mm inlet & 152mm outlet calming zones, air/water-glycerol (55% by weight) system
Brambilla (1969)	d_h=3-5mm, p=9-15mm, t=1-2mm, 10-12% opening, air/water system
Thomas & Haq (1976)	d_h=9.6mm, t=3.2mm, 10.8% opening, air/water-glycerol (50% by weight) system air/aq.Na_2CO_3 system

Table 2.4. Conditions for the empirical correlations in Table 2.3

2.3.2.3. Aeration Factor Method

This method predicts the sum of the clear liquid height and the residual head loss (see Section 2.3.3 later), known as h'_L. It relates the two-phase pressure head loss to the operating liquid seal (h_w+$h_{L,ow}$) at the tray outlet weir and also taking the tray hydraulic gradient into consideration. i.e.

$$h'_L = h_L + h_\sigma = \beta\left(h_w + h_{L,ow} + 0.5h_{hg}\right) \tag{2.35}$$

where h_σ is the residual head loss and h_{hg} is the hydraulic gradient

There are a number of ways to determine the aeration factor β although some authors reported that the value of β is reasonably constant over the range of their operating flowrates (β= 0.5-0.65). Hutchinson *et al* (1949) developed a theoretical relationship between the aeration factor, β and the average liquid fraction α.

$$\beta = \frac{\alpha + 1}{2} \tag{2.36}$$

However, the value of α is usually unknown and needs to be obtained from correlations. A more practical approach is to use the graph in Figure 2.13 which shows the value of β plotted against the hole F-factor at different weir heights.

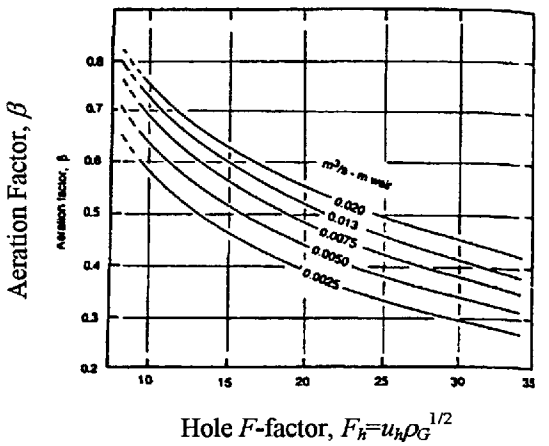


Figure 2.13. Aeration factor for pressure drop calculation (*Perry's Chemical Engineers' Handbook*, 1992)

For simplicity, the curves in the above figure can be represented by the equation:

$$\beta = 0.0825 \ln\left(\frac{Q_L}{W}\right) - 0.269 \ln F_h + 1.679 \tag{2.37}$$

The value of $h_{L,ow}$ can be estimated from the Francis weir equation depending on the outlet weir type, e.g. for a segmental weir:

$$h_{L,ow} = 0.664\left(\frac{Q_L}{W}\right)^{2/3} \tag{2.38}$$

2.3.3. Pressure Drop across a Sieve Tray

Generally, the pressure drop across a distillation tray consists of three parts: the pressure loss due to vapour flow through the tray perforations, the pressure loss due to the liquid above the tray floor and a residual term which accounts for the pressure loss during the bubble formation process. It is often more convenient to express the pressure drop in terms of liquid height:

$$h_T = h_D + h_L + h_\sigma \tag{2.39}$$

where h_T is the total pressure head loss (equivalent height of liquid), h_D is the pressure head loss due to a dry tray, h_L is the pressure loss due to the clear liquid on the tray, and h_σ is the pressure head loss due to bubble formation.

The following sections will describe each of these components of the pressure head loss and the ways to estimate them.

2.3.3.1. Dry Tray Pressure Loss Head, h_D

When gas passes through tray perforations, it experiences irreversible pressure losses which are due to the contribution of three different components, namely, contraction loss, hole friction loss, and expansion loss. This pressure drop is normally related to an orifice-type equation in the form of:

$$h_D = \frac{\xi \rho_G}{2g\rho_L} u_h^2 \tag{2.40}$$

where ξ is the orifice coefficient.

Since the 1950s, there have been more than twenty correlations for dry tray pressure drop published in the literature. Although most of these are based on limited amount of data, they generally have similar conclusions about the factors which affect the dry tray pressure drop. The orifice coefficient ξ is found to be dependent on four parameters: tray pitch (p), ratio of tray thickness to hole diameter (t/d_h), hole Reynolds number (Re_h), and the open area fraction (A_f). The biggest influencing factor is t/d_h and experimental results in the past showed that thicker trays generally have lower pressure drop than thinner ones. The physical explanation for this is that the vapour flowing through thick trays experiences a two-stage expansion comparing to a single-stage for thin ones, and the former case will give greater pressure recovery, therefore less pressure loss. For trays with the same thickness and open area fraction, the pressure drop is proportional to the hole size. A good example of this can be seen in gas industry columns where pressure loss is a critical factor to control; small hole size trays are used to minimise the dry tray pressure drop which will significantly reduce the total wet tray pressure drop. In what follows, some of most commonly used correlations are presented.

- **Leibson *et al* (1957)**

This is one of the oldest and perhaps the most frequently quoted correlation in chemical engineering handbooks. It is a standard orifice-type equation:

$$h_D = \frac{50.8}{C_v^2}\frac{\rho_G}{\rho_L}u_h^2 \tag{2.41}$$

where the discharge coefficient, C_v, can be obtained from Figure 2.14 according to the free area fraction (A_f) and the ratio of tray thickness to hole diameter (t/d_h).

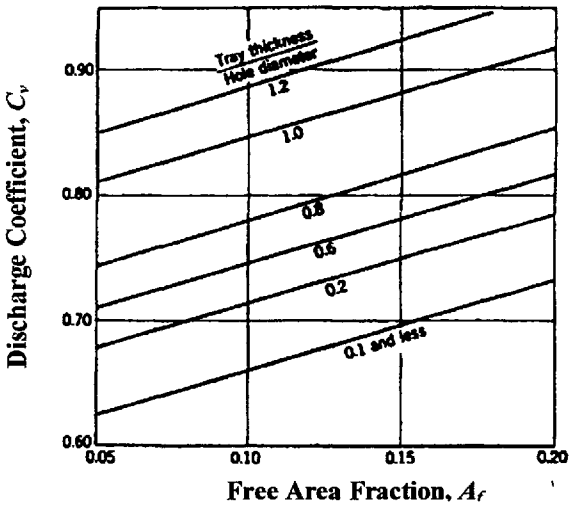


Figure 2.14. Discharge coefficients for gas flow (Leibson *et al* 1957)

- **McAllister *et al* (1958)**

McAllister *et al* (1958) proposed the following equation for predicting dry tray pressure loss where a dry-plate coefficient, k, was introduced:

$$h_D = k\left[0.4(1.25-A_f)+4f\left(t/d_h\right)+(1-A_f)^2\right]\frac{u_h^2}{6.562g} \tag{2.42}$$

The new parameter k was said to take account of the difference of equations derived from single orifice and an array of parallel paths (sieve tray holes). On sieve trays, the interference between adjacent jets, and the Couette correction and velocity gradient irregularities within holes are the major causes for the discrepancies. The values of k which is dependent on the t/d_h ratio can be obtained from Figure 2.15.

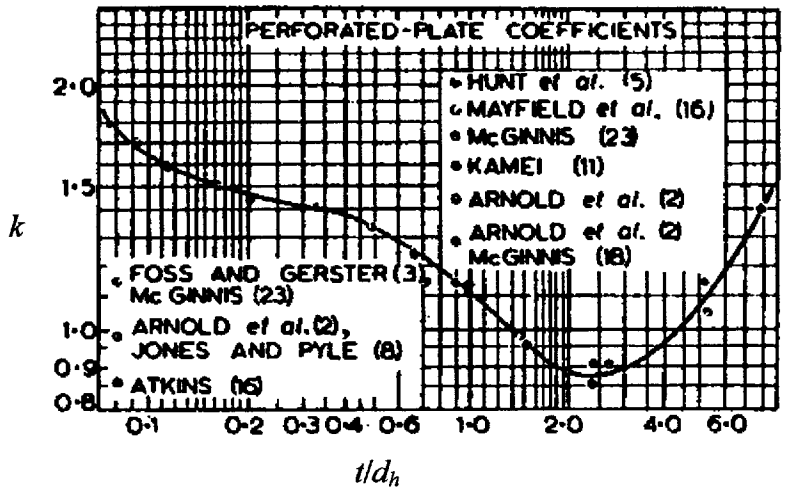


Figure 2.15. Dry-plate coefficient k as a function of t/d_h (McAllister *et al* 1958)

- **Smith and Van Winkle (1958)**

The Smith and Van Winkle (1958) correlation follows the standard orifice equation which involves the use of orifice coefficient ξ (Eq.2.40). These authors defined a parameter, K_w which depends on hole Reynolds number, Re_h; K_w can be determined from Figure 2.16.

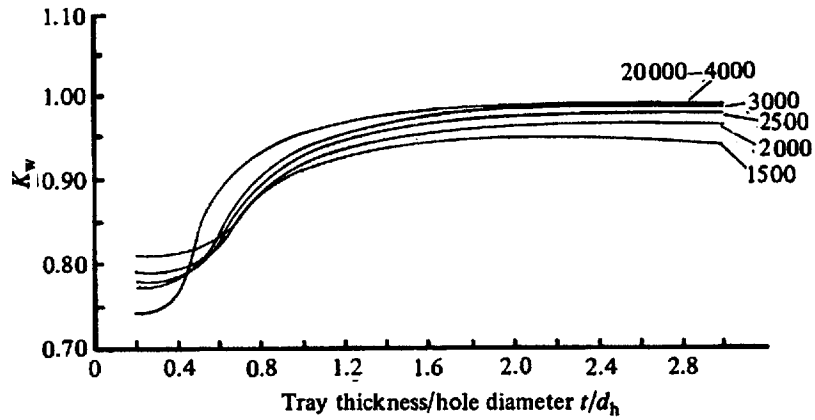


Figure 2.16. Correlation of Smith and Van Winkle (1958) for orifice coefficient, K_w (Lockett, 1986)

The orifice coefficient is related to K_w and other parameters by the equation:

$$\xi = \frac{\left(1 - A_f^2\right)\left(p/d_h\right)^{0.2}}{K_w^2} \tag{2.43}$$

- **Stichlmair and Mersmann (1978)**

Stichlmair and Mersmann (1978) introduced a new parameter, ξ_0, whose value is given as a function of hole Reynolds number and ratio of tray thickness to hole diameteras shown in Figure 2.17.

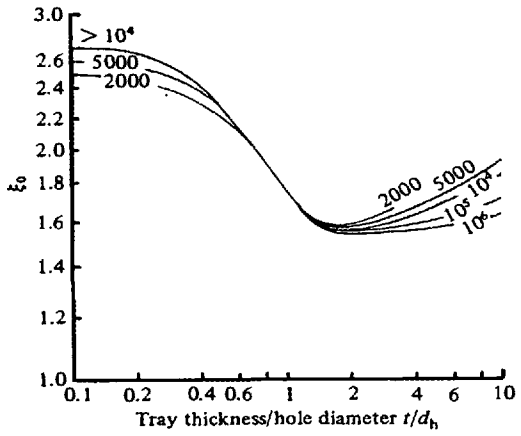


Figure 2.17. Orifice coefficient correlation due to Stichlmair & Mersmann (1978)

The authors argued that a correction for fractional perforation area is needed according to different ratio of t/d_h, and the corresponding equations for the orifice coefficient, ξ are as follows:

$$\xi = \xi_0 + A_f^2 - 2A_f\xi_0^{0.5} \qquad \text{for} \qquad t/d_h < 2 \tag{2.44}$$

$$\xi = \xi_0 + A_f^2 - 2A_f \qquad \text{for} \qquad t/d_h > 2 \tag{2.45}$$

- **Bekassy-Molnar and Mustafa (1991)**

Bekassy-Molnar and Mustafa (1991) argued that the pressure loss due to gas passing through the perforations cannot be accounted for only by the traditional dry tray pressure drop relationships. They pointed out that when the tray is wet, there is a thin film of liquid in the hole which decreases the cross-sectional area for gas passing through. This is shown in Figure 2.18.

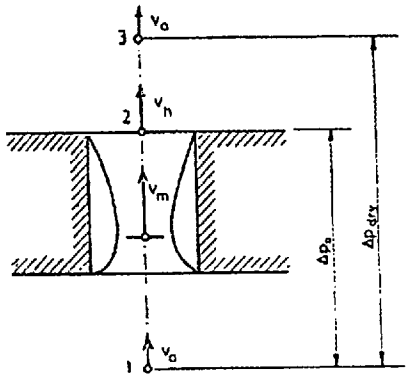


Figure 2.18. Pressure loss through an orifice

The thickness of the film is influenced by the surface tension and the authors included this effect in their dry tray pressure drop relationship given as follows:

$$h_D = \frac{18.3\sigma^{0.71}\rho_G}{2\rho_L g} u_h^2 \tag{2.46}$$

- **Tezock (1994) and Tahmasbi (1997)**

Several sieve trays were used in the experiments carried out independently by Tezock (1994) and Tahmasbi (1997) at Imperial College and their obtained dry pressure loss data were in line with the orifice-type equation.

$$\text{i.e. } h_D = c\, u_s^2 \tag{2.47}$$

where c was found experimentally and it is constant for each particular tray.

- **Correction to "Dry" tray pressure drop**

Although an orifice-type equation predicts the dry tray pressure drop reasonably well, it is only true when the tray is dry. In reality, the trays (and the holes) are wetted during operation, and therefore the "dry tray" pressure drop equation may not be valid and needs to be modified. So far, only the relationship by Bekassy-Molnar and Mustafa (1991) considered such "wetting" effects on the dry tray pressure drop. However, the exponent to surface tension in Eq.(2.46) is only valid for a certain range of fluids which limits its applicability. For practical purposes, a parameter e_m (ratio of liquid entrainment rate to vapour rate in mass) is used, and the corrected dry tray pressure drop becomes:

$$h_D = (h_D)_{e_m=0}(1+e_m) \tag{2.48}$$

There are other relationships to obtain the corrected h_D using the homogeneous model or the separated flow model of two-phase flow, however the equation above can provide reasonably good estimate.

2.3.3.2. Clear Liquid Head, h_L

This component of the pressure loss has already been discussed in Section 2.3.2 on clear liquid height.

2.3.3.3. Residual Head, h_σ

Traditionally, the residual head, h_σ, is related to the pressure required to overcome the surface tension forces when forming a bubble at a submerged orifice. The resultant equation is given as follows:

$$h_\sigma = \frac{4\sigma}{g\rho_L d_h} \tag{2.49}$$

Eq.(2.49) is probably the most popular expression for predicting h_σ since all the parameters in the equation can be easily obtained. However, there are also other types of relationships available for h_σ and some of these are discussed below.

- **Bennett *et al* (1983)**

The authors followed the theory given by Pavlov (1964) who expressed the residual head in terms of excess pressure inside the bubble during the formation period.

$$\text{i.e.} \quad h_\sigma = \frac{6\sigma}{g\rho_L D_{B\max}} \tag{2.50}$$

In order to obtain the bubble departure diameter, D_{Bmax}, a vertical force balance between the buoyancy and surface tension forces exerted on the bubble at departure was performed:

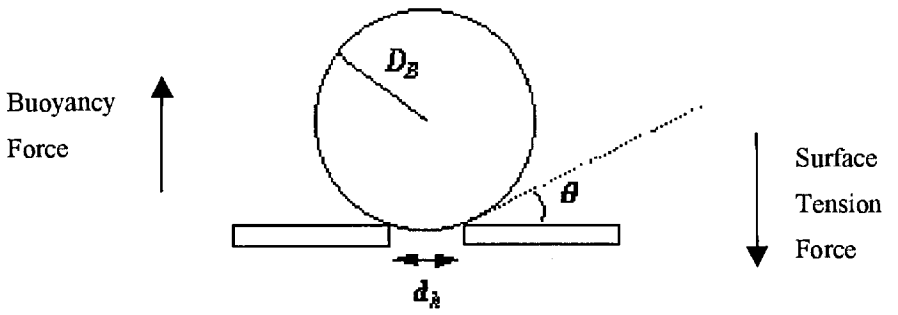


Figure 2.19 Bubble formation model

$$\text{Buoyancy Force} = \frac{\pi}{6} D_{B\max}^3 (\rho_L - \rho_G) g \tag{2.51}$$

$$\text{Surface Tension Force} = \pi d_h (\sigma \sin\theta) \tag{2.52}$$

Equating Eqs.(2.51) and (2.52):

$$\frac{\pi}{6} D_{B\max}^3 (\rho_L - \rho_G) g = \pi d_h (\sigma \sin\theta) \tag{2.53}$$

$$D_{B\max} = (6\sin\theta)^{1/3} \left[\frac{d_h \sigma}{g(\rho_L - \rho_G)} \right]^{1/3} \tag{2.54}$$

The departure contact angle θ was determined experimentally by the authors and it depends on the liquid used in the system. e.g. for air-water system, θ is about 20°.

- **Tezock (1994)**

A more mechanistic approach by Tezock (1994) looked at the dynamics of bubble formation and introduced a term called residual volume based on which a new bubble begins to grow. However, this quantity is difficult to obtain and it is case dependent. The model also involves bubble formation frequency, which has to be determined by other correlations. The proposed relationship is as follows:

$$h_\sigma = \frac{6\sigma}{d_h} \frac{3}{2\pi Q_G} \left[V_0^{1/3} (\alpha_r V_0 + Q_G \tau)^{2/3} - \alpha_r^{2/3} V_0 \right] \tag{2.55}$$

where α_r is the residual volume ratio, $\tau = 1$ / (bubbling frequency) and V_0 is the volume of a bubble whose diameter is equal to the orifice diameter.

- **Biddulph *et al* (1995)**

Biddulph *et al* (1995) pointed out the use of a static balance in the dynamic system (e.g. as employed in the model by Bennett *et al*, 1983) tends to introduce errors. A semi-empirical correlation was proposed in the following format:

$$h_\sigma = a_1\left[\frac{\sigma}{\rho_L g d_h}\right] + a_2 F + a_3 h_L \tag{2.56}$$

Note that the units for both h_σ and h_L in Eq.(2.56) are in mmH_2O, and the constants for three liquid systems are given in Table 2.5:

Liquid	a_1	a_2	a_3
Water	3350	8.34	0.04
Benzyl alcohol	5570	5.74	-0.21
***n*-Propanol**	8280	2.79	-0.38

Table 2.5. Values of coefficients found by experiment (Biddulph *et al*, 1995)

- **Other empirical correlations**

Apart from complex models/correlations above, some simple correlations are included in some distillation design handbooks. They are in the form of:

$$h_\sigma = \frac{4\sigma}{g\rho_L d_h} F_0 \tag{2.57}$$

where F_0 is given in Table 2.6 for different authors.

Author	F_0
Perry, 1984	1.0031
Rose, 1985	1.1029

Table 2.6. Coefficient for F_0

2.3.4. Characterisation of the Two-Phase Froth

The hydrodynamic parameters mentioned in the earlier chapters provide a macroscopic information of the two-phase flow and over the past forty years, there have also been great efforts on the characterisation of the froth body. This helps to better understand the froth structure by providing more microscopic information such as bubble/droplet size distributions above a tray. There are a few experimental techniques available to analyse the froth and the three major ones are discussed below.

2.3.4.1. Photography

Figures 2.20 is a side-view photograph of froth taken from a transparent column and it clearly shows the differences in bubble size from the bottom to the top of the froth. However, Porter *et al* (1967) argued that the characteristic sizes of bubbles observed in such photographs are not representative to the real system. There tends to be more small bubbles near the wall region (which the photograph shows) due to the local downflow of liquid films which drag mainly small bubbles.



Figure 2.20. Photograph of froth (taken from Fane, 1962)

One of the main disadvantages of using the photographic technique is that the image only shows the first layer (or two) of bubbles and the subsequent layers can not been seen due to optical aberration. With the wall effect explained above, the technique is less attractive for any quantitative analysis of the froth body. Some investigators have taken photographs of the top of the froth, however, the results still suffer from optical aberration.

2.3.4.2. Light Transmission and Scattering Technique

The technique was first developed by Calderbank (1959) and subsequently improved by many other researchers. The principle is based on the attenuation of the light intensity transmitted through bubbles due to four scattering mechanisms: diffraction, reflection, refraction and absorption. The applicability of the technique was extended by using a laser source which was introduced by Al Taweel *et al* (1984, 87) and this was also applied by Tezock (1994) and Tahmasbi (1997) to study the froth structure where some

encouraging results were obtained. More detailed descriptions of this technique can be found in the next chapter.

2.3.4.3. Bubble Probe

One of the most significant developments on the characterisation of froth body is the Calderbank bubble probe (Burgess & Calderbank, 1975). The system consists of five nickel-wire probes inserted in the froth and electrical signals are generated while bubbles being penetrated by the probes. Information on bubble size and velocity distributions in the froth could then be deduced from the signals. The Calderbank probe design was later improved by Raper *et al* (1982) and the measured Sauter mean bubble size distribution from a number of sieve trays are given in the shaded area in Figure 2.21 below.

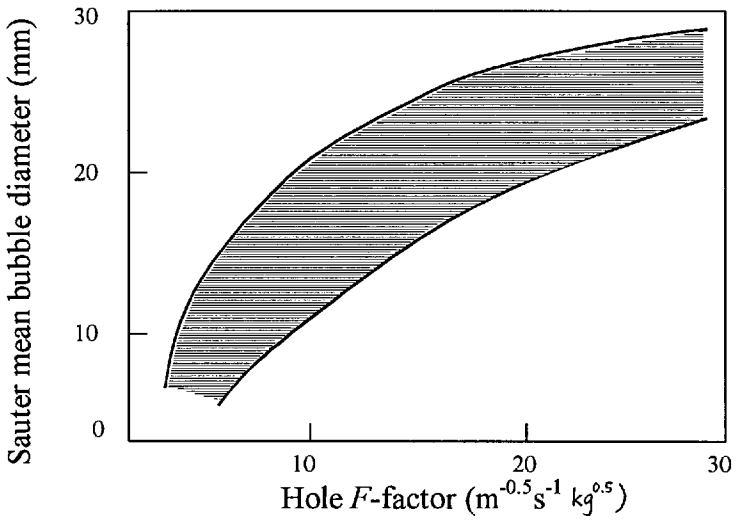


Figure 2.21. Sauter mean bubble size distribution (results from Raper *et al*, 1982)

The above results are very valuable; however, there have been no recent developments following this technique since then.

2.4. Vapour-Liquid Equilibrium in Distillation

Separation is a process involved phase equilibrium and in the case of distillation, this is governed by the Vapour-Liquid Equilibrium (VLE). This section describes how VLE is

applied to distillation theory and the way of predicting the VLE relationship by modern thermophysical property models.

2.4.1. Fundamentals

The well-known McCabe-Thiele graphical method (e.g. King, 1980) is used to represent the operating and vapour-liquid equilibrium relationships for a distillation column. A typical example of such graph is shown in Figure 2.22 below. The number of stages required for a separation can be determined graphically by counting the number of grey colour triangles between the operating and equilibrium lines.

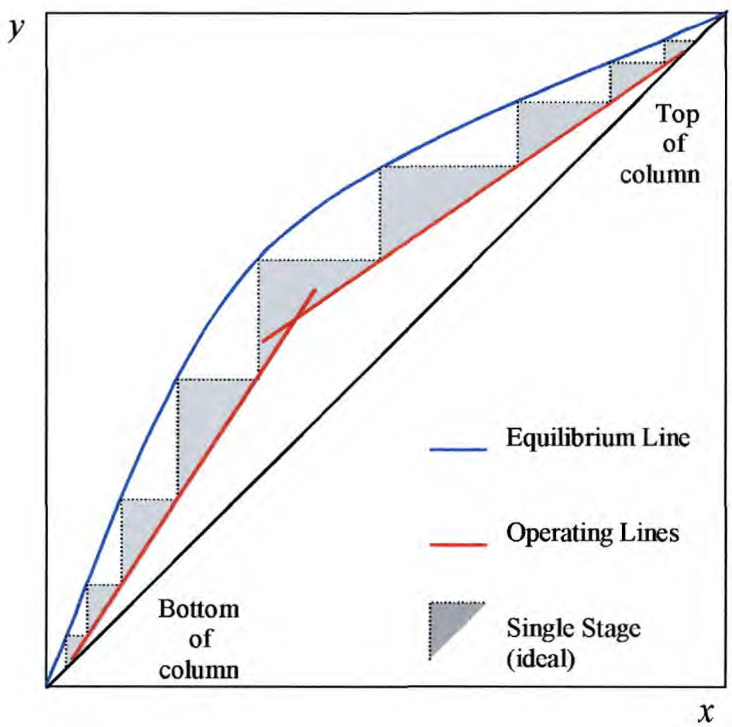


Figure 2.22. McCabe-Thiele graphical method for operating and VLE relationships

In order to construct the above graph, some input information is required. For the operating lines (shown in the red colour in Figure 2.22), the flowrates of both gas and liquid around the condenser and reboiler (at the top and bottom of the column respectively) are the essential information. The equilibrium line relationship depends on the system conditions (e.g. temperature, pressure, mixture composition ...etc). Although accurate vapour-liquid equilibrium relationships can be determined from laboratory

experiments, it is usually more convenient to predict such relationships using a thermophysical property model and the accuracy is generally reasonable for most cases.

2.4.2. Thermophysical Property Models for Predictions of VLE

In thermodynamics, fugacity is a property which relates the deviation of the *P-V-T* properties of a real gas from those of a perfect gas. The condition of phase equilibrium for any real mixture of n components under a certain temperature and pressure is expressed as:

$$f_i^V = f_i^L \qquad (i=1,2,\ldots n) \tag{2.58}$$

where f_i denotes the fugacity of component i and superscripts V, L denote vapour and liquid phases.

Eq.(2.58) can be written in a more useful form which involves the terms of fugacity coefficients:

$$y_i \phi_i^V P = x_i \phi_i^L P \qquad (i=1,2,\ldots n) \tag{2.59}$$

where y_i and x_i are the mole fractions of component i in the vapour and liquid phase respectively, ϕ_i is the fugacity coefficient of component i and P is the system pressure.

A convenient way of describing the thermodynamic equilibrium between the vapour and liquid phases is to define a vaporisation equilibrium ratio, K_i, where

$$K_i = y_i / x_i = \phi_i^L / \phi_i^V \tag{2.60}$$

In most of computational process simulators, such as AspenMax™ or HYSYS™, values of K_i's are given in the whole ranges of mole fractions and they are calculated from the ratio between the fugacity coefficients of the two phases. Fugacity coefficients are functions of temperature, pressure, composition and they can be estimated by two approaches:

1. Equation of state method
2. Activity coefficient method

Generally, an equation of state method can provide solutions of fugacity coefficients for both vapour and liquid phases. However, for some liquid systems, where strong molecular interactions exist, the equation of state approach cannot produce reliable results. Under these circumstances, predictions of liquid phase fugacity coefficients based on an activity coefficient method are preferred.

2.4.3. Equation of State

An Equation Of State (EOS) is an algebraic relationship between pressure (P), volume (V) or density (ρ), temperature (T) and composition (in the case of a mixture) and it provides a method of calculating the thermodynamic properties of a system within some domain of applicability. There are three general categories for equations of state: virial equations of state, cubic equations of state and complex equations of state. There is no true answer to which method is the best out of all, each has its own merits as well as drawbacks. The following sections provide brief introductions of these methods and guidelines for choosing appropriate methods are given.

- **Virial Equations of State**

From the study of statistical mechanics, the virial equation of state is a polynomial series of the form:

$$P = \frac{RT}{V} + \frac{RTB}{V^2} + \frac{RTC}{V^3} + \ldots \tag{2.61}$$

where B, C,... are called the second, third,... virial coefficients and they are functions of temperature (and composition in the case of mixtures).

Analytical evaluation of the virial coefficients may be possible and it depends on the intermolecular potential function given, e.g. hard-sphere potential, square-well potential,...etc. The expression for the second virial coefficient (from a given intermolecular potential) is relatively easy to obtain but coefficients higher than the third are proved to be far too complicated due to the difficult integrations involved. Therefore, Eq.(2.61) is usually truncated after the second or third term. Generally, using the truncated virial equation is simple, but it can only be applied on the vapour side.

Good accuracy can be expected for pure gases and gas mixtures which exhibit modest deviation from ideal gas/mixture behaviour

- **Cubic Equations of State**

The term "cubic" implies an equation that, when expanded, contains volume terms raised to either the first, second, or third power, and the cubic equations of state have the following form:

$$P = \frac{RT}{V-b} - \frac{a}{V^2 + ubV + wb^2} \tag{2.62}$$

where u, w are constants and a, b are so called the "two parameters" of the cubic equations of state. Both a and b are functions of temperature and a also depends on acentric factor (which indicates the complexity of a molecule with respect to both the geometry and polarity; proposed by Pitzer, 1955).

Since the earliest model developed by van der Waals in 1873, many other similar relationships of this type have been proposed. Although they do not provide more advanced scientific understanding, they are nevertheless valuable prediction tools in engineering applications. Three of the most well known models under this category are the equations of Redlich and Kwong (1949), Soave (1972) and Peng and Robingson (1976).

The merit of cubic equations of state is their ability to describe behaviours for both vapour and liquid phases and they can generally be solved noniteratively. However, when applying a cubic equation of state approach, a method should be chosen carefully, taking into consideration the ranges of its applicability to ensure that good accuracy can be achieved.

- **Complex Equations of State**

Many complex equations of state are variants of the equation proposed by Benedict, Webb and Rubin (1940, known as the "BWR" equation) and they are non-linear equations with 11 parameters based on critical properties and acentric factor. Compared to the cubic equations, they generally produce more accurate results with applicability

over wider ranges of temperature and pressure. However, an iterative scheme (such as Newton-Raphson method) is required to obtain solutions of these non-linear equations.

A popular modified version of BWR equation of state is by Lee and Kesler (1975) which is based on the theory of corresponding states. The principle of corresponding states is to relate the compressibility of a real fluid to the properties of a simple fluid and a reference fluid. This method is often combined with the mixing rules by Plöcker *et al* (1978) for the applications on mixtures. An example of this application is that by Saville and Szczepanski (1982).

2.4.4. Activity Coefficient Models

For a given system, an appropriate equation of state method can provide quick information on thermodynamic equilibrium with good accuracy. However, the theory of equations of state is usually only applicable to simple molecules, i.e. molecules without strong molecular interactions. This results in large errors in its predictions on the liquid phase fugacity coefficients of strong associating liquid mixtures, such as methanol and acetone. For this purpose, activity coefficient models are specially developed to predict the phase equilibrium on the liquid side. Thus, together with an equation of state for vapour phase, the two methods offer a practical solution to systems with associating liquids.

In an activity coefficient model, the fugacity of a component in the liquid phase may be expressed exactly in terms of the activity coefficient γ_i and other quantities as

$$f_i^L = x_i \gamma_i P_i^\sigma \phi_i^\sigma \mathcal{F}_i \tag{2.63}$$

where P_i^σ is the saturated vapour pressure of pure component i, ϕ_i^σ is the fugacity coefficient of the pure saturated vapour at the given temperature and $\mathcal{F}_i$ is the Poynting factor, a correction term for high pressure cases.

There are two categories of methods for activity coefficient models:

1. **Theoretical models with parameters fitted to experimental data**

   Typical examples: Wilson, NRTL and UNIQUAC models

   Experimental results on binary mixtures are obtained over ranges of temperature, pressure and composition and these are used to calculate the parameters defined in the activity coefficient model. In a multicomponent case, these methods require data on all possible binary subsystems that can be formed from the components of a system.

2. **Models based on the group contribution method**

   Typical example: ASOG and UNIFAC

   Contrary to the models above, no experimental data is required for this type of model. The calculations of activity coefficients are based on functional group parameters which are determined from a large set of experimental VLE data.

Methods of the first type usually give more accurate results than the second one. However, when there are insufficient experimental data, reasonable results can still be obtained from the group contribution methods.

When using activity coefficient models, Eqs.(2.59) and (2.60) can be re-written as:

$$f_i^{\mathrm{V}} = y_i \phi_i P = f_i^{\mathrm{L}} = x_i \gamma_i P_i^{\sigma} \phi_i^{\sigma} \mathcal{F}_i \tag{2.64}$$

$$K_i = \frac{y_i}{x_i} = \frac{\gamma_i P_i^{\sigma} \phi_i^{\sigma} \mathcal{F}_i}{\phi_i^{\mathrm{V}} P} \tag{2.65}$$

Instead of solving for Eq.(2.59) from an equation of state, the activity coefficient model would predict the numerators in Eq.(2.65). A major drawback for all activity coefficient models is their narrow range of applicability (i.e. temperature and pressure), although they have been continuously improved. In the present state of development, activity coefficient models are reliable only up to about 10-20 bars, depending on the substances involved.

2.5. Mass Transfer in Distillation

Separation will not occur without mass transfer taking place. In this section, the theory of mass transfer is reviewed, in particular for the case of distillation. This includes estimations of mass transfer coefficients (Section 2.5.1), diffusion coefficients (Sections 2.5.2, 2.5.3) and interfacial area (Section 2.5.4).

2.5.1. Mass Transfer Coefficients

The classical theory of forced convective mass transfer begins with the basic equation for molar flux N (kmol/m^{2}s) of the more volatile component across the interface:

$$N = k_G(y_i - y) = k_L(x - x_i) = K_{OG}(y^* - y) = K_{OL}(x - x^*) \tag{2.66}$$

This is graphically shown in Figure 2.23 where y and x the mole fraction of the more volatile component in the bulk gas and liquid phases and y_i and x_i the corresponding mole fraction at the interfaces. y_i and x_i are normally assumed to be in equilibrium. y^* and x^* are the equilibrium mole fraction in the vapour and liquid corresponding to a liquid phase composition x and a vapour phase composition y respectively. k and K are the corresponding mass transfer coefficients depending on which concentration difference is used in Eq.(2.66).

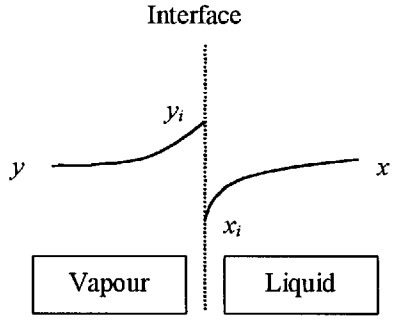


Figure 2.23. Concentration profile of the more volatile component near the interface in a binary mixture

In Eq.(2.66), the overall mass transfer coefficients, K_{OG} and K_{OL}, are defined in order to relate the mass transfer process to known values of mole fraction (i.e. x, y and the corresponding equilibrium values y^* and x^*). In distillation, K_{OG} is usually used instead of K_{OL}. The simplest relationship between K_{OG}, k_L and k_G can be determined by assuming a linear equilibrium relationship for a single tray in a column such that

$$y^* = mx + b \tag{2.67}$$

$$y_i = mx_i + b \tag{2.68}$$

These enable Eqs.(2.66) to Eq.(2.68) to be combined into the form:

$$\frac{1}{K_{OG}} = \frac{1}{k_G} + \frac{m}{k_L} \tag{2.69}$$

Theories are available to estimate the individual mass transfer coefficients, k_G and k_L and in particular for the cases of distillation, these are described briefly below.

2.5.1.1. Film Theory

In the film theory (first suggested by Nernst, 1904), the interfacial region is idealised as a hypothetical film or "unstirred layer" (usually unknown) and mass transfer involves diffusion across this thin film. The form of mass transfer coefficients under this theory is given as

$$k' = D/l \tag{2.70}$$

where k' is the mass transfer coefficient (m/s), D is the diffusion coefficient (m^2/s) and l is the film thickness (m).

2.5.1.2. Penetration Theory

In the penetration theory (suggested by Higbie, 1935), the interfacial region is considered as one in which transient diffusion is taking place after the two phases are brought into contact. The form of mass transfer coefficients under this theory is

$$k' = 2\sqrt{D/\pi t_c} \tag{2.71}$$

where t_c is the contact time between the phases.

The contact time t_c may not be exactly known a priori in complicated situations, just as the exact film thickness l was usually not known in the film theory.

2.5.1.3. Surface Renewal Theory

Introduced by Danckwerts (1951), the surface renewal theory tries to apply the mathematics of the penetration theory to a more plausible physical situation. The liquid is pictured as two regions: a large bulk region that is well mixed and a surface region that is renewed so fast that the mechanism of transient diffusion is dominant. The surface renewal is caused by liquid flow. The form of mass transfer coefficients under this theory is:

$$k' = \sqrt{D/\tau_r} \tag{2.72}$$

where τ_r is the average residence time for an element in the interfacial region (or called surface renewal rate)

This theory has similar mathematics to the penetration theory, but it does provide a better physical picture of the actual mass transfer. However, the surface renewal rate τ is an unknown parameter which has to be correlated.

2.5.1.4. Theory for Distillation Trays

Most of the correlations to estimate mass transfer coefficients in distillation trays have been based on Higbie's penetration theory, with empirical correlations being developed for estimating the contact time. The relationships by Stichlmair (1978) and Bennett *et al* (1997) are two of the most well-known correlations of this form and are stated below:

- **Stichlmair (1978)**

The Stichlmair (1978) correlations for gas and liquid mass transfer coefficients are as follows:

$$k'_G = 2\left(\frac{D_G u_s}{\pi h_f \varepsilon}\right)^{0.5} \quad \text{and} \quad k'_L = 2\left(\frac{D_L u_s}{\pi h_f \varepsilon}\right)^{0.5} \tag{2.73}$$

i.e. $t_c = h_f \varepsilon / u_s$ for both of the mass transfer coefficients, k'_G and k'_L.

The above mass transfer coefficients k'_G and k'_L are in m/s, and they can be converted to molar unit of kmol/m^{2}s (as defined in Eqs.(2.66) and (2.69) previously) by multiplying

molar densities of each phase, i.e. $k_G = \rho'_G k'_G$ and $k_L = \rho'_L k'_L$. In Eq.(2.73), h_f is the froth height and ε is the gas void fraction which can be estimated from the correlations by Stichlmair (1978) described in Section 2.3.2.1.

- **Bennett *et al* (1997)**

Bennett *et al* (1997) gave the following relationships for prediction of the mass transfer coefficients:

$$k'_L = 2\sqrt{\frac{D_L}{\pi t_c}} \text{ and } k'_G = 2\sqrt{\frac{D_G}{\pi t_c}} \tag{2.74}$$

where $t_c = \dfrac{d_b}{\left(u_s/\varepsilon\right)}$ for k'_G, $t_c = d_b/u_h$ for k'_L and d_b is the bubble diameter.

There are many other correlations available in the literature (a list extracted from Lockett 1986 is as follows: Geddes 1946, Chu *et al* 1951, West *et al* 1952, Garner & Porter 1960, Calderbank & Moo-Young 1960, Andrew 1961, de Goederen 1965, Fane & Sawistowski, 1969, Sharma *et al* 1969, McLachlan & Danckwerts 1972, Zuiderweg 1982, Neuburg & Chuang 1982). Some of these correlations predict the so-called combined volume coefficients (i.e. product of the mass transfer coefficient and interfacial area, $k'_G a$ and $k'_L a$; the parameter a, interfacial area per unit volume, will be discussed in the next section) so that the rate of mass transfer (instead of the flux defined in Eq.2.66) can be determined straight away. However, these correlations are rarely used in practice.

As it can be seen from Eqs.(2.73) and (2.74), in order to calculate the mass transfer coefficients in a distillation case, it is necessary to obtain the diffusion coefficients for both gas and liquid mixtures.

2.5.2. Diffusion Coefficients in Gas Mixtures

Both theoretical and empirical methods are available for the prediction of the gas-phase binary diffusion coefficient. In what follows, two of the most widely used methods are given: (1) the method by Chapman and by Enskog (documented in Chapman and

Cowling, 1970) based on the kinetic theory; (2) an empirical correlation by Fuller *et al* (1966). Effects of temperature and pressure on the prediction of diffusion coefficients are also reviewed.

2.5.2.1. Prediction Methods for Binary Gas Diffusion Coefficient

- **Chapman-Enskog Kinetic Theory**

A theoretical method of predicting the gaseous diffusion coefficients was derived independently by Chapman and by Enskog. The theory is based on the detailed analysis of molecular motion in dilute gases and the resultant equation is:

$$D_{AB} = \frac{2.596\times10^{-3}\,T^{3/2}}{PM_{AB}^{1/2}\sigma_{AB}^{2}\,\Omega_{D}} \tag{2.75}$$

where $M_{AB} = 2[(1/M_A)+(1/M_B)]^{-1}$ (2.76)

In Eq.(2.75), D_{AB} is the diffusion coefficient in cm^2/s, M_A, M_B are the molecular weights of components A and B, P is the pressure in bar, T is the absolute temperature in Kelvin, Ω_D is the dimensionless collision integral for diffusion and σ_{AB} is the characteristic length (Å).

To estimate the parameters Ω_D and σ_{AB}, an appropriate intermolecular force law is required. The Lennard-Jones 12-6 potential has been the most commonly chosen law for this purpose due to its simplicity and convenience. The governing equation is given by

$$\psi = 4\varepsilon\left[\left(\frac{\sigma}{r}\right)^{12} - \left(\frac{\sigma}{r}\right)^{6}\right] \tag{2.77}$$

where r is the separation distance between two molecules, ψ is the intermolecular energy, ε is the characteristic Lennard-Jones energy and σ is the characteristic Lennard-Jones length. The values of ε and σ for the 12-6 Lennard-Jones potential model can be determined from viscosity data; values for some common substances are given in Reid *et al* (1987).

The following "mixing rules" are chosen to combine the above parameters for two molecules, A and B:

$$\varepsilon_{AB} = (\varepsilon_A \varepsilon_B)^{1/2} \tag{2.78}$$

$$\sigma_{AB} = (\sigma_A + \sigma_B)/2 \tag{2.79}$$

For a particular intermolecular model, the collision integral for diffusion is only a function of "$k_B T/\varepsilon$", i.e.:

$$\Omega_D = f\left(k_B T / \varepsilon\right) \tag{2.80}$$

where k_B is the Boltzmann constant.

The values of collision integral for diffusion for the 12-6 Lennard-Jones model can be found in Hirschfelder *et al* (1954), however, various analytical approximations are also available. The method by Neufield *et al* (1972) is recommended by Reid *et al* (1987) and the relationships are given as follows:

$$\Omega_D = \frac{1.06036}{(T^*)^{0.15610}} + \frac{0.19300}{e^{0.47635T^*}} + \frac{1.03587}{e^{1.52996T^*}} + \frac{1.76474}{e^{3.89411T^*}} \tag{2.81}$$

$$\text{where } T^* = \frac{k_B T}{\varepsilon_{AB}} \tag{2.82}$$

Eq.(2.75) is applicable to dilute gases with spherical, non-polar, monatomic molecules. Reid *et al* (1987) reported that Eq.(2.75) gives good results over a wide range of temperatures and provides useful approximate values of D_{AB}.

- **Fuller *et al* (1966)**

Fuller *et al* (1966) developed a correlation for gas binary diffusion coefficient based on 340 experimental data points that cover 153 different binary systems and the authors claimed an average absolute error of about 4 % against their database. This method has been recommended in most papers in the literature and their proposed equation is:

$$D_{AB} = \frac{0.00143 T^{1.75}}{P M_{AB}^{1/2} \left[(\Sigma v)_A^{1/3} + (\Sigma v)_B^{1/3}\right]^2} \tag{2.83}$$

where D_{AB} is given in cm^2/s and $\sum v$ is a total molecular diffusion volume which can be found for each component by adding atomic diffusion volumes. Tables 2.7 and 2.8 show values obtained by Fuller *et al* (1966) for these atomic volumes for different components.

Atomic and Structural Diffusion Volume Increments			
C	15.9	(Br)	21.9
H	2.31	(I)	29.8
O	6.11	(S)	22.9
(N)	4.54	Aromatic or Hetero-cyclic rings	-18.3
(F)	14.7		
(Cl)	21.0		

Table 2.7. Atomic Diffusion Volumes for different components (Fuller *et al* 1966)

Diffusion Volumes of Simple Molecules			
H_2	6.12	CO	18.0
D_2	6.84	CO_2	26.9
He	2.67	N_2O	35.9
N_2	18.5	NH_3	20.7
O_2	16.3	H_2O	13.1
Air	19.7	(CCl_2F_2)	114.8
Ne	5.98	(SF_6)	71.3
Ar	16.2	(Cl_2)	38.4
Kr	24.5	(Br_2)	69.0
(Xe)	32.7	(SO_2)	41.8

( ) indicates that listed value is based on only a few data points.

Table 2.8. Diffusion volumes for simple molecules (Fuller *et al* 1966)

- **Alternative Methods**

As in the case of the method by Fuller *et al* (1966) described above, most of other empirical correlations still retain the general form of Eq.(2.75) and the constants in the equations are purely based on the experimental data. Some of the more significant ones are given below (the unit of D_{AB} is in cm^2/s):

(1) Gilliland (1934)

$$D_{AB} = \frac{0.00616T^{1.5}}{PM_{AB}^{1/2}\left[(\Sigma v)_A^{1/3} + (\Sigma v)_B^{1/3}\right]^2} \tag{2.84}$$

(2) Wilke & Lee (1955)

$$D_{AB} = \frac{\left[3.03 - \left(0.98/M_{AB}^{1/2}\right)\right]\left(10^{-3}\right)T^{1.5}}{PM_{AB}^{1/2}\sigma_{AB}^2\Omega_D} \tag{2.85}$$

(3) Chen & Othmer (1962)

$$D_{AB} = \frac{0.0150T^{1.81}}{P(T_{cA}T_{cA})^{0.1405}\left(V_{cA}^{0.40}+V_{cA}^{0.40}\right)^2}\sqrt{\frac{1}{M_A}+\frac{1}{M_B}} \tag{2.86}$$

(4) Othmer & Chen (1962)

$$D_{AB} = \left(2.52\times10^{7}\right)\mu_{air}^{2.74}\left[\frac{\sqrt{\frac{1}{M_A}+\frac{1}{M_B}}}{\left(V_{cA}^{0.4}+V_{cB}^{0.4}\right)^2}\right]^{1.23} \tag{2.87}$$

2.5.2.2. Effect of Temperature

Marrero and Mason (1972) pointed out that in diffusion coefficient relationships such as Eq.(2.82), the power to which T is raised depends on the actual temperature and in most cases, it can vary from 1.5 to 2.0. Fuller *et al* (1966) used a value of 1.75 which makes it a reliable method at moderate to high temperatures; however, at low temperatures, where the exponent is higher, this value may not give a satisfactory approximation. This is illustrated in Figure 2.24 below, where Marrero and Mason (1972) showed that the exponent first increases then decreases as temperature rises.

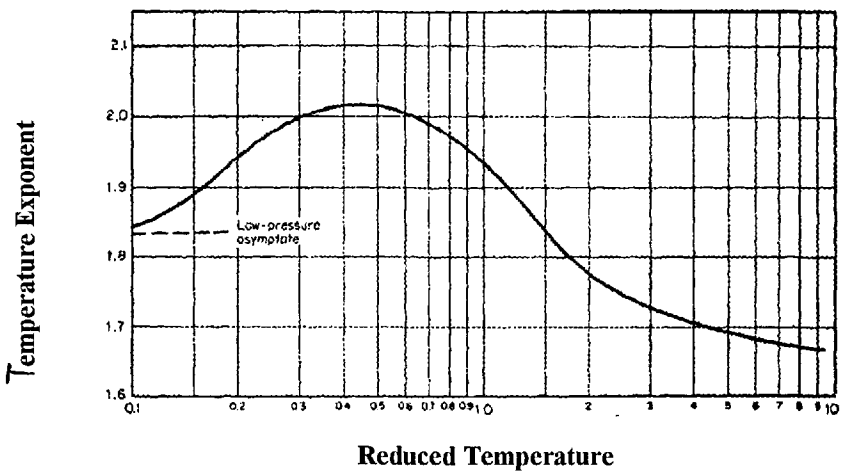


Figure 2.24. Exponent of temperature for diffusion coefficient in gases
(adapted from Marrero and Mason, 1972, with the approximation that $\varepsilon/k_B \approx 0.75T_c$)

A reasonable estimate (given in Skelland, 1985) for the diffusion coefficient at a temperature T_2 (from an reference diffusion coefficient at temperature T_1) can be obtained by means of a relationship that follows from Eq.(2.75):

$$D_{AB}\big|_{T_2} = D_{AB}\big|_{T_1}\left(\frac{T_2}{T_1}\right)^{3/2}\frac{\Omega_D\big|_{T_1}}{\Omega_D\big|_{T_2}} \tag{2.88}$$

Reid *et al* (1987) suggested that the Chapman-Enskog theory (Eq.2.75) and the Wilke-Lee method (Eq.2.85) are preferable to the one by Fuller *et al* (1966) when a wide temperature range is to be covered.

2.5.2.3. Effect of Pressure

For all the prediction equations mentioned above, the values of the binary diffusion coefficients at low to moderate pressure are inversely proportional to pressure (i.e. the product of diffusion coefficient and pressure is a constant). However, systems at higher pressure can behave rather differently, mainly due to gas non-idealities at high pressure.

- **Reid *et al* (1977)**

Cussler (1984) stated that the empirical relationship by Reid *et al* (1977) is a reasonable method for prediction of the high-pressure gas diffusion coefficient. This relationship suggests the product of gas density and diffusion coefficient is constant over the pressure range, i.e.

$$\rho D = (\rho D)^{+} \tag{2.89}$$

where $(\rho D)^{+}$ represents the value at low pressure but the same temperature as the high pressure condition.

- **Slattery and Bird (1958)**

Slattery and Bird (1958) produced a generalised chart, shown in Figure 2.25, which predicts gas phase self-diffusion coefficient as a function of reduced temperature and pressure. It was derived from the modified version of the Enskog's kinetic theory for a pure gas made up of rigid spheres, where a reduced equation of state can be written and

it gives an 11% error when compared to the experimental data of O'Hern & Martin (1955).

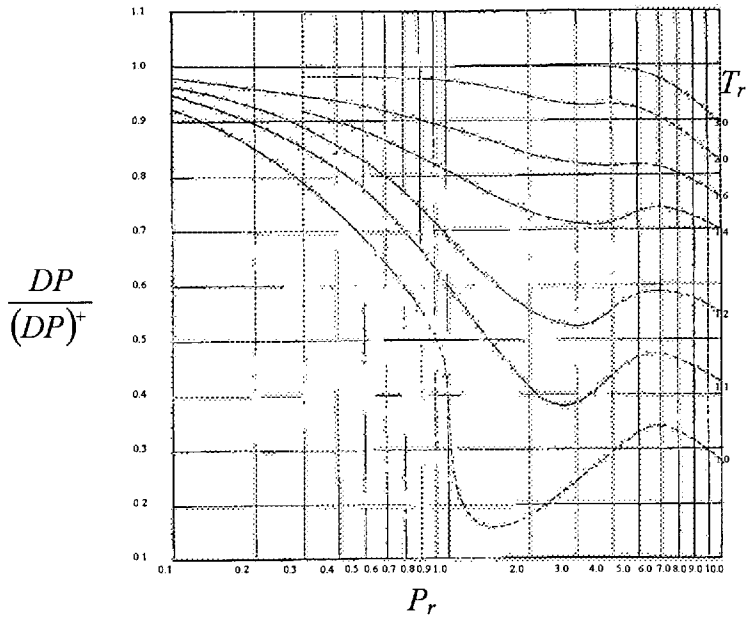


Figure 2.25. Slattery-Bird generalised chart for gas self-diffusion coefficient at high pressure where $(DP)^+$ is the product of diffusion coefficient and pressure at low pressure and T_r, P_r are the reduced temperature, pressure.

- **Takahashi (1974)**

Takahashi (1974) followed a similar approach to that used earlier by Slattery and Bird (1958) to correlate experimental data on self- and binary-diffusion coefficients and attempted to prepare another chart analogous to the chart by Slattery and Bird. When compared to the author's database, a lower average deviation of 4.9% was reported for the new chart than that obtained (7.9%) for the Slattery and Bird chart. The author's proposed relationship is:

$$\frac{D_{AB}P}{(D_{AB}P)_{1atm}} = f(T_r, P_r) \tag{2.90}$$

where $T_r = \frac{T}{T_c}$ (2.91)

$$T_c = y_A T_{cA} + y_B T_{cB} \tag{2.92}$$

$$P_r = \frac{P}{P_c} \tag{2.93}$$

$$P_c = y_A P_{cA} + y_B P_{cB} \tag{2.94}$$

The function, $f(T_r,P_r)$, can either be determined from Figure 2.26 below or calculated from Eq.(2.95) by choosing the appropriate constants (according to P_r) in Table 2.9.

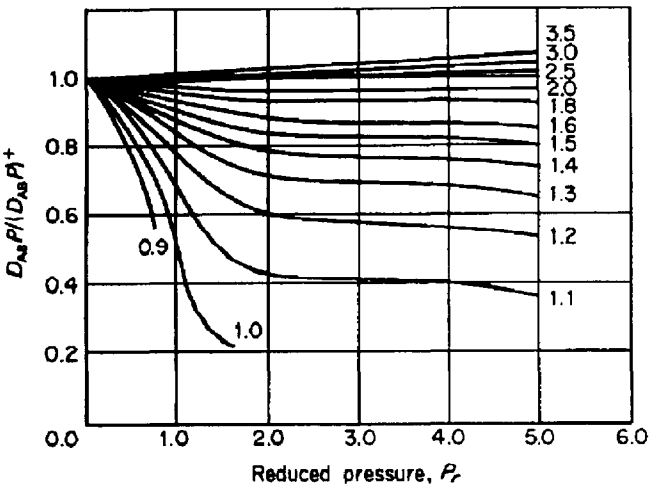


Figure 2.26.
Takahashi correlation (1974) for the effect of pressure and temperature on the binary gas diffusion coefficient

$$\frac{D_{AB}P}{(D_{AB}P)_{1atm}} = (D_{AB}P)_l\left(1 - AT_r^{-B}\right)\left(1 - CT_r^{-E}\right) \tag{2.95}$$

where $(D_{AB}P)_l$ is the limiting value of $D_{AB}P$ at T→∞ and this is a function of the reduced pressure, P_r.

P_r	$(D_{AB}P)_l$	A	B	C	E
0.1	1.01	0.038042	1.52267	0.0	
0.2	1.01	0.067433	2.16794	0.0	
0.3	1.01	0.098317	2.42910	0.0	
0.4	1.01	0.137610	2.77605	0.0	
0.5	1.01	0.175081	2.98256	0.0	
0.6	1.01	0.216376	3.11384	0.0	
0.8	1.01	0.314051	3.50264	0.0	
1.0	1.02	0.385736	3.07773	0.141211	13.45454
1.2	1.02	0.514553	3.54744	0.278407	14.00000
1.4	1.02	0.599184	3.61216	0.372683	10.00900
1.6	1.02	0.557725	3.41882	0.504894	8.57519
1.8	1.03	0.593007	3.18415	0.678469	10.37483
2.0	1.03	0.696001	3.37660	0.665702	11.21674
2.5	1.04	0.790770	3.27984	0.0	
3.0	1.05	0.502100	2.39031	0.602907	6.19043
4.0	1.06	0.837452	3.23513	0.0	
5.0	1.07	0.890390	3.13001	0.0	

Table 2.9. Constants defined in Eq.(2.95) by Takahashi (1974)

2.5.2.4. Multicomponent Gas Mixture Diffusion Coefficient

Generally, gas phase diffusion coefficients are assumed to be independent of composition (except at high pressure) and the following Stefan-Maxwell equation can be used to describe the diffusion process.

$$\frac{dy_i}{dz} = \sum_{j=1}^{n} \frac{c_i c_j}{c_m^2 D_{ij}} \left(\frac{J_j}{c_j} - \frac{J_i}{c_i} \right) \tag{2.96}$$

where c is the concentration, J is the flux, D_{ij} is binary diffusion coefficient of any ij system and (dy_i/dz) is the gradient in mole fraction of i in the z direction

For some engineering applications, Eq.(2.96) can be simplified by making certain assumptions. In the limiting case of one component i diffusing into a homogeneous mixture (i.e. $J_j \approx 0$ and $c_j/c_m = y_j$), the above equation can be simplified and re-written as

$$D_{im} = \frac{-J_i}{dy_i/dz} = \left(\sum_{\substack{j=1 \\ j \neq i}}^{n} \frac{y_j}{D_{ij}} \right)^{-1} \tag{2.97}$$

which is known as the Blanc's Law and where D_{im} is the binary coefficient between the dilute component and the mixture.

Fairbanks and Wilke (1950) suggested a nearly identical relationship to Eq.(2.97) for predicting gas phase diffusion coefficient, $D_{G,i}$ for each component i in the presence of all other components:

$$D_{G,i} = \frac{1 - y_i}{\sum_{j=1 \neq i}^{n} (y_j / D_{ij})} \tag{2.98}$$

2.5.3. Diffusion Coefficients in Liquid Mixtures

Unlike the gas phase diffusion coefficient, theoretical prediction methods for the diffusion coefficient of a binary liquid mixture have not been satisfactory. This is because liquid molecules are packed at a high density and can be strongly affected by the force fields of neighbouring molecules. This means that the diffusion coefficient for

a liquid mixture is strongly dependent on concentration. Thus, the term "infinite dilution" is always added when estimating a liquid phase diffusion coefficient. In this section, the theoretical method based on the Stokes-Einstein kinetic theory equation is introduced and this is followed by a description of the empirical Wilke-Chang method (1955). Temperature, pressure and concentration effects on the liquid phase diffusion coefficients are also discussed in this section.

2.5.3.1. Prediction Methods for Binary Liquid Diffusion Coefficient

- **Stokes-Einstein Kinetic Theory**

The Stokes-Einstein method is based on a representation of the kinetics of molecular motions and provides a fundamental basis for estimating diffusion coefficients in liquids. The resultant equation, based on an analysis of large spherical molecules diffusing in a dilute solution, is as follows:

$$D_{AB}^{\circ} = \frac{k_B T}{6\pi\eta_B r_A} \tag{2.99}$$

where D_{AB}° is the liquid diffusion coefficient at infinite dilution in cm^2/s, r_A is the radius of the "spherical" solute A in cm, η_B is the viscosity of solvent B in cP, k_B is the Boltzmann constant and T is the absolute temperature in Kelvin.

Despite the restricted condition (size of solute molecules to be very large relative to solvent) for this relationship to be applicable, it still served as a good starting point for the development of later prediction methods. Reid *et al* (1977) reported that the coefficients calculated from Eq.(2.99) are accurate to only about 20%. Further modifications for this equation to accommodate other shapes of molecules (e.g. ellipsoid) are listed in Cussler (1984).

- **Wilke and Chang (1955)**

The empirical Wilke-Chang (1955) equation was developed by correlating against 285 data points from 251 different solute-solvent systems and it showed an average deviation of 10%. The proposed correlation is as follows:

$$D_{AB}^{\circ} = \frac{7.4\times10^{-8}(\phi M_B)^{1/2} T}{\eta_B V_A^{0.6}} \tag{2.100}$$

where D°_{AB} is given in cm^2/s, M_B is the molecular weight of solvent B, η_B is the viscosity of solvent B (cP), V_A is the molar volume of solute A at its normal boiling temperature (cm^3/mol), ϕ is the association factor of solvent B. The parameter ϕ is dimensionless and normally lies between 1.0 and 2.6.

The recommended values of ϕ for some common solvents are: $\phi = 2.6$ if the solvent is water, $\phi = 1.9$ if it is methanol, $\phi = 1.5$ if it is ethanol and $\phi = 1.0$ if it is unassociated. Experimental values of molar volume, V_A, can be used if available. Otherwise, V_A can be obtained by summing the Le Bas atomic additive volumes (Appendix A). Table 2.10 below gives the values of V_A for a few common substances.

Molecular Volume, cm^3/mol			
H_2	14.3	N_2O	36.4
O_2	25.6	NH_3	25.8
N_2	31.2	H_2O	18.9
Air	29.9	H_2S	32.9
CO	30.7	COS	51.5
CO_2	34.0	Cl_2	48.4
SO_2	44.8	Br_2	53.2
NO	23.6	I_2	71.5
D_2O (estimated)	20.0		

Table 2.10. Molecular volumes for some common substances

- **Alternative Methods**

Empirical correlations have been proved to be the more accurate ways of predicting the liquid diffusion coefficient at infinite dilution. Thus, there exist a large number of them in the open literature, some of which are given below:

(1) Hayduk and Laudie (1974)

Correlation for aqueous mixtures (water as solvent)

$$D^{\circ}_{AB} = 13.26 \times 10^{-5} \eta_B^{-1.14} V_A^{-0.589} \tag{2.101}$$

(2) Hayduk and Minhas (1982)

General correlation for polar and nonpolar systems

$$D^{\circ}_{AB} = 1.55 \times 10^{-8} \eta_B^{-0.92} V_B^{-0.23} \left(P_B^{0.5} / P_A^{0.42} \right) T^{1.29} \tag{2.102}$$

where $P_A = V\sigma_A^{1/4}$, is the parachor of the solute A and σ_A is the surface tension of A (dyne/cm).

General correlation for *n*-alkanes

$$D_{AB}^{\circ} = 13.3\times10^{-8}\eta_B^{\left(10.2/V_A - 0.791\right)}V_A^{-0.71}T^{1.47} \tag{2.103}$$

(solutes from C_5 to C_{32} in normal paraffin solvents encompassing C_5 to C_{16})

Correlation for aqueous mixtures (water as solvent)

$$D_{AB}^{\circ} = 1.25\times10^{-8}\left(V_A^{-0.19} - 0.292\right)\eta_w^{\left(9.58/V_A - 1.12\right)}T^{1.52} \tag{2.104}$$

(3) Siddiqi and Lucas (1986)

General correlation for polar and nonpolar systems

$$D_{AB}^{\circ} = 9.89\times10^{-8}\eta_B^{-0.907}V_A^{-0.45}V_B^{0.265}T \tag{2.105}$$

Correlation for aqueous mixtures (water as solvent)

$$D_{AB}^{\circ} = 2.98\times10^{-7}\eta_B^{-1.0267}V_A^{-0.5473}T \tag{2.106}$$

These authors reported that their correlation for diffusion of a solute in water had a noticeably low average error than any other correlation when evaluated against 658 measured diffusivities.

(4) Wong and Hayduk (1990)

Three empirical correlations were developed for three distinct solute-solvent systems and these are:

$$D_{AB}^{\circ} = 3.17\times10^{-4}M_B M_A^{-0.596}\exp\left[\left(-487.7 - 8.57M_B + 0.009M_B^2\right)/T\right] \tag{2.107}$$

$$D_{AB}^{\circ} = 2.77\times10^{-3}\eta_B^{-0.559}\left(V_{cB}/V_{cA}^{1.59}\right)^{0.335}\left(M_A M_B^{1.31}\right)^{-0.166}\exp\left(-685.5/T\right) \tag{2.108}$$

$$D_{AW}^{\circ} = 1.014V_{cA}^{-0.712}\exp\left(2278.1/T\right) \tag{2.109}$$

where V_{cA} and V_{cB} are critical volume for solute and solvent respectively.

Eq.(2.107) is for *n*-alkane solutions and was validated with 282 data points; Eq.(2.108) is for dissolved gases in organic solvents and was validated with 421 data

points; Eq.(2.109) is for dissolved gases in water and was validated with 287 data points.

2.5.3.2. Effect of Temperature

There is no generalised method for predicting liquid diffusion coefficients under high temperature conditions. In the theoretical equation of Stokes-Einstein and also in the Wilke-Chang (1955) correlation, the temperature effect can be accounted for by assuming

$$\frac{D^{\circ}_{AB}\eta_B}{T} = \text{constant} \tag{2.110}$$

where the solvent viscosity is also a function of temperature.

However, different treatments can be found depending on the choice of the empirical prediction method used for normal temperature conditions. This is due to the fact that in the different correlations the power to which the temperature and other parameters are raised to are not unity; they are just coefficients obtained from fitting experimental data. As a result, they are usually valid over small temperature ranges. An example of this type can be found in Hayduk-Minhas (1982) method.

2.5.3.3. Effect of Pressure

Very little effort seems have been made towards the investigation of the pressure effect on liquid diffusion coefficients. Easteal (1985) developed a general correlation based on high pressure self-diffusion data for *n*-hexane. The author reported that the variation for a typical liquid shows a decreasing trend on diffusion coefficient as the pressure increases and the slope of the curve (on a D°_{AB} vs. P plot) decreases considerably with increasing pressure, particularly at elevated temperature. The dimensional working equation is in the form of

$$\ln D^{*}_{j} = a + bP^{0.75} \tag{2.111}$$

where D^{*}_{j} is the tracer or self-diffusion coefficient (m^2/s), a, b are the constants for a given solute and P is the pressure (MPa).

Though Eq.(2.111) is useful, it is difficult to apply to real cases since the necessary experimental data on high pressure liquid diffusion coefficients are usually unavailable.

If the solvent viscosity data is available at the elevated pressure, then an estimate can be obtained by using Eq.(2.110), i.e. the product of D°_{AB} and η_B is constant (at a given temperature).

2.5.3.4. Diffusion Coefficients in Concentrated Liquid Mixtures

As mentioned earlier, binary liquid diffusion coefficient depends strongly on the composition of the liquid mixture. Darken (1948) published a simple rule of combining two dilute diffusion coefficients into a single (concentrated) mixture one. The proposed equation was:

$$D_{AB} = \left(x_B D^{\circ}_{AB}\Big|_{x_B=1} + x_A D^{\circ}_{AB}\Big|_{x_A=1} \right) \left[\frac{\partial \ln a_A}{\partial \ln x_A} \right]_{T,P} \tag{2.112}$$

where D_{AB} is the concentrated mixture diffusion coefficient, $D^{\circ}_{AB}\Big|_{x_B=1}$ is the dilute diffusion coefficient for solute A in solvent B (calculated from one of the methods described in Section 2.5.3.1), x_A is the mole fraction of solute A in the concentrated mixture and a_A is the activity of component A.

The last term is known as a thermodynamic correction factor which can be predicted with thermodynamics models such as UNIQUAC or NRTL (see Section 2.4)

However, another relationship by Vignes (1966) seems to have gained more acceptance in most of the literature and it is given as follows:

$$D_{AB} = \left(D^{\circ}_{AB}\Big|_{x_B=1} \right)^{x_B} \left(D^{\circ}_{AB}\Big|_{x_A=1} \right)^{x_A} \left[\frac{\partial \ln a_A}{\partial \ln x_A} \right]_{T,P} \tag{2.113}$$

There are at least 15 other alternative methods available and they can be found in the extensive review by Pertler *et al* (1996).

2.5.3.5. Multicomponent Liquid Mixture Diffusion Coefficient

The situation on predictions of multicomponent liquid phase diffusion coefficients is more complex due to the fact that they are dependent on concentrations of other components in the mixture. There have been a few approaches to deal with this problem but they usually have limited applicability. The difficulties usually lie in the extensive thermodynamic activity data required in the correlations, not to mention the lack of actual multicomponent liquid diffusion coefficients data for validation of these correlations.

In the limiting case where a solute is to diffuse through a mixed solvents which may be treated as a homogeneous solution, Perkins and Geankoplis (1969) suggested that Wilke-Chang correlation can be modified to apply in this case:

$$D^{\circ}_{Am} = \frac{7.4\times10^{-8}\left(\sum_{j=1\neq A}^{N} x_j \phi_j M_j\right)^{1/2} T}{\eta_m V_A^{0.6}} \tag{2.114}$$

where η_m is the mixture viscosity

An alternative method suggested by the same authors was:

$$D^{\circ}_{Am}\eta_m^{0.8} = \sum_{j=1\neq A}^{N} x_j D^{\circ}_{Aj}\eta_j^{0.8} \tag{2.115}$$

2.5.4. Interfacial Area

Interfacial area is an important parameter as it governs the mass transfer occurring between the two phases. Two methods for estimating this parameter above a distillation tray are described below.

2.5.4.1. Stichlmair (1978)

The model of Stichlmair (1978) for point efficiency includes predictions for mass transfer coefficients for both phases (mentioned in the previous section) and interfacial area. The equations (given in Lockett, 1986) to predict the interfacial area per unit volume of the froth, a, are as follows:

- When $F_s/F_{s\,max} \le 0.7$:

$$a = a_B - \left(\frac{F_s/F_{s\,max}}{0.7}\right)\left(a_B^* - a_T^*\right) \tag{2.116}$$

$$\text{where } a_B = 6\left[\frac{(\rho_L - \rho_G)g}{6\sigma}\right]^{0.5}\left(\frac{F_s}{F_{s\,max}}\right)^{0.28} \tag{2.117}$$

$$a_B^* = 6\left[\frac{(\rho_L - \rho_G)g}{6\sigma}\right]^{0.5}(0.7)^{0.28} \tag{2.118}$$

$$a_T^* = \frac{(0.7F_s)^2}{2\sigma A_f^2}\left(1 - 0.7^{0.28}\right) \tag{2.119}$$

where F_s and $F_{s\max}$ were previously defined in Table 2.2.

- When $F_s/F_{s\,max} > 0.7$:

$$a = \frac{F_s^2}{2\sigma A_f^2}\left[1 - \left(F_s/F_{s\,max}\right)^{0.28}\right] \tag{2.120}$$

Lockett (1986) stated that the author correlated the interfacial area per volume under surface-tension dominated conditions but this is questionable. Previous research results showed that under normal circumstances, bubble size on a sieve tray is independent of surface tension and is perhaps more relevant to the action of bubble coalescence.

2.5.4.2. Zuiderweg (1982)

Zuiderweg (1982) developed a correlation based primarily on FRI (*Fractionation Research Inc.*) data, which was analysed using a "slope and intercept" method (see Section 2.6.2.4) from efficiency measurement on a distillation tray. The proposed equations for predicting interfacial area per volume are as follows

- For spray regime: $ah_f = \frac{40}{A_f^{0.3}}\left(\frac{u_s^2 \rho_G h_L FP}{\sigma}\right)^{0.37}$ (2.121)

- For froth regime: $ah_f = \frac{43}{A_f^{0.3}}\left(\frac{u_s^2 \rho_G h_L FP}{\sigma}\right)^{0.53}$ (2.122)

2.5.4.3. Other Correlations

Again, as for the correlations for k'_G and k'_L, there also exist several alternative correlations for predicting interfacial area; Lockett (1986) lists three of the relevant ones: Andrew (1961), Sharma *et al* (1969) and McLachlan and Danckwerts (1972). However, these results have not yet been used to any significant extent for the design of trays. Possible reasons for this are:

- limited range of conditions covered.
- poor agreement between the experimental data measured by different workers (Stichlmair, 1978).

2.6. Efficiency of a Distillation Tray

Efficiency is a user-defined term which gives an indication of how well a tray performs compared to the desired extent of separation. Over the years, there have been a number of definitions for efficiency and three of the most common ones are described in detail in this section.

2.6.1. Overall Column Efficiency and Tray Efficiency

Three most common types of efficiency defined for tray distillation are: Overall Column Efficiency, Tray Efficiency and Point Efficiency. The simplest definition is the overall efficiency which is the ratio of the number of theoretical stages to the number of actual stages in a column.

$$E_0 = N_{Theo} / N_{Actual} \quad (2.123)$$

The Murphree (1925) tray efficiency compares the exit streams concentrations of an actual tray to an ideal tray. It can be defined either in terms of the vapour (E_{MV}) or the liquid phase (E_{ML}):

$$E_{MV} = \frac{\bar{y}_n - \bar{y}_{n-1}}{y_n^* - \bar{y}_{n-1}} \tag{2.124}$$

$$E_{ML} = \frac{\bar{x}_n - \bar{x}_{n+1}}{x_n^* - \bar{x}_{n+1}} \tag{2.125}$$

where $y_n^* = m\bar{x}_n + b$, $\bar{y}_n = mx_n^* + b$ and b is the intercept of equilibrium line for a binary mixture system as shown in Figure 2.27.

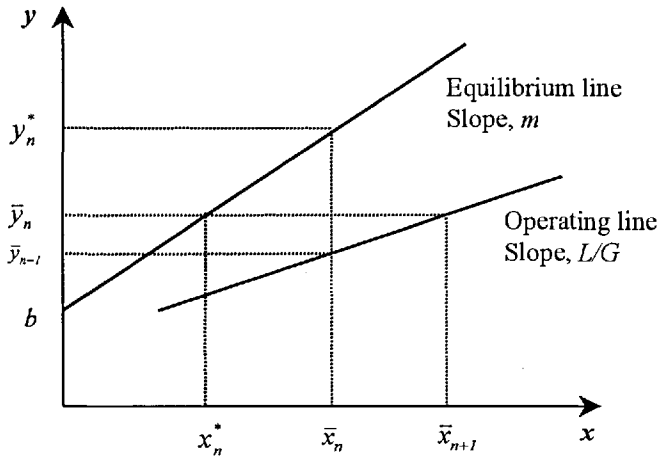


Figure 2.27. Simple vapour-liquid relationship of a binary mixture system in a column

The relationship between E_{MV} and E_{ML} is given by

$$E_{MV} = \frac{E_{ML}}{E_{ML} + \lambda(1 - E_{ML})} \tag{2.126}$$

where λ is the "stripping factor", namely the ratio of the slope of the equilibrium line to the slope of the operating line, i.e. mG/L, assuming that the operating and equilibrium lines are straight.

The relationship between E_0 and E_{MV} (Lewis, 1936) is as follows:

$$E_0 = \frac{\ln[1 + E_{MV}(\lambda - 1)]}{\ln\lambda} \tag{2.127}$$

Eq.(2.127) is based on the assumptions that the operating and equilibrium lines are straight and also that E_{MV} is constant from tray to tray.

Empirical correlations exist for overall and tray efficiencies and the ones for overall efficiency usually relate to a few key variables, e.g.

$$E_0 = 9.06(\mu_L \alpha)^{-0.245} \quad \text{by O'Connell (1946)} \tag{2.128}$$

where α is the relative volatility of the two components and is defined as $\alpha = \frac{y_1 x_2}{y_2 x_1}$.

Correlations for tray efficiency tend to be expressed in terms of relevant dimensionless groups; a typical example of such a correlation is that of MacFarland *et al* (1972).

$$E_{MV} = 7.0\left(\frac{\sigma}{\mu_L u_s}\right)^{0.14}\left(\frac{\mu_L}{\rho_L D_L}\right)^{0.25}\left(\frac{h_w u_h \rho_G}{\mu_L}\right)^{0.08} \tag{2.129}$$

$$\text{or } E_{MV} = 6.8\left(\frac{\sigma}{\mu_L u_s}\right)^{0.115}\left(\frac{\mu_L}{\rho_L D_L}\right)^{0.215}\left(\frac{h_w u_h \rho_G}{\mu_L}\right)^{0.1} \tag{2.130}$$

However, tray efficiency correlations can only be used for preliminary design purpose. For more accurate predictions, more detailed analysis are required. This has been done by the introduction of "Point Efficiency".

2.6.2. Point Efficiency

The theory of point efficiency begins with the definition of the diffusional rate equations for all phases based on a two-resistance model. The major assumptions are: (1) that the rate of mass transfer of a component within a phase is proportional to the difference in concentration or partial pressure of a component in the bulk of the phase and at the interface, (2) that equilibrium exists between phases at the interface, and (3) that the holdup of the transferring component in the boundary layer or region near the phase boundary is negligible with respect to the amount transferred in the process. (AIChE *Bubble Tray Design Manual*, 1958)

Previously, the molar flux of the more volatile component was defined as:

$$N = k_G(y_i - y) = k_L(x - x_i) = K_{OG}(y^* - y) \tag{2.66}$$

It was also previously stated (Section 2.5.1) that if the equilibrium line can be expressed by a linear relationship such that $y^* = mx + b$ and $y_i = mx_i + b$, then

$$\frac{1}{K_{OG}} = \frac{1}{k_G} + \frac{m}{k_L} \tag{2.69}$$

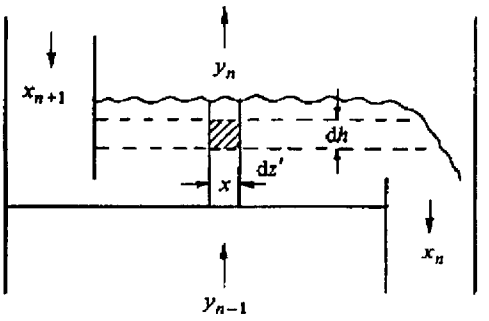


Figure 2.28. Elemental strips used to define transfer units (Lockett, 1986)

According to Figure 2.28, the mass balance on the vapour in the shaded area gives

$$G'Wdz'dy = K_{OG}(y^* - y)aWdz'dh \tag{2.131}$$

where G' is the vapour flow per unit bubbling area (kg-mol s^{-1} m^{-2})

In writing Eq.(2.131), it is assumed that the vapour is in plug flow and that there is no horizontal vapour mixing (or known as *vapour back mixing*). The number of differential transfer units is defined as the ratio of the vapour concentration change over the differential element to the driving force causing the change.

$$N_{OG} = \int dN_{OG} = \int_{y_{n-1}}^{y_n} \frac{dy}{y^* - y} = \int_0^{h_f} \frac{K_{OG}adh}{G'} = \frac{K_{OG}ah_f}{G'} \tag{2.132}$$

The gas and liquid phase transfer units are obtained by assuming the absence of liquid and vapour-phase resistance respectively. ($K_{OG} = k_G$ and $K_{OG} = k_L/m$) i.e. $N_G = \frac{k_G ah_f}{G'}$ and $N_L = \frac{k_L ah_f}{mG'}$. Therefore, the number of overall vapour-phase transfer units can be obtained from Eq.(2.69) in the previous page, i.e.

$$\frac{1}{N_{OG}} = \frac{1}{N_G} + \frac{1}{N_L} \tag{2.133}$$

It is sometimes useful to express the transfer units in terms of a phase residence time:

Vapour residence time, t_G $$t_G = \frac{h_f \varepsilon}{u_s} = \frac{h_f \varepsilon \rho'_G}{G'} \tag{2.134}$$

N_{OG} in terms of t_G: $$N_{OG} = \frac{k'_G a t_G}{1 + \frac{m k'_G \rho'_G}{k'_L \rho'_L}} \tag{2.135}$$

An alternative approach can be used for the definition of N_L. It is assumed that the liquid flows horizontally in plug flow and that there is no vertical liquid mixing, a steady mass balance of the control volume gives

$$L \frac{dh}{h_f} dx = k_L (x_i - x) a W dh dz' \tag{2.136}$$

and $$N'_L = \int dN'_L = \int_{x_{n+1}}^{x_n} \frac{dx}{x_i - x} = \int_0^z \frac{k_L a h_f W dz'}{L} = \frac{k_L a h_f W Z}{L} \tag{2.137}$$

where $N'_L = \lambda N_L$ and $\lambda = \frac{mG}{L}$

Therefore, Eq.(2.133) can be re-written as

$$\frac{1}{N_{OG}} = \frac{1}{N_G} + \frac{\lambda}{N'_L} \tag{2.138}$$

N'_L is often expressed in terms of the mean liquid residence time on the tray. Defining the horizontal liquid velocity (u_L) and the liquid residence time (t_L),

$$u_L = \frac{L}{\rho'_L a h_f W} \tag{2.139}$$

$$t_L = Z / u_L \tag{2.140}$$

and substituting these into Eq.(2.137),

$$N'_L = k'_L \bar{a} t_L \qquad \text{where } \bar{a} = \frac{a}{\alpha} \tag{2.141}$$

However, Lockett (1986) pointed out the use of N'_L rather than N_L as the definition of the number of liquid transfer units has led to some confusion. Using N'_L may give the

incorrect impression that E_{OG} depends on the mean liquid residence time on the tray. It appears to be so because only one part of the effect of liquid flowrate is considered in Eq.(2.141). In reality, the combined effects of liquid flowrate in both Eqs.(2.138) and (2.141) must be considered together. Furthermore, it should be now clear that the implication given in the *Bubble Tray Design Manual* (AIChE 1958) that some systems can be vapour phase controlled simply because $t_G << t_L$ is also incorrect. A final criticism of the use of N'_L is that it makes it more difficult to develop correlations for the number of transfer units. By correlating data in terms of N_G and N_L, the similarities between vapour and liquid phase controlled mass transfer can be exploited. There is considerable potential for improving tray efficiency prediction methods by correlating existing data in terms of N_L and N_G rather than N'_L and N_G (Lockett, 1986).

In order to define the point efficiency in a practically useful way, it is necessary to assume that the liquid is completely mixed in the vertical direction. The Murphree vapour-phase point efficiency is:

$$E_{OG} = \frac{y_n - y_{n-1}}{y^* - y_{n-1}} \tag{2.142}$$

Two simple cases for the vapour flow analysis are given below:

1. For plug flow of vapour and with y^* constant, integration of Eq.(2.132) gives:

$$N_{OG} = -\ln\left(\frac{y^* - y_n}{y^* - y_{n-1}}\right) \tag{2.143}$$

$$\text{so that } E_{OG} = 1 - \exp(-N_{OG}) \tag{2.144}$$

2. Alternatively, if the vapour is completely mixed vertically, following the mass balance of Eq.(2.132) gives:

$$G'Wdz'(y_n - y_{n-1}) = K_{OG}(y^* - y_n)aWdz'h_f \tag{2.145}$$

$$\text{and } E_{OG} = \frac{N_{OG}}{1 + N_{OG}} \tag{2.146}$$

The mechanism when the vapour passes through the froth, is important for all point efficiency prediction methods and the above mentioned methods are the two extreme cases. For a real operating tray, it is usually difficult to describe this mechanism quantitatively. There are a number of alternative ways to obtain the point efficiency for a sieve tray. Correlations and models have been established since late 1950's, and they can be classified into four main types:

1. The slope and intercept method
2. Correlations based on absorption, stripping, and humidification experiments
3. Correlations based on distillation data
4. Correlations of individual values of k'_L, k'_G, a

Selected models for point efficiency prediction are briefly described below. Most of these relate point efficiency either to the number of transfer units (N_G, N_L, N'_L) or the mass transfer coefficients (k'_G, k'_L, K'_{OG}) with the interfacial area per unit volume (a).

2.6.2.1. AIChE correlation (1958)

The AIChE (1958) correlation is probably one of the earliest correlations for efficiency prediction and correlations of this type are usually based on experimental data from absorption, stripping and humidification. In the *AIChE Bubble Tray Design Manual* (1958), the following correlations were proposed:

$$N_G = \left(0.776 + 4.57h_w - 0.238F_s + 104.8\frac{Q_L}{W}\right)Sc_G^{-0.5} \tag{2.147}$$

$$N'_L = 1.97\times10^4 D_L^{0.5}\left(0.4F_s + 0.17\right)t_L \tag{2.148}$$

where the gas phase Schmidt number is given as $Sc_G = \dfrac{\mu_G}{\rho_G D_G}$ and the liquid residence time is defined as $t_L = \dfrac{h_L ZW}{Q_L}$

These correlations are said to underestimate the percentage liquid-phase resistance (Lockett, 1986). Other correlations of similar type include: Harris (1965), Asano and

Fujita (1966), Jeromin *et al.* (1969) for sieve trays, and Hughmark (1971) for bubble cap trays.

2.6.2.2. Stichlmair (1978)

The Stichlmair (1978) correlation (quoted in Lockett, 1986) estimates point efficiency by giving prediction methods for the individual mass transfer coefficients and interfacial area per volume of the two-phase mixture. The proposed equations for mass transfer coefficient and interfacial area were given earlier in Section 2.5.1.4 and 2.5.4.1 respectively.

2.6.2.3. Neuburg and Chuang (1982)

Neuburg and Chuang (1982) proposed the following equation for the overall combined volume coefficient for distillation:

$$K'_{OG}a = 12\left(\frac{D_L u_s \varepsilon}{\pi d_b^3}\right)^{0.5}\left[\left(\frac{D_L}{D_G}\right)^{0.5} + \frac{m\rho'_G}{\rho'_L}\right]^{-1} \tag{2.149}$$

The accurate prediction of d_b presents a major problem for this correlation. For the development of this model, d_b was back-calculated from E_{OG} data taken from pilot-scale experiments, and then used in predicting E_{OG} in full-size columns.

2.6.2.4. Zuiderweg (1983)

The Zuiderweg (1983) correlation is mainly based on the FRI data. E_0 or E_{MV} were measured over a range of concentrations and E_{OG} is calculated according to the appropriate liquid flow model. N_{OG} was back-calculated using Eq.(2.144) and $1/N_{OG}$ was plotted against the slope of equilibrium line, m. The slope and intercept of this line is $(G'/k_L a h_f)$ and $(1/N_G)$ respectively. The conditions for this method to remain valid are that: (1) the value of m to be a reasonably strong function of concentration and (2) the volumetric mass transfer coefficients and h_f to be independent of concentration.
The following equations were proposed:

$$k'_G = \frac{0.13}{\rho_G} - \frac{0.065}{\rho_G^2} \qquad \text{for } 1.0 < \rho_G < 80 \tag{2.150}$$

$$k'_L = 2.6\times10^{-5}\mu_L^{-0.25} \text{ or } k'_L = 0.024D_L^{0.25} \tag{2.151}$$

for spray regime: $$ah_f = \frac{40}{A_f^{0.3}}\left(\frac{u_s^2\rho_G h_L FP}{\sigma}\right)^{0.37} \tag{2.152}$$

for froth regime: $$ah_f = \frac{43}{A_f^{0.3}}\left(\frac{u_s^2\rho_G h_L FP}{\sigma}\right)^{0.53} \tag{2.153}$$

The inclusion of the surface tension effect is open to question since the physical properties for the systems used in FRI data tend to change in unison. (Lockett, 1986)

2.6.2.5. Chan and Fair (1984)

A frequently quoted correlation for point efficiency is that of Chan and Fair (1984). The authors extracted E_{OG} from distillation data and then used Eq.(2.144) to determine N_{OG}. AIChE correlation for N'_L is used and together with Eq.(2.138), N_G can be calculated. Based on the authors' databank, they proposed:

$$N_G = \frac{1000D_G^{0.5}\left[10.3(FF)-8.67(FF)^2\right]t_G}{h_L^{0.5}} \tag{2.154}$$

$$N'_L = 1.97\times10^4 D_L^{0.5}(0.4F_s+0.17)t_L \tag{2.155}$$

where FF is the flooding factor defined as $FF = \frac{u_s}{u_{s,flood}}$ and the residence time for gas and liquid phase are given as $t_G = \frac{(1-\phi_e)h_L}{\phi_e u_s}$ and $t_L = \frac{h_L ZW}{Q_L}$ respectively; the value of h_L and ϕ_e are calculated using correlations by Bennett *et al* (1983).

2.6.2.6. Bennett *et al* (1997)

Bennett *et al* (1997) gave a complete set of prediction procedures for point efficiency. The authors considered the fluid on the distillation tray to be contained in a liquid-continuous region near the tray deck and a vapour-continuous region on top of the liquid-continuous region. This model allows estimates of the proportion of the mass transfer that occurs in each region and mass transfer resistance that exists on the liquid side and vapour side of the interface. For most cases, most of the mass transfer occurs

within the liquid-continuous region and the liquid side resistance is often significant. Therefore, the authors proposed the following relationships under two conditions:

- Liquid-Continuous-only point efficiency model:

$$E_{OG,LC}=1-\exp\left[\left(\frac{-0.0029}{1+m\frac{\rho'_G}{\rho'_L}\sqrt{\frac{D_G(1-\phi_e)}{D_L A_f}}}\right)\left(\frac{\rho_G u_h h_L}{\mu_G \phi_e}\right)^{0.4136}\left(\frac{h_L}{d_h}\right)^{0.6074} A_f^{-0.3195}\right] \tag{2.156}$$

- Point efficiency model for both Liquid- and Vapour-Continuous Regions:

$$E_{OG,LC}=1-\exp\left[\left(\frac{-0.0029}{1+m\frac{\rho'_G}{\rho'_L}\sqrt{\frac{D_G(1-\phi_{LC})}{D_L A_f}}}\right)\left(\frac{\rho_G u_h h_L}{\mu_G \phi_e}\right)^{0.4136}\left(\frac{h_L \phi_{LC}}{\phi_e d_h}\right)^{0.6074} A_f^{-0.3195}\right] \tag{2.157}$$

$$E_{OG,VC}=1-\exp\left[\frac{-3.2}{CF\left(1+m\frac{\rho'_G}{\rho'_L}\sqrt{\frac{D_G\left(h_f-h_L/\phi_e\right)}{D_L d_P}}\right)}\sqrt{\frac{D_G u_{ej}}{\pi d_P}\frac{\rho_G}{\rho_L-\rho_G}}\frac{h_f-h_L/\phi_e}{d_P}\phi_{VC}\right] \tag{2.158}$$

where u_{ej} is the ejection velocity of the droplet from the top of the liquid-continuous region and is defined as $u_{ej}=3CF\sqrt{\frac{\sqrt{3}}{A_f\phi_e}}$; the average froth densities for the vapour- and the liquid-continuous are given as $\phi_{VC}=\frac{h_L}{h_f-h_L/\phi_e}f$ and $\phi_{LC}=\phi_e(1-f)$ respectively; the parameter f is the ratio of the total mass within the vapour-continuous region to the total liquid inventory and is defined as $f=\left(1-\frac{h_L}{h_f\phi_e}\right)e^{-0.1(h_L/d_h)}$; the overall point efficiency, E_{OG}, can be obtained by $E_{OG}=E_{OG,VC}+E_{OG,LC}\left(1-E_{OG,VC}\right)$

Note that in the above equations, the correlation by Bennett *et al* (1983) is used for the prediction of h_L and ϕ_e whereas the mechanistic model by Bennett *et al* (1995) is used to calculate the froth height, h_f.

2.6.3. Relationship between Point Efficiency and Tray Efficiency

The point efficiency is the ratio of the change of composition at a point to the change that would occur on a theoretical stage. The Murphree tray efficiency is the same as point efficiency, except that it applies for the entire tray instead of to a single point (Kister, 1992). The relationship between the Murphree tray efficiency E_{MV} and the Murphree point efficiency E_{OG} can be well described in Figure 2.29 below.

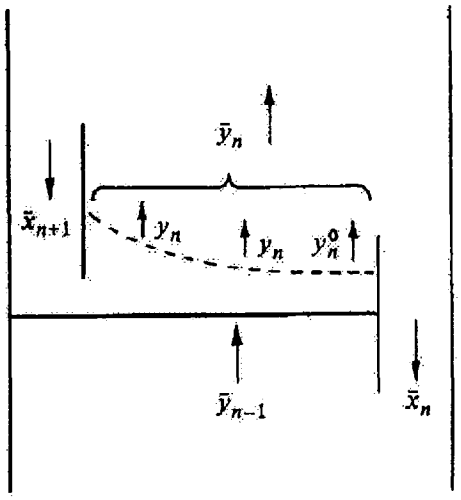


Figure 2.29. Concentration profile for more volatile component in the vapour leaving a tray (Lockett, 1986)

The definitions for Murphree tray (E_{MV}) and point efficiency (E_{OG}) are:

$$E_{MV} = \frac{\bar{y}_n - \bar{y}_{n-1}}{y_n^* - \bar{y}_{n-1}} \text{ and } E_{OG} = \frac{y_{n,local} - \bar{y}_{n-1}}{y_{n,local}^* - \bar{y}_{n-1}} = \frac{y_n^0 - \bar{y}_{n-1}}{y_n^* - \bar{y}_{n-1}}$$

The above expressions assume the inlet vapour is completely mixed. E_{OG} can be defined at any point on the tray, and the last term (of the E_{OG} definition) shows the definition for E_{OG} at the outlet weir.

In practice, a concentration gradient exists in the liquid, and x_n at the tray outlet is lower than x_n on the tray and this frequently lowers y_n^* (in the above expression of E_{MV}) relative to y_n^0 (in the above expression of E_{OG}), thus enhancing tray efficiency compared to point efficiency. y_n^* may even drop below $\bar{y}_n$; in this case, E_{MV} exceeds 100 percent.

Liquid mixing is the key to relate these two types of efficiency. Imperfect liquid mixing on a tray causes concentration gradients in both liquid and vapour phases along the tray. Lewis (1936) attempted to determine quantitative relationships between E_{MV} and E_{OG} for three special cases of liquid phase in plug flow.

Lewis's Case 1: Assuming well mixed vapour, the liquid flow direction on successive trays is immaterial. In this case, it follows that:

$$E_{MV} = \frac{\exp(\lambda E_{OG}) - 1}{\lambda} \tag{2.159}$$

where $\lambda = mG/L$

Lewis's Case 2: Assuming unmixed vapour, and the liquid flows in the same direction on successive trays then

$$E_{MV} = \frac{\alpha - 1}{\lambda' - 1} \tag{2.160}$$

where $\alpha = \dfrac{y_n - y_n^0}{y_{n-1} - y_{n-1}^0}$ and $\lambda' = \left(\dfrac{1}{E_{OG}} + \dfrac{1}{\alpha - 1}\right)\ln\alpha$

Lewis's Case 3: Assuming unmixed vapour, and the liquid flows in alternate directions on successive trays then

$$E_{MV} = \frac{\alpha - 1}{\lambda'' - 1} \tag{2.161}$$

where $\alpha = \dfrac{(y_n - y_n^0)_{z'}}{(y_{n-1} - y_{n-1}^0)_{1-z'}}$ and z' is a number representing the position on the tray; z' changes from unity to zero as the liquid flows from the inlet weir to the outlet weir.

$$\text{if } \alpha < 1;\ \lambda'' = \left[\frac{\alpha^2 - (1 - E_{OG})^2}{E_{OG}^2(\alpha^2 - 1)}\right]^{0.5} \cos^{-1}\left[1 + \frac{(1-\alpha)(\alpha - 1 + E_{OG})}{\alpha(2 - E_{OG})}\right]$$

$$\text{if } \alpha > 1;\ \lambda'' = \left[\frac{\alpha^2 - (1 - E_{OG})^2}{E_{OG}^2(\alpha^2 - 1)}\right]^{0.5} \cosh^{-1}\left[1 + \frac{(\alpha-1)(\alpha - 1 + E_{OG})}{\alpha(2 - E_{OG})}\right]$$

Case 1 is generally applied in efficiency models and the other two cases are hardly used (Kister, 1992). These equations give the maximum tray efficiency that can be achieved. In reality, the efficiency falls short of the maximum value because of:

1. Vapour and liquid mixing
2. Non-uniform vapour and liquid flow above the tray
3. Entrainment and weeping effects

Some models and correlations for converting point efficiency to tray efficiency are briefly described in the following sections.

2.6.3.1. Simple Backmixing Model

This is one of the main approaches of converting point efficiency to tray efficiency comes from simplifications of the mass balance over dispersion in a differential control volume and these are associated with the prediction of the eddy diffusivity for a sieve tray. A two-dimensional tray co-ordinate system is defined and the mass conservation equation can be written, which account for the liquid mixing caused by the vapour, bulk liquid flow, transfer to vapour, entrainment and weeping. This is illustrated in Figures 2.30, 2.31 and Eq.(2.162) below.

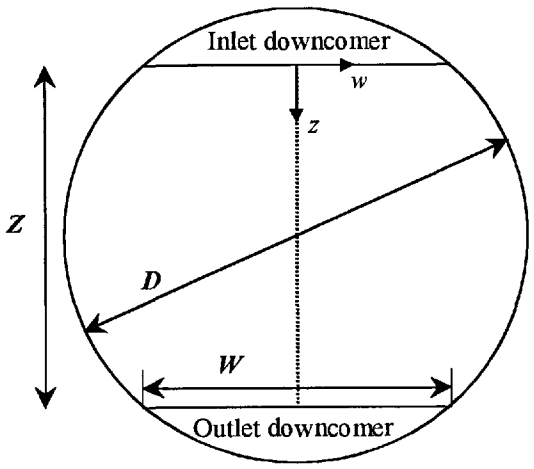


Figure 2.30. Geometry of a tray

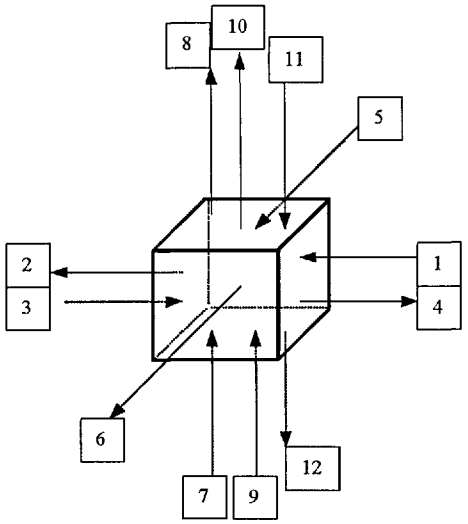


Figure 2.31. Mass balance over dispersion on a differential control volume

At steady state for tray n, the liquid concentration x at point (w, z) is given by:

$$De\,h_L\rho'_L\left(\frac{\partial^2 x}{\partial z^2}+\frac{\partial^2 x}{\partial w^2}\right)-L'\frac{\partial x}{\partial z}+G'(y_{n-1}-y_n)+eG'(x'_{n-1}-x)-L'_w(x-x'_{n+1})=0 \quad (2.162)$$

where equal eddy diffusion coefficient, De, in all horizontal directions is assumed. The terms in the above equation represent actions of mass transfer caused by vapour flow (*1,2* in Figure 2.31), bulk liquid flow (*3,4,5,6*), transfer to the vapour (*7,8*), entrainment (*9,10*) and weeping (*11,12*).

In order to solve Eq.(2.162), the simple backmixing model treats the tray as being rectangular in shape and the effects of weeping and entrainment are ignored. For the Lewis's case 1, it is possible to obtain analytical solutions for Eq.(2.162) and providing uniform liquid residence time distribution is achieved, this model can be used on circular tray efficiency calculation by replacing the weir width (in the Peclet number definition) with a term called effective width, S. This gives the allowance for the curved walls in a circular tray over the flat ones for a rectangular tray (an assumption used in the model), i.e.

Lewis's case 1:

$$\frac{E_{MV}}{E_{OG}}=\frac{1-\exp[-(\eta+Pe)]}{(\eta+Pe)\{1+[(\eta+Pe)/\eta]\}}+\frac{\exp\eta-1}{\eta\{1+[\eta/(\eta+Pe)]\}} \quad (2.163)$$

where $Pe = \frac{Q_L Z}{S\, h_L De}$, $\eta = \frac{Pe}{2}\left[\left(1+\frac{4\lambda E_{OG}}{Pe}\right)^{0.5} - 1\right]$ and

$$S = 0.5W + \frac{D\left(0.5\pi/180\right)\sin^{-1}\left\{\left[1-(W/D)^2\right]^{0.5}\right\}}{\left[1-(W/D)^2\right]^{0.5}}$$

For the Lewis's cases 2 & 3, analytical solutions have not been obtained. Numerical solutions have been given by Diener (1967) and Lockett *et al* (1973) using different approaches, however, there is no "standard solution" for this problem. The soultion derived by Lockett *et al* (1973) is given as

Lewis's cases 2 & 3:

$$E_{MV} = E_{OG} + \left[\left(E_{MV}\right)_{case3}^{Pe=\infty} - E_{OG}\right]\frac{\left(E_{MV}\right)_{case1}^{Pe} - E_{OG}}{\left(E_{MV}\right)_{case1}^{Pe=\infty} - E_{OG}} \tag{2.164}$$

where $\left(E_{MV}\right)_{case1}^{Pe}$ can be obtained from the "**Lewis's case 1**" above, $\left(E_{MV}\right)_{case1}^{Pe=\infty}$ is calculated from Eq.(2.159) and whereas $\left(E_{MV}\right)_{case3}^{Pe=\infty}$ is calculated using Eq.(2.161). This method does not work well at low Peclet number where the assumption of no vapour mixing inherent in Lewis's cases 2&3 is itself open to question (Lockett, 1986).

2.6.3.2. Mixed Pools Model for liquid mixing:

An alternative to the simple backmixing model is called the **Mixed Pools Model** in which the liquid is envisaged as a series of completely mixed pools extending along the length of the tray. The resulted relationship is

$$\frac{E_{MV}}{E_{OG}} = \frac{\left[1+\left(\lambda E_{OG}/N\right)^N\right]-1}{\lambda E_{OG}} \tag{2.165}$$

where N can be related to the Peclet number defined as $Pe = \frac{Q_L Z}{W\, h_L De}$ and two available relationships for N are as follows:

Williams *et al* (1960) $\qquad N = \frac{Pe+2}{2}$

Ashley and Haselden (1970) $N = \frac{Pe+1}{2}$ when Pe is large

$N = \frac{Pe+2}{2}$ when $Pe > 2$, $\lambda E_{OG} < 0.5$

2.6.3.3. Stagnant Region Model (SRM)

A distillation tray has a circular geometry and the liquid flow diverges as it enters the tray from the downcomer. It has little tendency to move sideways to follow the curved walls. Instead it tends to channel preferentially down the central past of the tray taking the shortest route between the inlet and the outlet downcomers. This is the well-known liquid maldistribution effect on a tray. Liquid maldistribution is especially important for single-pass, large diameter trays and it has a more significant effect on tray efficiency than the vapour flow maldistribution. The 'Stagnant Region Model' (SRM) by Porter *et al* (1972) is a simple but useful model describing this effect and it has been served as a backbone of all the later models.

The liquid is taken to flow uniformly from inlet weir to outlet weir in the 'active' region leaving segmental 'stagnant' regions at the sides of the tray as shown in Figure 2.32.

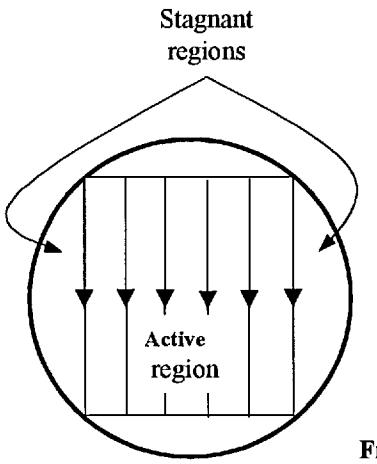


Figure 2.32. Assumed liquid flow profile for the SRM

Mathematically, it follows the same analysis of mass balance as that used in the simple backmixing model with the same boundary conditions. In the active region, the previous analysis holds as it stands. In the stagnant region, there are two extra conditions stated:

1. there is no bulk flow and $dx/dz=0$
2. equal value of De in both axial and transverse directions

These equations were solved numerically to give the liquid concentration profile on the tray. Comparison with the experimental values from *Fractionation Research Inc* shows that SRM is adequate for predicting the observed concentration profile.

2.6.3.4. Bennett *et al* (1997)

All the models described so far are based on the mass transfer equation (Eq.2.162). Bennett *et al* (1997) developed their own correlations for converting their predicted point efficiency (Section 2.6.2.6) to the Murphree tray efficiency. This was done by considering the extent of mixing for both phases and the flow direction. The extent of vapour mixing is defined by the gas phase Peclet number as follows:

$$Pe_G = \frac{u_s Z^2}{De_G\left(T_s - h_f\right)}$$

where typically, $De_G = 0.01$ and according to Katayamo and Imoto (1972), the vapour can be considered to be unmixed when $Pe_G \geq 50$ and well-mixed when $Pe_G < 50$.

For the extent of liquid mixing, the following parameters are defined:

$$N = \frac{Pe_L + 2}{2}\ ,\ Pe_L = \frac{Q_L Z^2}{A_s h_L De_L} \text{ and } De_L = 0.096\left(g h_f^3\right)^{0.5}$$

De_L is based on the correlation by Bennett and Grimm (1991) and the above expression for De_L has been modified to compensate for the inlet maldistribution and tray curvature.

The three cases considered by the authors are:

$$E_{MV} = \frac{\left[1+\left(\lambda E_{OG}/N\right)\right]^N - 1}{\lambda} \qquad (2.166)$$

for well-mixed vapour and partially mixed liquid, $0.5 \leq \lambda \leq 3.0$, $0.4 \leq E_{OG} \leq 1.0$, $0 \leq Pe_L \leq 1000$

$$E_{MV} = \frac{\left[1+\left(\lambda E_{OG}/N\right)\right]^{N}-1}{\lambda}\left(1+0.0463\lambda^{0.6255}E_{OG}^{1.69591}Pe_{L}^{0.16625}\right) \qquad (2.167)$$

for unmixed vapour and parallel flow liquid, $0.5 \le \lambda \le 3.0$, $0.4 \le E_{OG} \le 1.0$, $0 \le Pe_L \le 1000$

$$E_{MV} = \frac{\left[1+\left(\lambda E_{OG}/N\right)\right]^{N}-1}{\lambda}\left(1-0.0335\lambda^{1.07272}E_{OG}^{2.51844}Pe_{L}^{0.17524}\right) \qquad (2.168)$$

for unmixed vapour and crossflow liquid direction, $0.5 \le \lambda \le 3.0$, $0.4 \le E_{OG} \le 1.0$, $0 \le Pe_L \le 1000$

The authors also included some correction terms to take account of weeping and entrainments, however, these are not emphasised here.

2.6.4. Calculation Procedure

Figure 2.33 below gives a summary of typical procedures for predicting efficiencies of a sieve tray and of a column. It begins with the prediction of point efficiency, methods of which are described in Section 2.6.2, and this is followed by an appropriate liquid flow model. The combination of these two results will form a "normal" tray efficiency which can then be corrected to take account of other situations such as entrainment or weeping. Finally, an overall efficiency can be determined when individual tray efficiencies are known.

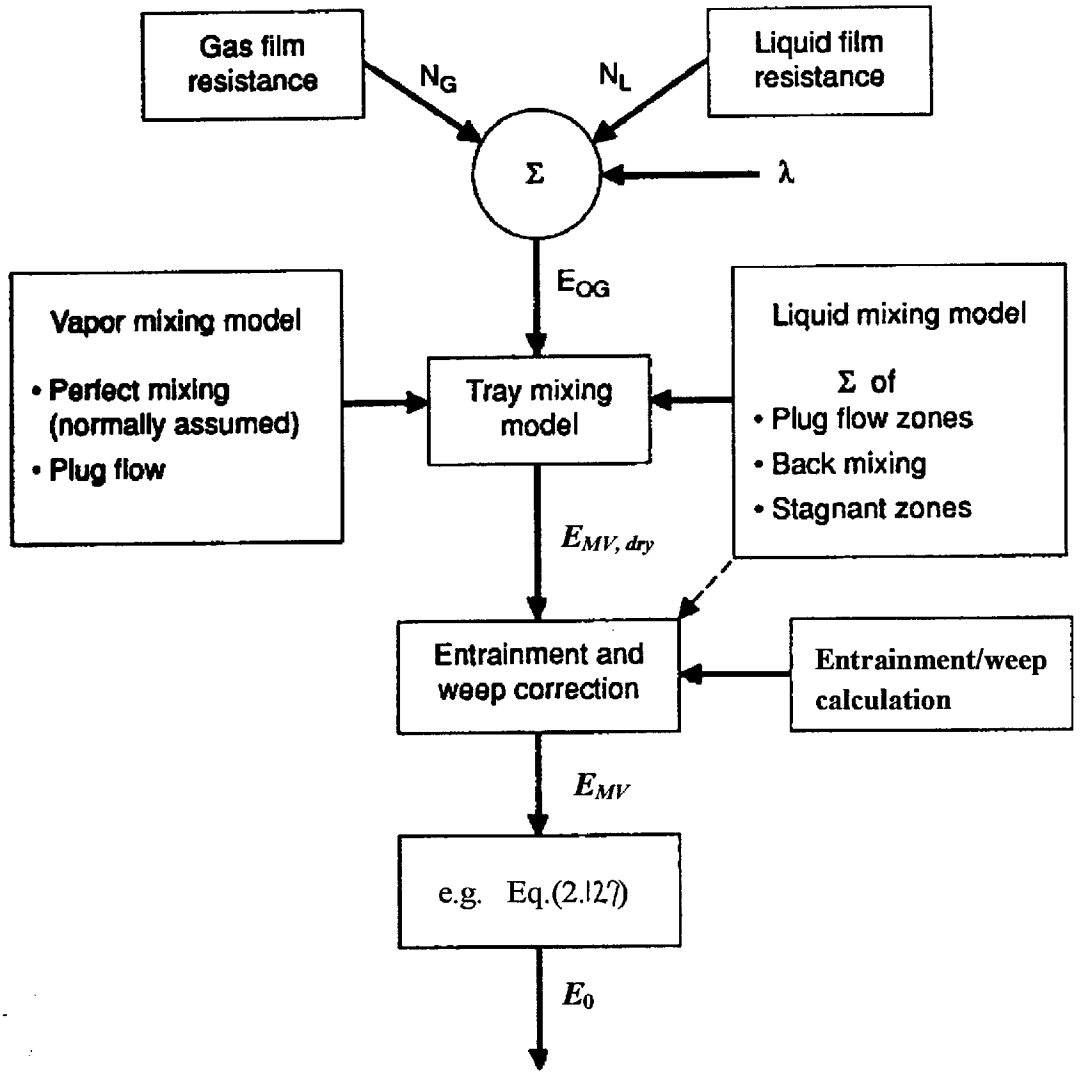


Figure 2.33. Sequence of steps for the prediction of tray efficiency (modified from Kister, 1992)

2.7. CFD Challenges

Computational Fluid Dynamics (CFD) has become an useful tool for calculating fluid flow, and its application can also be extended to heat and mass transfer problems. In recent years, CFD applications on multiphase flow systems, e.g. oil pipeline flow and chemical reactors have been of particular interest to industry.

CFD involves the process of solving conservation equations (mass, momentum and energy) with the user specified initial and boundary conditions. Most experienced users

can comfortably handle single-phase calculations and the predictions are in good agreement with experimental results. However, CFD applications on multiphase flow, especially in gas-liquid flow, are more difficult because of the changing interface, where local interfacial relationships are not well established. The conservation equations describe the global flow but there is considerable difficulty in formulating constituitive relations or closure relationship governing the exchange between the phases of the conserved quantities (Tezock, 1994).

The work sponsored by the ASID (Advanced Studies In Distillation) Consortium uses a commercial CFD package (CFX Version 4.3 by *AEA Technology Ltd*) to predict the two-phase hydrodynamics on a sieve tray and experimental results from distillation simulators are used to validate the code.

Daly (1997) assumed a factor which modifies the constituitive relationships to allow for bubble formation, coalescence, break-up, etc. phenomena to occur in multiple bubbling. Figure 2.34 is an example (by Daly, 1997) of a CFD prediction of a two-dimensional velocity profile on a 2.44-metre diameter distillation simulation rig in Aston University.

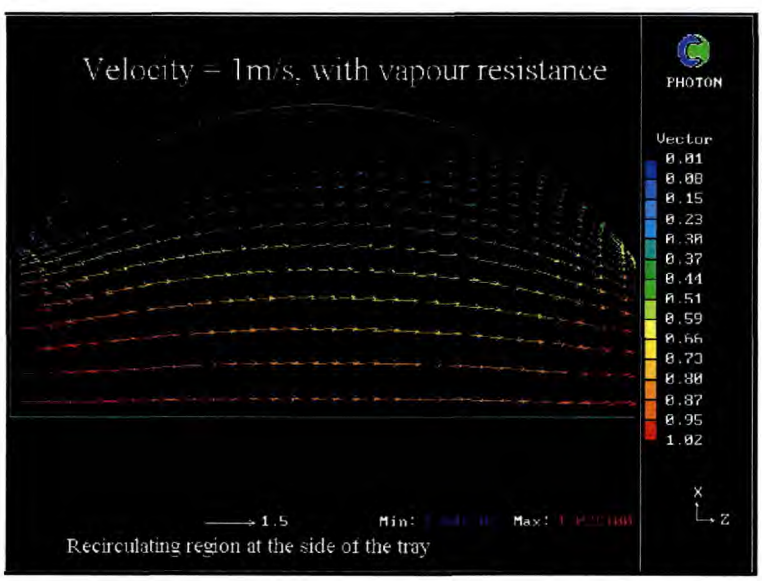


Figure 2.34. CFD predictions of velocity profile on Aston's rig

Fischer (1999) followed up the work by Daly (1997) and applied the following CFD methodologies on two-phase flow:

- Homogeneous two-phase
- Homogeneous two-phase with algebraic shear
- Heterogeneous two-phase with IPSA (Inter Phase Slip Algorithm)

Figures 2.35 and 2.36 show the predictions of dispersion density on a crossflow distillation simulator at Imperial College (CRODIS) and on the 2.44-metre rig in Aston University respectively. The results are in reasonable agreement with the experimental data.

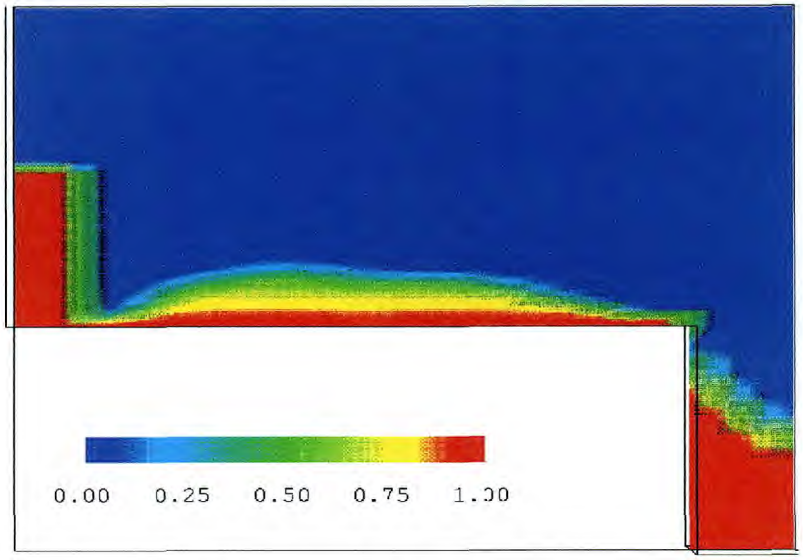


Figure 2.35. CFD predictions of dispersion density on CRODIS

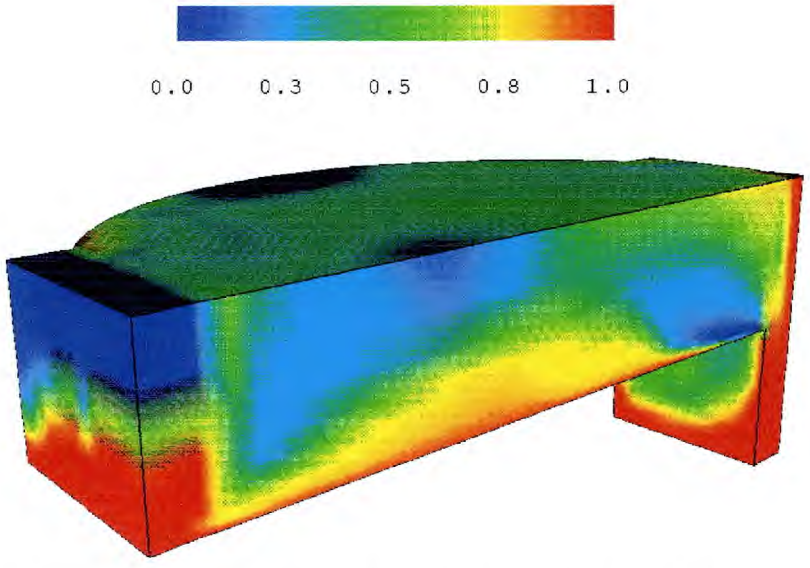


Figure 2.36. CFD predictions of dispersion density on Aston's rig

More recently, Krishna *et al* (1999) developed a transient three-dimensional CFD model where gas and liquid are treated as interpenetrating continuums and modelled within the Eulerian framework. The only empirical input of the model is the slip velocity between the interface which is given by Bennett's correlation (1983). The authors claimed that the model over-predicts the clear liquid height compared to their air-water test results and this is due to the choice of input correlation for the slip velocity. They concluded that there is a need for developing more fundamental models for the closure relationships between the gas and liquid phases on a sieve tray.

2.8. Objectives of Present Work

In research on tray flows, the hydrodynamic aspects have been well explored. However, the resultant predictive relationships for the hydrodynamic parameters are less satisfactory and discrepancies are usually found between them. These discrepancies arise mainly due to the fact that the experimental data used to develop correlations were obtained under different conditions, e.g. some experiments were carried out in rather small scale equipment and the results obtained may not be representative of the real situation. Thus, more experimental data, under appropriate conditions, are required to check against some common prediction methods for hydrodynamic parameters (e.g. clear liquid height, ...etc). Furthermore, the experimental data also plays an important role on the validations of any CFD model. Although the present developments on CFD show some encouraging results on simulating a single tray (e.g. Fischer, 1999 and Krishna *et al*, 1999), they do share a common conclusion that there is still a need to investigate the very fundamental relationships for multi-phase flow (e.g. interfacial drag law, ...etc).

There are still lots of other areas in distillation requiring further improvement, however, based on the above discussions, the following points stand out as clear objectives for the present work:

- To obtain general experimental data on hydrodynamic properties (such as pressure drop, dispersion density profiles, Sauter mean bubble diameter profiles) for different tray geometries. The results can be used to compare with existing correlations and also can be used to validate CFD models.

- To develop a new experimental technique in order to obtain more detailed information on the froth structure, e.g. characterise the froth body into bubbles and droplets. This will help to develop new closure relationships to be used in future CFD models

- To look for any alternative approach to the current CFD models (e.g. Fischer, 1999) on the sieve tray flow. A good starting point may be to consider the situation in bubbly flow where bubble break-up and coalescence mechanisms co-exist.

- To develop a "bridging" methodology by which the flow distributions predicted by CFD models (validated by the experimental data) can be used to predict tray efficiency.

Chapter 3

Gas-Liquid Simulation Experiment (1) -

CRODIS Facility

3.1. Introduction

The main objective of the work described in this chapter was to investigate the hydrodynamic properties of two sieve trays: 1.8mm and 6mm hole diameters with 8% open area. The results are used to develop and validate the CFD study carried out on a sieve tray as part of the ASID consortium research programme.

The most important data for this validation process is the froth structure expressed in terms of a froth density profile (i.e. gas or liquid fraction) and this is used to compare to the one produced by a CFD model. The second part of the present work is to obtain an average diameter (of bubbles or droplets) distribution above a sieve tray. This information, together with an appropriate interfacial drag law, is important in further development of CFD models.

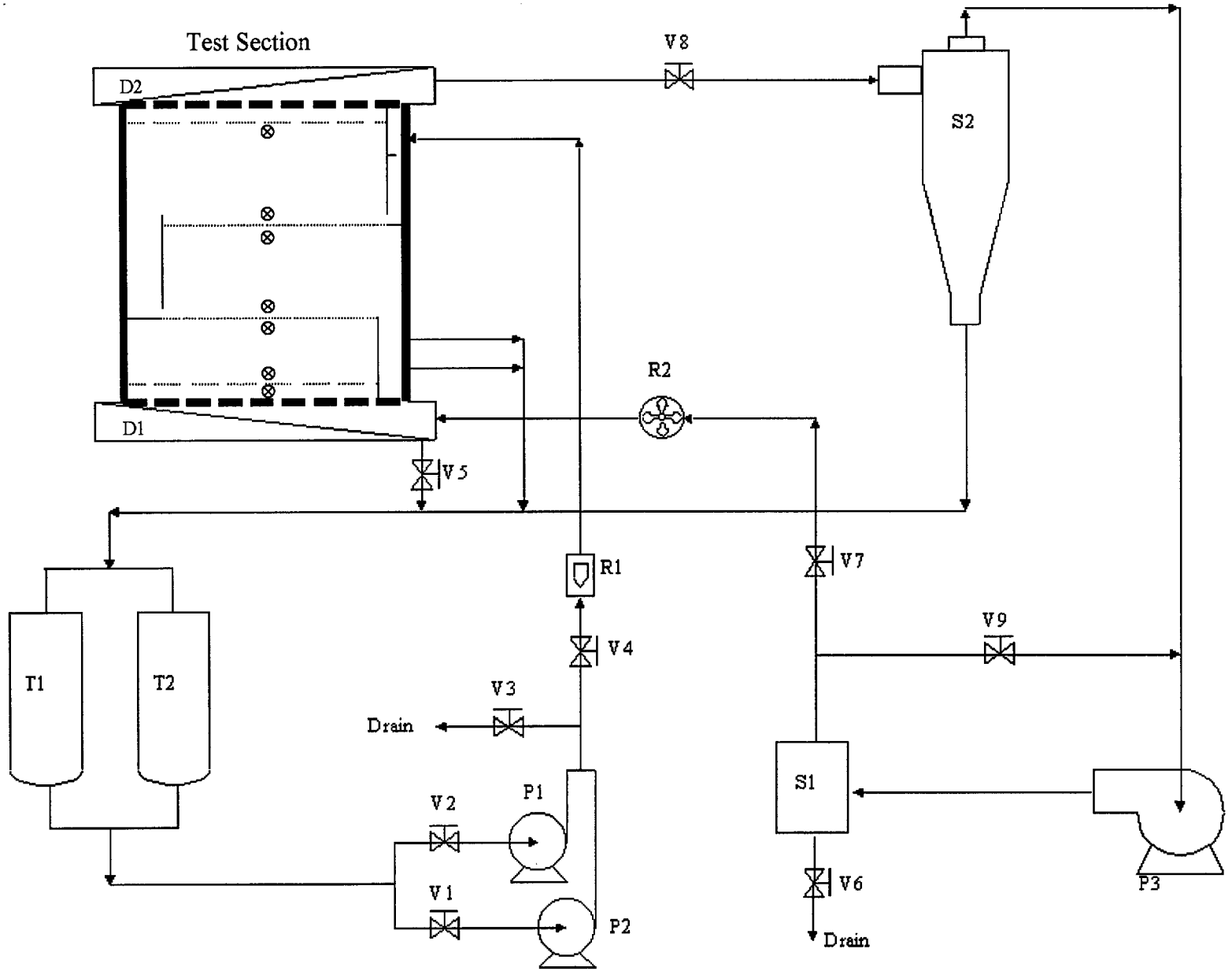
The task was undertaken using the CRODIS facility at Imperial College and the experimental rig is described in Section 3.2. In the experiment, measurements of phase holdup, pressure drop and bubble/droplet size distributions have been obtained over a range of gas and liquid flowrates with several configurations of both trays. Section 3.3 details the associated measuring techniques used in this study. Experimental results are presented and discussed in Section 3.4 which includes comparisons with some published work. Finally, a brief summary on the experimental results is made in Section 3.5.

3.2. The CRODIS Facility

Experiments have been performed on a gas-liquid CROssflow DIstillation Simulator (CRODIS), first constructed by Tahmasbi (1997) and subsequently modified for the purpose of the present work. Figure 3.1 shows the latest flowsheet of the CRODIS facility and as a comparison, the old flowsheet of CRODIS by Tahmasbi (1997) is shown in Figure 3.2. The detailed description on the modifications on the CRODIS facility for this work will be discussed later in this section.

Air and laboratory distilled water are used to simulate the gas and liquid phase fluids in a real distillation situation. Air is introduced into the column via a centrifugal fan blower (*Secomak 492/3*) shown as **P3** in Figure 3.1 and is recycled within the system. Distilled water is pumped into the column from two glass storage tanks (**T1** & **T2**) by two pumps (**P1** & **P2**) and eventually flows back to the two tanks again for recycle. A new cyclone has replaced an old impact-plate separator (used in the original design by Tahmasbi, 1997) to separate the carried-over droplets of water in the air return line. This is to avoid excessive moisture which can damage the centrifugal blower. The air flowrate is measured by a vane anemometer (**R2**) which was specially calibrated in a 4-inch duct, the same size as the one used in CRODIS and the water flowrate is measured by an *ABCM* metric size 18X rotameter (**R1**).

The detailed dimensions of the test section in the CRODIS facility are shown in Figure 3.3. The section is made of transparent perspex and its rectangular geometry (with the dimensions of 1300×1200×60 mm in height, length, width) is ideal for visualisation of the two-phase flow. There are four sieve trays installed in the column and the second tray from the top is the test tray where measurements were taken. The dimensions of the test tray are shown in Figure 3.4. The trays are chosen to be rectangular to simplify the liquid flow path compared to a normal circular tray (circular trays give the rise of re-circulating flow regions) and they are used to simulate the conditions similar to the central channel of a normal circular distillation tray.



List of symbols:

P1	Water pumps 1
P2	Water pumps 2
P3	Air circulator
T1	Water storage tank 1
T2	Water storage tank 2
V's	Valves
S1	Air chamber
S2	Cyclone
R1	Water rotameter
R2	Anemometer
D1	Air distribution box 1
D2	Air distribution box 2
⊗	Manometer tappings

Figure 3.1.
The flowsheet of CRODIS

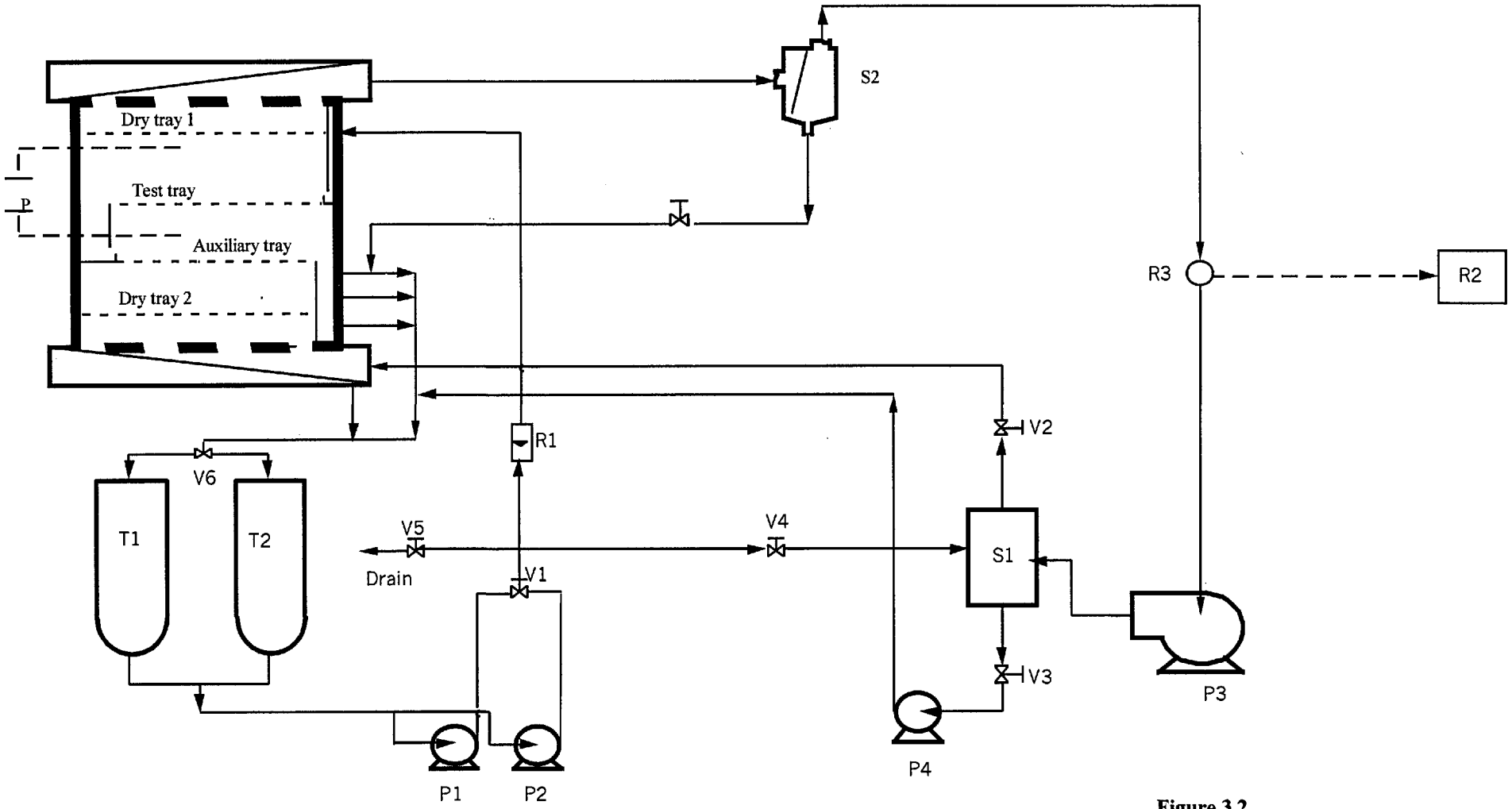


Figure 3.2.

The old flowsheet of CRODIS
(by Tahmasbi, 1997)

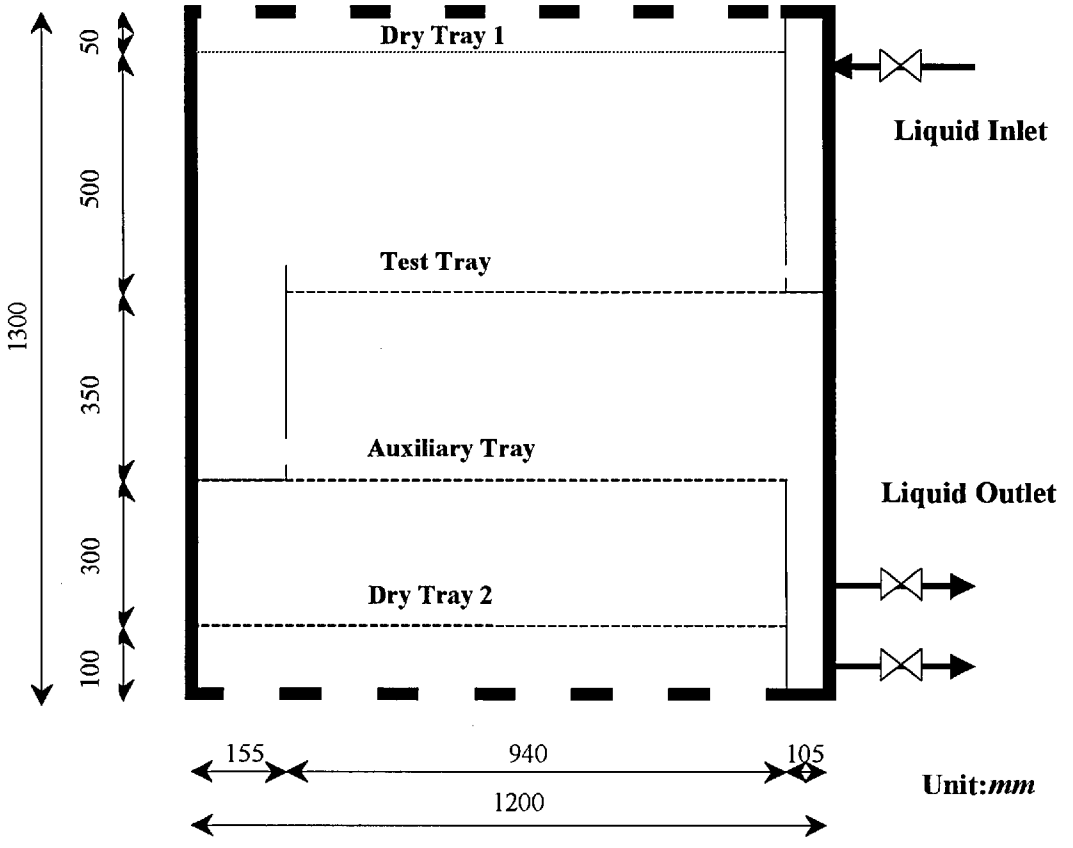


Figure 3.3. The detailed dimensions (in mm) of CRODIS test section

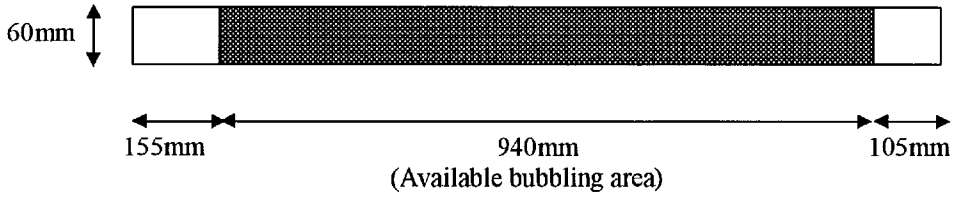


Figure 3.4. Configuration of the test tray

For some tests described in this thesis, 50mm at each end of the 940mm bubbling area was blanked-off underneath the tray with a layer of silicon sealant

Prior to entering the test section, the air flow passes through a distribution box attached to the bottom of the test section. This ensures the air flow to be evenly distributed across the whole cross-section of the column. The two trays below the test tray help to achieve a more realistic air flow distribution at the bottom of the test tray. The distilled water enters the test section from the top right corner which connects to the inlet downcomer of the test tray. The crossflow water engages with the up-flowing air on both test tray and auxiliary tray before leaving the test section from the bottom right corner. The test section was designed such that, under normal operating conditions, water should only be present on the test and auxiliary trays, not on the top and bottom dry trays (unless entrainment or weeping occurs).

There have been some operational difficulties with parts of the original CRODIS setup by Tahmasbi (1997). Three main areas have been identified and some modifications have been implemented so that the CRODIS facility can be operated more efficiently. These changes are:

- Modifications to the air circulation loop (Section 3.2.1)
- Modifications to the air-water separator (Section 3.2.2)
- Modifications to the test tray inlet downcomer (Section 3.2.3)

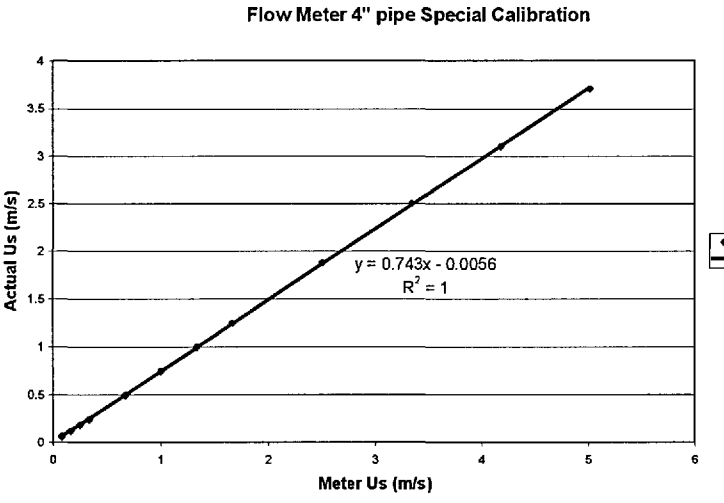
3.2.1. Modifications on Air Circulation Loop

The original location of the air flow anemometer was on the air return line (see **R2** in Figure 3.2). This was thought to be inappropriate as it is suspected that some of the air might escape from the water outlet of the impact-plate air-water separator. Therefore, for the current work, the anemometer was placed at the inlet pipe (after the air circulator, **P3**, in Figure 3.1) and this ensured accurate measurements of the air flowrate into the column.

In the original design, the air flowrate was controlled by a 4-inch ball valve installed in the air inlet pipe (**V2** in Figure 3.2). However, when the valve was not completely open, the air flow from the centrifugal fan (i.e. the air circulator, **P3**) was restricted and was being compressed in the fan chamber. As a result, extra friction on the impeller bearing generated excessive heat and mechanical vibrations. The heat caused the air temperature to rise and subsequently increased the temperature of the water in the system. The

mechanical vibrations on the circulator were clearly observed during experiments and these caused flow instability. This suggested that the air circulator was not working at its full efficiency as some of the energy was wasted. The way to solve such a problem was to introduce an inlet air flow bypass which allows the circulator to run at its maximum efficiency. The bypass connects the air inlet pipe to the air return pipe and involves an extra ball valve (**V9** in Figure 3.1), which works together with the original valve (i.e. **V7** in Figure 3.1 or **V2** in Figure 3.2) to control the air flow rate. This allowed the excessive air, which was under the restriction of the main valve (**V7** in Figure 3.1), to return to the circulator again via the bypass. i.e. avoiding excess pressurisation of the fan chamber.

The manufacturer of the air-flow anemometer, *AIRFLOW Development Ltd*, suggested a special calibration for the 4-inch pipe in a blowing mode. The special calibration was carried out between two straight 4-inch pipes, each of length 1000mm. The anemometer velocity readings (in the 4-inch pipe) were plotted against the actual mean velocity in the duct as measured by a British Standard orifice plate, and the results are shown in Figure 3.5.



Meter Reading Velocity (m/s)	Mean Duct Velocity (m/s)
0.5	0.32
1	0.68
1.5	1.05
2	1.42
4	2.93
6	4.43
8	5.94
10	7.44
15	11.17
20	14.92
25	18.53
30	22.16

Figure 3.5. Calibration results for the anemometer in a 4-inch duct

3.2.2. Modifications to the Air-Water Separator

In the original CRODIS circuit used by Tahmasbi (1997) (see Figure 3.2), an impact-plate air-water separator (shown in Figure 3.6 below) was used to separate any water

droplets found in the air stream leaving the test section. It was found that most of the entrained water did not follow the designated outlet (i.e. flowing back to the water storage tank) and instead, it was carried over to the air return line. This caused damage to the bearing systems of the anemometer and if the problem was not corrected, it could also potentially damage the centrifugal blower.

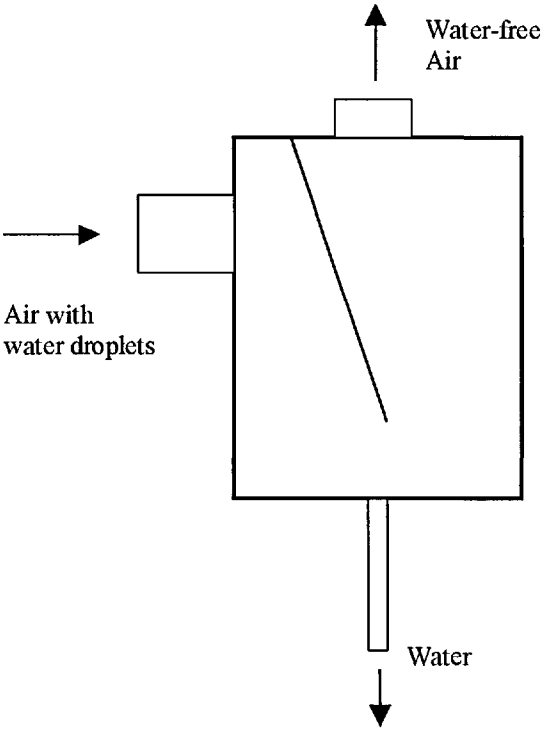
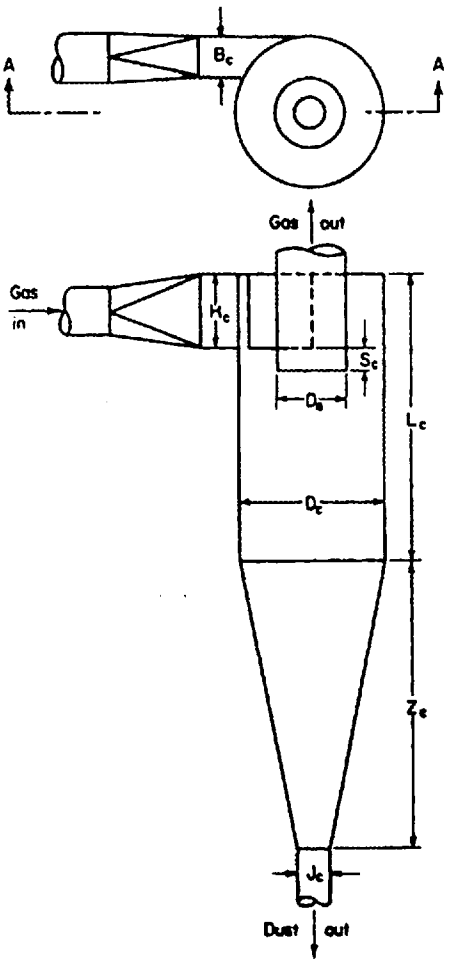


Figure 3.6. Impact-plate air-water separator used by Tahmasbi (1997)

Thus, it was necessary to substitute this unit with a more efficient separator to ensure that no further damage occurred in the future due to the poor separation. After considering several options and carrying out a cost evaluation process, it was decided to replace the impact-plate separator with a conventional cyclone. The design of the cyclone separator was based on guidelines in the *Perry's Chemical Engineers' Handbook* and the dimensions are given in Figure 3.7 and Table 3.1 below.



D_c	200
B_c	50
D_e	100
H_c	100
L_c	400
S_c	150
Z_c	400
J_c	50

Table 3.1.
Dimensions of the cyclone separator

Figure 3.7. Conventional design of a cyclone separator (pictures taken from the *Perry's Chemical Engineers' Handbook*, 7th Edition)

A practical concern in using a cyclone in the CRODIS facility was the potential pressure drop due to this unit. The pressure loss at various sections of the cyclone can be calculated as follows:

For the air inlet velocity, v_{in}, of the cyclone to be 25 m/s (which corresponds to a tray superficial velocity of at least 2.2m/s, slightly higher than the upper limit used in the experiments), the air exit velocity, v_{exit} (leaving from the top of the cyclone), becomes 15.9 m/s. i.e.

$$v_{in} \times B_c \times H_c = v_{exit} \times D_e^2 \times \pi/4 \qquad (3.1)$$

$$\text{i.e.} \quad v_{exit} = 15.9 \text{ (m/s)}$$

(1) The pressure loss due to inlet contraction is given by:

$$\Delta P_1 = 0.5 \rho_G \left(v_{in}^2 - v_{vessel}^2 + K v_{in}^2 \right) \qquad (3.2)$$

K depends on the area ratio between the barrel and the outlet, and it reaches its maximum value (K=0.5) when the ratio tends to zero. Therefore, by assuming K=0.5, and v_{vessel}=0, the maximum possible pressure loss for this component becomes

$$\Delta P_1 = 565 \text{ (Pa)}$$

(2) The pressure loss due to particle acceleration is given by:

$$\Delta P_2 = L v_{in}\left(v_{pin} - v_{pvessel}\right) \tag{3.3}$$

Assuming the mass of entrained water per unit volume, L to be 0.5 kg/m^3 (this was a high estimate, according to previous experimental results obtained by Tahmasbi, 1997) and assuming that the inlet velocity of the water droplet v_{pin} is the same as the air (in fact, it is less than the value of air) and $v_{pvessel}$ to be zero so as to calculate the maximum possible pressure drop due to particle acceleration, it follows that:

$$\Delta P_2 = 313 \text{ (Pa)}$$

(3) The pressure loss due to barrel friction is given by:

$$\Delta P_3 = \frac{2 f \rho_G v_{in}^2 \pi D_c N_s}{d_{in}} \tag{3.4}$$

where $f = 0.079 Re^{-0.25}$ is used to calculate the gas phase friction factor and the Reynolds number is defined as $Re = \rho_G v_{in} d_{in} / \eta_G$. N_s is the effective number of spiral paths taken by the gas within the body of a cyclone and was determined graphically (as a function of the maximum gas velocity of gas, i.e. v_{in}=25 m/s) to be 4.5. The parameter, d_{in}, is the equivalent diameter of the rectangular inlet and is calculated to be 0.0667. Therefore,

$$f = 4.33 \times 10^{-3}$$

and $$\Delta P_3 = 276 \text{ (Pa)}$$

(4) The pressure loss due to gas flow reversal is given by:

$$\Delta P_4 = \frac{\rho_G v_{in}^2}{2} \tag{3.5}$$

Therefore,

$$\Delta P_4 = 377 \text{ (Pa)}$$

(5) The pressure loss due to exit contraction is given by:

$$\Delta P_5 = 0.5\rho_G\left(v_{exit}^2 - v_c^2 + Kv_{exit}^2\right) \tag{3.6}$$

Again, taking v_c=0 and K=0 (to estimate the largest possible pressure loss) and v_{exit} as 15.9 m/s (assuming all the air leave the cyclone from the top), the exit contraction pressure loss is calculated:

$$\Delta P_5 = 229 \text{ (Pa)}$$

By summing up all the above components, the maximum potential pressure loss due to the cyclone is estimated to be about 1760 Pa which is small enough compared to the head generated by the CRODIS air circulator. Therefore, the installation of the new cyclone unit was considered practically feasible.

3.2.3. Modifications to the Test Tray Inlet Downcomer

In a downcomer in an industrial distillation column, any vapour entrained by the liquid leaving the tray and entering the liquid leg feeding the next lower tray would be expected to separate. Thus, the vapour would rise in counter-current flow to the liquid in the liquid leg and (ideally) the liquid entering the lower tray would contain no vapour. Of course, vapour carry-under can and does occur in such equipment but, for the CRODIS facility, it was essential to avoid it. In the original CRODIS arrangement, the water entered the downcomer tangentially as drown in Figure 3.8. This arrangement could lead to bubble entrainment and to air entering the test tray from the downcomer as shown in Figure 3.8. A perspex impact plate was added to correct the flow direction and it is shown (in red) in Figure 3.9 below.

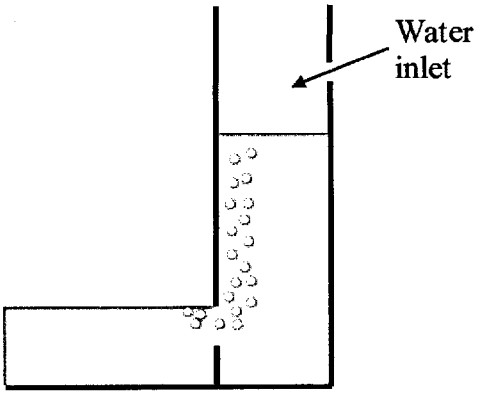


Figure 3.8. Old inlet downcomer arrangement (Tahmasbi, 1997)

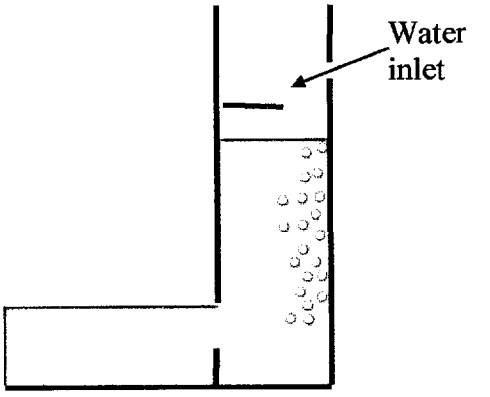


Figure 3.9. New inlet downcomer arrangement (present work)

3.3. Measuring Techniques

There are two main techniques used in CRODIS to measure the two-phase flow parameters (liquid holdup and dispersion bubble or drop size), namely, the gamma densitometry system, and the laser light transmission system. Pressure drop is another important parameter to be investigated in two-phase flow and various manometers are used to measure different components of the sieve tray pressure drop. Descriptions of these measuring systems are given briefly in the following section and the full details can be found in the theses of Tezock (1993) and Tahmasbi (1997).

3.3.1. Gamma Densitometry

Principle

The gamma densitometry technique has been widely used to measure the gas/liquid fraction of the two-phase flow. The principle is based on the fact that different media absorb gamma radiation to different extents. The absorption of a parallel mono-energetic beam of gamma photons by a medium of density ρ and thickness x above the test tray is described by an exponential law:

$$I = I_o e^{-\mu\rho x} \tag{3.7}$$

where μ is the mass absorption coefficient of the medium, I is the incident intensity and I_o is the transmitted intensity of gamma photons. The intensity of the transmitted

radiation is inversely proportional to the time (t) taken to record a fixed number of counts (N) i.e.

$$I \propto t^{-1} \tag{3.8}$$

For a gas-liquid dispersion of liquid fraction α, Eq.(3.7) may be written as

$$t = t_0 e^{\mu_L \rho_L \alpha x} \Rightarrow \ln t = \ln t_0 + \mu_L \rho_L \alpha x \tag{3.9}$$

where t_0 is the time for N counts with the transmitted intensity I_0. This analysis leads to a simple procedure for measuring the liquid fraction in a gas-liquid dispersion. The intensity of the transmitted beam is measured by the time taken to record a fixed number of counts. This count time is measured when the test cell is empty (t_G) and when the test cell is filled with liquid (t_L) respectively. The liquid fraction α is zero for a gas-filled column and unity for a liquid-filled column. Thus, α can be calculated from the following equation which derives from Eqs.(3.7) and (3.9):

$$\alpha = \frac{ln\left(t/t_G\right)}{ln\left(t_L/t_G\right)} \tag{3.10}$$

where t is time taken by a scintillation counter to register N counts for the two phase mixture, t_G and t_L are the times taken for the same number of counts when the calibration cell is gas and liquid filled respectively.

Experimental Implementation

In the CRODIS facility, an enclosed 0.03-milliCurie Caesium 137 gamma ray source of 660 keV energy is mounted on a traversing platform which allows a full scan across the whole test section. Opposite to the source (i.e. at the other side the platform across the test section), a *Labgear* directional scintillation counter with a built-in photo-multiplier tube is coupled to an *Ortec* preamplifier and an *Ortec* counting unit. The entire system is controlled by an *IBM* PC which gives an on-line analysis of the gamma radiation count rate, $\dot{N}$.

In the air-water system, when the gamma ray passes through pure air more radiation is transmitted and hence received at the counter than when the gamma ray passes through pure water. The gamma densitometer measures the void fraction at all locations above the test tray by moving the traversing platform (both horizontally and vertically). The liquid fraction relationship, Eq.(3.10) can be re-written in terms of a more convenient gamma count rate (given directly in the PC):

$$\alpha = \frac{ln\left(t/t_G\right)}{ln\left(t_L/t_G\right)} = \frac{ln\left(N/\dot{N}/N/\dot{N}_A\right)}{ln\left(N/\dot{N}_W/N/\dot{N}_A\right)} \tag{3.11}$$

$$\text{i.e. } \alpha = \frac{ln\left(\dot{N}/\dot{N}_A\right)}{ln\left(\dot{N}_W/\dot{N}_A\right)} \tag{3.12}$$

where $\dot{N}$ is the gamma count rate of the froth, $\dot{N}_A$ is the count rate for pure air and $\dot{N}_W$ is the count rate for pure water.

In all experiments, the location where the liquid fraction falls with vertical direction to a value of 0.05 is defined to be the top of froth. In this work, ten horizontal locations were selected for measurements; these are shown in Figure 3.10 (marked as 0-900mm). The vertical measuring locations depend on the operating conditions (e.g. flowrates and outlet weir height), i.e. they begin at the tray floor and end at the top of the froth. The measuring time at each of these locations is set at 60 seconds for all the experiments.

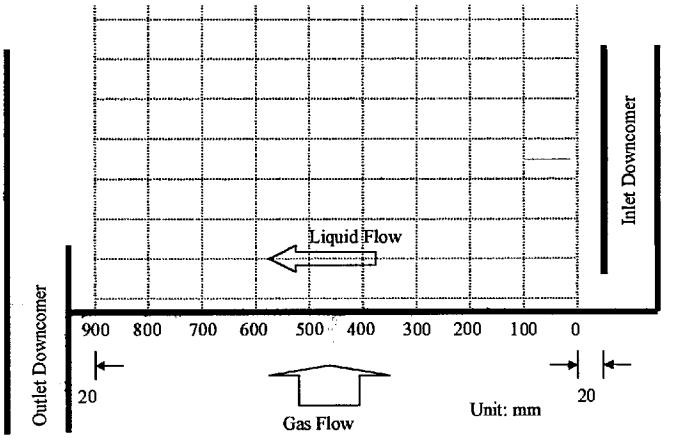


Figure 3.10. Measuring locations above the test tray

Calibration

For calibration purposes, the column had to be completely filled with air (i.e. empty position) and completely filled with water for measuring the gamma count rates in each case. The former condition was easily performed but the latter condition was clearly not possible for the present test section since flow of water into the inlet air stream could cause serious damage to the air circulator bearing. In order to overcome this problem, a small calibration test cell (shown in Figure 3.11) was used instead of the experimental column. The test cell was filled with water and placed on a small platform positioned next to the column. The advantage of using this test cell was that the gamma densitometer calibration could be checked before each run (in fact, similar results were obtained for all runs). The average count rate for the air-filled column is 240 (counts per second) and the average count rate for the water-filled calibration cell is 142 (counts per second).

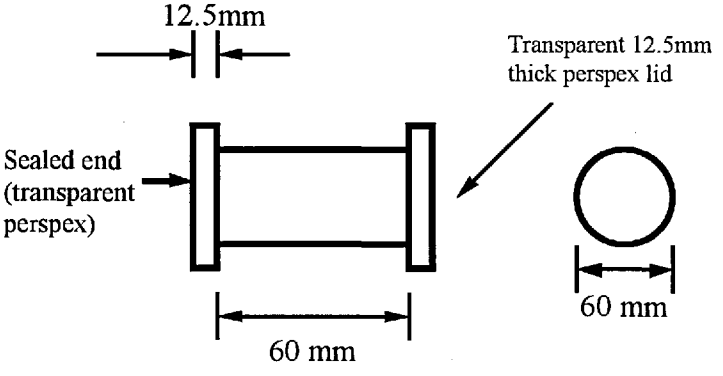


Figure 3.11. Calibration cell for gamma densitometer

However, on the CRODIS facility, it has been identified that when the gamma source position is near the tray floor, some of the radiation is scattered or absorbed by the tray material. A region of vertical distance up to about 10mm above the tray floor was affected. Therefore, the above 'off-column' calibration method may not be appropriate in this case.

The near-tray floor region contains the most interesting information and calculations on other relevant parameters (e.g. h_L, D_{sm}, etc.) require an accurate value of liquid fraction in this region. Therefore, it becomes important to have this measurement taken with the

highest accuracy possible. A way to solve this problem is to carry out a localised calibration at each point of interest in the affected region and the positions of these points are shown in Figure 3.11.

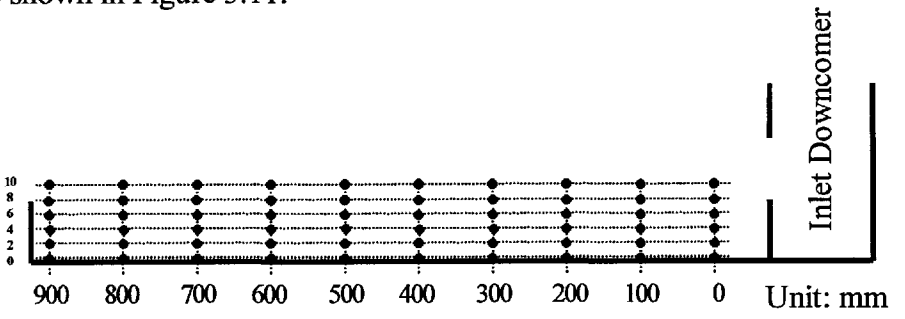


Figure 3.12. Special near-tray floor calibration

The test tray can hold a moving layer of water without any bubbles at a relatively high liquid load and with gas supply virtually switched off (i.e. with the gas pressure holding the liquid on the tray). This moving layer of water has a height of at least around 15mm (for cases of 8mm outlet weir and higher for 38mm outlet weir) which is enough for the calibration. The localised calibration results are presented in Table 3.2 below.

	Calibration with air									
Distance Above tray (mm)	10	237.6	240.8	240.8	239.8	239.2	240	240.4	240.2	240.8	241.1
	8	233.1	233.5	233.5	235.3	237.1	237.1	236.3	236.7	238.5	238.6
	6	208.3	203.3	204.4	211.3	215.4	221.4	223	231.5	235	234.7
	4	177.5	181	178.7	179.5	181.2	186.2	189.5	201.7	218.2	221.2
	2	148.1	166.6	164.8	169.2	168.2	172.2	174.3	182	192.5	196.8
	0	146.4	178.1	176.7	176.4	171.5	167.8	168.2	169.3	170.8	164
		900	800	700	600	500	400	300	200	100	0
		Distance along tray (mm)									
	Calibration with water									
Distance Above tray (mm)	10	142.7	140.5	139.9	140.3	141.9	142.6	143.3	142.4	142	141.9
	8	139.7	140.3	139	140.6	142.7	141.4	142.1	141.5	140	142
	6	133.5	132.3	132.9	136.7	138	139.7	140.6	140.4	141.9	139.7
	4	124.9	131.4	132.3	130.8	130.9	130.5	131.9	135.2	137.7	139
	2	119.7	146.1	143.1	143.4	136.7	134.7	135.4	131.2	129.6	128
	0	139	173	167	165.7	155.7	154.3	150.4	141.8	136.2	111.9
		900	800	700	600	500	400	300	200	100	0
		Distance along tray (mm)									

Unit: counts/second

Table 3.2. Calibration data for gamma densitometer system

Although all the trays are made of the same material and the position of the test tray is unlikely to be changed; it is still recommended that this calibration should be checked every time the column is dismantled so that accurate results can be obtained.

3.3.2. Multiple Light Scattering Technique

Principles

In a dispersed two-phase flow, it is important to know the distribution of the dispersed phase in the system and usually an average size of the dispersed phase is useful. In the gas-liquid flow, the "Sauter mean bubble diameter", D_{sm}, has been commonly used as such an average value. It is a statistical dimension of a dispersed system containing n discrete particles and it is defined as:

$$D_{sm} = \frac{\sum nd^3}{\sum nd^2} = \frac{6\varepsilon}{A} \tag{3.13}$$

where d is the diameter of dispersed particles (i.e. bubbles or drops) and ε is the volume fraction of the dispersed phase (i.e. $\varepsilon = (1-\alpha)$ for a gas bubble dispersion in a liquid and $\varepsilon = \alpha$ for a drop dispersion in a gas) and A is the interfacial area per unit volume.

When a parallel beam of light passes through a dispersed system, its intensity is attenuated by diffraction, reflection, refraction and absorption. The contribution of the first three mechanisms is usually lumped together and termed scattering. If one drop or bubble is considered, the angular scattering of the parallel rays can be pictured as in Figure 3.13. As illustrated, each of the four scattering mechanisms prevents the rays from maintaining their original direction. Multiple scattering occurs when light which has been scattered by one particle, is scattered again by another particle. The transmitted light intensity is therefore a function of both position and direction. This is one of the common characteristics of dense dispersion systems.

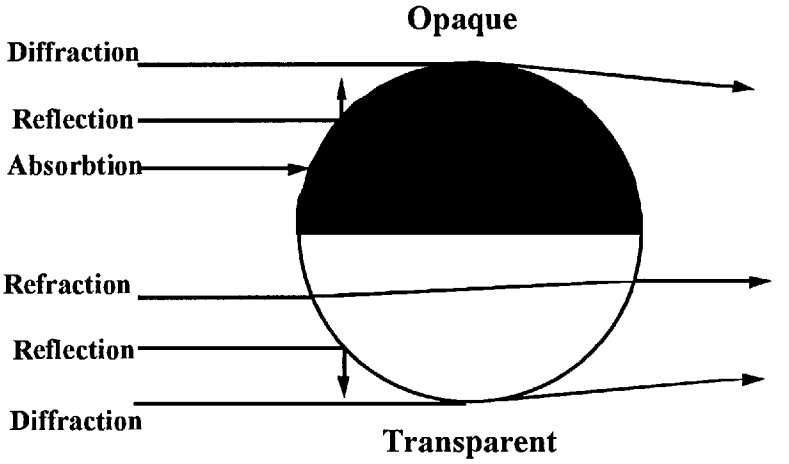


Figure 3.13. The four mechanisms of light attenuation through particles

The multiple-light transmission technique has been used to determine the Sauter mean diameter of bubbles above a sieve tray (Tezock, 1993 and Tahmasbi, 1997). Multiple light scattering arises when the light beam is scattered by the froth body which consists of a large number of bubbles and droplets. Thus, the transmitted intensity of light can be related to the density of the dispersed phase and path length in the system (Tezock, 1993 and Tahmasbi, 1997). Furthermore, it can be used (with a known value of dispersed phase fraction) to calculate the Sauter mean diameter of the dispersed phase.

Experimental Implementation

In the CRODIS facility, the optical assembly consists of a Helium-Neon 30.0-milliwatt laser source, a mechanical signal modulator and highly polished mirrors. The electronic assembly consisted of an infrared sensor, a silicon photo diode unit, an *EG&G model 5104* lock-in amplifier and an *IEEE-488* data card installed in a desktop computer. A lock-in amplifier is a sophisticated low-level signal measurement system using the phase detection principle. The system has two inputs: a signal to be measured and a reference signal having the same frequency as the measured signal (i.e. the reference signal has an arbitrary but constant phase shift with respect to the measured signal).

The measured signal is pre-filtered after amplification and is fed to a phase sensitive detector. The reference signal is also filtered and after passing through a 0 to 360° continuously controllable phase shifter, is fed to the phase-sensitive detector (PSD) through a driver. The output of the PSD is low-pass filtered and after further amplification becomes the final output. Any noise present in the input produces a PSD

output that is filtered out by the low-pass filter. The main advantage of a lock-in amplifier is that low signal levels can be detected even in the presence of large interfering noise because of an *a priori* knowledge of the frequency of the output. The instrument therefore eliminates completely the main interference at 50 Hz (i.e. noises under ambient conditions). The provision of a serial communications port on the lock-in amplifier permits remote control and data storage on a personal computer. Tahmasbi (1997) modified the control code (Tezock, 1993) written to interface the lock-in amplifier to the microprocessor for the existing experimental set up. This enabled automatic adjustment of the time constant of the signal integrating circuit. The code also sets the instrument sensitivity range to match the intensity of light received by the silicone photo diode and dynamic adjustment of the phase angle between the signal and the reference input to optimise the input signal.

A schematic diagram of the optical measurement set-up installed in the CRODIS facility is shown in Figure 3.14.

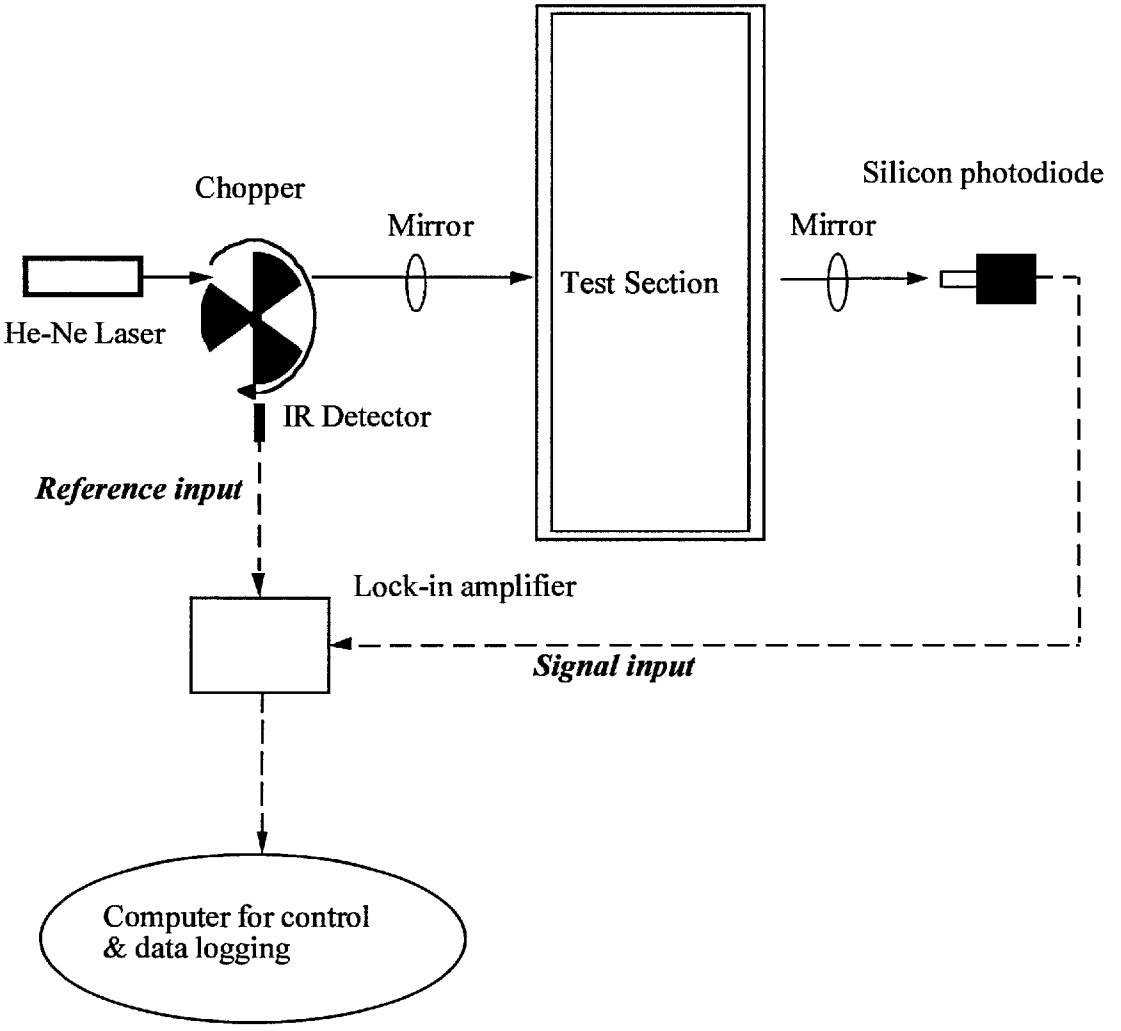


Figure 3.14. Schematic presentation of the optical set-up for the Sauter mean bubble size measurement

The laser beam is modulated by the mechanical chopper at 120.0 Hz and the pulses are reflected by pre-set optical mirrors to propagate axially through the dispersion in the test section. The transmitted light is reflected by another pre-set mirror to fall into the silicone photo diode. The intensity of the incident light as recorded by the photo diode is fed to the lock-in amplifier as a voltage. An infrared sensor attached to the mechanical chopper detects and feeds the modulation frequency of the light pulses to the lock-in amplifier as illustrated in Figure 3.14.

The optical path density (AL), the product of the interfacial area per unit volume, A, and the path length, L (column width in this case) is a function of the intensity of the laser light beam received at the photo diode:

$$AL = f\left[ln\left(I_0/I\right)\right] \tag{3.14}$$

where I_0 and I are the incident and transmitted intensities of light beam respectively.

A number of alternative correlations are available in the literature in the form of Eq.(3.14); however, it is best if the relationship is determined from experimental data obtained under similar conditions to the proposed application.

Calibrations

Calibration data for the system used in the present experiment were previously obtained by Tahmasbi (1997) using a system of glass beads dispersed in a solid jelly in a calibration cell. The glass beads simulate the gas bubbles on the tray and the jelly the continuous (water) phase. In the preparation for such a cell, depending on the required solid fraction, a specified number of glass beads were randomly placed into the cell and a layer of household jelly was poured to submerge them. The cell (with the glass beads-in-jelly dispersion in it) was then placed in a refrigerator to allow it to harden before the filling process was repeated several times until the level of the jelly reached the brim of the cell. This repeated filling allowed a reasonable uniform dispersion of beads through the jelly. The laser beam was transmitted through the calibration cell at several locations to obtain an average reading for each known solid fraction (i.e. representing a known volume fraction of the dispersed phase). Thirteen levels of solid fraction were tested and the best-fit relationships to these data are as follows:

$$AL = 3.384\, ln\left(I_0/I\right) + 0.0241 \qquad \text{for} \qquad ln\left(I_0/I\right) < 1.5 \tag{3.15}$$

$$AL = 0.305\, ln\left(I_0/I\right) + 4.5035 \qquad \text{for} \qquad 1.5 \le ln\left(I_0/I\right) \le 9.3 \tag{3.16}$$

$$AL = 8.858\, ln\left(I_0/I\right) - 75.644 \qquad \text{for} \qquad ln\left(I_0/I\right) > 9.3 \tag{3.17}$$

Eqs.(3.15) to (3.17) have been used in the present study to calculate the interfacial area per unit volume.

It is often difficult to determine *a priori* whether the froth above a distillation tray is a drops-in-gas or a bubbles-in-liquid dispersion. The value of AL given by Eqs.(3.15) to (3.17) could characterise either form of dispersion. The results are therefore interpreted to give effective Sauter mean diameter for *both* cases by substitutions $\varepsilon = (1-\alpha)$ (for the bubbles-in-liquid case) or $\varepsilon = \alpha$ (for the drops-in-gas case) into Eq.(3.13). Clearly, the bubbles-in-liquid value of D_{sm} is more appropriate near the tray surface and the drops-in-gas value is more appropriate near the top surface of the froth.

3.3.3. Paraffin Manometer

A conventional U-tube manometer (filled with paraffin, specific gravity of 0.8) is installed on the bottom dry tray to measure the dry tray pressure drop and another one is installed on the test tray to measure the wet-tray pressure drop. Tappings are also available at the other two trays and all these are shown in Figure 3.1.

3.3.4. Error Analysis

The measuring techniques employed in the current study are not so straightforward, therefore it is realised that the estimation of potential error can be difficult. In what follows, the error associated with the measurement using the gamma densitometer system is estimated.

If a gamma beam of intensity I is counted for a time t, the mean number of counts N measured during the counting interval will be It. The root mean square magnitude of the random variation or standard deviation in the number of counts measured will be given by:

$$\Delta(It) = \sqrt{It} = \sqrt{N} \tag{3.18}$$

This statistical variation arises from the random nature of photon emission from the source. The randomness in the count rate gives rise to random fluctuations in the computed liquid fraction. The magnitude of the fluctuation is given by:

$$|\Delta\alpha| = \left|\frac{\partial\alpha}{\partial t}\right||\Delta t| \tag{3.19}$$

Differentiating Eq.(3.9) with respect to time t, it follows that

$$\frac{d\alpha}{dt} = \frac{1}{\mu_L \rho_L x t} \tag{3.20}$$

For an infinitesimal amount of time Δt, Eq.(3.20) can be re-written as

$$\begin{aligned}\Delta\alpha &= \frac{1}{\mu_L \rho_L x}\frac{\Delta t}{t} \\ &= \frac{1}{\mu_L \rho_L x}\frac{\Delta(It)}{It} \\ &= \frac{1}{\mu_L \rho_L x}\frac{\sqrt{N}}{N} = \frac{1}{\mu\rho_L x\sqrt{N}}\end{aligned} \tag{3.21}$$

The mass absorption coefficient of distilled water is 0.0085 m^2/kg for gamma radiation with energy 660 keV. For N = 10000 (an estimated number of count over 60-second period) and $\rho_L = 1000$ kg/m^3, the error in the liquid fraction for a path length of x=0.06m is

$$\Delta\alpha = \frac{1}{0.0085\times 1000\times 0.06\times\sqrt{10000}} = 0.02 \tag{3.22}$$

It must be stressed that the above figure is only a statistical error which was obtained by assuming perfect instrumentation. The sources of errors in the measuring devices are difficult to be traced, however, thirty sequential measurements on the calibration cell (filled with water) showed consistent count rates (all readings were within 5%). This implies that the expected error on the instrumentation is likely to be very small and therefore the overall error would be close to Eq.(3.22). It is also important to note that for the same number of counts, the relative error in measuring small values of liquid fraction is higher than for high magnitudes of liquid fraction. The actual number of counts (N=10000) used in Eq.(3.22) is in fact already a lower number than the average froth (generally range from 180-220 counts per second over the 60-second period).

Thus, the expected overall error for liquid fraction is unlikely to exceed the estimate in Eq.(3.22).

For the measurements using the laser light scattering technique, it is even more difficult to evaluate the overall error because the liquid fraction error is propagated in calculating the Sauter mean diameter. However, it is always helpful to make sure that the signals received from penetrating a single-phase medium are self-consistent before evaluating the signals received from a two-phase dispersion. The data obtained by Tahmasbi (1997) on light transmission through two different continuous mediums (water and jelly) showed good consistency over a long period of runs. This confirms the error associated with the measuring devices is like to be small. The "stationary" calibration data (Tahmasbi, 1997) of glass beads and jelly system also showed very little error on the system. The likely error on the Sauter mean diameter can be estimated by considering upper and lower limits of liquid fraction (using the error calculated in Eq.3.22 above).

3.4. Results and Discussions

3.4.1. CRODIS Flow Visualisation

Figure 3.15 below shows a general picture of the CRODIS test tray in operation. The tests have been carried out on two types of sieve trays: a 1.8mm hole size sieve tray with 6mm equilateral triangular pitch and a 6 mm hole size sieve tray with 20mm equilateral triangular pitch; both have 8% open area. The thickness of the trays is 2mm. Configurations of the test trays selected for the experiments are listed below:

- Active bubbling length: 940mm (full length), 840mm (50mm blanked-off zones at each end of tray)
- Inlet weir height: 8mm, 0mm
- Outlet weir height: 38mm, 8mm
- Gas superficial velocity: 0.73 - 1.68 m/s
- Liquid volumetric flowrate: 6.3 - 11.25 lit/min



Figure 3.15. CRODIS test tray in operation

Figures 3.16 and 3.17 show the bubbling process on the tray. When these pictures were taken, the gas flowrate was sufficiently high for coalescence to occur between two consecutive bubbles from the same orifice thus forming jets. The shape (or direction) of the jet body changed with the local liquid flow field, i.e. most of the jets were projecting upwards (i.e. low liquid flow) in Figure 3.16 whereas in Figure 3.17, the jet bodies were bent towards the direction of the liquid flow (high liquid flow). By visual observation, adjacent jets joined together very near to the tray floor, this means that the separated jet region is only a few millimetres high. Above this zone, the system becomes a dense bubbly flow where both break-up and coalescence of bubbles and liquid droplets occur frequently.

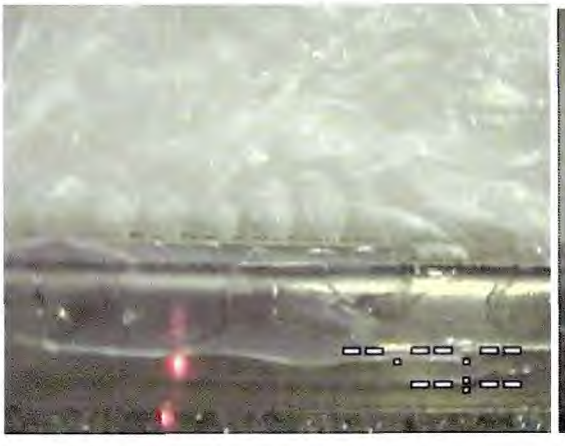


Figure 3.16. Bubbling on the tray (1)

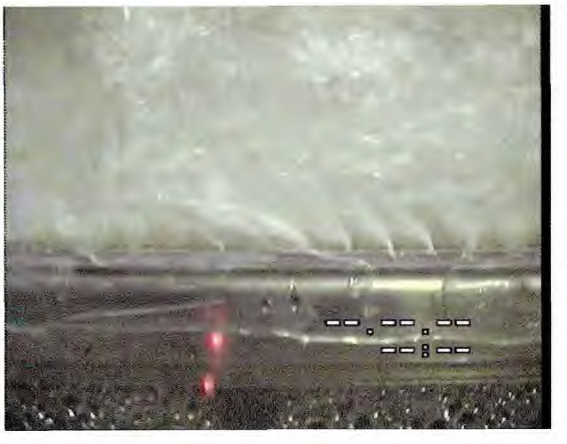


Figure 3.17. Bubbling on the tray (2)

Figures 3.18 and 3.19 illustrate the effect of the calming zones. At the inlet zone, the section was filled up with mostly water with only some small gas bubbles (mostly entrained from the inlet downcomer). At the outlet zone, the clear layer of water above the tray was disturbed by the projected liquid droplets/splashes. High-speed video images (taken at 1000 frames/second) show that liquid re-circulation occurred in both zones; more at the inlet and less at the outlet.



Figure 3.18. Outlet calming zone



Figure 3.19. Inlet calming zone

3.4.2. Dispersion Density Profile and Clear Liquid Height

Full results of the two-dimensional dispersion density profiles above the test tray are given in Appendix B. They are the average values over a short period of time (60 seconds in this case) and also averaged across the width of the column. The results can be re-plotted as shown in Figures 3.20 and 3.21, where clear distinction of froth and spray regime is illustrated (Figure 3.22).

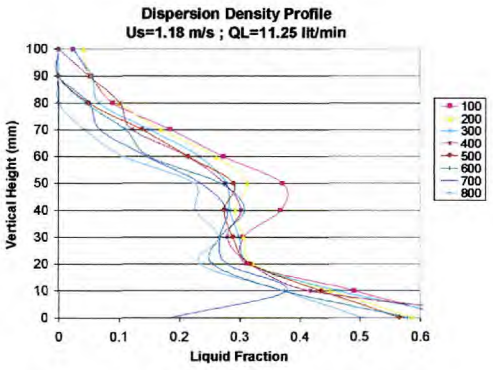


Figure 3.20. Froth regime operation

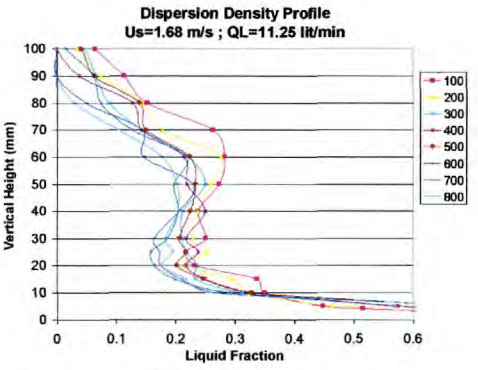


Figure 3.21. Spray regime operation

(in the above figures, different colours represent different horizontal positions)

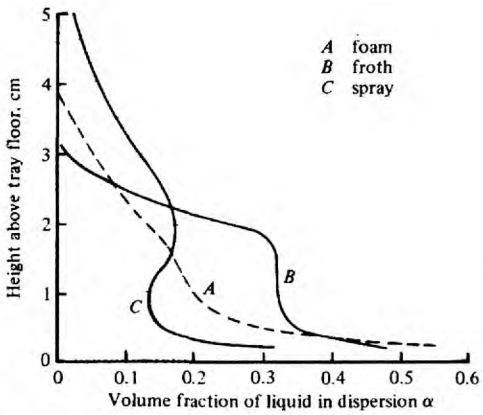


Figure 3.22. Dependence of froth density profile on flow regime, taken from Lockett, *Distillation tray fundamentals* (1986)

The froth density profile (at a fixed horizontal position) can also be used to calculate the local clear liquid height:

$$h_L = \int_0^{h_f} \alpha(y)\, dy \tag{3.23}$$

where $\alpha(y)$ is the local liquid fraction at vertical position y and h_f is the froth height which the maximum height a droplet can travel. Figures 3.23 to 3.25 show selected results on the clear liquid height which are plotted along the test tray.

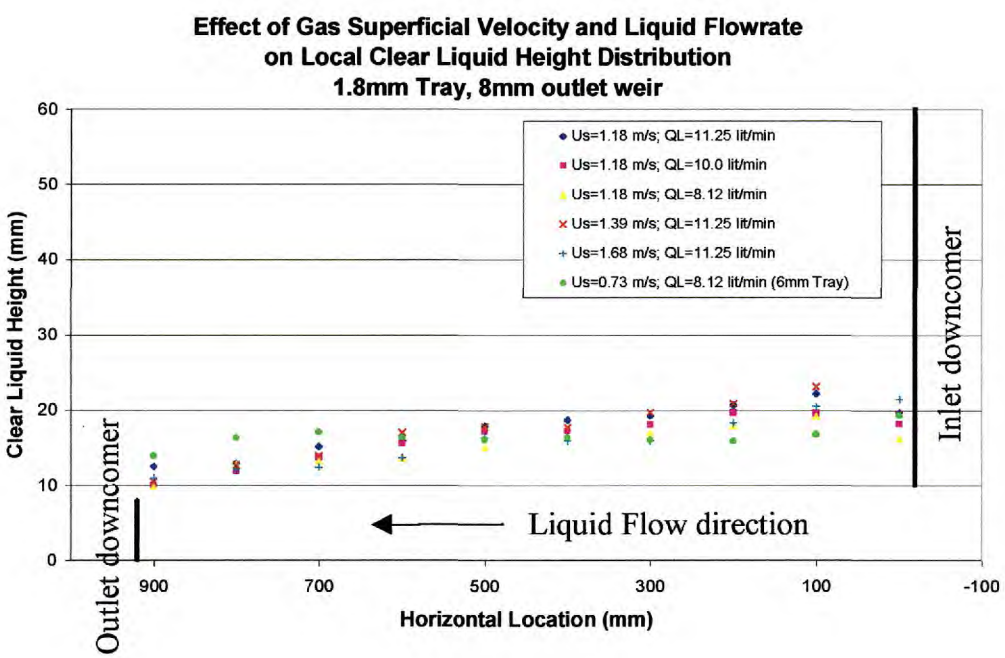


Figure 3.23. Local clear liquid height distribution for 1.8mm tray, 8mm outlet weir

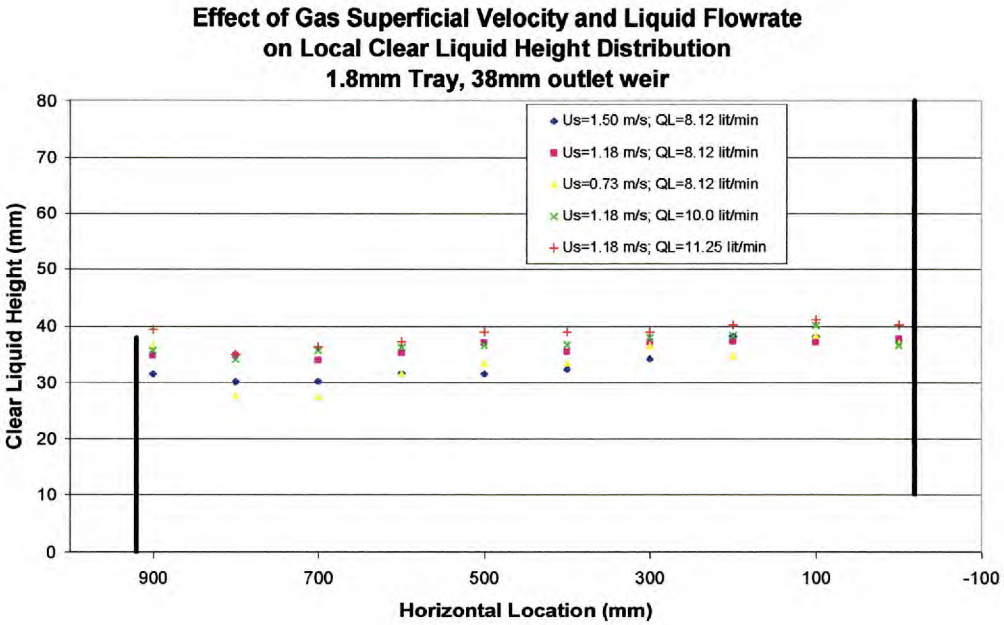


Figure 3.24. Local clear liquid height distribution for 1.8mm tray, 38mm outlet weir

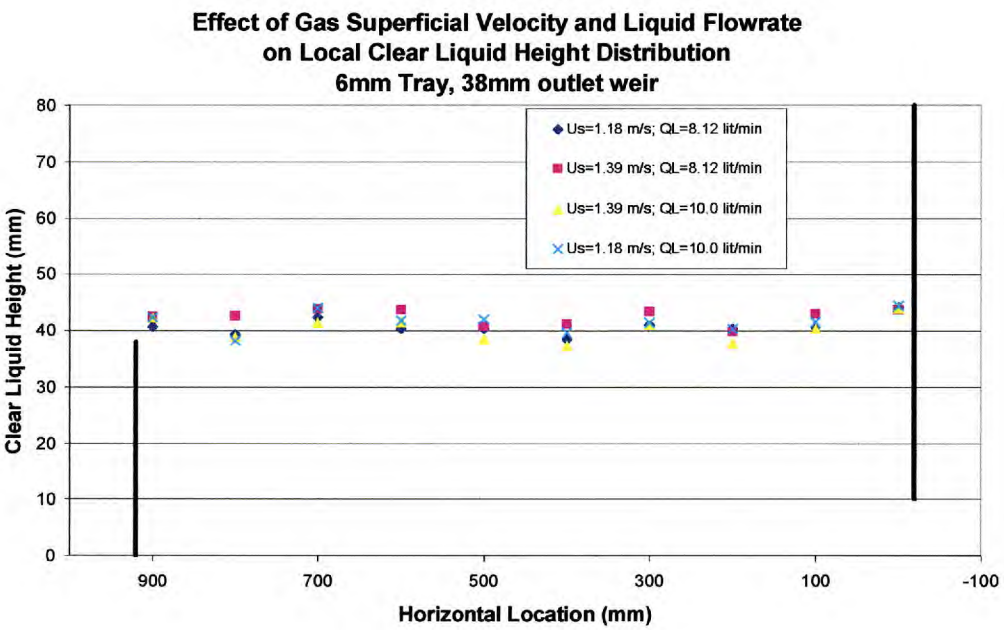


Figure 3.25. Local clear liquid height distribution for 6mm tray, 38mm outlet weir

With the length of the trays installed in CRODIS, hydraulic gradients are observed in some experiments, especially for the 1.8mm tray with the 8mm outlet weir (Figure 3.23). The phenomenon seems to be independent of both gas and liquid although the values of clear liquid heights do vary with flowrates. The magnitude of the hydraulic

gradient is about 10mm along the bubbling section of the tray. For the 38mm outlet weir cases (Figures 3.24 and 3.25), the hydraulic gradient seems to disappear and only fluctuations on the clear liquid levels are observed. However, it is interesting to note that in Figure 3.24, the gap between the highest and lowest clear liquid heights at a position seems to increase from tray inlet (location 0mm) to outlet (location 900mm).

The froth height is predominantly dependent on the gas flowrate since the highest level which a droplet can travel to depends on the momentum transferred from the gas flow. The figures in Appendix B provide good confirmation to this. It is worth noting that there seems to be a gradient of froth height for the 8mm outlet weir cases, regardless of the tray hole sizes. This is probably due to the small liquid holdup and hydraulic gradient occurred in the lower outlet weir cases.

Figures 3.26 and 3.27 below are the local liquid fraction profiles above the calming zones and they were obtained by performing the gamma densitometer measurements at smaller horizontal intervals at both ends of the test tray (i.e. from position –20 to 30mm near inlet and position 870-920mm near outlet). Above these zones, the froth body contains very little gas and the slight increase on the froth height (i.e. more light blue colour at higher vertical positions) can be clearly seen at locations near to the bubbling area (i.e. x = 870mm and 30mm).

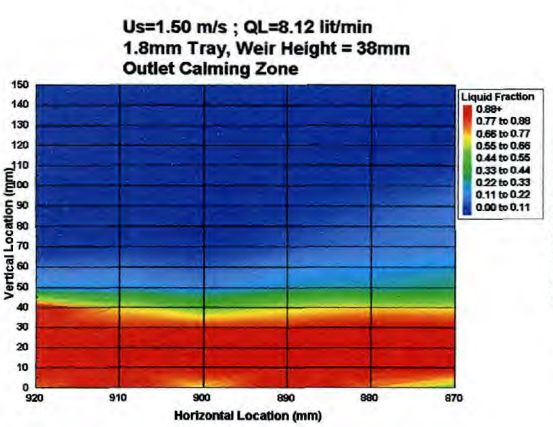


Figure 3.26. Dispersion density profile at outlet calming zone

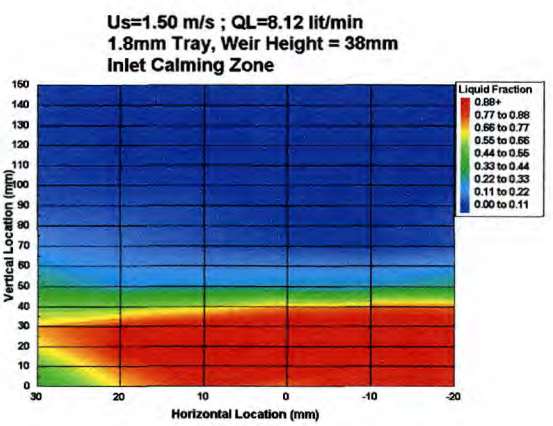


Figure 3.27. Dispersion density profile at inlet calming zone

3.4.3. Tray Pressure Drop

The total pressure drop (h_T) across a tray has three components:

$$h_T = h_D + h_L + h_\sigma \tag{3.24}$$

where h_D is the dry tray pressure drop component, h_L is the pressure loss due to clear liquid height and h_σ is the residual pressure loss. Each of these components is to be discussed below.

- **Dry Tray Pressure Loss Head, h_D**

The dry tray pressure loss can be estimated fairly well with the correlation by Leibson *et al* (1957). It follows a standard orifice-type equation:

$$h_D = \frac{50.8}{C_v^2}\frac{\rho_G}{\rho_L}u_h^2 \tag{3.25}$$

where the discharge coefficient, C_v, can be obtained from Figure 3.28 according to the free area fraction (A_f) and the ratio of tray thickness to hole diameter (t/d_h).

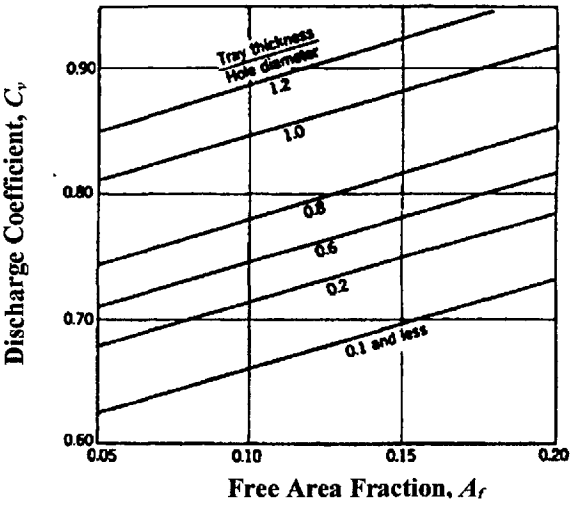


Figure 3.28. Discharge coefficients for gas flow (Leibson *et al* 1957)

A previous study (Yang, 1998) on the 1.8mm tray gives a good agreement between this correlation with the experimental data obtained from CRODIS. This is shown in Figure 3.29 below.

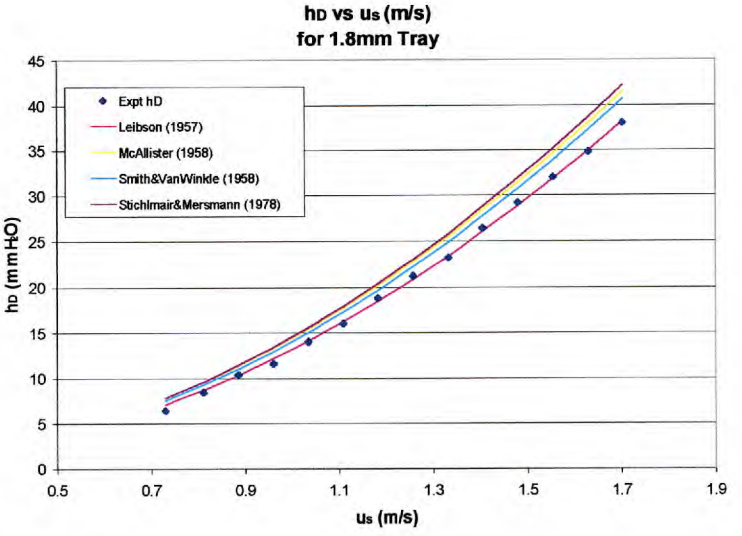


Figure 3.29. Prediction of dry tray pressure drop using various correlations

For the two trays investigated here, the relationships for the dry tray pressure loss are:

for the 1.8mm tray $$h_D = 13.2\,u_s^2 \tag{3.26}$$

for the 6mm tray $$h_D = 18.8\,u_s^2 \tag{3.27}$$

- **Residual Head, h_σ**

There are two different physical explanations for the residual head term. The traditional approach is to relate h_σ to the pressure required to overcome the surface tension forces when forming a bubble at a submerged orifice. The other approach is to relate the way bubbles form at tray holes in terms of excess pressure inside a bubble during its formation period. In the present study, the former approach of predicting h_σ is adopted and it follows the equation below.

$$h_\sigma = \frac{4\sigma}{g\rho_L d_h} \tag{3.28}$$

- **Clear Liquid Head, h_L**

As mentioned in Section 3.4.2, the clear liquid height can be calculated from the froth density profile. There are also a number of correlations available for the prediction of the clear liquid height, h_L (see, for example, the literature review by Yang, 1998) and the experimental results from CRODIS have been used to test the following selected correlations:

- Bennett *et al* (1983) for h_L
- Stichlmair (1978) for h_L
- Thomas and Campbell (1967) for h_L
- Tahmasbi (1997) for h_T

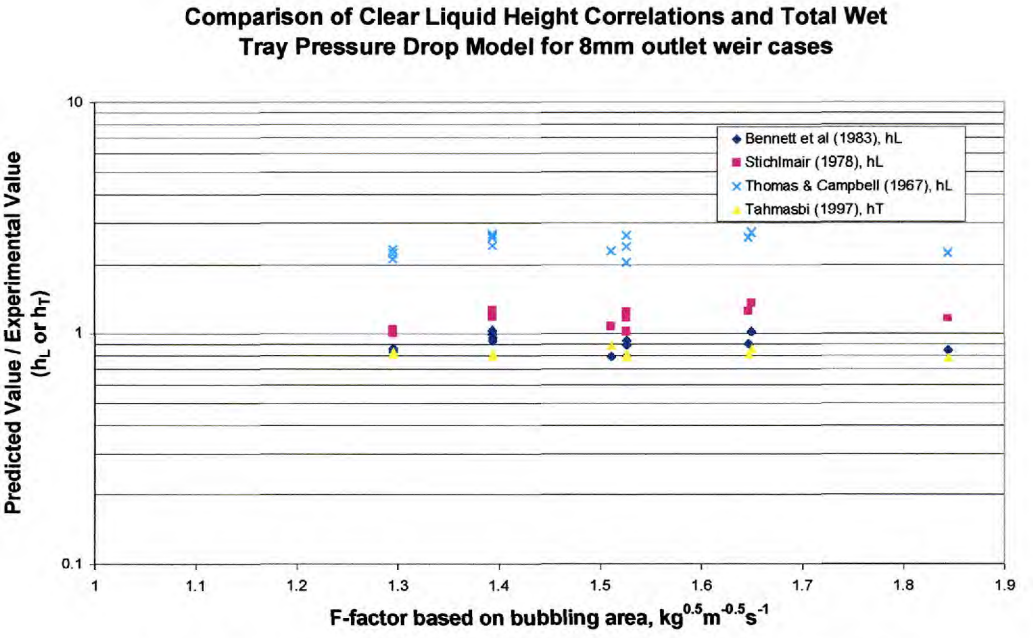


Figure 3.30. CRODIS results: comparisons with correlations (8mm weir)

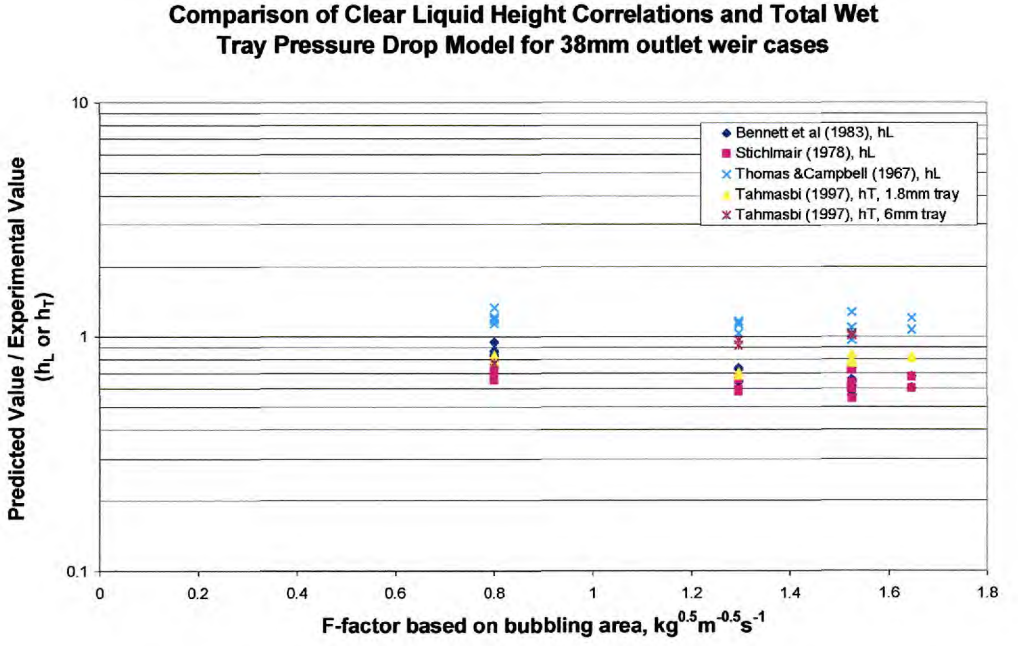


Figure 3.31. CRODIS results: comparisons with correlations (38mm weir)

From Figure 3.30, it can be concluded that both Bennett *et al* (1983) and Stichlmair (1978) correlations are reasonably accurate across the range of gas superficial velocity investigated. In Figure 3.31, the correlation by Thomas and Campbell (1967) seems to be the better one for 38mm outlet weir cases, especially at higher gas flowrate. The majority of the data here were collected from trays with calming zones which are known to increase both clear liquid height and froth height, especially under higher outlet weir conditions. The data which Thomas and Campbell used to develop their correlation were also obtained from trays with outlet calming zones and much higher outlet weirs (75mm and 100mm). Thus, for the low weir cases (i.e. 8mm), the effect of calming zones on clear liquid height is less significant and therefore it is more accurate to use the more common correlations such as the ones by Bennett *et al* (1983) and Stichlmair (1978). When a higher weir is used (i.e. 38mm), where calming zones become effective, it is more desirable to use a correlation based on similar conditions to those used in CRODIS, i.e. that of Thomas and Campbell (1967). However, there are significant discrepancies between the experimental and the predicted results for h_L and even the best prediction approaches are likely.

- **Total Pressure Loss Head, h_T**

Tahmasbi (1997) developed an algorithm to calculate total tray pressure drop, which involves an orifice-type equation for the dry tray pressure drop and a simple bubble formation model for the residual one. However, users are required to input a value of the clear liquid height, h_L based on the given conditions. Tahmasbi (1997) substituted this value by an experimental one and encouraging results on the prediction of the total pressure drop were obtained. In the present work, the code by Tahmasbi (1997) was modified and the Stichlmair's correlation (1978) on h_L was chosen for this input. The results on tray pressure drop predictions are plotted in Figures 3.30 and 3.31.

Discrepancies of about 20% between the predicted and experimental total pressure drop for the 8mm outlet weir cases (mostly 1.8mm hole tray data) are found. This can be explained by uncertainties of some parameters specified in the model. Tahmasbi (1997) noted that the pressure drop model is sensitive to the pre-entered value of bubbling frequency for 1.8mm hole size tray, but not to the 6mm one. As for the higher weir cases, the calming zone enhancement on clear liquid height is not included in

Stichlmair's correlation, therefore lower values of total pressure loss are predicted. The situation will be improved if h_L predictions are obtained from Thomas and Campbell's (1967) correlation instead.

3.4.4. Sauter Mean Bubble Diameter

A typical profile of Sauter mean bubble and droplet diameter measure on a CRODIS sieve tray is given in Figure 3.32. Note that there are two vertical axes in the figure: apparent bubble diameter is at the left and apparent droplet diameter is at the right. As will be seen, the apparent bubble diameter initially rises with distance from the tray floor, then becomes relatively constant and then rises rapidly with distance. This latter region is probably closer and being dispersed droplet rather than dispersed bubbles. The converse (and therefore consistent) behaviour is observed with the apparent drop diameter. Further sets of data on Sauter mean bubble and droplet diameters are given in Appendix C.

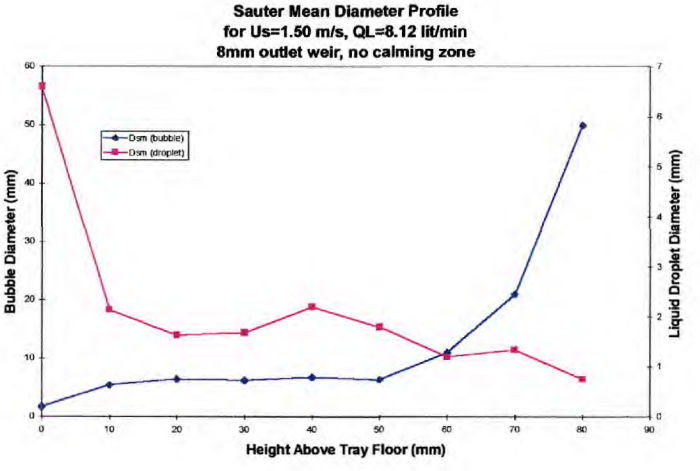


Figure 3.32. Sauter mean bubble/droplet diameter profile

One interesting point to note is that the initial bubble sizes seem to depend slightly on the gas flowrate but not on the liquid one; this is clearly seen in both 1.8mm and 6mm hole-size trays. The profiles for Sauter mean diameter (see also the complete set of results in Appendix C) are not entirely smooth and this is due to the fact that the output signal contains an appreciable level of noise. It is difficult to quantify the errors in this

data, but nevertheless, the data do provide a useful and consistent set of information about the characteristics of the froth.

3.4.5. Partial Bubbling/Moving Froth Phenomenon

Tahmasbi (1997) reported the partial bubbling and moving froth phenomenon in CRODIS which occurred at low gas superficial velocity and this is also known to occur in industrial columns. A schematic diagram is shown in Figure 3.33. The liquid around this bubble patch remained relatively undisturbed and clear. Once the bubble patch of bubbles had reached the outlet weir, a new patch of bubbles was formed at the inlet weir and the process repeated itself periodically.

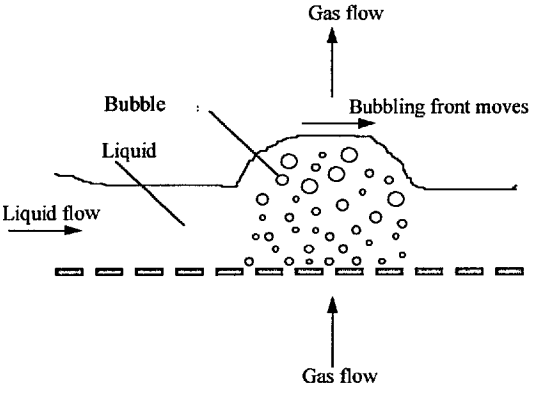


Figure 3.33. Schematic of partial bubbling phenomenon

Partial bubbling has been reported before, however, it relates the phenomenon to the hydraulic gradient which causes the preferential bubbling action at the outlet weir region. Fischer *et al* (1998) presented a simple theory relating this phenomena to the liquid entry condition. First of all, the Froude number for a distillation case is defined as:

$$Fr = \frac{u_L}{(gh_1)^{0.5}} \tag{3.29}$$

where h_1 is the inlet gap at the inlet downcomer (shown in Figure 3.34 below).

Equation (3.29) gives the condition of the liquid entry which becomes supercritical when $Fr > 1$ and this causes a "hydraulic jump" to occur as shown in Figure 3.34. The liquid depth at the inlet weir is less than the depth at the downstream, i.e. providing a

small resistance for the gas to bubble through. Experimental results showed that the patch of bubbles travelled at the speed of the mean liquid velocity which suggested that the movement of the bubbling zone is simply driven by the liquid flow across the tray.

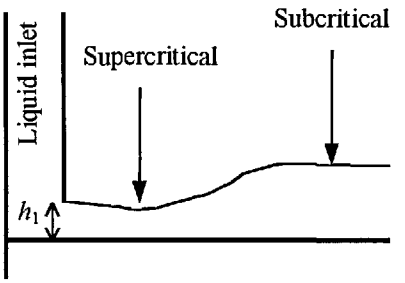


Figure 3.34. Hydraulic jump at liquid inlet region

3.5. Summary

Hydrodynamic tests on the sieve trays have been performed and good agreement is found between general observations and previously published work. Part of the results presented in this work have been used by Fischer (1999) to validate his CFD studies on sieve trays.

A more detailed experimental study of the two-phase flow above sieve trays using local phase detection probes is to be described and discussed in the next chapter.

Chapter 4

Gas-Liquid Simulation Experiment (2) -

Flying Optical Probe System

4.1. Introduction

As mentioned in the previous chapter, in order to further improve on the current understanding of the two-phase flow above a sieve tray, localised measurements should be obtained. For this purpose, a new experimental technique named the "Flying Optical Probe System" has been developed for the CRODIS facility. Optical probes have long been used for phase detection in gas-liquid flows and in particular for void fraction, bubble size distributions and bubble velocity measurement in bubbly flows. Though such probes have been used in distillation trays, the environment in the froth above the tray is not really conductive to their use for obtaining quantitative data. The froth motion is multi-dimensional and signals received from static optical probes placed in the froth are difficult to interpret in terms of, for instance, bubble size. The situation is analogous to that for hot-wire probes in a highly turbulent single-phase flow. For root-mean-square (RMS) turbulent velocity fluctuations greater than around 10%, a significant number of flow reversals may occur relative to the probe and the signal cannot be meaningfully analysed.

The idea for the flying optical probe arose from a solution to the problem of using hot wire probes in situations with high turbulence, namely the *flying hot wire probe*. By advancing ("flying") the hot wire probe into the flow in a direction opposite to the flow, the relative velocity between the probe and the flow is increased and even large turbulent fluctuations in the flow itself can be within the measurable range (i.e. less than around 10% RMS of the probe-to-fluid relative velocity).

In the flying optical probe system, an array of optical probes is swept through the froth and the responses analysed to give distributions of phase element sizes (bubble size/drop size). In what follows, Section 4.2 briefly describes the principle and application of ordinary (static) optical probes in two-phase flows. The detailed design and some performance tests of the flying optical probes system are presented in Section 4.3. The experimental procedures for CRODIS have been described in Chapter 3 and they remained the same for the measurements by new probe system. The actual conditions and associated signal processing for the new experiments are given in Section 4.4 while the results are analysed and discussed in Section 4.5.

4.2. Optical Probes Measurements in Two-Phase Flows

4.2.1. Principle

The theory of optical probe measurement in multiphase flows has been well documented. Optical probes work on the basis of different refractive indexes between gas and liquid phase and the operational principles for optical probes are based on the Snell's law which relates how light is bent as it passes through a surface where the refractive index changes. Consider the situation shown in Figure 4.1 below.

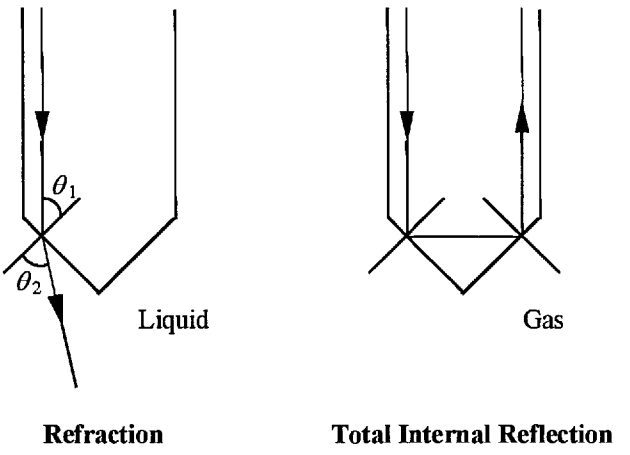


Figure 4.1. The principle of the optical fibre probe

Snell's Law states that when light is passed through two materials of different refractive indices, the ratio of the sine of the angle of incidence (θ_1- see Figure 4.1) to the sine of the angle (θ_2) of refraction is constant and it is equal to the reciprocal of the ratio of the two refractive indices, i.e.

$$\frac{\sin\theta_1}{\sin\theta_2} = \frac{n_2}{n_1} \tag{4.1}$$

According to Eq.(4.1), light is refracted away from the perpendicular line when passing from an optically thicker to an optically thinner medium. When $\theta_2 \geq 90°$, the incoming light is totally reflected inside the probe. A glass optical fibre tip has a refractive index of around 1.62 and the incidence angle is usually about 45°. A limiting value for n_2 under these conditions can be obtained according to Eq.(4.1):

$$n_2 = 1.62\frac{\sin 45^\circ}{\sin 90^\circ} = 1.15 \tag{4.2}$$

This limiting value of refractive index represents the transition point from transmission ($\theta_2 < 90°$) to total internal reflection ($\theta_2 > 90°$) of the incident light. Thus, for a gas-liquid flow experiment, e.g. air-water system ($n_{air} = 1$ and $n_{water} = 1.33$), refraction will occur when the probe tip is immersed in the water whereas total internal reflection will take place when the probe is exposed to the air.

4.2.2. Applications

Over the past 30 years, there have been a number of designs developed for the optical fibre probes. Cartellier (1990), Cartellier and Archard (1991) both gave extensive reviews on optical probes measurements in multiphase flows. Lehner and Mewes (1999) also provided a survey of recent up-to-date developments in the subject. Generally, there are three main types of optical fibre probes based on the principles of the Snell's law. The main difference between them is on the design of the probe tips which are illustrated in Figure 4.2 below.

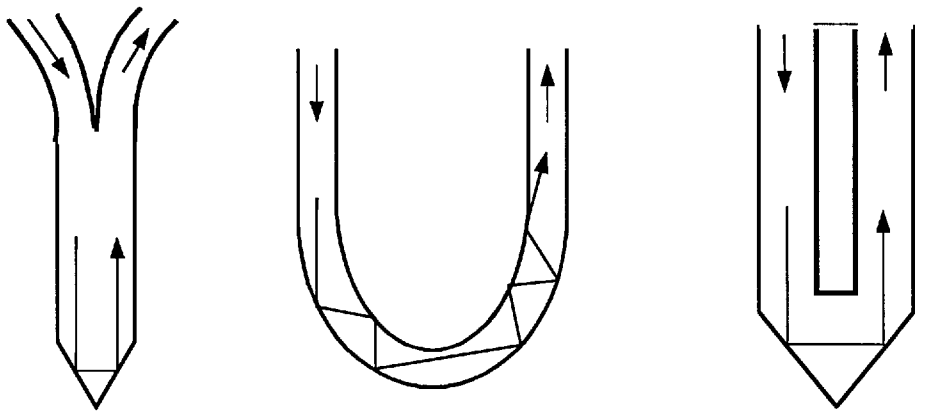


Figure 4.2. Various types of optical fibre probe

Monofibre Probes

Miller and Mitchie (1969, 1970) used a 2mm diameter glass rod which was reduced to 0.3mm and polished to form a 90° conical shape tip. The authors demonstrated that the 0.3mm tip can detect a bubble of 0.5mm diameter at a superficial liquid velocity of 3m/s. Calderbank and Pereira (1977) later designed a new optical probe system followed their earlier success on measuring bubble sizes and velocities on a distillation tray using a compound optical probe system. Each optical probe is made of glass fibre with a diameter of 3mm and this is drawn to a 0.2mm rod towards the probe tip where it is ground and polished to a point. Four such optical probes were used under a special arrangement so that the compound probe system is able to measure bubble diameter and velocity.

U-Shaped Probes

Danel and Delhaye (1971) first made an U-shaped optical fibre probe. It consists of an optical fibre with 40μm diameter which is bent into a U-shaped tip of about 0.1mm diameter. The probe was reportedly successful in a number of two-phase flow investigations by Galaup and Delhaye (1974, 1976). Later, *AID S.A.* (1983) marketed a similar probe to the one developed by Danel and Delhaye; they recommended that the minimum penetration length of the bubble must be three to four times greater than the diameter of the optical fibre.

Prism-Linked Probes

Abuaf *et al* (1978) produced an optical probe by joining two 125μm fibres inserted in a 500μm outer diameter stainless steel tube. The tip is ground and polished to a 90° conical shape tip. It was found that when the probe penetrates a bubble, a water film is left on the probe tip. From the authors' experimental results, they concluded that the film thickness increases with the bubble velocity.

The way these probes were made depended very much on the available facilities, e.g. especially on tip polishing. There are always advantages and disadvantages for using any type of optical probes. Previous experience showed that satisfactory results on dispersed two-phase flows could be obtained by all types of the probes. However, in the present study, the flow condition is quite different to those encountered in the past. Thus, careful precautions must be taken when designing a probe tip.

4.3. Design of the Flying Optical Probes System

4.3.1. Background Theory

The chaotic nature of the sieve tray two-phase flows makes it almost impossible to find the appropriate descriptions (both qualitative and quantitative) of the situation. Figures 4.3 below are two experimental photographs (side views) of the froth structure observed at the same spot on the test tray of the CRODIS facility; one was taken at about 0.5 second later than the other one. The attempt on establishing any connection between the flows from the two snapshots seems extremely difficult.

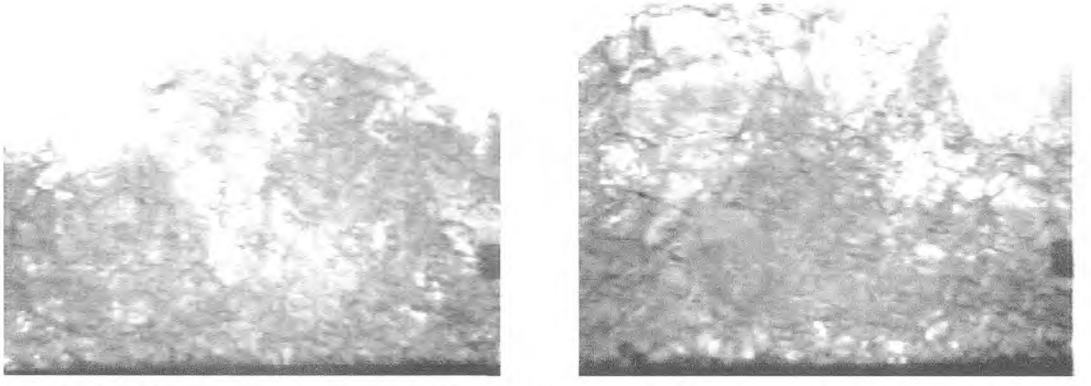


Figure 4.3. Instantaneous image of the froth structure (left) and at 0.5 second later (right)

Traditionally in multiphase flows, probes (either conductivity or optical one) have been used to measure local parameters (e.g. Serizawa, 1975). A probe is kept stationary at a fixed position in the flow field and the tip is pointing the opposite direction to the flow. An electrical signal is generated when a bubble or droplet approaches to strike the probe.

Multiple probe systems have been used to provide discrimination on the "useful" bubbles/droplets signals, e.g. the compound probe system used by Calderbank and Pereira (1977) on a distillation sieve tray. Their compound probe is an array of four sensors in which a leading probe is symmetrically surmounted by three identical probes placed above it. The arrangement is shown in Figure 4.4 below.

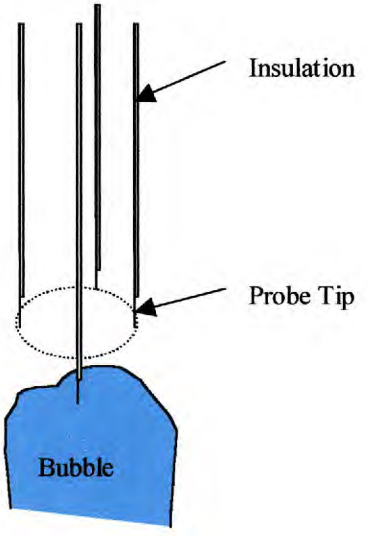


Figure 4.4. The Calderbank bubble probe

A rising bubble is known to be coaxial with the leading probe when it is later coincidentally sensed by the three upper probes. The time delay between the first signal from the lower probe and the "simultaneous" signals from the three upper probes determines the bubble velocity. The duration time for which the lower probe stays in the particular bubble can then be used to determine the maximum bubble height. Subsequent work on such a system were carried out by Calderbank and Pereira (1979) and Raper *et al* (1977, 1978, 1982).

Bubbles and droplets on a sieve tray move violently at different speeds and in different directions. Thus, when performing probe measurements on a sieve tray, the traditional approach (single/double probe systems, e.g. Serizawa, 1975) would suffer from lack of

discriminating useful signals. Although the Calderbank's approach (1979) seemed to have overcome such a difficulty, the bubble count rate obtained was quite low (200 bubbles per 3 hours; reported by Raper *et al*, 1978). The useful signals all came from those bubbles which rise vertically and coaxial with all four probes. These bubbles may not represent the whole spectrum of bubble sizes which exists in the froth.

In the present work, a new design named the "flying optical probes system" has been developed. The idea of "flying" the probes along the tray is to try to obtain, as closely as possible, an instantaneous scan of the froth body. An illustrative drawing for such a system is shown in Figure 4.5 below.

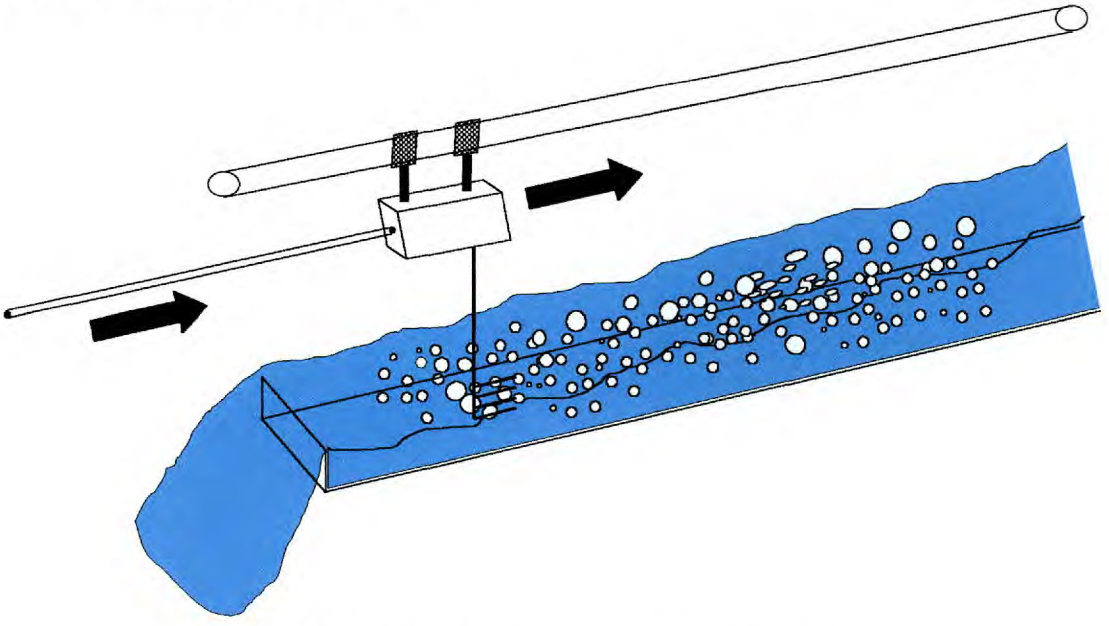


Figure 4.5. Proposed design of the new probes measuring system

The flying unit is attached on the linear bearing spline and is pushed along the tray (moving at a fast, but constant, speed) by a stainless steel tube driven by a motor. The probes are fixed at various heights and the optical cables leading to the appropriate electronic equipment outside the system, are enclosed in the stainless steel tube.

The principle is to drive the unit at a high speed such that the local velocities (forwards, sideways and vertical) of the multiphase mixture are relatively small compared with the probe velocity. The main assumption here is that the motion of the froth is unaffected by the probes up until the time at which the probes pass through. Hopefully, by flying

the probes repeatedly, statistical information on the structure of the two-phase flow can be drawn from the signals obtained following appropriate treatments.

4.3.2. The Optical Fibre Probes

4.3.2.1. Optical Fibre Cables

The fibre optics used in the present work was purchased from *RS Ltd.* It is a plastic coated silica (PCS) fibre of 200 μm core diameter, step index, numerical aperture 0·27. The optical fibre is housed, with Kevlar™ strength membranes, in a polyvinyl chloride (PVC) sheath with an overall diameter of 4.8 mm nominal. The fibre is terminated at each end with a 9 mm SMA connector and this is shown in Figure 4.6 below.



Figure 4.6. 200μm optical fibre used in the present work

This cable has been designed to operate in the wavelength range 800-880 nm. Outside these wavelengths, the attenuation increases appreciably and is not specified by the vendor. The level of attenuation (at 820 nm) is typically 7 dB/km with a maximum of 10 dB/km and the designated bandwidth is at 25 MHz/km. The operating temperature range for these fibres is between -15°C and +50°C. Mechanically, a maximum tensile load of 300N is allowed and the minimum bend radius is given at 50 mm. The material used for the end SMA connectors are nickel-plated brass and the maximum in-line attenuation between connectors is 2 dB per connector.

The fabrication of an optical probe to be used in the CRODIS facility requires a 10-metre length of the fibre optics cable described above. The cable was first cut into half and a small part (about 50cm) of the yellow PVC jacket was carefully removed from each of the two broken ends. A special tool was then used to peel off the plastic coating so that the optical fibre is totally naked. An 800-μm-o.d. stainless-steel syringe needle was chosen to house the two naked optical fibres. The sharp tip of the needle needed to be polished flat before the fibres were inserted. A mini-torch was used to "fuse" the two naked fibres at one end of the needle tube, forming a spherical bead. This fused tip was then slightly pulled back into the needle tube and epoxied in place. Figure 4.7 below shows a finished tip of the optical probe.



Figure 4.7. The tip of the optical probe

The final step is to carefully remove the rest of the PVC jacket remaining on the cables, leaving only about 10cm at each end near to the connector. This is purely for the convenience on the assembly of the whole system later on. The above procedures were repeated to manufacture five optical probes.

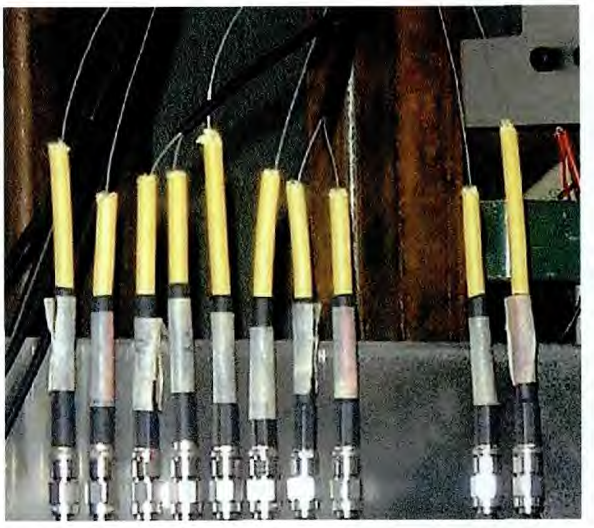


Figure 4.8. Five pairs of optical fibres with/without external protection jacket

4.3.2.2. Emitter (the Light Source)

When a probe has been successfully manufactured, one of the connectors is screwed onto a light source (emitter) whereas the other onto a receiver. The emitter used in the present work, purchased from *RS Ltd*, is a high power GaAlAs surface emitting LED (Light-Emitting Diode). It is optically aligned in SMA housings with a bulkhead mounting (i.e. the connector on the cable) to provide direct connection to the above described fibre optic cables. Figure 4.9 and Table 4.1 below shows the picture and some specifications of the actual emitter used in the present work.



Figure 4.9.
High power emitter with bulkhead SMA

Operating temperature range	-40°C to +100°C
Peak emission wavelength	850 nm
Spectral bandwidth	50 nm
Response time	6 ns (typ) 8 ns (max)
Launch power for 200 μm PCS cable	160 μW min. (-8dBm)

Table 4.1.
Technical specifications of the high power emitter

4.3.2.3. Receiver

To match the high power emitter described above, a planner silicon PIN diode optically aligned in SMA housings, with bulkhead mounting was used to connect the other end of the cable. The device features low junction capacitance, fast response and it can be used at rates up to 50MHz. The receiver has the same appearance as the emitter (i.e. Figure 4.9) and some technical specifications are given in Table 4.2 below.

Operating temperature	-40°C to +100°C
Peak spectral response (typ)	850nm
Peak responsivity 850nm (50μm)	0·58A/W
Capacitance	2·1pF
Rise/Fall time (5V)	17ns

Table 4.2. Technical specifications of the receiver

4.3.3. Probes Testing

The optical probe, fully connected to both an emitter and a receiver, underwent some basic tests before it could be used reliably in the CRODIS rig. The first step of the testing procedure was to examine the response from the probe when it passes through a gas-liquid interface. This was done by manually moving the probe tip in and out of the water surface in a glass beaker. The receiver is connected to an oscilloscope and the signal is given in voltage. The experimental setup and the resultant signal profile for the test are given in Figure 4.10 below.

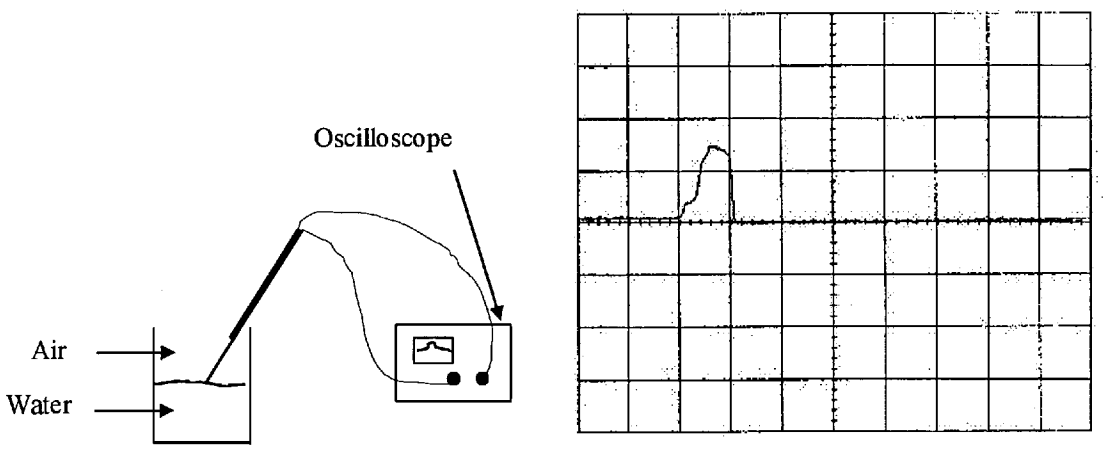


Figure 4.10. Experimental setup for probe testing and signal response (scale: 200mV, 5ms)

All five probes show good response when passing through the gas-liquid interface. The next step is to perform more complicated tests on bubble/droplet penetrations. The experimental setup includes the use of a digital high-speed video camera, which enables a comparison to the signal profile from the oscilloscope. The arrangements for these tests are shown in Figure 4.11 below.

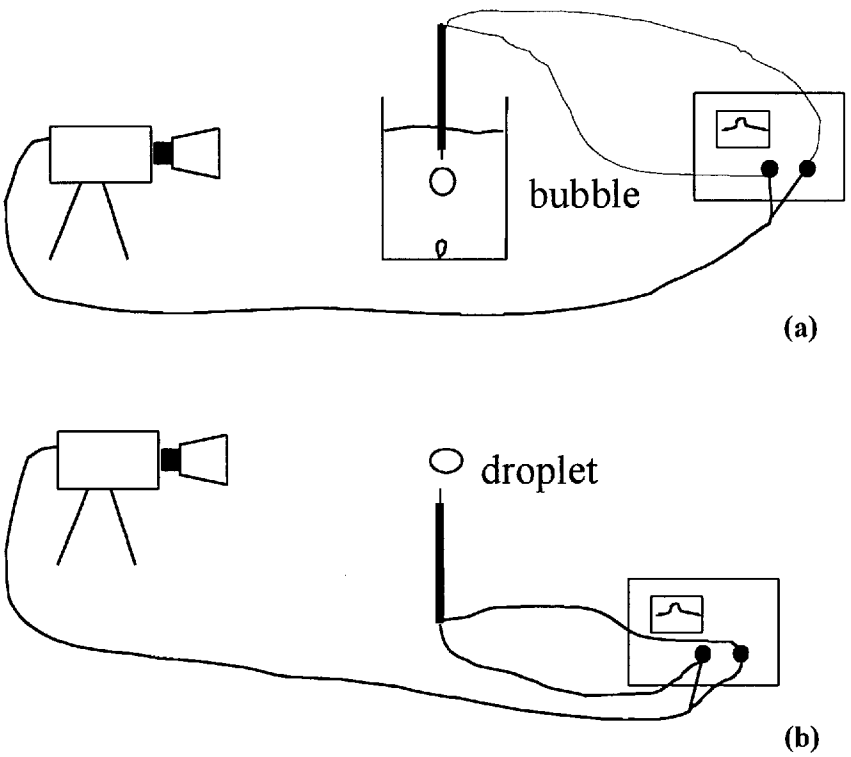


Figure 4.11. Experimental setup for optical probe testing on bubble (a) and droplet (b) signals

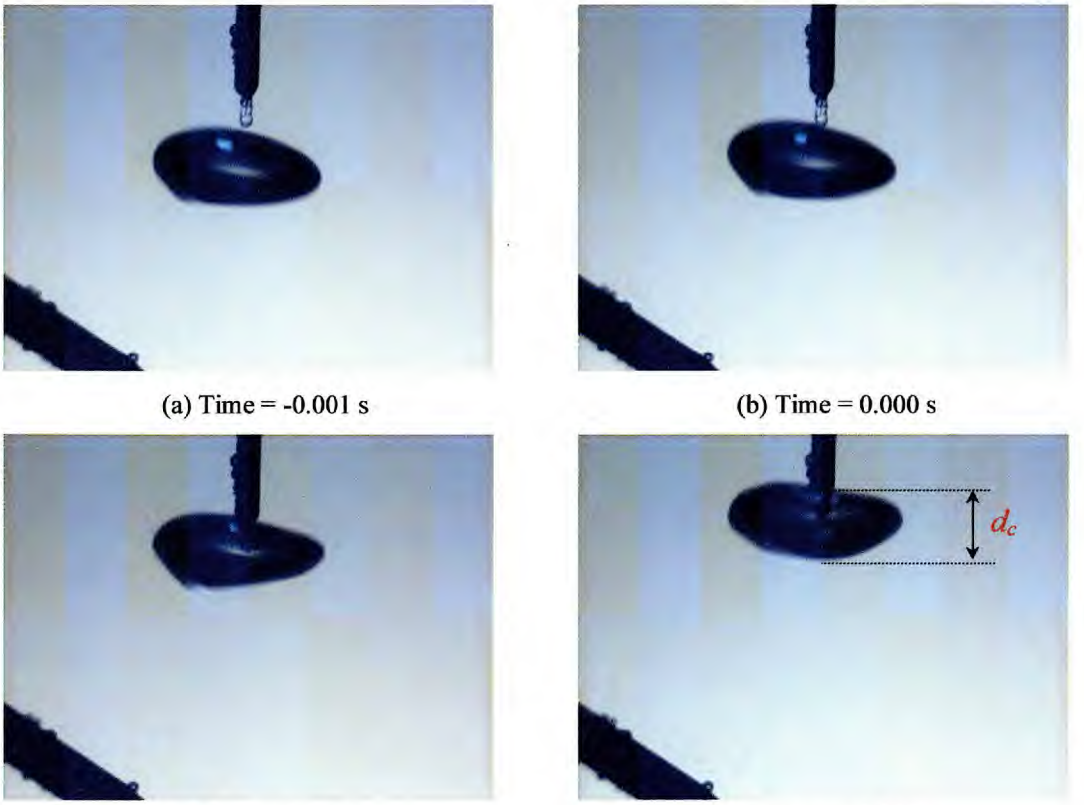
The photographs taken are in a pre-set time interval (0.001 second for bubbles, 0.0005 second for droplets) and these can be used to determine the time and the location of the bubble. The analysis is divided into the following parts:

1. Determine the probe-penetrated bubble chord length (d_c) from the photographs; penetration time (t_p) from the signal output graph and then calculate the bubble rise velocity (v_{b1}).
2. Choose an initial position of the bubble (say 0.01 second before it was in contact with the probe) and determine the distance (l) between the bubble and the probe tip in this pre-contact period. Calculate the bubble rise velocity (v_{b2}) in this period with the rising time estimated from the photographs.

3. Examine how well v_{b1} and v_{b2} match each other and investigate any large discrepancy if exists.

4.3.3.1. Bubble signal test (1) – An elliptical bubble

Step 1:



(a) Time = -0.001 s (b) Time = 0.000 s

(c) Time = 0.006 s (d) Time = 0.011 s

Figure 4.12(a) to (d). Sequential pictures of an elliptical bubble passing through a probe

As shown in the figures above, the bubble chord length does not vary significantly at the beginning and the end of the penetration process. It is determined (after appropriate scaling) that d_c = 2.25mm.

The penetration time is determined from the signal output graph shown in Figure 4.13. When a bubble hits the probe tip, there will be a sharp increase on the output voltage. This is clearly observed in the graph. However, it can be noted that the point of the sharp increase on voltage does not fall at the "zero time" spot. This is because the triggering voltage set in the electronic device used to trigger the digital camera is higher than the average value of water signal voltage. The actual "shape" of the bubble signal

can be identified visually (shown in red box below) and this gives an approximate penetration period (t_p) of 0.011 second.

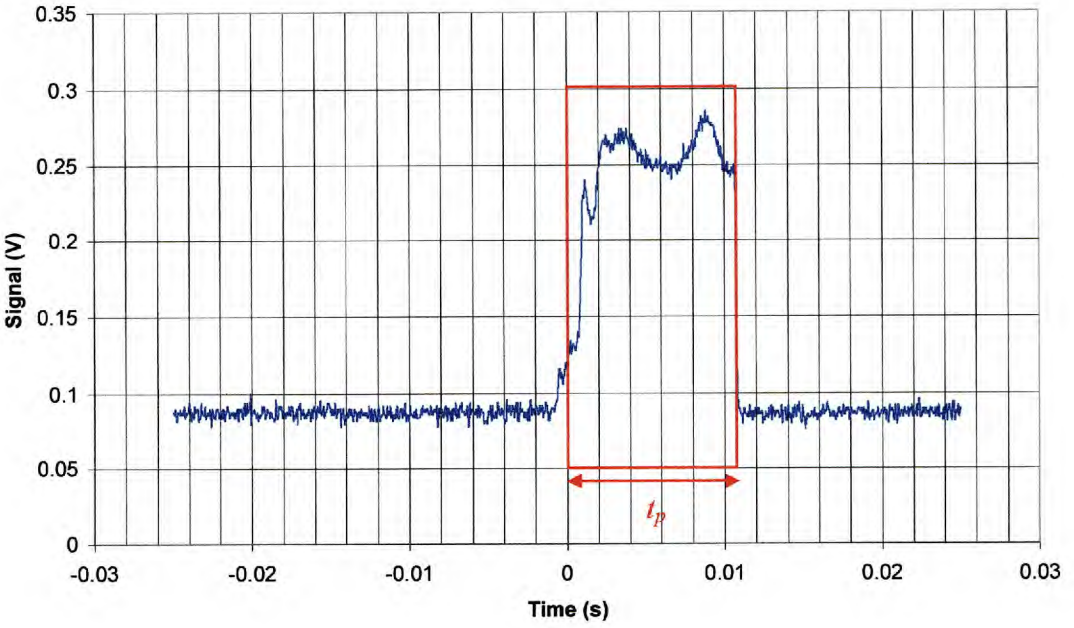
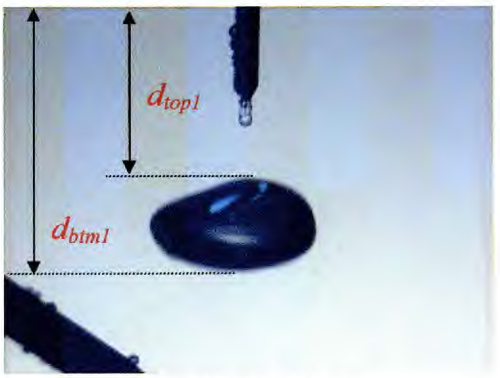


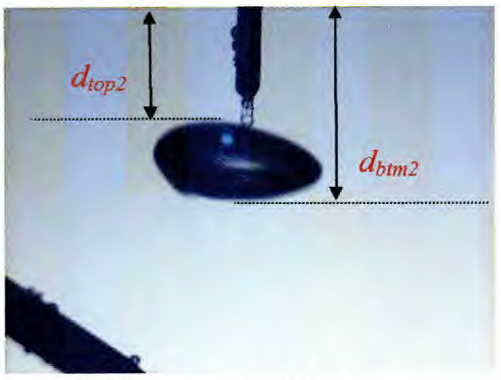
Figure 4.13. Signal profile of a bubble passing through a probe (corresponds to Figure 4.12.)

The bubble rise velocity, $v_{b1} = {}^{d_c}/_{t_p} = 2.25\times10^{-3}/0.011 = 0.205$ (m/s)

Step 2:



(a) Time = -0.01s



(b) Time = 0.00 s

Figure 4.14(a) and (b). Motion of a bubble before in contact with a probe

In a gas-liquid flow, the interface undergoes continuous deformation and this can be seen from the photos above. The width of the bubble remains the same at (also in

between) the two incidents of time, however, the upper surface of the bubble seems to "swing" from right to left. In the photographs above, d_{top1} and d_{top2} are the vertical distances between the top of the bubble to the top edge of the picture at time -0.01s and 0.00s respectively. Similarly, d_{btm1} and d_{btm2} are the vertical distances between the bottom of the bubble to the top edge of the picture. In order to obtain an average vertical distance (l) between the upper surface of the bubble to the probe tip, an average vertical bubble chord length, d_{av}, is required and this is defined as the mean of d_1 and d_2. As a result, l = 2.1mm.

$$\Delta d_{top} = d_{top1} - d_{top2} = 5.43 - 3.66 = 1.77 \text{ (mm)}$$

$$\Delta d_{btm} = d_{btm1} - d_{btm2} = 8.34 - 6.17 = 2.17 \text{ (mm)}$$

$$l = (1.77 + 2.17) / 2 = 1.97 \text{ (mm)}$$

The photographs indicate that the rising time is 0.01 second, and therefore the average pre-contact period bubble rise velocity is:

$$v_{b2} = 1.97 \times 10^{-3} / 0.01 = 0.197 \text{ (m/s)}$$

Step 3:

$$v_{b1} = 0.205 \text{ (m/s)}$$

$$v_{b2} = 0.197 \text{ (m/s)}$$

The difference is less than 5% which shows a very good consistency between the probe measurement and photographic method.

4.3.3.2. Bubble signal test (2) – A larger bubble

Step 1:



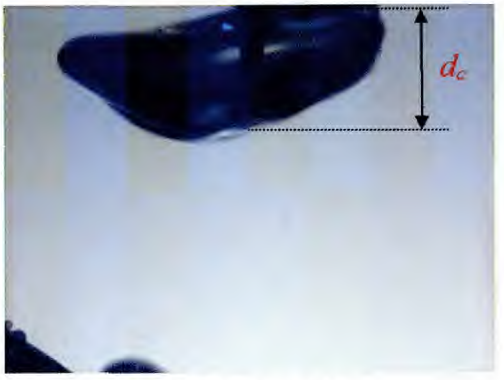
(a) Time = -0.001 s



(b) Time = 0.000 s



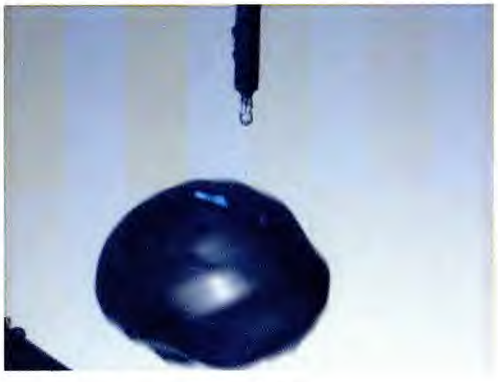
(c) Time = 0.011 s



(d) Time = 0.023 s

Figure 4.15(a) to (d). Sequential pictures of a large bubble passing through a probe

The shape of the bubble varies from the beginning to the end of the penetration and this has significant effect on the bubble chord length. One may argue that this is because of the intrusive nature of probe measurement, i.e. the probe is changing the shape of the bubble. However, this phenomenon occurs frequently in free bubbly flow (even without the presence of a probe) and this has been observed many times in the current series of tests. One example is shown in the photographs below (changing from a round bubble to an elliptical one).



(a)



(b)

Figure 4.16(a) and (b). Change of the shape of a rising bubble before in contact with a probe

Thus, the bubble chord length is estimated from the photo taken at the end of the penetration and it is determined to be d_c = 3.89mm.

The recorded voltage output from the electronic device is shown below and the red box identifies the penetration time to be t_p = 0.023 second.

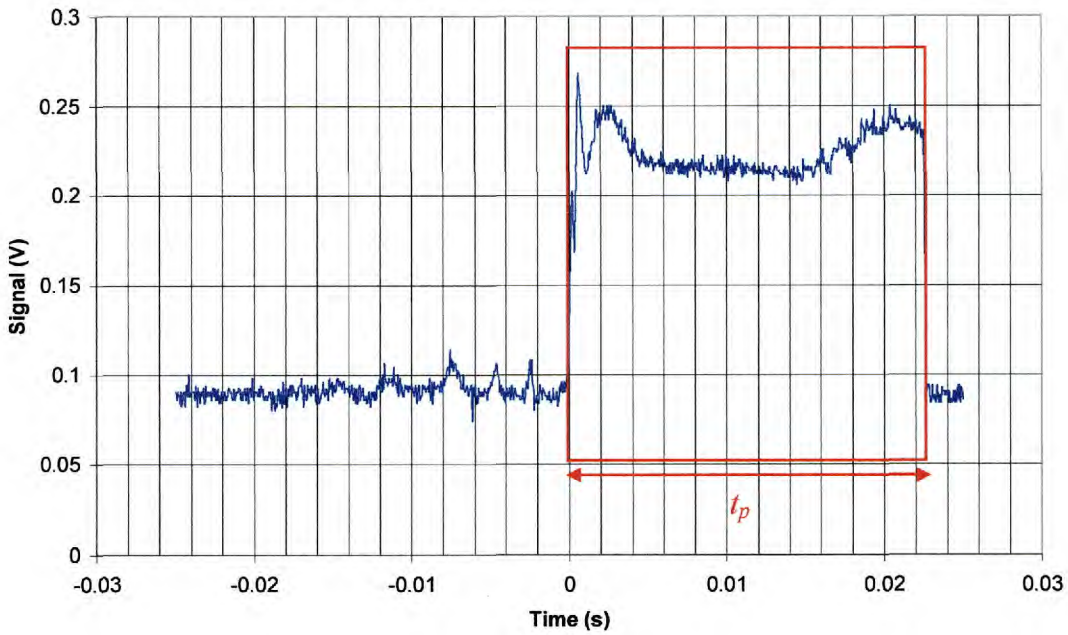
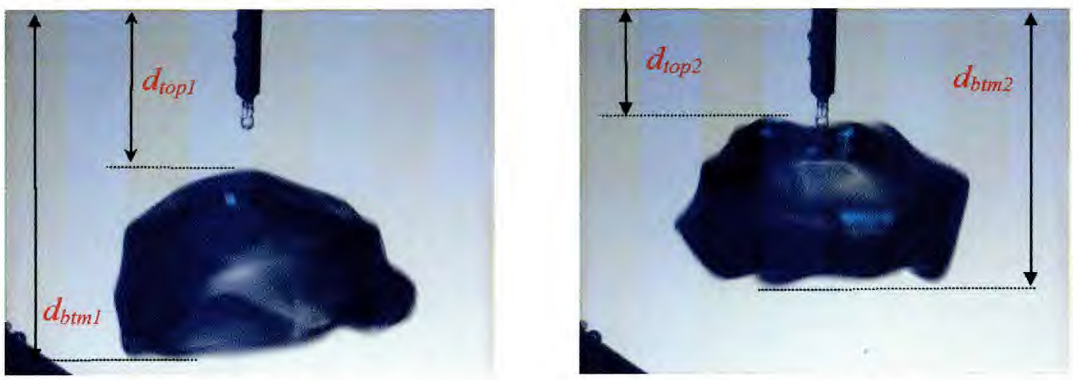


Figure 4.17. Signal profile of a bubble passing through a probe (corresponds to Figure 4.10.)

The bubble rising velocity, $v_{b1} = 3.89\times10^{-3} / 0.023 = 0.169$ (m/s)

Step 2:



(a) Time = -0.01 s (b) Time = 0.00 s

Figure 4.18(a) and (b). Motion of a bubble before in contact with a probe

Following the same analysis as Example 1,

$$\Delta d_{top} = d_{top1} - d_{top2} = 5.03 - 3.4 = 1.63 \text{ (mm)}$$

$$\Delta d_{btm} = d_{btm1} - d_{btm2} = 11.14 - 8.8 = 2.34 \text{ (mm)}$$

$$l = (1.63 + 2.34) / 2 = 1.99 \text{ (mm)}$$

Therefore, the average pre-contact period bubble rise velocity is:

$$v_{b2} = 1.99\times10^{-3} / 0.01 = 0.199 \text{ (m/s)}$$

Step 3:

$$v_{b1} = 0.169 \text{ (m/s)}$$

$$v_{b2} = 0.199 \text{ (m/s)}$$

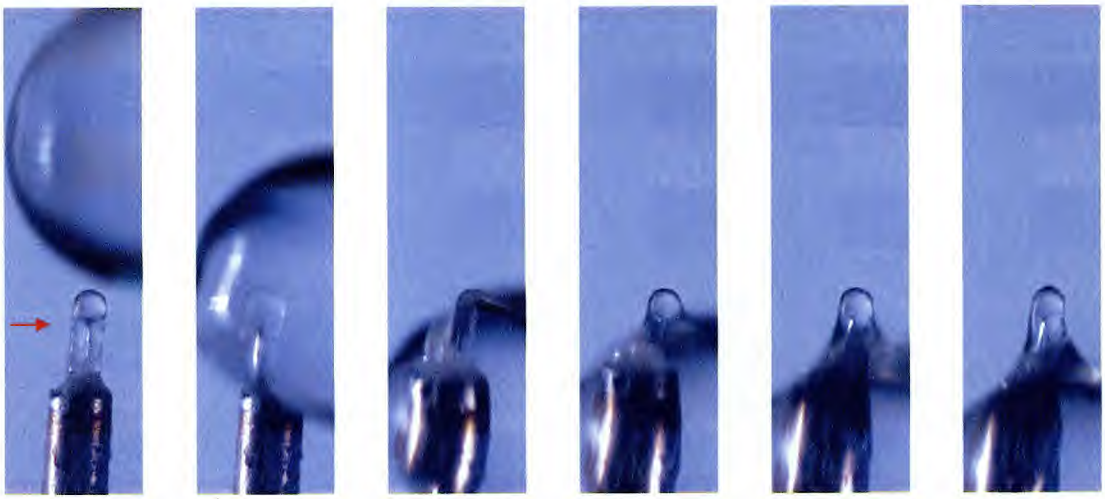
The large difference here can be explained by the following two reasons:

1. The surface of the large bubble is under constant deformation. Examining the photographic evidence (Figures 4.15(a) to (d)), the shape of the bubble seems to have developed side ways along its path. The extent of such deformation is significant enough to slow down the post-contact bubble rise velocity.
2. Both top and bottom surface of the bubble are constantly "oscillating" in the vertical direction. In Figure 4.18(b), the probe did not strike the highest point of the bubble, therefore a smaller value of d_{top2} is obtained. Furthermore, the shape of the bubble is similar to a mushroom cap and this increases the observed value of d_{btm1}. Thus, the combined effect from the two observations gives a higher average pre-contact bubble rise velocity.

4.3.3.3. Droplet signal testing (1) – A single droplet

Step 1:

The probe testing analysis of the actions on droplets are relatively more difficult. As shown in Figure 4.11, a droplet of water is falling onto the probe under the gravity. The speed at which the droplet is travelling is much higher (about double) than the bubbles in the previous two cases. Therefore, it is necessary to increase the framing rate on the high-speed video camera in order to capture useful images. A framing rate of 2000 frames per second was used for the current droplet tests, however, the size of each image has to be reduced to accommodate the large number of images. Figures 4.19 below shows some pictures of a droplet passing through the probe.



(a) 0.0000s (b) 0.0035s (c) 0.0065s (d) 0.0070s (e) 0.0075s (f) 0.0080s

Figure 4.19(a) to (f). Sequential pictures of a droplet passing through a probe

The signals received at the oscilloscope are given in Figure 4.20 below. When the water droplet hits the tip of the probe, the light travelling inside the optical fibre leaks out and this cause a drop on the output voltage received at the oscilloscope. Therefore it is possible, together with the above images, to identify the actual penetration period of the droplet and this is shown in a red box in Figure 4.20.

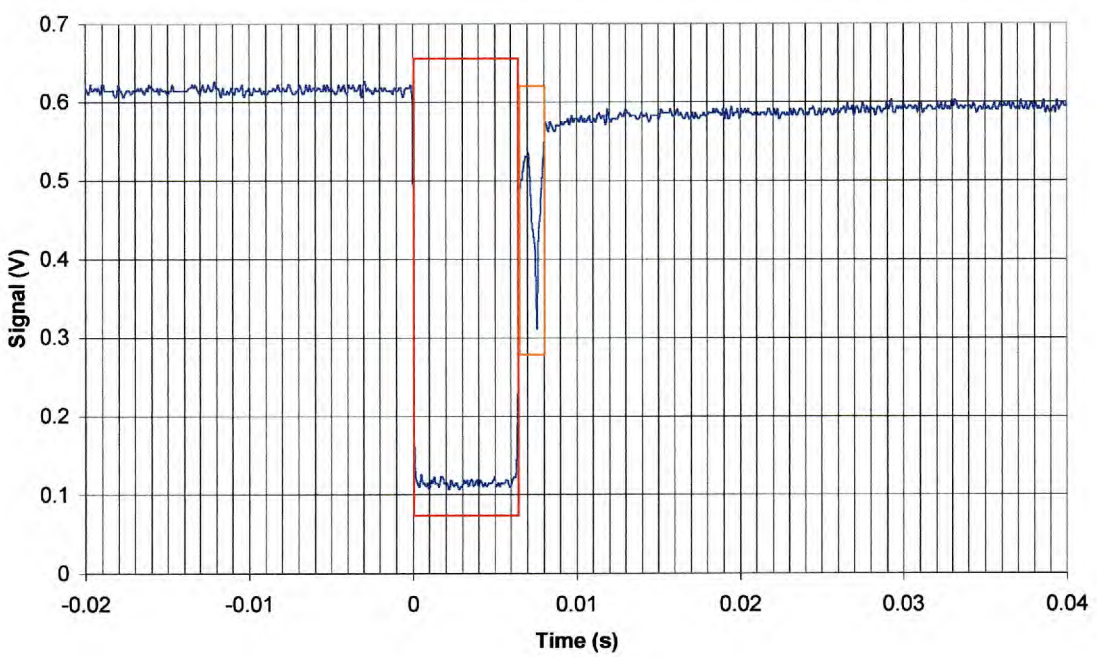


Figure 4.20. Signal profile of a droplet passing through a probe (corresponds to Figure 4.14.) The red box represents the actual penetration period for the droplet

The pictures concludes that the probe tip is exposed to air again at about 0.0065 second after initial contact and the signal also shows an increase in voltage at this point. However, the signal level drops again at 0.007 second (immediately after it recovers at 0.0065 second) before it finally stabilises at a constant level (after 0.008 second). This phenomenon is highlighted in an orange box in Figure 4.20.

The reason for such a phenomenon can be explained by the capillary effect, which is caused by the large surface tension and small contact angle of the water leading to the transient trapping of water between the two optical fibres. In Figure 4.19(a), a fine gap can be observed between the two optical fibres just underneath the joined tip (indicated by a red arrow). When a water droplet passes through the probe, there will always be a thin film of residual water left on the tip. As soon as the top surface of the droplet passes beyond the level of the red arrow (i.e. Figures 4.19(d) and (e)), the capillary effect begins to pull up water from the leaving droplet. The action causes a sudden drop on the signal profile but it quickly recovers again as the excess water gained from the capillary effect quickly drains.

4.3.3.4. Droplet signal testing (2) – Three continuous droplets

The purpose of this example was to test the response of the probe under continuously approaching droplets. Figure 4.21 below shows the signal profile of this test and three droplets chosen for the discussions of this investigation are boxed in red, green and orange.

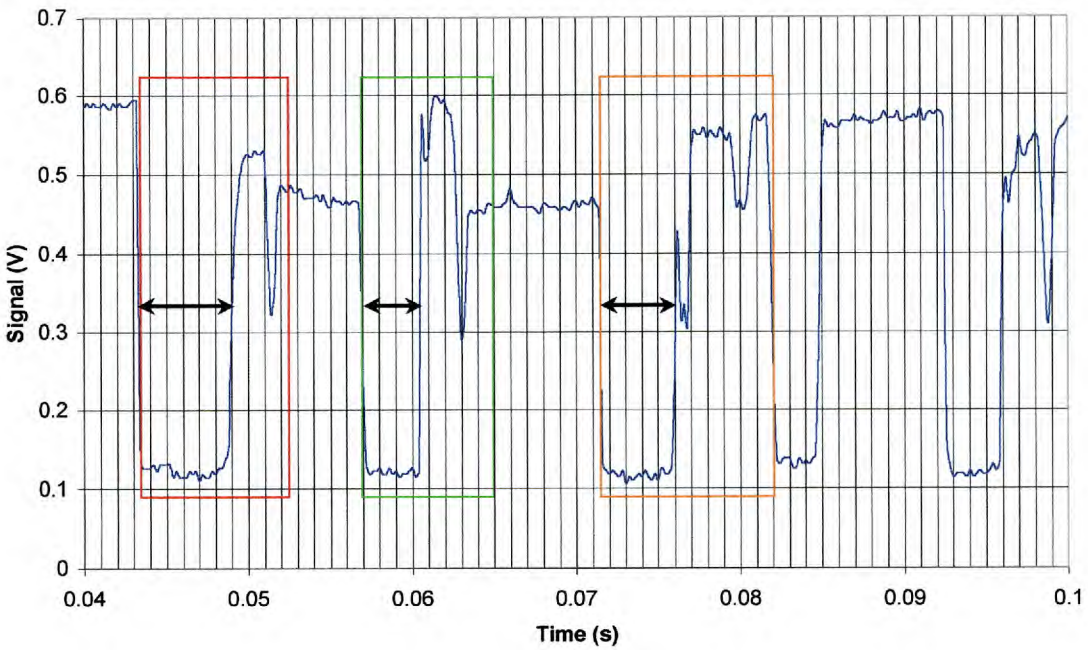
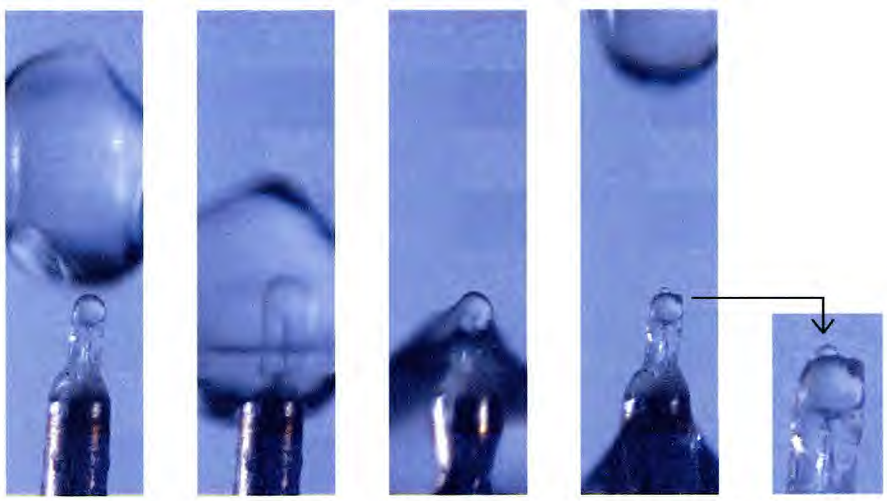


Figure 4.21. Signal profile of several droplets continuously passing through a probe
The arrow " ⟷ " represents the actual penetration periods for each droplet

Figures 4.22(a) to (e) below show the first droplet (correspond to the red box in Figure 4.21) passing through the probe.

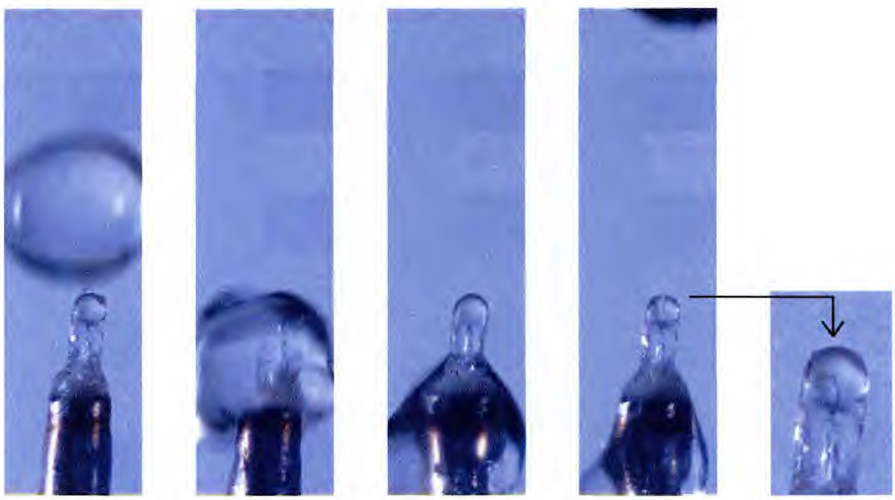


(a) 0.0435s (b) 0.0465s (c) 0.0495s (d) 0.0525s (e)

Figure 4.22(a) to (e). Sequential pictures of the first droplet passing through a probe

The interesting point to note here is the two fine drops of water left on the probe tip in Figure 4.22(e). After the droplet swept through, these drops keep the signal at a level

below 0.5 volt instead of recovering to a level near 0.6 volt. The next droplet also showed similar behaviour and the pictures of this droplet are shown in Figures 4.23(a) to (e) below (correspond to the green box in Figure 4.21).

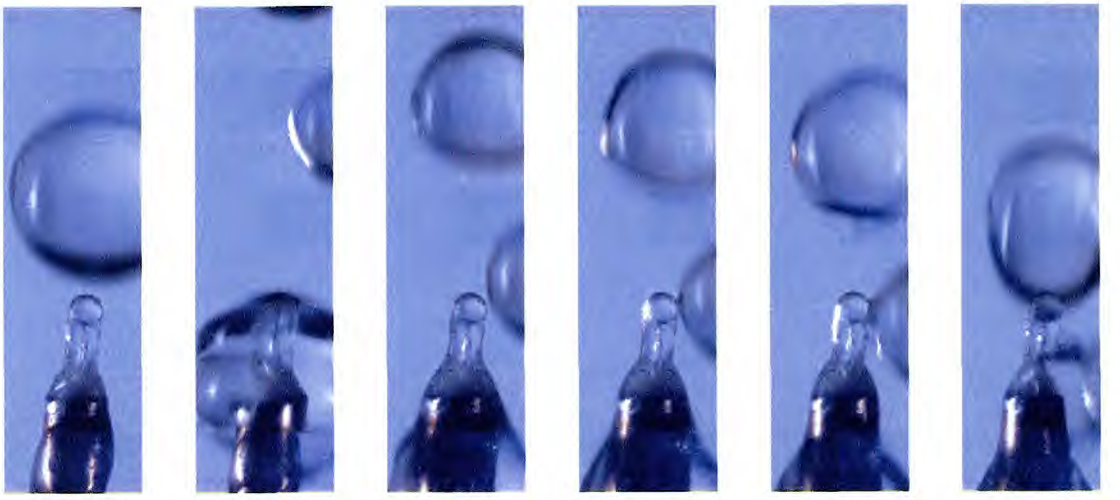


(a) 0.0570s (b) 0.0605s (c) 0.0630s (d) 0.0650s (e)

Figure 4.23(a) to (e). Sequential pictures of the second droplet passing through a probe

In this case, there is large area of residual water covered on the probe tip as observed in Figures 4.23(d) and (e). This causes similar effect as the previous droplet, i.e. the signal stays below 0.5 volt.

The pictures for the motion of the third droplet are given in Figures 4.24(a) to (f) below. When comparing the first three pictures to the signal profile, it follows the usual response as described before. However, there is one small droplet which just managed to touch the probe tip from the side and it has caused a little disturbance in the signal profile.



(a) 0.0715s (b) 0.0760s (c) 0.0795s (d) 0.0800s (e) 0.0805s (f) 0.0820s

Figure 4.24(a) to (f). Sequential pictures of the third droplet passing through a probe

4.3.3.5. Conclusion from the Probe Testing Experiments

Bubbles

The signal profile of a bubble passing through the probe is distinct and easy to identify. If the velocity of the bubble is known (e.g. from photographs), it is then possible to determine the bubble chord length (i.e. the distance which the probe penetrates the bubble).

Droplets

The signal profile of a droplet is slightly more complicated. Generally, the probe responds consistently to all the droplets, i.e. the signal shows a big fall on contacting the droplet and this is followed by a recovering tail which includes a second fall caused by the capillary effect. The shape of the signal profile (especially the tail part) is believed to depend on the following factors:

- the size of the droplet
- the position where the probe and droplet came in contact
- the pre-contact condition on the surface of the probe tip

From the present exercise, there is no obvious correlation between these factors and the observed signals. However, the profile for the actual body of the droplet can be clearly identified regardless the shape of the "tail".

4.3.4. The Actuation Mechanism

Figure 4.25 below shows the overall design of the actuation mechanism for the system. The basic design concept is to fix the ends of the optical fibres at which the light is injected and received while allowing the other ends (which are, of course, fused together to form the probe) to move through the froths. The fibres from all the probes pass through a stainless steel tube which also acts as a push rod for activating the motions. This stainless steel tube passes though a seal to the outside of the CRODIS vessel and the optical fibres hang from the end of the tube so that they can move without disturbing their contact with the emitter/receiver diodes. In order to mount the components for the external actuation system, an extra sheet of acrylic resin (Perspex^{TM}) was fixed to the CRODIS rig structure.

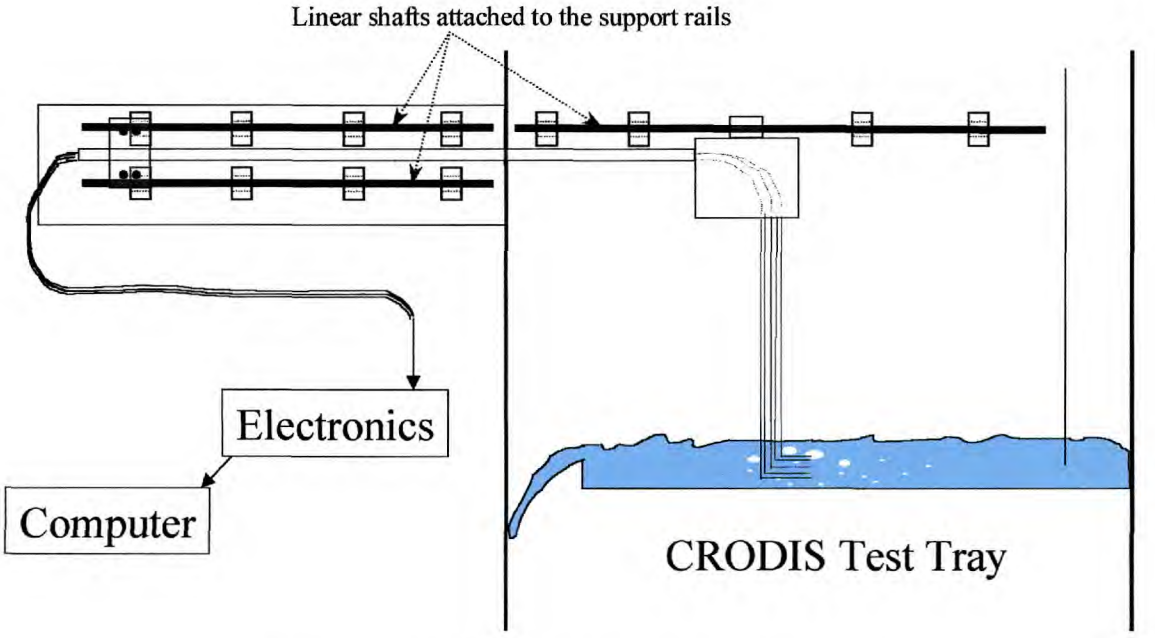


Figure 4.25. Mechanical structure of the actuation mechanism

Optical Probes and Internal Configurations

The naked optical probes are very fragile and in order to perform measurements in the CRODIS facility, they need to be protected by various sizes of stainless steel tubes along the way as shown in Figure 4.26 below. Each probe is housed by a thin 2mm I.D. stainless steel tube which is bent into 90°. These tubes are tightly clamped onto a piece of stainless steel plate which provides a good support and prevents excessive vibration in the experiments.

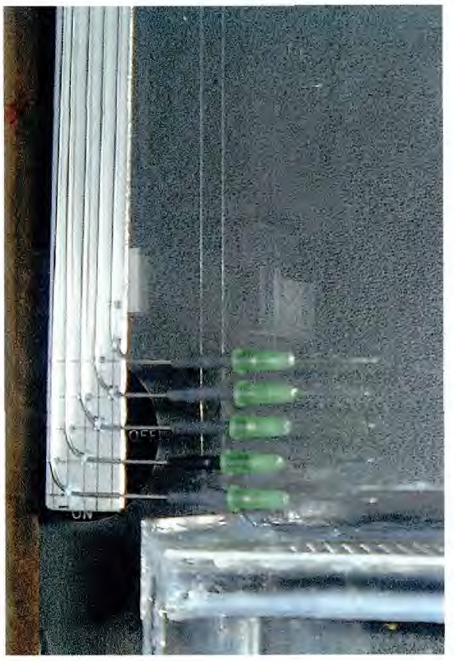


Figure 4.26. Geometry of the probes inside CRODIS facility

The combined unit (of tubes and plate) is clamped by an aluminium box which is sprayed with a layer of waterproof paints and this is shown in Figure 4.27. The box serves as an intermediate protection compartment for the naked fibres as well as the travelling vehicle inside the column. The fibres leave the box from the top left corner where a 12mm I.D. stainless steel tube which acts as a moving tunnel through which the fibres exit the column.

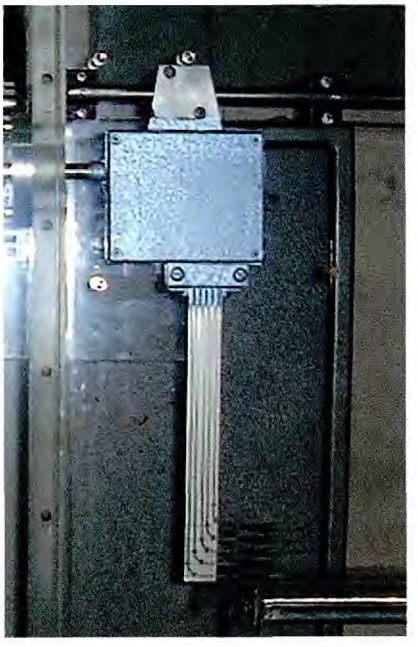


Figure 4.27. Five probes with the stainless steel plate clamped by an aluminium box

A special design of flange, illustrated in Figure 4.28 below, is used to allow the 12mm tube to move in and out of the column easily whilst, at the same time, a seal is maintained between the inside and outside of the CRODIS column. It involves a piece of hollow PTFE (shown in yellow) which is smaller than the space between the two flanges (shown in red). The PTFE spacer is drilled through at a size slightly larger than the outer diameter of the tube (15mm) so that the tube can pass through it easily. Because the tube is not perfectly straight (or align), when the tube moves, it may cause some sideways movement onto the PTFE spacer which is free to move within the flanges to avoid the possibility of excessive friction on the system.

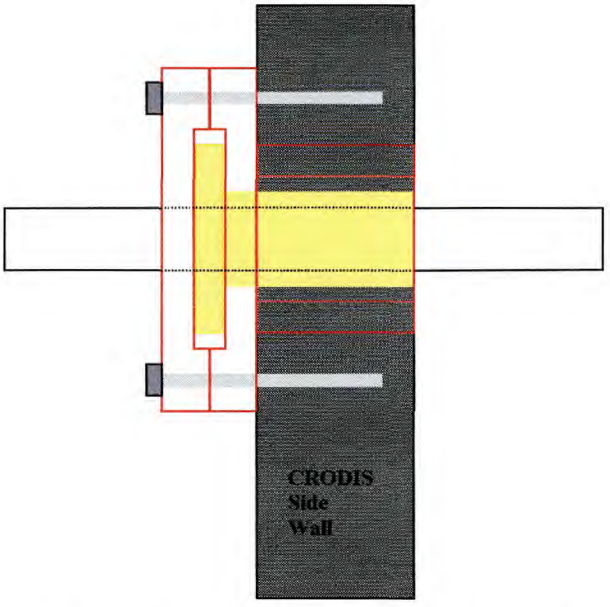


Figure 4.28. Special flange design for the moving stainless steel tube

Linear Shaft and Supporting Rail

The support system (whether it is internal or external) is based on a simple design of linear shaft with supporting rail and linear bush; these are shown in Figures 4.29, 4.30 and 4.31 respectively.

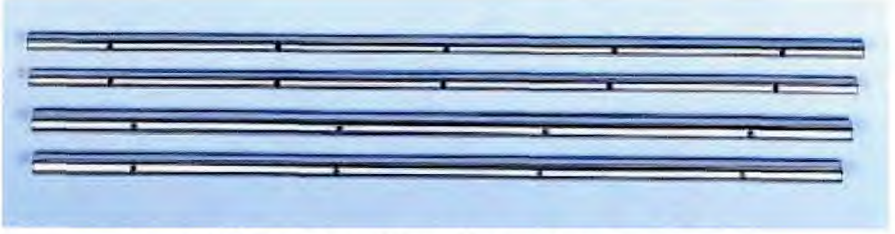


Figure 4.29. Pre-drilled linear shaft used for support system



Figure 4.30. Support rail for the linear shaft

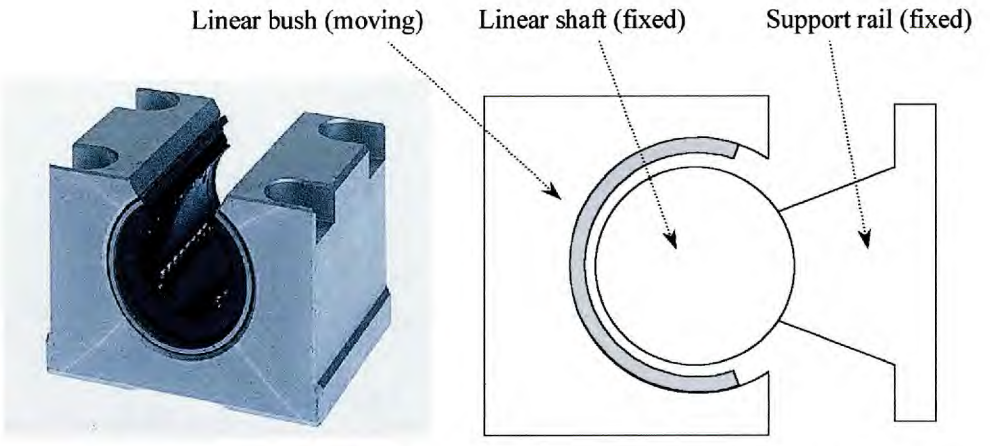


Figure 4.31. Waterproof linear bush and the assembly with the linear shaft and support rail

The system works as follows:

(1) Support rails (Figure 4.30) are attached to the back wall inside the CRODIS column and also to the Perspex plate extension outside the column. One such rail is fixed inside and two on the outside (see Figure 4.25).

(2) Pre-drilled linear shafts (Figure 4.29) are then screwed to the support rails with one such shaft inside and two such shafts outside the column (see Figure 4.25).

(3) The moving parts (i.e. the aluminium compartment (Figure 4.27) and the stainless steel tube) are then mounted onto the linear shafts by linear bushes as shown in Figure 4.31. The moving parts connected to such bushes are

(a) On the outside, the end of the stainless steel tube which is fixed to an aluminium plate which in turn is screwed to the bushes which run

along the two external linear shafts (see Figures 4.31 and 4.32). This unit is known as the "flying" unit later in this section.

(b) The aluminium probe box on the inside of the CRODIS column is attached to the inner linear shaft via a bush as shown in Figure 4.27.

It was found that this system worked very well. Trials were conducted in which the probes were moved by hand. Once trial had been successfully completed, the system was automated as described in the next section.

External Drive and Positioning System

The external actuation system (built on the added sheet of perspex) is illustrated in Figure 4.32 below.

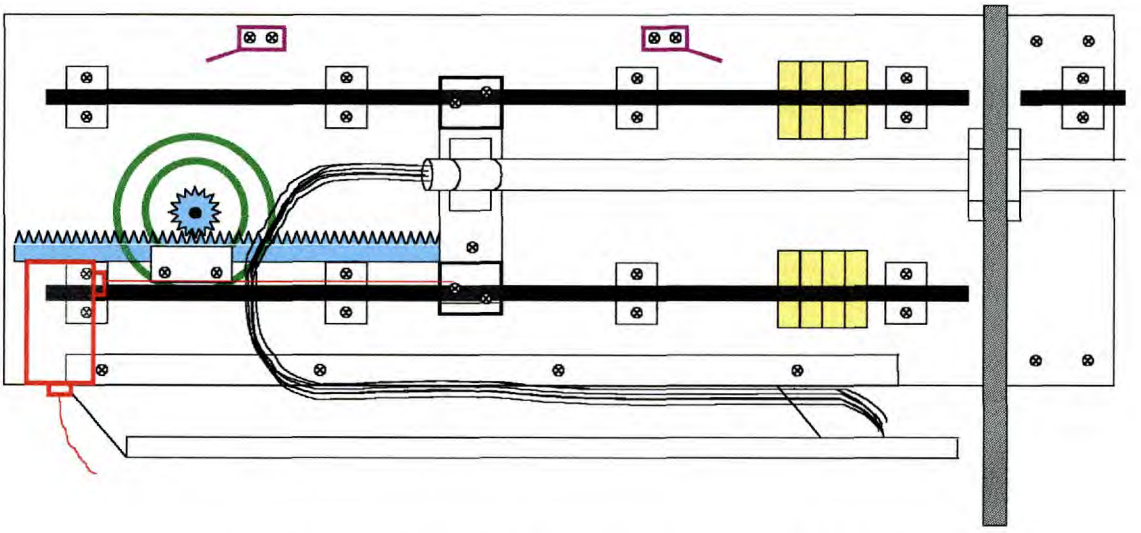


Figure 4.32. "Pinion and rack" motor-driven actuation mechanism

As was mentioned above, the stainless steel tube housing the optical fibres is fixed on a "flying" unit which consists of a thick sheet of aluminium plate attached to two linear bushes. A long PTFE rack (shown in blue) rests horizontally on the bottom bush and is screwed on the aluminium plate. This is used to drive the entire system and the driving force is provided by a gear motor (shown in green) with a pinion (shown in blue) attached to it. The gear motor is carefully selected so that the torque it generates can exceed the maximum friction in the system.

A position sensor is used to record the position of the "flying" unit and this is shown in red colour in Figure 4.32 and also in Figure 4.33(left). The sensor is a string-attached (maximum 1250mm) linear potentiometer, purchased from *Automation Sensors Measurement Ltd.* The device has an analogue synchronous serial output which allows easy data collection by a data acquisition card.



Figure 4.33. Front view (left) and side view (right) of the driving mechanism

The distance which the "flying" unit can travel is controlled by two control switches at the top of the perspex sheet. When the unit hits any one of the switches, it will stop regardless the direction it is travelling. The unit will only move again (in opposite direction) when it is manually restarted from the electronic control box. The system is arranged to travel at full speed in the forward direction (i.e. travelling upstream) and at much lower speed in the reverse direction (i.e. pulling back the unit and preparing for the next run). Although the control switches are used to stop the system, some household washing-up sponges are attached on the shafts to provide an effective way to decelerate the system without any damage. The deceleration mechanism is shown in Figure 4.34 below.



Figure 4.34. Forward control switch (left) and decelerating pads (right)

The Complete Mechanical System with Probes

The picture of the complete mechanical system with probes on the flying unit is shown in Figure 4.35 below. There are two heights of outlet weirs available for the experiments. For the higher outlet weir case, the measuring section is reduced because the flying unit can not be pulled back beyond the outlet downcomer whereas Figure 4.35 shows the lower weir case. The available travelling distances are 720mm and 650mm for the 8mm and 38mm weirs respectively.

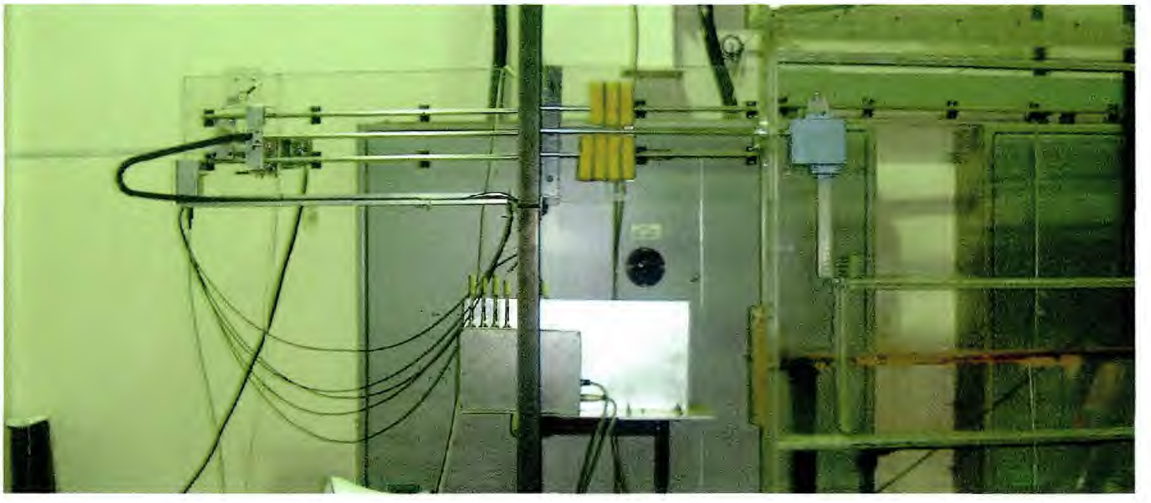


Figure 4.35. The Complete Flying Optical Probes System

4.3.5. The Electronics System

The associated electronics and control equipment for the flying optical probes system was constructed by the Electronics Workshop in the Department of Chemical Engineering and Chemical Technology at Imperial College. Figure 4.36 shows the electronic circuit for the optical probes. The circuit is a typical current/voltage amplifier which takes the signals current from the photodiode receiver (top left corner in Figure 4.36). The signals are then passed through the "Offset" and "Gain" sections where the two potential meters are used to calibrate the five probes so that the current is converted into an appropriate range of voltage (±5 volts) which is then fed into a data acquisition card.

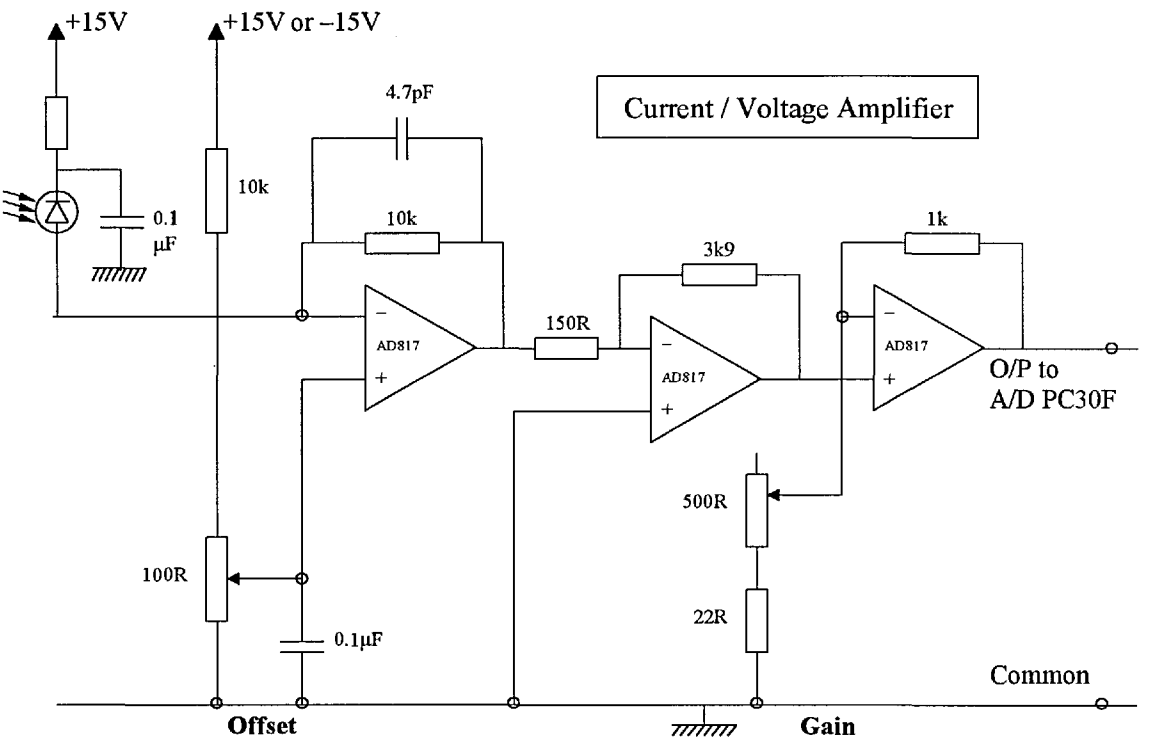


Figure 4.36. Electronic circuit for the optical probes

In the present study, an Intel Pentium III-550MHz with 64MB RAM computer from *Viglen Ltd* is used to accommodate the data acquisition card which is a 16-channel, 330kHz analogue and digital I/O board (made by *Eagle Technology Ltd*). A commercial software package, HPVEE (version 5.0), was installed to provide a user-friendly interface between the signals (from the electronic circuit) and the final results (in a format to be further processed in Microsoft Excel™). Six channels on the card are used

for the system: one for each of the five probes and one for the position sensor. The data collection frequency has been set at 5kHz for each channel and this means that over a period of 2 seconds of measurement, a total of 60000 points of data are recorded into the computer.

4.4. Experiments and Probes Signal Processing

The experimental procedures for operating the CRODIS facility have been described previously in Chapter 3. While the air and water are in contact, the optical probes unit travels in the opposite direction to the liquid flow path. This provides a quick scan of the froth structure. For each combination of liquid and gas flowrates, such a scan was repeated for twenty times in order to obtain representative results compared to the real situation. There are twelve combinations of flowrates, two types of sieve trays (1.8mm and 6mm hole sizes) and two different height of outlet weir. These conditions are indicated by a simple name in the experiments and this is explained in Table 4.3 below.

Name	Gas Flowrate u_s (m^3/s)	Liquid Flowrate Q_L (l/min)
Test1	0.73	8.12
Test2	1.18	8.12
Test3	1.39	8.12
Test4	1.50	8.12
Test5	0.73	6.3
Test6	1.18	6.3
Test7	1.39	6.3
Test8	1.50	6.3
Test9	0.73	10
Test10	1.18	10
Test11	1.39	10
Test12	1.50	10

Name	Hole Size
h1.8	1.8 mm
h6	6.0 mm

Name	Weir Height
w8	8 mm
w38	38 mm

Example
"h1.8_w8_test1" represents
1.8mm hole, 8mm weir,
$u_s = 0.73$, $Q_L = 8.12$

Table 4.3. Combinations of gas and liquid flowrates in the experiments

Twenty runs were taken for each of the conditions listed in Table 4.3 and the data from the twenty runs were collected together for further processing as described in the following sections.

4.4.1. Experimental Raw Data

Figure 4.37 shows a typical result for a probe obtained from a single run and of course, there are four other sets of signals for the other four probes. The blue dots represent data points collected from the optical probe while the pink line (which actually consists of data points, too) shows the data obtained from the position sensor.

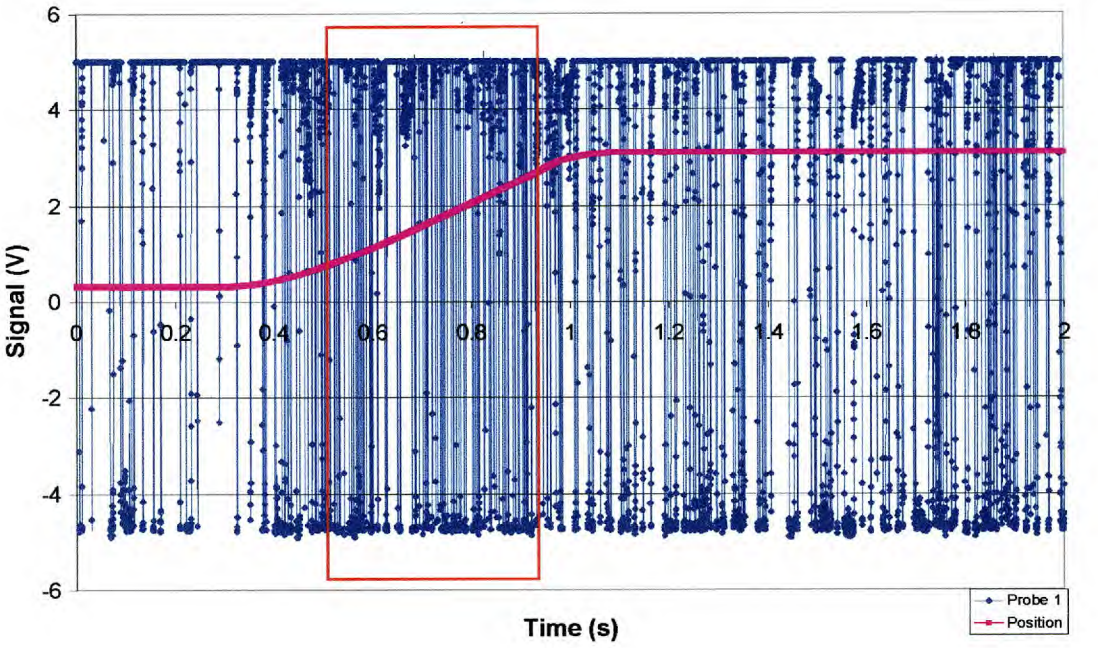


Figure 4.37. Signal profiles for Probe 1 and position (one scan), taken from Run1 of "h1.8_w8_test1"

Because the position sensor is a simple linear potential meter, the signal profile received from it is similar to a typical "distance-time" plot where the gradient of the line represents the "velocity". The red box in Figure 4.37 highlights the part where such a gradient is constant, i.e. the velocity is constant. According to the theory of the flying optical probes system described in Section 4.3.1, this is the "useful" part of the data points collected and the detailed profiles in this range are re-plotted in Figure 4.38 below.

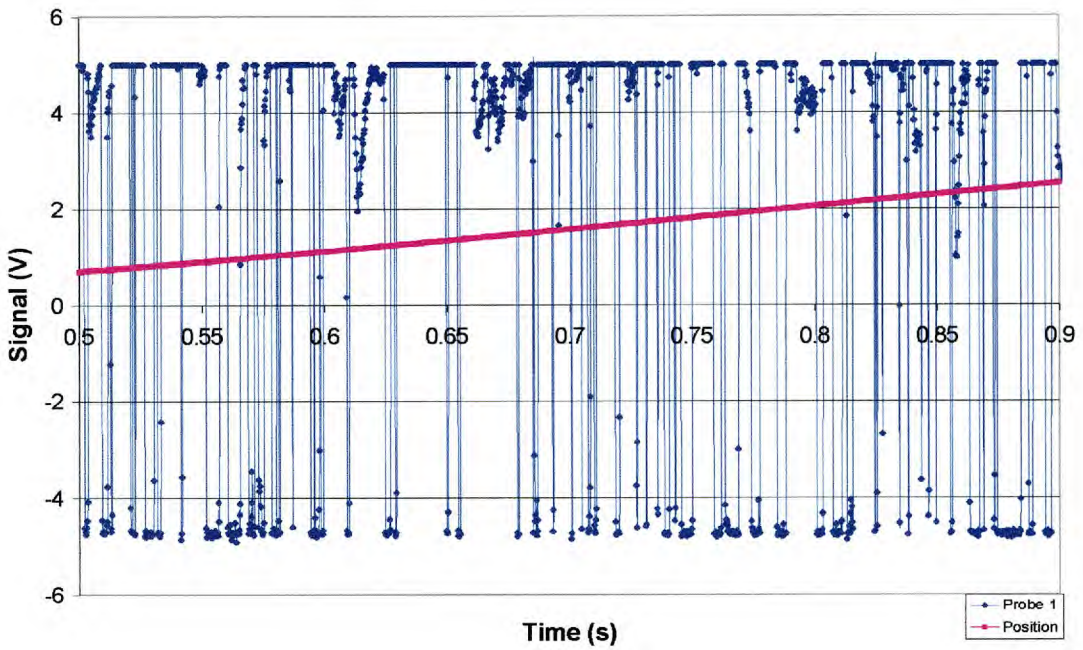


Figure 4.38. The "useful" part of the full signal profile (red box in Figure 4.37)

The voltages recorded (for the position sensor) at start and end positions (in Figure 4.37) of the flying unit are taken as the reference points on calculating the velocity in Figure 4.38. The calculated velocity varies slightly from one run to another but it stays in the range of 1.1-1.2 m/s. The next step is to apply this velocity to determine the chord length which the probes have penetrated (both in gas and liquid phases) in each run.

4.4.2. Chord Length Distributions

Signal profiles such as Figure 4.38 provide the information on where (in gas or in liquid) the probe is and for how long (penetration time) it stayed there. These can be easily converted to penetration chord length for both gas and liquid by multiplying together the penetration time and the probe velocity. Because the size of the probe tip (400μm) and also taking some considerations for the actual flow conditions, it was decided that any gas chord length less than 3mm and liquid chord length less than 2mm will be discarded. The limiting values are different for gas and liquid phase because the fact that the penetration time for a probe into a bubble (or gas phase) is considerably longer than into a droplet (or liquid phase).

The chord length results from twenty runs are collected together and they are separated into several size groups. There are seven groups ranging from 3mm to 25±1mm (equal division) for the gas chord length and six groups ranging from 2mm to 20±1mm (equal division) for liquid chord length. The actual upper limit of the chord length chosen does vary slightly, mainly to promote convergence of data conversion procedure described in the next section, however, the difference is small enough (i.e. ±1mm) so that each size group remains literally identical between different sets of experiments. Figures 4.39 and 4.40 below are examples for one set of conditions.

Group	Gas Phase Size (mm)	Liquid Phase (mm)
1	2.00 – 5.29	3.00 – 5.83
2	5.29 – 8.57	5.83 – 8.67
3	8.57 – 11.86	8.67 – 11.50
4	11.86 – 15.14	11.50 – 14.33
5	15.14 – 18.43	14.33 – 17.17
6	18.43 – 21.71	17.17 – 20.00
7	21.71 – 25.00	N/A

Table 4.4. Information on group sizes used in the data interpretation

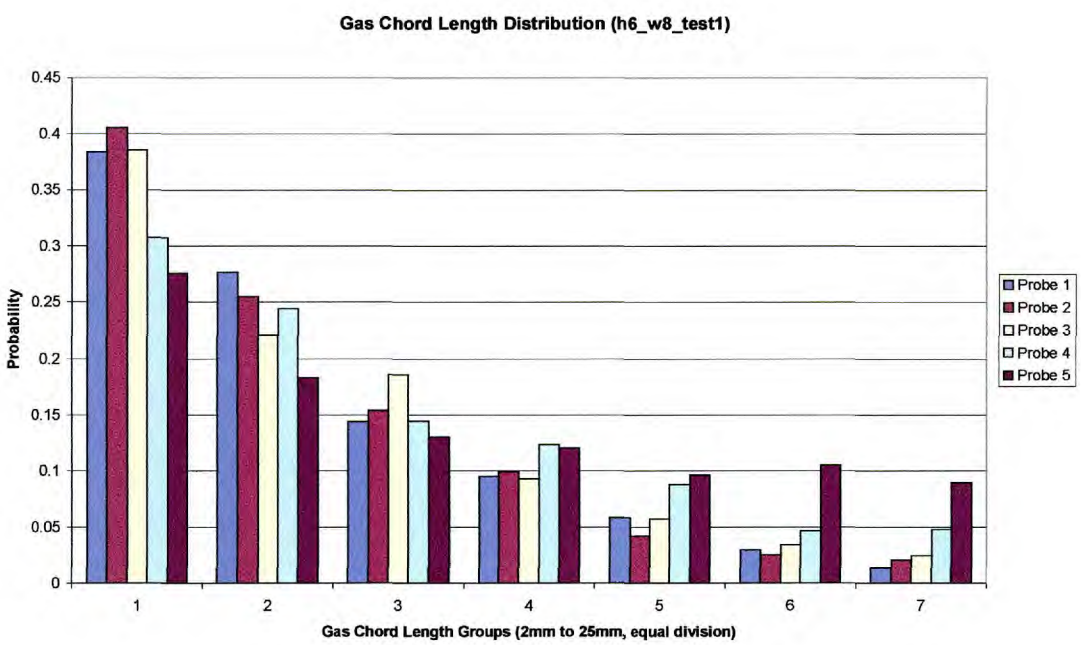


Figure 4.39. Gas chord length distribution for the condition of "h6_w8_test1"

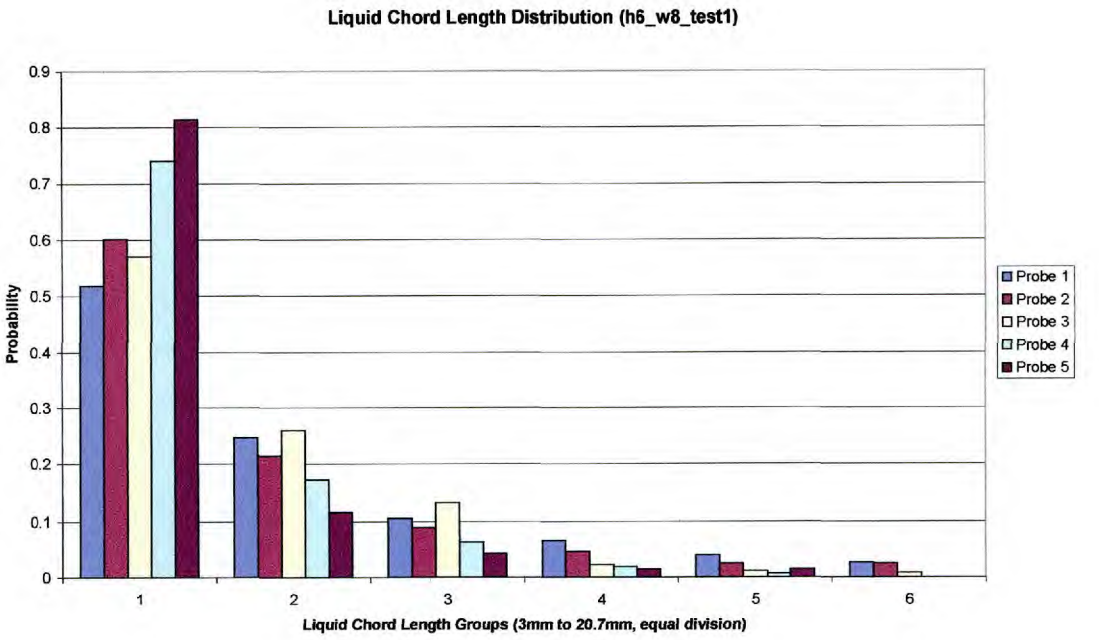


Figure 4.40. Liquid chord length distribution for the condition of "h6_w8_test1"

It must be stressed that the chord length obtained according to the procedures in Section 4.4.2 is only an "apparent" chord length, i.e. there is a difference between the "actual chord length" which the probe "penetrates" and the "apparent chord length" which the probe "sees" a bubble or droplet. As previously mentioned in Section 4.3.1, the horizontal component velocity of the bubbles and droplets are relatively small compared to the speed at which the probes are travelling. However, the fact is that most bubbles and droplets do have a vertical velocity component and one might question how the "apparent" chord length analysis relates to the real situation.

Generally speaking, the froth body consists of irregular shapes and sizes of bubbles, droplets, gas voids and liquid lumps and these structures are constantly in the process of coalescence and break-up. In order to obtain results for phase element (bubble or drop) size from the chord length distribution, it is necessary to pre-assume a structure of the froth prior to analysing the signals. In the present study, it has been assumed that the froth only consists of spherical bubbles and droplets of various sizes. The irregularity of any gas and liquid (e.g. gas voids and liquid lumps) content in the real froth can be approximated by the agglomerate of bubbles and droplets. Figure 4.41 provides a detailed illustration for this postulate. The interstices between the "bubbles" and "drops" are assumed to be filled with smaller drops or bubbles. This formal description

of the structure allows interesting information to be generated without having to make a decision on whether the particular region is gas-continuous or liquid-continuous.

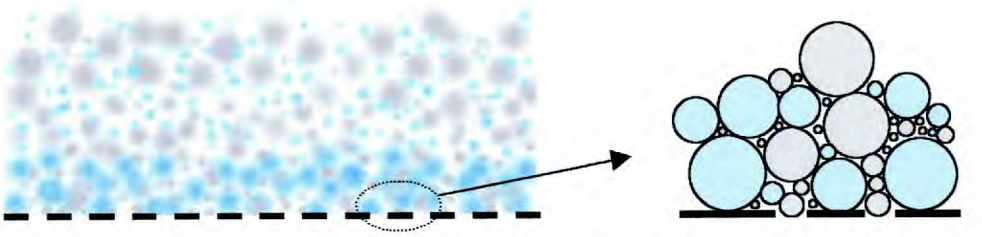


Figure 4.41. Pre-assumed froth structure for data interpretation (grey represents gas, blue represents liquid and imagine the white areas filled up by smaller gas and liquid elements).

Imagine a probe coming in contact (at a speed, v_p) with a vertically rising bubble (at a speed, v_b), as shown in Figure 4.42 below (the same analysis also applies to a droplet).

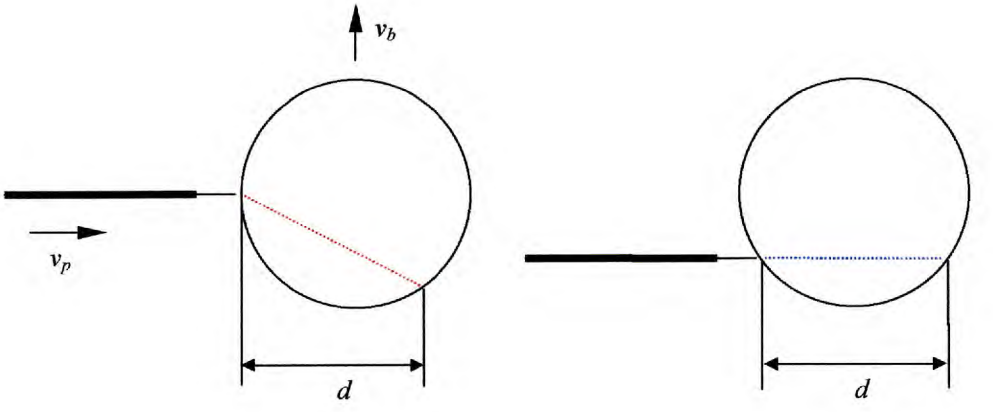


Figure 4.42. A probe penetrates a spherical bubble

The actual path for which the probe penetrates a bubble is given by the red dotted line in Figure 4.42 while the "apparent" path, which the probe "sees", is shown in blue. The action of a moving probe hitting a rising bubble can be re-interpreted as the action of a moving probe hitting a stationary bubble at a different location. The probe may attack from any point on the left surface and the bubble being penetrated can travel at any velocity. The combination of the above two events is completely random but if a large amount of data is collected, the whole range of the possible chord lengths of a bubble can be covered, i.e. as shown in Figure 4.43 below.

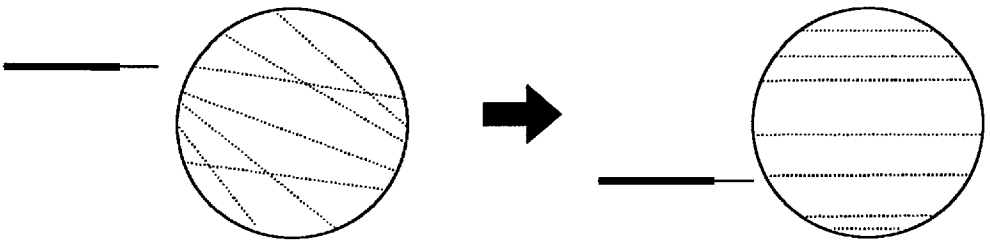


Figure 4.43. "Actual" vs. "Apparent" penetration path

There are two extreme cases where the above method may become invalid:

1. When a bubble or droplet travels (upwards) at a speed much faster than the speed of the flying unit.
2. When a bubble or droplet does have a significant horizontal velocity component and travels in opposite direction to the movement of the probe.

Both of these cases would generate small chord length data. However, the treatment of filtering out small chord lengths (less than 2mm for gas, less than 3mm for liquid) will minimise the effect of data from these two cases to be counted towards the final distribution.

4.4.3. Bubble / Droplet Size Distributions

In any single-probe measurement in a multiphase flow system, the probe generally intersects a bubble (or droplet) with a chord length other than the largest chord length of the bubble (or droplet). The matter is further complicated by the fact that there is a distribution of bubble sizes in most systems, e.g. in the two-phase flows occurring on a distillation tray. Moreover, a chord length distribution alone, such as the ones given in the previous section, does not provide sufficient information on the froth structure.

Clark and Turton (1988) established a theoretical method of converting a chord length distribution to a bubble size distribution for a pre-assumed shape of the bubble (e.g. spherical). Their theory began with defining the probability density function for the distance between bubble centres and the probe tip is in direct proportion to the distance *r*, i.e. as shown in Figure 4.44 below.

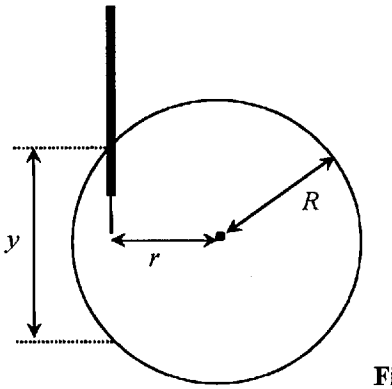


Figure 4.44. A probe intersecting a bubble

The expression for such a probability density function was given as:

$$P(r|R) = ar \qquad \text{for} \qquad 0 \le r \le R \tag{4.3}$$

$$P(r|R) = 0 \qquad \text{otherwise} \tag{4.4}$$

where a depends on the shape of the bubble ($a = 2/R^2$ for a spherical bubble with radius, R). Assuming the shape of the bubble can be represented by a sphere, it is possible to determine the probability density function which describes the likelihood of finding a chord length y for a specified bubble size R :

$$\begin{aligned} P(y|R) &= P(r|R)\left|\frac{dr}{dy}\right| \\ &= \frac{y}{2R^2} \end{aligned} \tag{4.5}$$

The next step is to include into consideration the full spectrum of bubble sizes which may touch the probe. This spectrum can be described by another probability density function $P(R)$. Thus, considering the whole distribution, the probability that a bubble of size R will intersect the probe with a chord length y is given as:

$$P(y, R) = P(y|R)\,P(R) \tag{4.6}$$

Therefore, the probability of measuring a particular chord length y for any bubble size R in the system is given as:

$$P(y) = \int_{R_{min}}^{R_{max}} P(y, R)\, dR = \int_{R_{min}}^{R_{max}} P(y|R)\, P(R) \tag{4.7}$$

In real experiments, it is required to apply the above theory in the reverse order, i.e. knowing $P(y)$ from experimental results and working backwards to obtain $P(R)$.

Consider a set of data consisting of n observations of chord lengths y. Let us divide the chord lengths into m equal length partitions between two limiting chord lengths (y_{max} and y_{min}) such that

$$y_i = y_{max} - i\,\Delta R, \qquad 0 \le i \le m \tag{4.8}$$

where

$$\Delta y = (y_{max} - y_{min})/m \tag{4.9}$$

and

$$y_0 = y_{max}, \quad y_m = y_{min}$$

An approximation to the probability of finding a chord length y between y_i and y_{i+1}, $W(y_{i+1} < y < y_i)$, is given by

$$W(y_{i+1} < y < y_i) = \frac{\text{Number of observations of chord lengths between } y_i \text{ and } y_{i+1}}{\text{Total number of observations, } n}$$

From Eq.(4.7), the following expression can be derived

$$\begin{aligned} W(y_{i+1} < y < y_i) &= \int_{y_{i+1}}^{y_i} P(y)dy = \int_{y_{i+1}}^{y_i} \int_{R_{min}}^{R_{max}} P(y|R)P(R)dR\,dy \\ &= \int_{y_{i+1}}^{y_i} \left[\begin{array}{l} \int_{R_{min}}^{R_{m-1}} P(y|R)P(R)dR + \int_{R_{m-1}}^{R_{m-2}} P(y|R)P(R)dR + \cdots \\ + \int_{R_1}^{R_0} P(y|R)P(R)dR \end{array} \right] dy \\ &\cong \int_{y_{i+1}}^{y_i} \sum_{j=0}^{m-1} P(y|R_j)P_j(R_j)\Delta R\, dy \\ &\cong \sum_{j=0}^{m-1} \int_{y_{i+1}}^{y_i} P(y|R_j)\, dy\, P_j(R_j)\Delta R \end{aligned} \tag{4.10}$$

where $R_j = R_{\max} - j\Delta R, \qquad 0 \le j \le m$ (4.11)

with $\Delta R = \dfrac{R_{\max} - R_{\min}}{m}$, $R_0 = R_{\max}$, $R_m = R_{\min}$ (4.12)

and $P_j(R_j)$ is the probability of finding a bubble with a radius between R_i and R_{i+1}.

Eq.(4.10) can be further simplified and written as

$$W_i = W(y_{i+1} < y \le y_i) \cong \sum_{j=0}^{m-1} C_{i,j} P_j(R_j) \Delta R \tag{4.13}$$

where $C_{i,j} = \int_{y_{i+1}}^{y_i} P(y|R_j)\, dy$ (4.14)

In the present work, the shape of the bubble is assumed to be spherical and Eq.(4.13) can be written as

$$C_{i,j} = \int_{y_{i+1}}^{y_i} \frac{y}{2R_j^2}\, dy = \left[\frac{y^2}{4R_j^2}\right]_{y_{i+1}}^{y_i} = \frac{y_i^2 - y_{i+1}^2}{4R_j^2} \tag{4.15}$$

$C_{i,j}$ has a value of zero when $i < j$, i.e. a chord length y_i can only come from a bubble of radius R_i or greater (R_{i-1}, R_{i-2}, ...etc). Thus, by combining Eqs.(4.10) and (4.15), a triangular matrix of the following form can be constructed:

$$\begin{aligned}
W_0 &= C_{0,0} P_0(R_0) \Delta R \\
W_1 &= C_{1,0} P_0(R_0) \Delta R + C_{1,1} P_1(R_0) \Delta R \\
&\vdots \\
W_{m-1} &= C_{m-1,0} P_0(R_0) \Delta R + C_{m-1,1} P_1(R_1) \Delta R + \cdots + C_{m-1,m-1} P_{m-1}(R_{m-1}) \Delta R
\end{aligned} \tag{4.16}$$

Experimental results (e.g. Figures 4.39 and 4.40) provide information on W_i's in Eq.(4.16) and the final results on the size distribution $P_j(R_j)$'s can therefore be sequentially calculated.

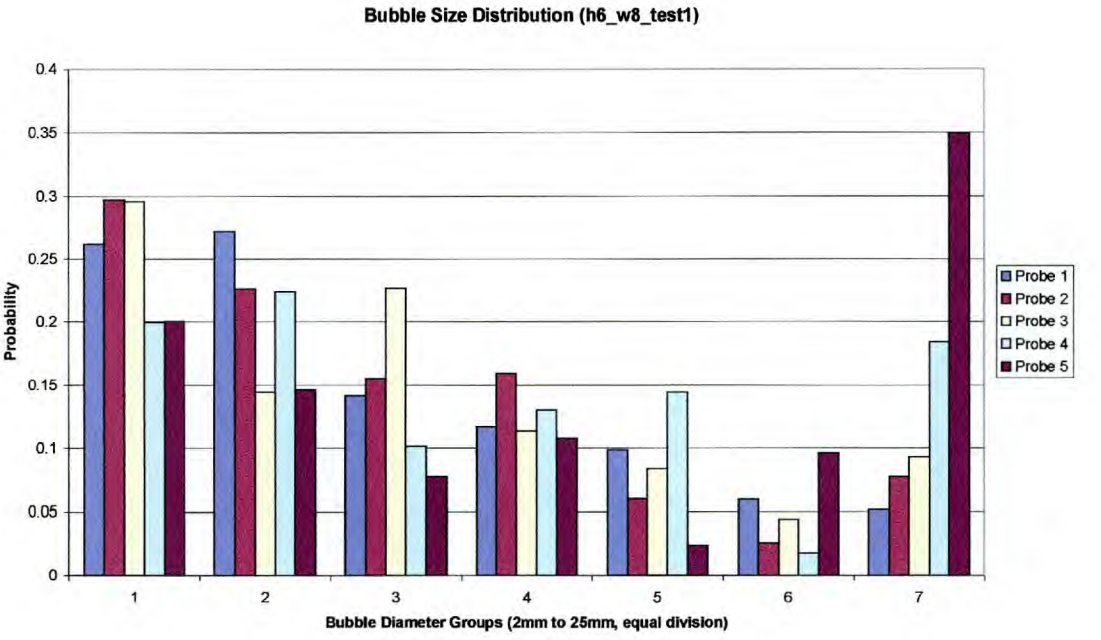


Figure 4.45. Conversion from Figure 4.39 into bubble size distribution (h6_w8_test1)

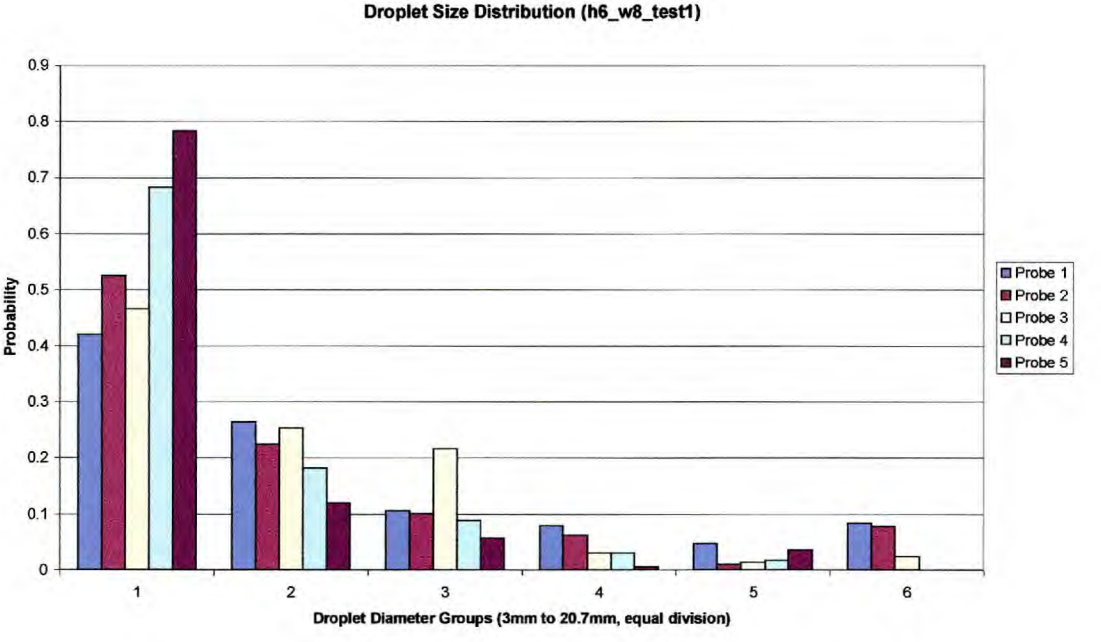


Figure 4.46. Conversion from Figure 4.40 into droplet size distribution (h6_w8_test1)

All the above-mentioned procedures on signal processing and data interpretation have been built into a Visual Basic program in Microsoft Excel™. A copy of the codes is given in Appendix D.

4.5. Results Analysis and Discussions

Results on chord length distributions (e.g. Figures 4.39 and 4.40) and on bubble/droplet size distributions (e.g. Figures 4.45 and 4.46) have been obtained over the whole range of experimental conditions stated in Section 4.4. These data have successfully revealed the structure of the tray flows and the graphical results are stored separately in the supplementary CD-ROM attached on this thesis.

When analysing the enormous amount of data contained in the CD-ROM, the following criteria are considered:

1. The changes in results due to the changes in flowrates are expected to be gradual, e.g. the results from a "Test 2" condition are usually quite similar to those from a "Test 3" condition. The two sets of flowrates which would display the most significantly different results are "Test 8" and "Test 9" where the conditions are closer to the froth and spray regime respectively.
2. The effects of changing tray configurations and flow regimes on the size distributions should be noted.
3. The use of mean bubble and droplet size instead of the actual distributions can be helpful.

4.5.1. The Effect of Flow Regimes on Distribution Results

Figure 4.47 below shows the chord length and bubble size distributions for a froth flow condition. Here, the gas chord length distributions for all five probes are nearly identical. This suggests that the froth remain more or less the same structure, at least up to the level of Probe 5. The resultant bubble size distribution clearly shows that larger bubbles (e.g. Group 6 and 7) were detected more frequently from higher position probes (e.g. Probes 4 and 5) than lowers ones (e.g. Probes 1 and 2). This agrees well to the actual physical situation.

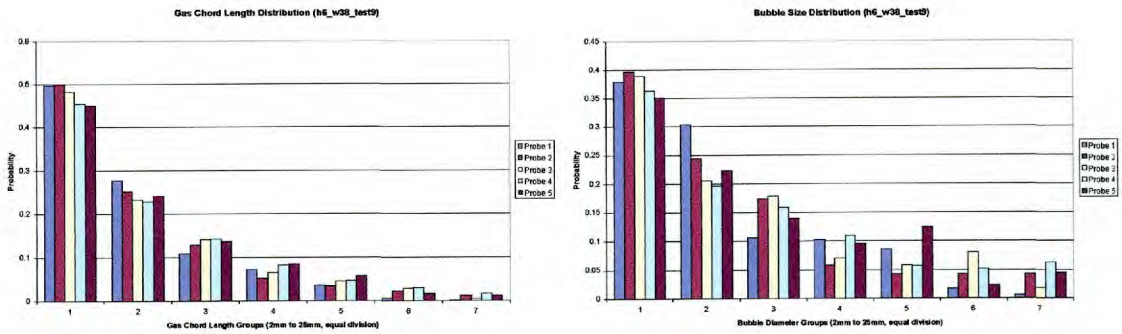


Figure 4.47. Gas chord length and bubble size distribution for "h6_w38_test9" experiment

Figure 4.48 below shows the chord length and bubble size distributions under a spray condition. Here, there are significant differences between the chord length distributions obtained from each probe, especially in the larger chord length groups. The effect of changing the flow regime from froth to spray on the bubble size distribution is that the chances of finding bubbles in larger sizes groups actually increases at all levels (of probes).

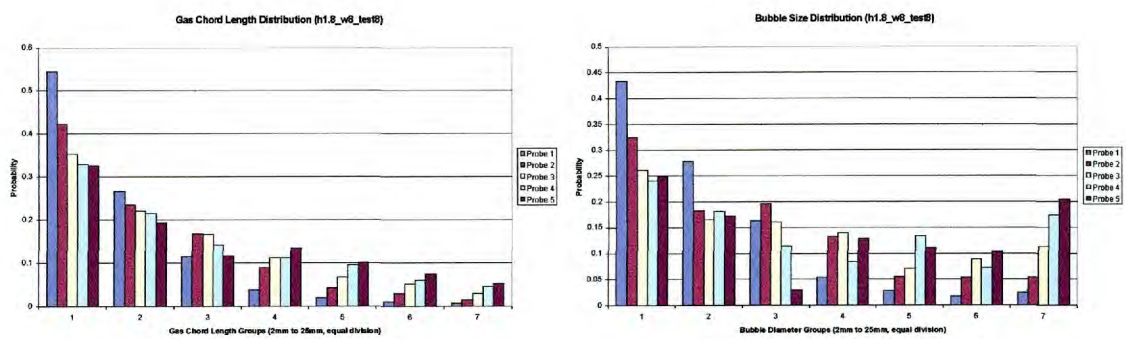


Figure 4.48. Gas chord length and bubble size distribution for "h1.8_w8_test8" experiment

The liquid phase distribution results are given in Figures 4.49 and 4.50 below. The effect of changing the flow regime from froth to spray on the droplet size distribution is that the chances of finding droplets in larger sizes groups actually decreases at all levels (of probes). This is in-line with expectation.

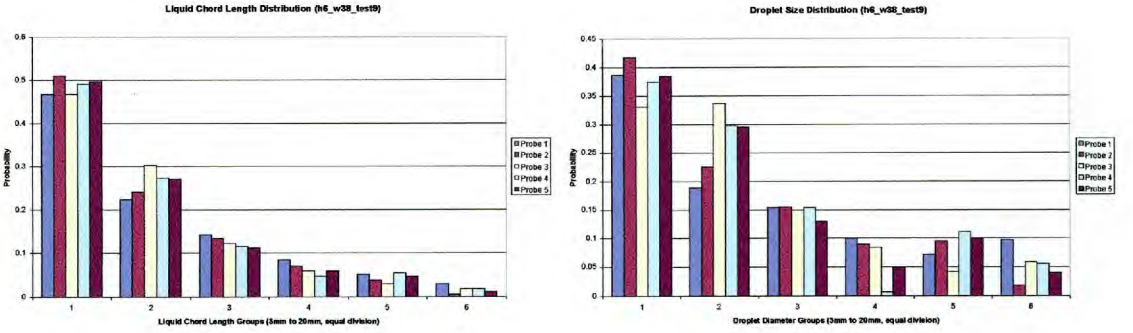


Figure 4.49. Liquid chord length and droplet size distribution for "h6_w38_test9" experiment

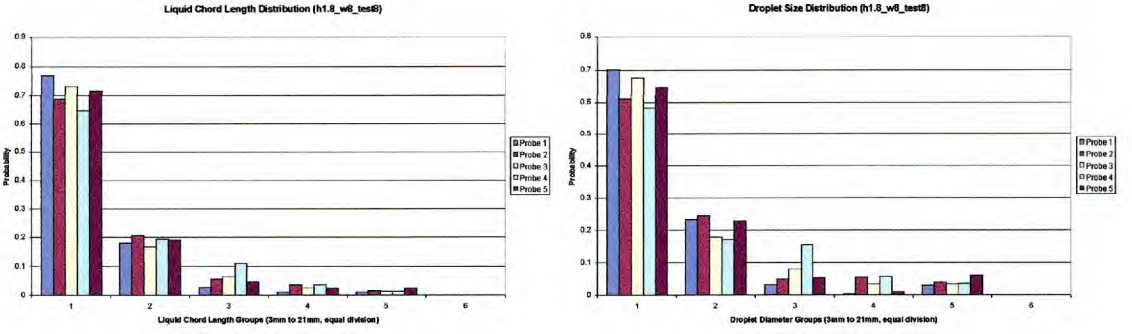


Figure 4.50. Liquid chord length and droplet size distribution for "h1.8_w8_test8" experiment

4.5.2. Sauter Mean Size Distributions

The bubble/droplet size distributions tell us a lot of important information about the two-phase structure, perhaps too much to examine at once. Thus, the graphical results such as Figures 4.45 and 4.46 may not always be the most appropriate format when trying to study the results.

A standard practice in dealing with statistical data is to use some kind of mean values to represent the whole range of data. As mentioned in Chapter 3, the Sauter mean diameter is a very helpful parameter in characterising the froth structure. The definition of the Sauter mean diameter is given as follows:

$$D_{32} = \frac{\int_0^{D_{\max}} D^3 n(D) dD}{\int_0^{D_{\max}} D^2 n(D) dD} \approx \frac{\sum_i D_i^3 n(D_i)}{\sum_i D_i^2 n(D_i)} \tag{4.17}$$

where $n(D)$ is the number of bubbles (or drops) of size D.

Results from the bubble/droplet size distributions have been further computed using Eq.(4.17) to obtain the Sauter mean bubble/droplet diameter for each probe. Figures 4.51 to 4.54 show the Sauter mean bubble/droplet diameters for all five probes and four tray configuration under "Test 8" and "Test 9" flow conditions. Results under other flow conditions are also given in the attached CD-ROM.

General observations from Figures 4.51 and 4.53 (Sauter mean bubble diameter):

1. As expected, the measured Sauter mean bubble diameter increases from Probe 1 to Probe 5 in both figures, regardless the tray configurations.
2. Consistent increases in the mean bubble size are seen on all probes under all tray configurations when the flow regime shifts from a more froth-like case (Test 9) to a more spray-like one (Test 8).
3. A larger-hole tray promotes bigger bubble diameter. This is clearly observed from all five probes in every case.
4. A higher outlet weir reduces the mean bubble size. Although this phenomenon is observed on all cases, the effect is shown more strongly in the small-hole tray than the large-hole one.

General observations from Figures 4.52 and 4.54 (Sauter mean droplet diameter):

1. The variation of the droplet sizes obtained from the five probes is not clearly seen but three out of the four tray configuration cases (except the case "h1.8_w8") show a decreasing trend in droplet size from Probe 1 to Probe 5.
2. There seems to be no obvious trends for the mean droplet diameter profiles in spray-like experiments.
3. In the froth-like experiments (Test 9, Figure 4.54), an increase on both the hole size and the outlet weir seems to enlarge the mean droplet size, however, this phenomenon is not as clear as the bubble case.

Sauter mean bubble diameter (mm)

	h1.8_w8	h1.8_w38	h6_w8	h6_w38
Probe 1	13.57	10.61	14.95	12.86
Probe 2	16.07	13.43	16.27	13.88
Probe 3	17.97	15.50	18.14	17.26
Probe 4	19.11	16.68	19.23	16.92
Probe 5	19.70	17.89	20.13	18.32

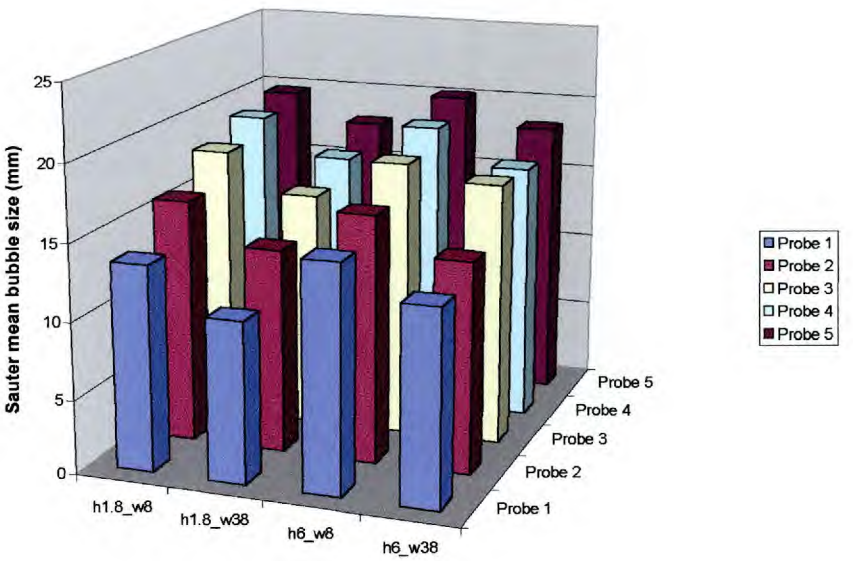


Figure 4.51. Sauter mean bubble diameter for Test 8

Sauter mean droplet diameter (mm)

	h1.8_w8	h1.8_w38	h6_w8	h6_w38
Probe 1	8.22	10.82	10.84	10.39
Probe 2	9.60	10.02	9.35	11.10
Probe 3	9.21	9.12	11.75	9.28
Probe 4	9.84	9.35	11.57	9.77
Probe 5	9.78	9.95	8.19	10.29

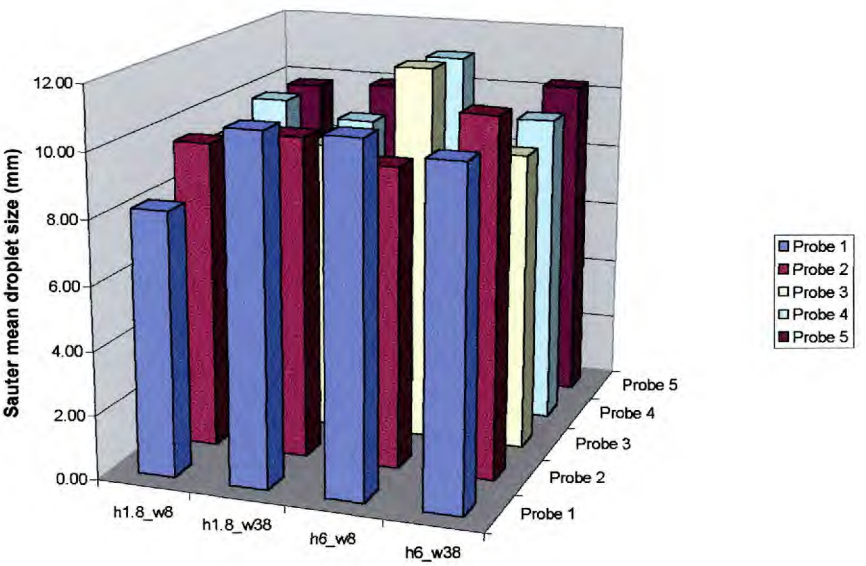


Figure 4.52. Sauter mean droplet diameter for Test 8

Sauter mean bubble diameter (mm)

	h1.8_w8	h1.8_w38	h6_w8	h6_w38
Probe 1	12.77	9.45	14.27	13.22
Probe 2	15.59	11.24	15.14	15.45
Probe 3	16.57	13.29	16.61	15.29
Probe 4	17.41	13.86	17.92	16.49
Probe 5	17.10	16.23	20.03	15.66

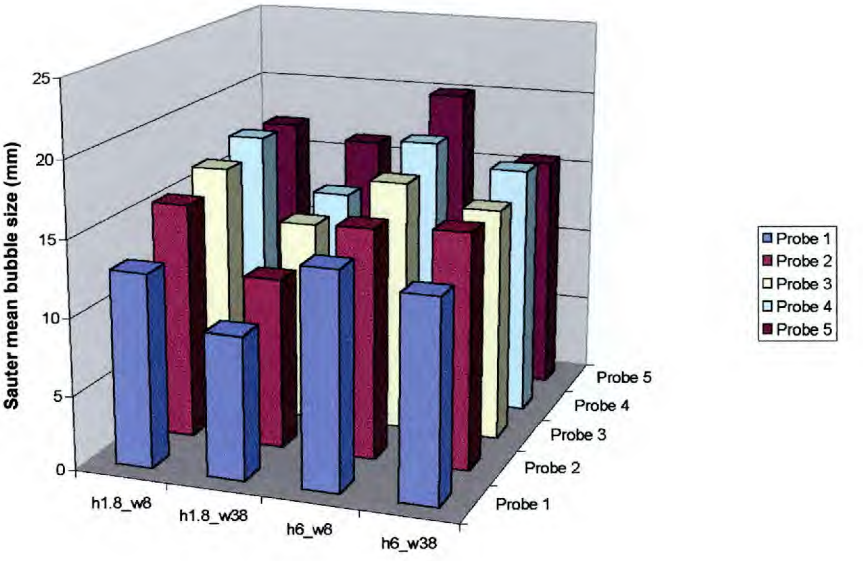


Figure 4.53. Sauter mean bubble diameter for Test 9

Sauter mean droplet diameter (mm)

	h1.8_w8	h1.8_w38	h6_w8	h6_w38
Probe 1	9.27	11.52	10.98	13.66
Probe 2	9.76	12.46	11.44	11.93
Probe 3	8.74	11.40	10.49	12.25
Probe 4	10.99	11.03	10.37	12.81
Probe 5	10.57	10.53	9.11	12.45

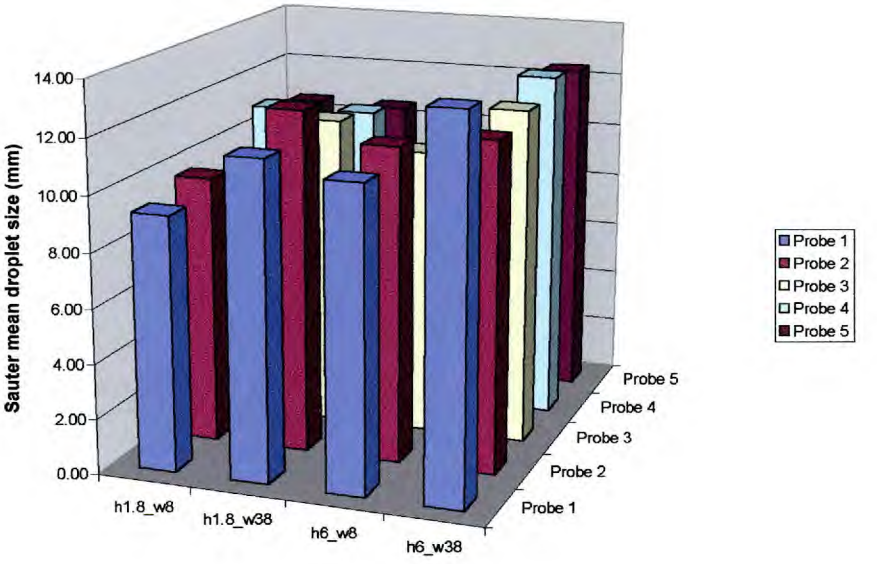


Figure 4.54. Sauter mean droplet diameter for Test 9

4.5.3. Limitations on the Clark & Turton's (1988) Method

Although the Clark and Turton's (1988) conversion method (from chord length to bubble size distributions) seems to have produced some highly sensible results, there are still a number of limitations. In the present work, there are 7 groups for bubble sizes and 6 groups for droplet sizes. Clark and Turton (1988, 1989) reported that the conversion process could become unstable if too many divisions or too few chord length measurements were taken. This would, in the extreme case, generate even negative probabilities. This is also why the upper limit of the chord length (mentioned earlier in Section 4.4.2) sometimes needed to be changed slightly so that the calculation process remained stable.

4.5.4. Multiple Region Experiment

All the chord length distribution results included so far are independent of the locations where they were collected, i.e. this is the same as assuming that the whole froth body can be described by only one set of bubble/droplet distribution. In reality, this may not be the case because some operational phenomenon can affect the local distributions. Some examples of these include: inlet/outlet calming zones, vapour cross-flow phenomenon, liquid inlet, preferential bubbling due to hydraulic gradient,....etc.

Hence, the flying optical probe technique can be extended further to account for "different regions" on a tray. The way to implement this is to divide the useful signal (the red box in Figure 4.37) into a few regions and then process the data individually in each region following exactly the same procedure. An example of this was carried out for the case of "h6_w8_test4" where the data were split into two equal-size regions. The results are given in Figures 4.55 and 4.56 below. Due to the limitations described in Section 4.5.3, the number of divisions used in the data conversion was reduced for both phases, i.e. 6 groups for gas and 5 groups for liquid.

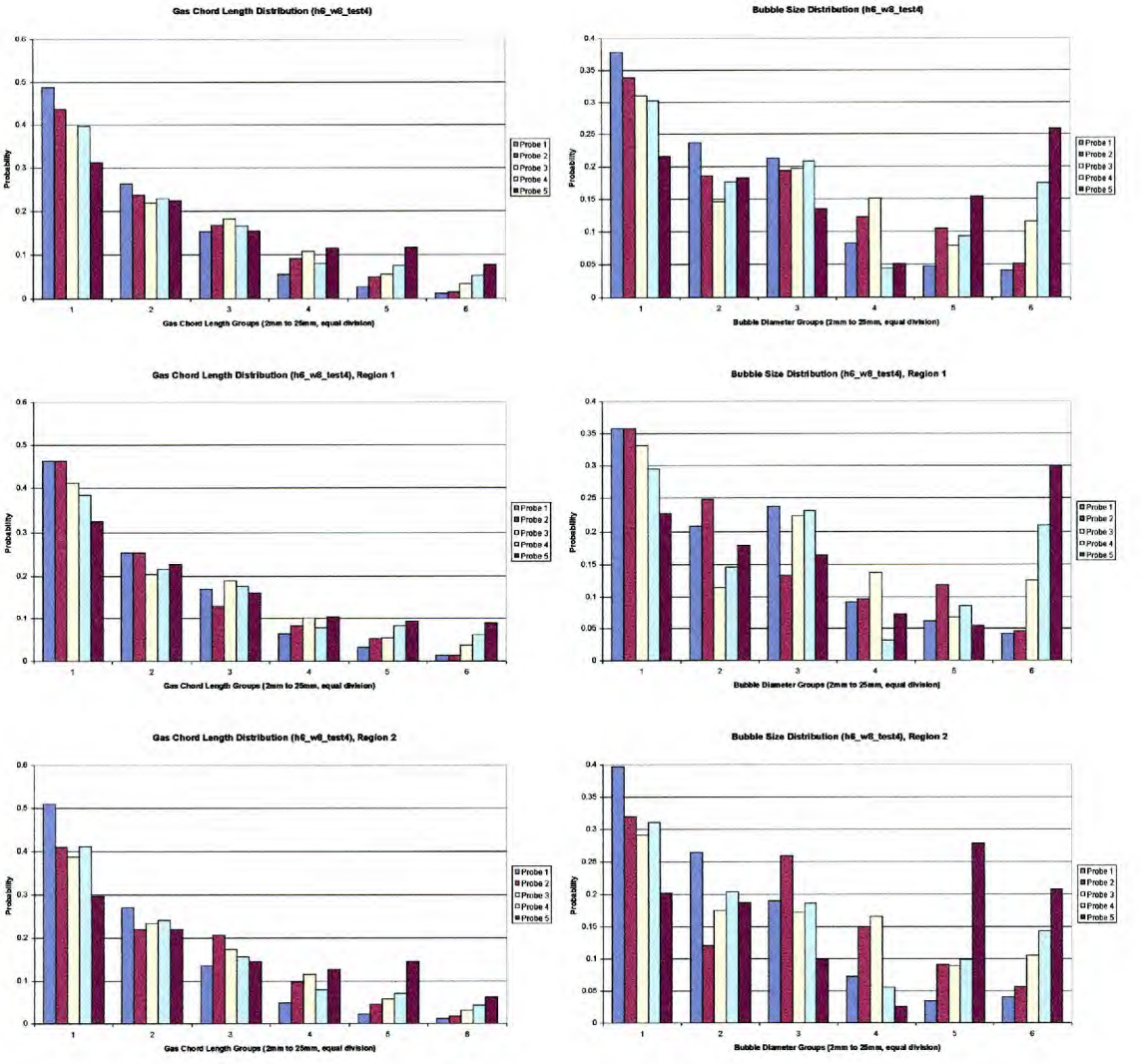


Figure 4.55. A "two-region" signal processing example with the gas phase results

Here, the gas phase results from each of the two regions are not very much different from the results obtained for one region, except for the large bubble size groups. In "Region 1", which is upstream near to the inlet downcomer, there seem to be more large bubbles whereas in "Region 2", the large bubbles may have been broken-up into slightly smaller ones.

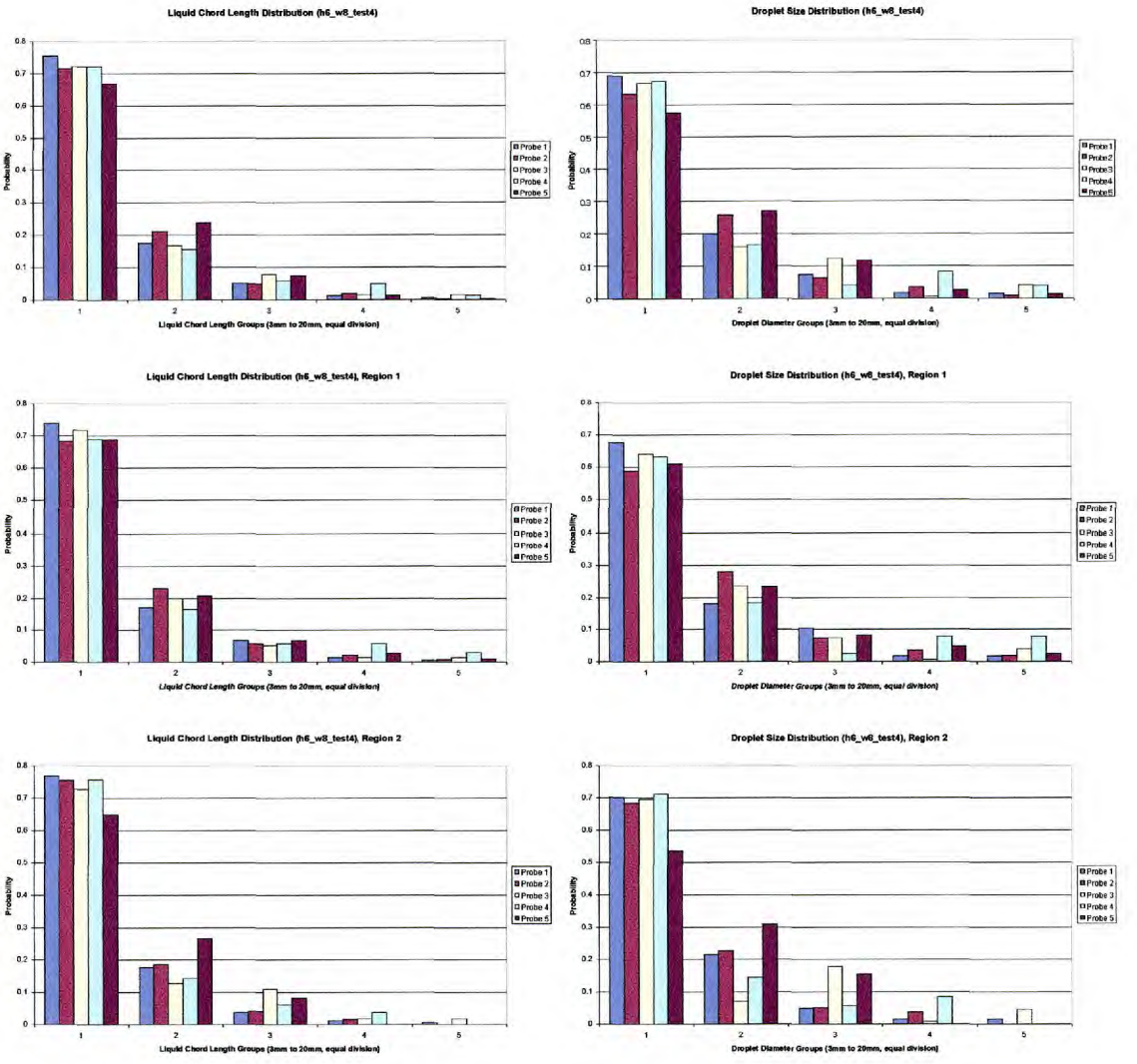


Figure 4.56. A "two-region" signal processing example with the liquid phase results

As for the liquid phase distribution, there seems to be fewer variations between the regions, only that the populations for large liquid chord length and droplet in "Region 2" are less than those in "Region 1" or for the entire tray.

The above results are just examples of how the flying optical probe technique can be used in the future. The actual accuracy of these results may not be good enough because the number of data on the chord length was literally halved when splitting the entire tray into two regions. One way to solve the problem is simply measuring another twenty runs for each condition so that there is a sufficient number of chord length data to be processed.

4.6. Summary

The flying optical probes system has been successfully developed. Experimental data covering a wide range of flowrates and tray configurations have been collected. The signals from the optical probes are treated with several processing methods, one of which is based on the work by Clark and Turton (1988). The results are very encouraging and they confirm some of the phenomena in the sieve tray two-phase flows. The bubble/droplet size distribution is a very important piece of information and this is particularly helpful on the Computational Fluid Dynamics (CFD) model validations and also potentially for the construction of any new CFD models on tray flows in the future. CFD modelling will be discussed further in Chapter 6.

Chapter 5

Liquid-Liquid Crossflow Simulation

5.1. Introduction

The true mechanisms that govern gas-liquid crossflow on a distillation tray are not well known and understood due to the difficulty in carrying out a direct visualisation of the froth layer on the tray. What is known is that the main mechanisms include the bubble formation process at given tray hole, the interactions between bubbles formed through adjacent holes and the bubble coalescence and break-up processes which lead to a transition between the froth and spray flow pattern. To improve the understanding of these mechanisms, a system of two immiscible liquids has been used to simulate the gas-liquid crossflow on a sieve tray and a description of this work is presented in this Chapter. The objective of the work was to visualise the two-phase flow field in more detail and to capture the motion of individual bubbles after their departure from the holes. The basic problem of visualising the processes occurring on a distillation tray is that these processes cannot be clearly visualised because of the complex nature of the interfaces involved. These reflect and refract incident light making observation of phenomena within the froth impossible. The work described in this chapter is aimed at visualising the processes by using a liquid-liquid system, namely kerosene as the light fluid (simulating the vapour) and an aqueous solution (simulating the liquid). Liquid-liquid systems suffer, of course, from the same problem as gas-liquid systems in that the multiple interfaces reflect and refract light making it impossible to see into the flow. However, by matching the refractive index of the two fluids, it is possible to leave a clear view through the fluid mixture on the tray. This in itself is not sufficient unless some means of selectively identifying selected regions of the mixture is found. This

may be achieved by dyeing the fluid entering one or more holes in the tray. The dyed droplets can then be seen within the two-phase mixture on the tray.

If a *permanent* dye were added to the stream entering the selected hole or holes, (with undyed fluid entering the other holes on the tray) thus the dye would ultimately mix with all the lighter fluid and the visualisation would again be obscured. The solution to this problem was to use a *photochromic* dyestuff which was dissolved in the whole kerosene phase. UV excitation of the kerosene streams entering the selected hole or holes caused the generation of a colour in those streams which allowed visualisation of processes on the tray. The dye decays slowly back to its colourless state allowing the fluid to be continuously circulated.

The first attempt to use the photochromic dye tracing technique in studying processes in simulated distillation trays was made by Tezock (1993) and an improved circuit was developed by Tahmaski (1997). The work described here builds on these earlier studies.

In what follows below, section 5.2 reviews the photochromic dye tracing technique and section 5.3 describes how the method was applied in the present work. Section 5.4 describes the liquid-liquid flow circuit and Section 5.5 describes the observation made. Finally, Section 5.6 summarises the findings.

5.2. Photochromic Dye Tracing Technique

5.2.1. Background Theory

Photochromism is defined as a reversible change of a single chemical species between two states having distinguishably different absorption spectra, such change being induced in at least one direction by the action of electromagnetic radiation (Brown, 1971). Generally, the equilibrium between the colourless and coloured species is presented by Eq.(5.1) showing that the reaction can be established in either direction:

$$\underset{\text{colourless}}{\mathbf{A}\ (\lambda 1)} \underset{\text{dark}}{\overset{h\lambda}{\rightleftharpoons}} \underset{\text{coloured}}{\mathbf{B}\ (\lambda 2)} \qquad (5.1)$$

Figure 5.1 below is a schematic representation of this reversible reaction.

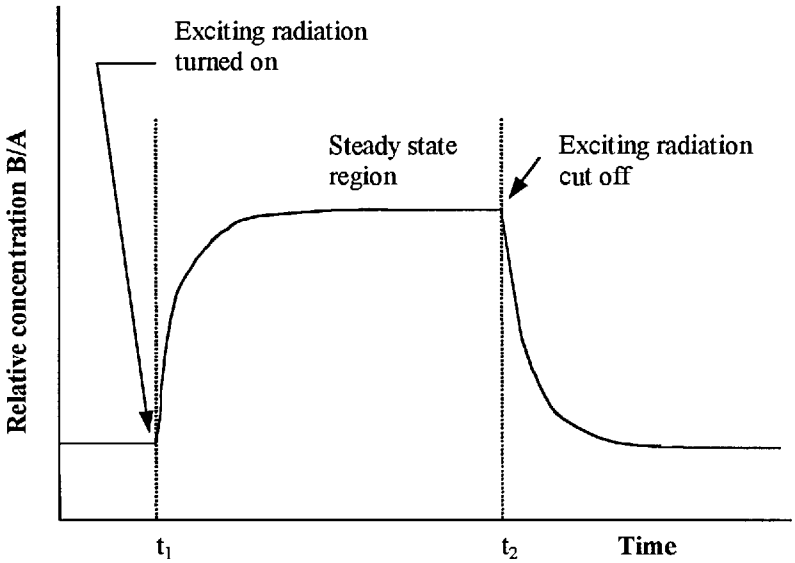


Figure 5.1. Behaviour of a photochromic substance (after Brown, 1971)

External excitation is applied at time t_1 and removed at t_2. During this excitation period, the forward reaction in Eq.(5.1) is favoured and the concentration of the coloured species increases before equilibrium is reached. After the time t_2, the backward reaction is dominant and the colour begins to fade away. The colour nature of this reversible reaction makes it attractive to be used as a dye tracing technique in fluid flow visualisation experiments.

5.2.2. Literature Survey

Humphrey (1977) published an extensive review on the application of photochromic dye tracing technique in fluid flow visualisation experiments and all the dyes discussed in this paper are only soluble in organic solvents. Later, Fogwell and Hope (1987) gave a comparison on the strengths and weaknesses of some commonly used photochromic dyes. The authors also introduced a new, water-soluble dye, which removed the previous restriction of the technique to non-aqueous systems.

The major developments of this technique over the past three decades are summarised in Table 5.1 below. In each case, the visualisation experiment is briefly described and where applicable, the weaknesses for such set-up are given.

Group	Dye	Excitation Source	Description
Popovich *et al* (1967)	2-(2',4'-dinitro-benzyl)-pyridine (DNBP)	Xenon flash-tube; UV wavelength	Experiments on non-distributing turbulent flow measurements very close to wall; suffer from weak contrast, short excitation period
Frantisak *et al* (1969)	2-(2',4'-dinitro-benzyl)-pyridine (DNBP)	UV pulsed laser; UV wavelength	Extending the work by Popovich *et al (1967)*, measurements on turbulent velocity profile and shear stress; the dye still has short excitation period (≈ 4ms)
Zolotorofe *et al* (1970)	1,3,3-trimethylindolino-6'-nitrobenopyrylospiran (TMINBPS)	High-pressure mercury lamp, UV light	Measurement of fully developed isothermal laminar velocity profiles in a pipe; overcome the short excitation time problem with the new oil-soluble dye
Fowlis (1979)	1,3,3, Trimethyl, 6, Nitro Indoline, 2, Spiro 2, 2 Benzo Pyrane	Xenon flash lamp; continuous mercury lamp; UV laser	Technique adopted for NASA Spacelab fluid flow experiments (free convection within fluids)
Fogwell and Hope (1987, 90)	Triarylmethane dye (Acid Violet 19)	Xenon-chloride excimer laser, UV light	Water soluble dye to enable larger experiments covering a wider range of Reynolds number
Tezock (1993)	1,3,3,-trimethyl indoline-6-nitrobenzospiropyran (TNSB)	UV light, wavelength 365nm	Simulation of two-phase flow on a cross-flow distillation sieve tray (more details are given below)

Table 5.1. Applications of photochromic dyes on fluid flow visualisation experiments

Tezock (1993) was the first to apply the photochromic dye tracing technique on the visualisation to the two-phase flow mechanisms above a sieve plate. The principle of the experiment was to use two immiscible liquids, the lighter of which contained a photochromic dye and simulated the gas phase flow while the heavier one simulates the

liquid phase flow in the real situation. To overcome the usual difficulty in the visualisation of any liquid-liquid or gas-liquid system due to optical aberration, two liquids with the same refractive index were chosen so that the transmission of light is free from the effects of refraction and scattering at the liquid interfaces. However, perfect matching of the refractive index means that no interfaces can be seen. The use of photochromic dye helps to identify particular events in one of the phases and their development can then be recorded. This experiment was carried out by Tezock (1993) and later by Tahmasbi (1997) where kerosene and calcium chloride solution were used as the liquid pair and an oil-soluble dye, 1,3,3,-trimethyl indoline-6-nitrobenzospiropyran (TNSB), was used. Some encouraging results were obtained but the following experimental problems were identified:

- Optical aberration due to imperfect refractive index matching
- Optical aberration due to the formation of a pink permanently coloured substance
- Insufficient flowrate for the liquid used to simulate the real gas phase flow (in previous attempts, only 5 holes are simulated simultaneously!)

Tahmasbi (1997) concluded that the technique had great potential and the work described in the following sections of this chapter presents the modifications made to the previous experimental system used by Tezock (1993) and Tahmasbi (1997). The aim is to attempt to overcome the above-mentioned problems and obtain good visualisation of the two-phase flows which occur above a sieve tray.

5.3. Experimental Fluids System

5.3.1. Photochromic Dye - TNSB

The oil-soluble photochromic dye, 1,3,3,-trimethyl indoline-6-nitrobenzospiropyran (TNSB), used to in the present study was manufactured and supplied by Photochromic Sciences Laboratories at the University of Toronto. The dye, which appears as pale yellow crystals under ambient conditions, has a low solubility in kerosene and other

saturated aliphatic solvents. It undergoes a reversible photochromic reaction when irradiated by ultra-violet (UV) light and the mechanism is thought to be heterolytic cleavage (Brown, 1971) involving the breakage of the oxygen-carbon bond and this is shown in Figure 5.2.

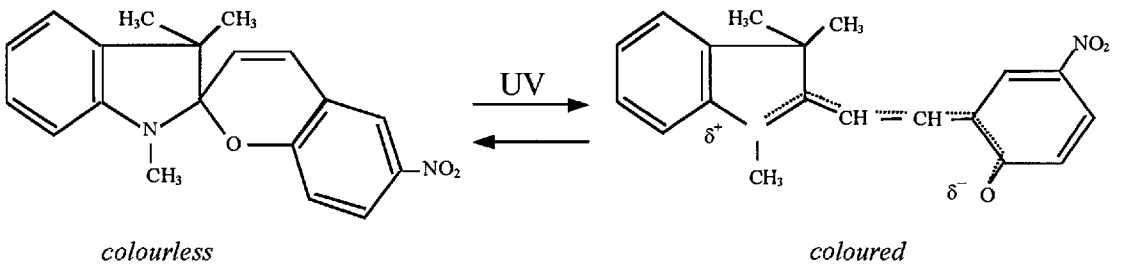


Figure 5.2. Reversible photochromic reaction of the dye, TNSB

In the experiments carried out by Tezock (1993) and Tahmasbi (1997), a hand-held UV-lamp (manufactured by *UVP Inc.*, USA; wavelength of 365nm) was used to irradiate the dyed kerosene. The absorption spectrum, kinetics and the fading rate of this reversible photochromic reaction was measured by Tezock (1993) using a Perkin Elmer 554 spectrophotometer. It was found that the coloured species disappear completely after about 5 minutes and the best contrast can be observed in the first two minutes after irradiation. This is illustrated in Figure 5.3.

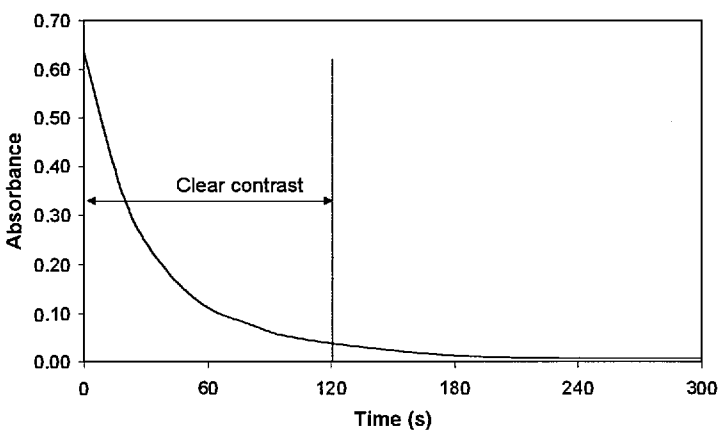


Figure 5.3. Fading rate of the photochromic dye TNSB (Tezock, 1993)

5.3.2. Refractive Index Matching Fluids

To satisfy laboratory safety regulations, a high flash-point kerosene (81°C) has been used as the solvent for the photochromic dye, TNSB. Some research work was required to find a complementary liquid, and the selection criteria was set to be as follows:

1. Immiscible and non-reacting with kerosene
2. Identical refractive index to kerosene
3. Zero solubility for the photochromic dye
4. Large density (relative to kerosene) to enhance the buoyancy effect
5. Economical (due to large quantity needed)

After extensive search for a suitable second liquid phase, it was concluded that the original choice of aqueous calcium chloride solution used by both Tezock (1993) and Tahmasbi (1997) was the best option. An *ABBE* refractometer was used to determine the refractive index of both liquids, which for the calcium chloride solution, it varies from 1.39 to 1.45 as the concentration (by weight) increases from 20% to just under 40% (near saturation). At 39%, the refractive index for calcium chloride and kerosene are exactly matched at 1.442 and this is illustrated in Figure 5.4.

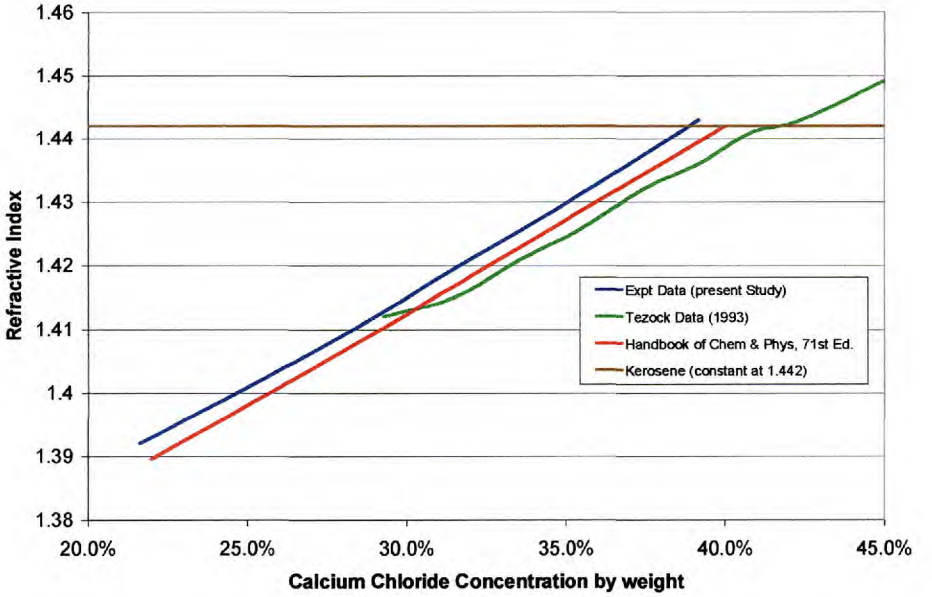


Figure 5.4. Refractive index of aqueous calcium chloride solution under different concentrations

Other physical properties of these two liquids were measured under the experimental conditions and these are summarised in Table 5.2.

Property	Kerosene	Calcium chloride
Refractive Index	1.442	1.442
Density (kg/m^3)	800	1400
Viscosity (Ns/m)	0.00202	0.01184
Surface Tension (N/m)	0.0262	0.0914
Interfacial Tension (N/m)	0.0190	

Table 5.2. Other physical properties of kerosene and aqueous calcium chloride solution

5.3.3. Fluid Preparation Procedures

- **Kerosene**

Previous experiences (Tezock, 1993; Tahmasbi, 1997) in the performance of this experiment showed that excessive amount (0.2g per litre of kerosene) of dye dissolved in the kerosene can lead to the formation of some unknown pink coloured substance in the system. The reason for the use of such a high concentration by previous researchers had been to enhance the contrast of the dyed kerosene. This phenomenon was confirmed by the dye vendor and the formation of the pink product has been explained to be caused by the local saturation and over-irradiation of the dye stuff. The solubility of the dye in kerosene at the excited state is lower than at the normal state. Therefore, when the dyed-kerosene is irradiated, a certain amount of dye could be crystallised out since 0.2g of TNSB per litre of kerosene is near the saturation point at normal state. These extra amounts of dye will undergo irreversible reactions if exposed to the UV for a long period of time. Experimental results in the present study showed that the pink substances were found after about 2 minutes of exposure time. In other experiments performed by the dye vendor, a much lower concentration (say, 10ppm by weight) was used. Therefore, by trial-and-error, a lower concentration of 0.05g of the TNSB dye per litre of kerosene was set for the present study. The loss on contrast due to the lower concentration can be regained by a new design of the activation chamber (described in section 5.4.2) which allows longer exposure time for the dye. A total of 45 litres of kerosene (low odour, flash point 81°C) was purchased from *Sigma-Aldrich Co Ltd* for the present work.

- **Calcium chloride**

Pure calcium chloride crystals are very expensive and it is more economical to prepare the aqueous solutions from an anhydrous white powder of about 92% purity which was

purchased from *Sigma-Aldrich Co Ltd.* To make up the calcium chloride solution of 39% concentration 70g of the anhydrous powder per 100 cm^3 of distilled water are required. The process of dissolving the salt in water is exothermic and therefore the powder had to be added slowly and carefully. Because the target concentration (39%) is very near to the saturation at room temperature, the solution was continuously stirred by a magnetic stirrer and regularly cooled down by a cold water bath. The cooled solutions were left overnight for some undesired white precipitates (impurities) to settle out before being filtered out, leaving behind a clear translucent liquid having a slightly yellowish tint. The filtration step was repeated again if the filtered solution was still unclear.

5.4. Liquid-Liquid Experimental Rig

The first step of the present work was to revamp the experimental rig used by Tezock (1993) and Tahmasbi (1997). This was done by thoroughly cleaning the test section, replacing parts (e.g. rubber tubings, test tray,...etc) and adding new equipment to the system (such as a new pump). It was decided to operate the revamped rig as a batch process so that the fluids could be properly separated after each run. The dyed-kerosene and aqueous calcium chloride solution were prepared according to the instructions given in the previous section.

5.4.1. Flowsheet

The new experimental rig consists of a test section, storage and dump tanks, an activation chamber and circulation pumps. These components are joined up by rubber tubing and the flow diagram is given in Figure 5.5. The units and flow circulation loops are described as follows:

Storage / Dump tank

Two 50-litre plastic tanks were used to store the dyed-kerosene and calcium chloride solutions separately and tappings were fitted tightly onto the tanks using PTFE tapes to

prevent leakage. Three 25-litre tanks were used as dump tanks to collect liquid at three outflow points for temporary storage before the mixtures were separated.

Rotameters and Valves

Three PLATON rotameters (**R1**, **R2** and **R3**) were used for measuring liquid flowrates in various streams. These rotameters were pre-calibrated for water at 20°C and further calibrations were carried out by Tezock (1993) for measurement of kerosene and aqueous calcium chloride which has specific gravity of 0.8 and 1.4 respectively. The resultant relationships (Tezock, 1993) for correlating the rotameter readings to the actual volumetric flowrates are:

Dyed-kerosene $$Q_{kerosene} = 1.134 Q_{water} \quad (5.2)$$

Calcium chloride solution $$Q_{CaCl_2} = 0.820 Q_{water} \quad (5.3)$$

Various types of valve are used to control or restrict the flows in the rig and these are marked as **V1** to **V9** in Figure 5.5.

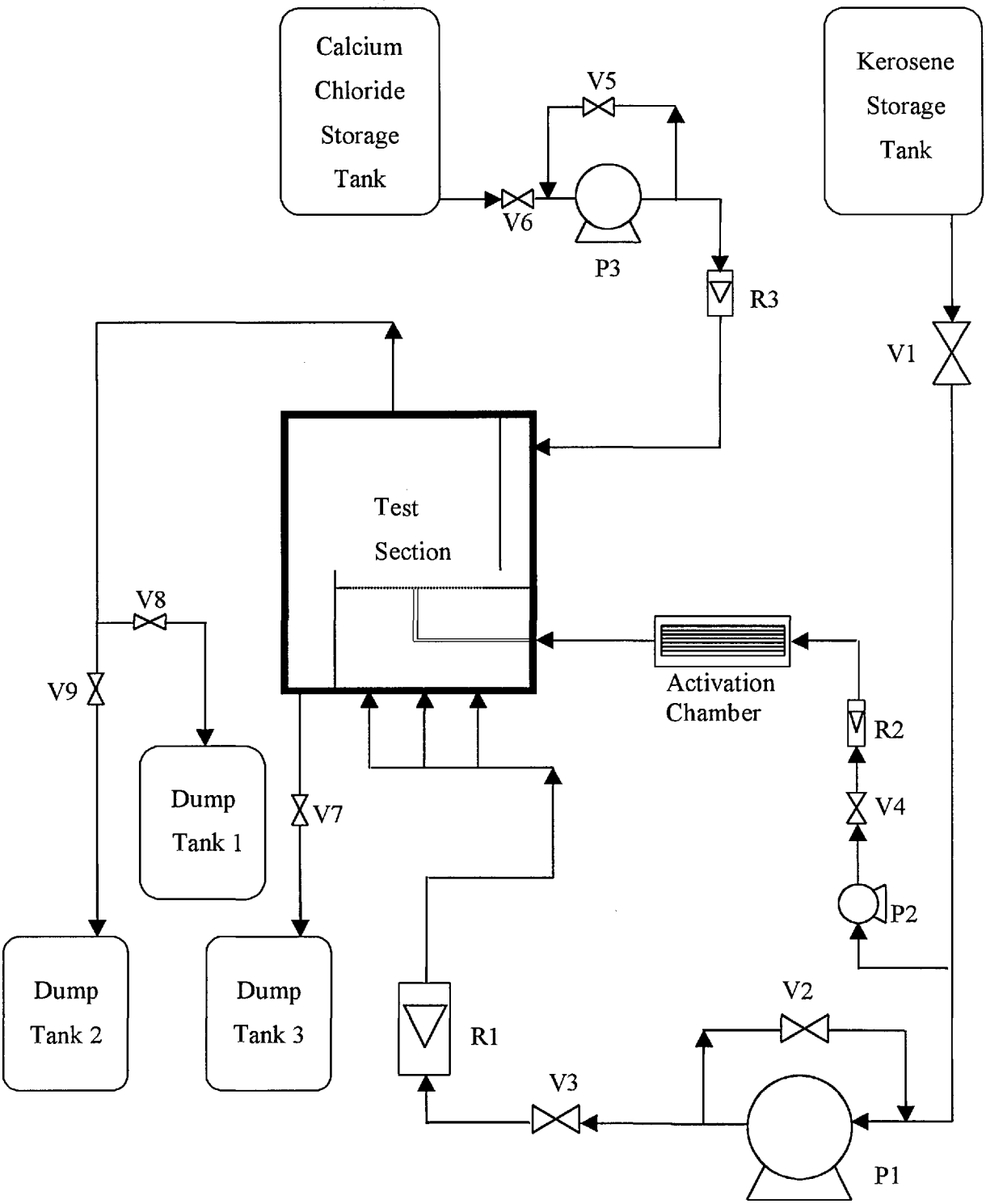


Figure 5.5. Diagram of the liquid-liquid crossflow experiment

Test section

The test section is a small-scale rectangular tray column made of acryllic resin (Perspex^{TM}) and this is in Figure 5.6. There are five ports available in the test section: three for the inlet of the fluids (**F1** to **F3**) and two for their outlet (**S1** and **S2**).

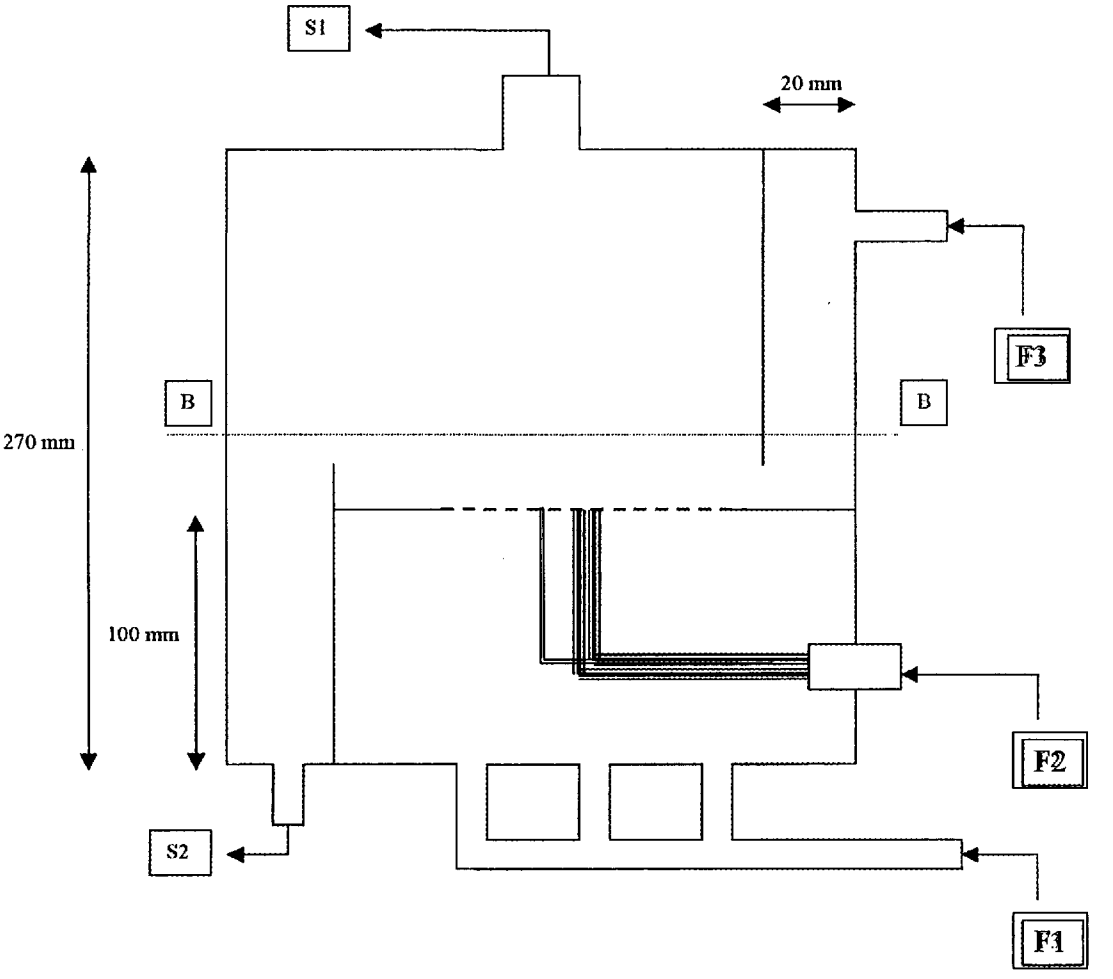


Figure 5.6. Test section of the liquid-liquid crossflow experiment

Sieve Tray

The dimension of the sieve tray used in the test section is shown in Figure 5.7. The sieve tray has a hole size of 1.8mm and the pitch is 6mm. In order to increase the superficial celocity of the kerosene, the open area of the sieve tray has been purposely reduced (compared to the one used by Tezock, 1993) to 180mm×75mm. The red circle

in the Figure 5.7 represents the position of the hole connected directly to the irradiated kerosene stream.

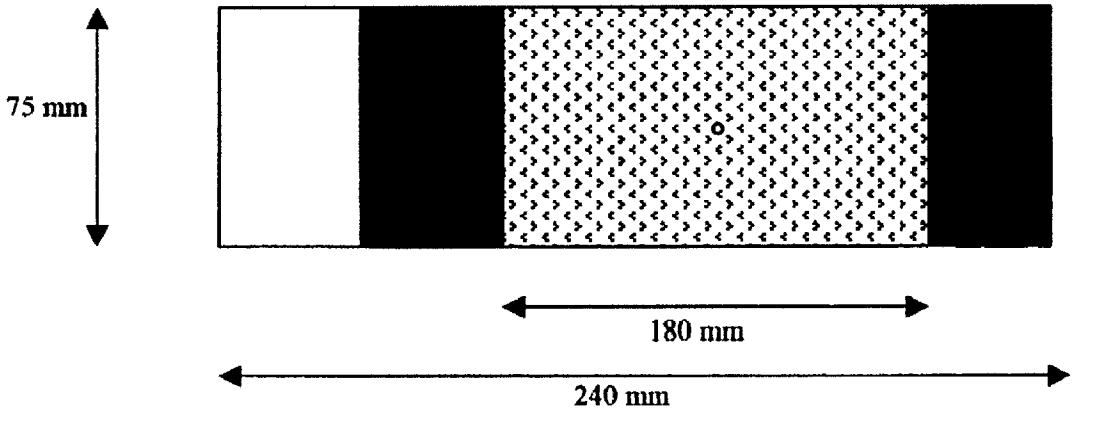


Figure 5.7. Dimension of the 1.8mm hole size sieve tray (top view)

Kerosene circulation

After leaving the storage tank, the flow of kerosene is divided into two paths. The majority of the flow is circulated by a three-phase gear pump, **P1** (made by *Albany Ltd*) and enters the test section from the bottom (**F1**). The smaller kerosene flow, which is due to be irradiated in the activation chamber, is pumped by a small variable-speed gear pump, **P2** (made by *Watson-Marlow Ltd*). Once irradiated, this stream of kerosene enters the test section from the side (**F2**) and the inlet is connected directly to a single hole on the sieve tray by a thin silicon rubber capillary (1.8mm bore diameter). The "clean" and the irradiated kerosene mixes with calcium chloride solution on the tray floor before leaving the test section either at the top (**S1**) as pure kerosene or at the downcomer (**S2**) as a mixture with calcium chloride solution.

Calcium chloride circulation

The calcium chloride solution is circulated by a centrifugal pump, **P3** (made by *Sutton Ltd*). The aqueous solution enters the test section from the top right corner (**F3**) before making contact with kerosene on the tray floor. To ensure a good simulation of the liquid-liquid system with the real situation, the valve **V7** plays a very important role in controlling the level of calcium chloride solution at the outlet downcomer. The valve is

kept closed until the level of the calcium chloride solution builds up to about 50mm before the valve is partially opened. V7 is then carefully opened to the extent necessary to keep a constant level of calcium chloride solution in the downcomer. This ensures that the calcium chloride solution to be able to leave the test section at the bottom of the downcomer (**S2**).

Activation chamber

The activation chamber is for irradiating the stream of kerosene before entering the test section at the inlet **F2**. The chamber consists of a small, open-top metal box covered up by a 5 watt UV lamp (wavelength 365nm). Inside the box, there are six 2mm bore diameter quartz-glass capillaries running in parallel providing a large UV exposure surface for the kerosene. The original design of the quartz-glass capillaries used by Tezock (1993) and Tahmasbi (1997) is shown in Figure 5.8.

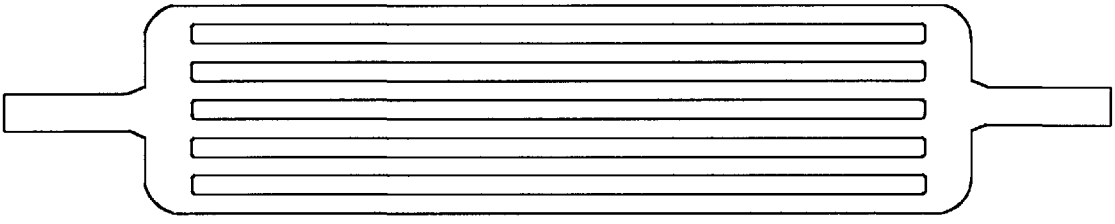


Figure 5.8. Original quartz capillary used by Tezock (1993) and Tahmasbi (1997)

As discussed earlier in sections 5.2.2 and 5.3.2, a high concentration of dye (dissolved in kerosene) was used previously to increase the contrast, however, this suffers from the formation of the pink substance mentioned before which has been confirmed to be a product of the dye undergoing an irreversible reaction. Over a certain period of time, these substances were found to deposit inside some of the capillaries (especially the outer two capillaries at each side) and partially block the flow of kerosene. This is caused by the fact that the kerosene is not evenly distributed into the six capillaries in the original design. i.e. fast moving flows in the central channels (the two tubes in the middle) and much slower flows are found at the sides. Eventually, most of the kerosene passes through the capillaries via the central channel, and this shortens the UV-radiation

exposure time. The slow moving kerosene at the sides was over irradiated due to the prolonged residence time in the chamber and the undesired pink substance was formed and circulated in the entire system. To overcome this problem, a new design of the quartz capillaries has been used in the present work and this is shown in Figure 5.9 below.

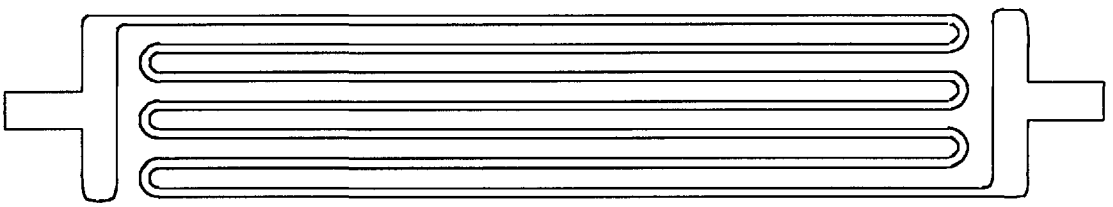


Figure 5.9. New design of activation chamber in the present work

For the same amount of kerosene flowing through the capillaries, the flow path of the new design is estimated to be about 10 times longer than the original design. i.e. the UV-radiation exposure time is also increased about 10 times. The lower concentration of dye (therefore lower contrast) used in the present study is compensated by the longer UV-radiation exposure. In the trial runs of the experiment, the contrast shown was actually better than the previous results.

Separation system

Trial runs of the rig showed that the liquid leaving the test section at **S1** contain only kerosene while from the other outlet **S2**, a mixture of kerosene and calcium chloride solution are passed to dump tank 3. The mixture was transported into a large glass tank with a draining tap at the bottom. After allowing a few minutes for the mixture to settle, a clear interface could be identified and the calcium chloride solution can be drained out by opening the tap before taking out the remaining kerosene in.

5.4.2. Proposed Experiments

The main objective of the present study is to understand the flow behaviour on a sieve tray. Two digital cameras were employed to take the photographic images on the flow

field: (1) a Sony digital video camera model DCR-TR410E filming at 25 frames per second and (2) a Kodak high-speed digital video camera running at 250 frames per second. The low speed camera provides a good idea of the flow field while the high-speed one gives a more detailed picture of the flow behaviour near the bubbling region. There were two main types of experiment in the present work:

- **Single hole bubbling of kerosene with calcium chloride solution crossflow**

This is a simplified situation of the ultimate experiment to be performed. The aim of this set of runs is to investigate the bubbling process without the disturbances from the neighbouring holes. The transition from bubbling to jetting from a single hole can be studied in this test.

- **Full simulation – kerosene bubbling on all active area of the tray with calcium chloride solution crossflow**

This set of runs is the true liquid-liquid simulation of the gas-liquid flows on a sieve tray. The flowrates of the bulk (non-irradiated) and the single stream (irradiated) kerosene are matched exactly so that a truly synchronised flow, simulating the gas flow in real situation, can be established. The actions such as break-up or coalescence of the irradiated kerosene can be traced in the flow field. The effect of multiple-hole bubbling on the bubble-jet transition and therefore on the froth-spray transition on sieve tray operations was also investigated.

5.5. Observations and Discussions

5.5.1. Single-hole Bubbling Experiment

Experiments under seven different sets of conditions were performed and the flowrates for each run are summarised in Table 5.3.

Run	Kerosene hole velocity (m/s)	$CaCl_2$ flowrate (lit/min)
1	0.25	2.46
2	0.25	3.28
3	0.25	4.10
4	0.37	2.46
5	0.50	2.46
6	0.57	2.46
7	0.62	2.46

Table 5.3. Flowrates of each experimental run

Photographic images were taken using the Kodak high speed video camera and Figure 5.10 shows a typical snapshot of the flow field near the bubbling point (shown with an upward arrow). In this figure, a clear layer of calcium chloride solution is situated underneath the bulk kerosene and the direction of the crossflow liquid is shown by the red arrow.

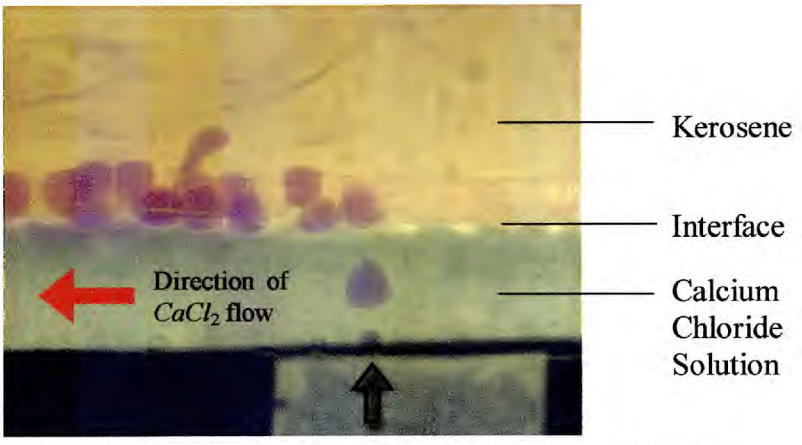


Figure 5.10. Typical snapshot of the flow field in single hole bubbling experiment

Full results (including still pictures and animated video clips) of the seven sets of experiment are stored in the CD-ROM attached at the end of this thesis, however, the results of the most important three sets (Run 5, 6 and 7) are shown in Figures 5.11, 5.12 and 5.13 respectively.

In Figures 5.11 (a)-(e), individual kerosene droplets are formed and detached from the hole and in Figures 5.13 (a)-(e), consecutive droplets are joined by small residual volumes of kerosene which were formed due to the formation of droplets. Figures 5.12 (a)-(e) show transitional behaviour between the two phenomena above. The kerosene

flowrate has increased from Figure 5.11 to 5.13 and the pictures give a good demonstration of the transition from "bubbling" to "jetting" through a single hole. A common observation in all of the runs is that the kerosene always arrives at the interface as individual droplets, regardless of the way it travels through the layer of calcium chloride solution (i.e. "bubbling" or "jetting"). These droplets are then transported horizontally towards the outlet downcomer and no coalescence between droplets was observed during this process.

Generally, the observations from the liquid-liquid rig correspond very well to the theory of bubble formation (see Section 2.2.1) in the gas-liquid case. The encouraging results from this set of experiments provide good confidence in the results obtained in the full simulation experiments presented in the next section.

Figure 5.11(a) to (e). Single bubbling phenomenon (Run 5); kerosene hole velocity, u_h=0.50m/s, $CaCl_2$ flowrate Q_L=2.46lit/min

Figure 5.12(a) to (e). Single bubbling phenomenon (Run 6); kerosene hole velocity, u_h=0.57m/s, $CaCl_2$ flowrate Q_L=2.46lit/min

Figure 5.13(a) to (e). Single bubbling phenomenon (Run 7); kerosene hole velocity, u_h=0.62m/s, $CaCl_2$ flowrate Q_L=2.46lit/min

5.5.2. Full Simulation (Multiple-hole Bubbling) Experiment

Experiments under six different sets of conditions were performed and the flowrates for each run are summarised in Table 5.4.

Run	Kerosene hole velocity (m/s)	$CaCl_2$ flowrate (l/min)
1	0.08	2.46
2	0.32	2.46
3	0.39	2.46
4	0.39	1.64
5	0.39	3.28
6	0.39	4.10

Table 5.4. Flowrates of each experimental run

Full results (including still pictures and animated video clips) of the six sets of experiments are stored in the CD-ROM attached at the end of this thesis and only selected results will be shown and discussed in this section.

The first objective of the full simulation experiment was to provide a clear visualisation of the two-phase flow field. Figure 5.14 is a typical snapshot (taken by the Sony digital video camera) of the flow field where three regions can be identified. These regions are separated by the drawn dotted lines **L1** and **L2**.

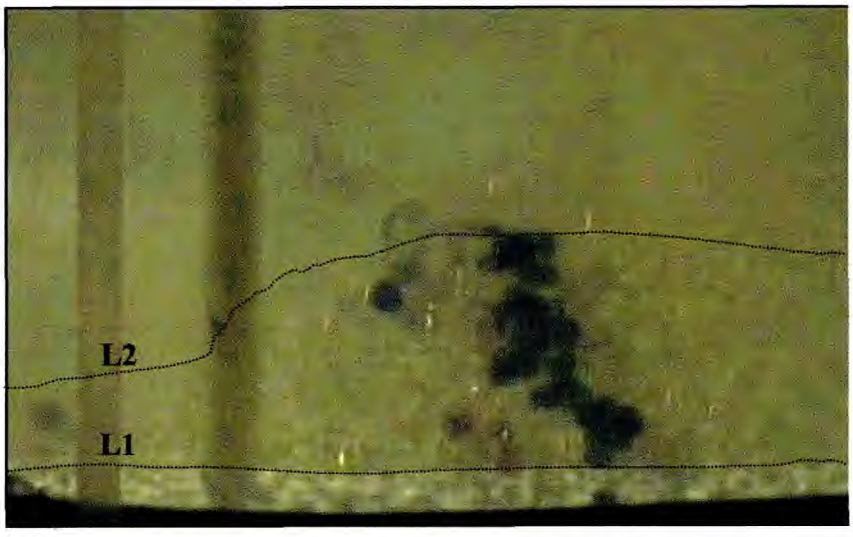


Figure 5.14. A typical snapshot of the flow field (taken from Run 1)

The three regions are defined here as:

- **"Heavy-phase continuous" region**

  This is similar to the liquid-continuous phase occurred near to a sieve tray floor. In the present study, the majority of this region is occupied by the calcium chloride solution.

- **"Mixed" region**

  In this region, bound by the two lines **L1** and **L2** in Figure 5.14, the two liquids are well mixed and this is similar to the froth region above a distillation tray.

- **"Light-phase continuous" region**

  This is opposite to the "heavy-phase continuous" one and literally, no heavy-phase liquid can be found in this region. This is the same as the gas-continuous region occurring above the top of the froth body in a distillation tray case.

Figures 5.15 to 5.22 are photographs taken from the Sony digital video camera and they represent the flow field observed in Run 1 every 2 seconds in time. These pictures contain a lot of useful information on two-phase flows which are usually impossible to visualise. In this particular case, where the kerosene hole velocity is 0.08 m/s and the volumetric flowrate of calcium chloride solution is 2.46 l/min, the system is simulating a slow bubbling case of the gas-liquid flow.

There are a few general observations:

- There seems to be no obvious interaction between adjacent holes bubbling under this condition. (observations near the tray floor)
- There seems to be no clear coalescence or break-up actions for droplets in the mixed region. (observation in the mixed region)
- Dyed-kerosene droplets join the bulk kerosene at the upper edge of the mixed region boundary.

In what follows, an attempt is made to describe the event occurring in terms of stills taken from the video sequences (Sony camera). To help to emphasise some points, "boxes" defined by coloured lines are drawn on the stills and the motion of phase

elements in the boxes is followed at successive time increment. However, it should be emphasised that there is always a difficulty in describing complex phenomena in terms of still shot taken from film or video sequences. The reader is referred to the animated sequences given in the CD-ROM at the end of this thesis for further clarifications. Four moving boxes are marked with different colours in Figure 5.15 to 5.22 which are stills sampled at 2 second intervals from a video sequence. Each box surrounds a group of dispersed phase elements. The events illustrated by the various boxes are as follows:

- **Release of kerosene into bulk phase (Red box)**

In Figure 5.15, there are several distinct dyed-kerosene droplets within the red box which is situated near the top boundary of the mixed region. The liquid film (of calcium chloride solution) surrounding the droplets in the box ruptures 2 seconds later (Figure 5.16). The dyed-kerosene inside these droplets is therefore released into the bulk kerosene at the top. The flow into the bulk produces a "mushroom-shape" pattern and this is shown in Figure 5.16.

- **Motion in upper part of mixed region (Orange box)**

The droplets inside the orange box are originally situated below the red box in Figure 5.15. As the droplets in the red box diffuse into the bulk kerosene, the orange box moves closer to the upper boundary of the mixed region. When drops in the orange box finally reach the boundary, they rupture and are dispersed into bulk kerosene (as was the case with the drops in the red box).

- **Motion near outlet weir (Blue box)**

The kerosene droplets inside the blue box have been swept towards the outlet by the crossflow calcium chloride solution. About 10 seconds later, the droplet broke up and it disappeared into the bulk kerosene.

- **Motion in lower part of mixed region (Black box)**

The residual of the droplets from each box (red, orange and blue) can still vaguely be observed in Figure 5.20. However, as a comparison to Figure 5.15, the local concentration of the dyed-kerosene (above its bubbling point) seems to be much lower

in Figure 5.20 (shown in dotted black box). In the following 4 seconds (Figures 5.21 and 5.22), more dyed-kerosene droplets are detached from the hole and move upwards. Tahmasbi (1997) reported that, owing to the irregular movement of liquid across the tray floor, some holes, or groups of holes may be discharging rapidly at a given instant, while others may temporarily be inactive. The above observation in the black box confirms this phenomena in the gas-liquid case.

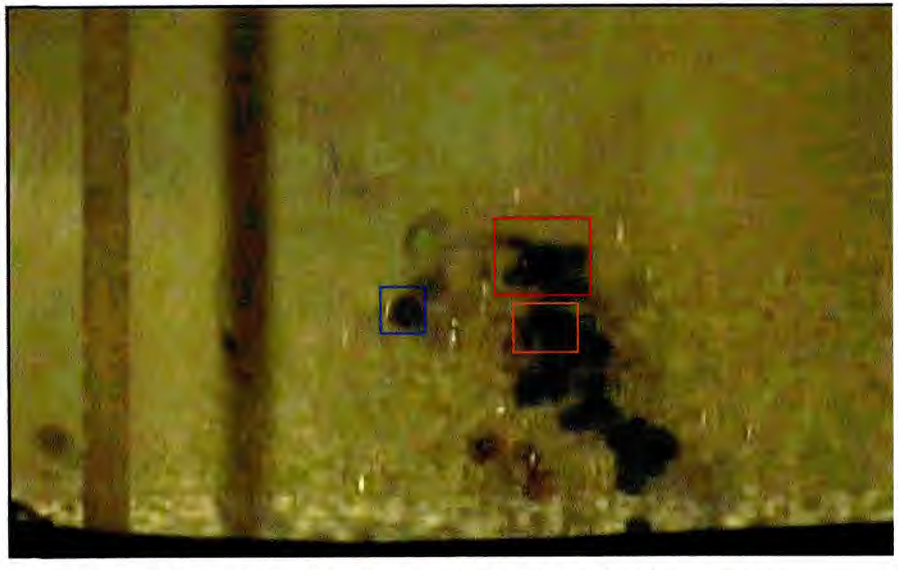


Figure 5.15. Photograph of the flow field at t = 0.0s (taken from Run1)



Figure 5.16. Photograph of the flow field at t = 2.0s (taken from Run1)

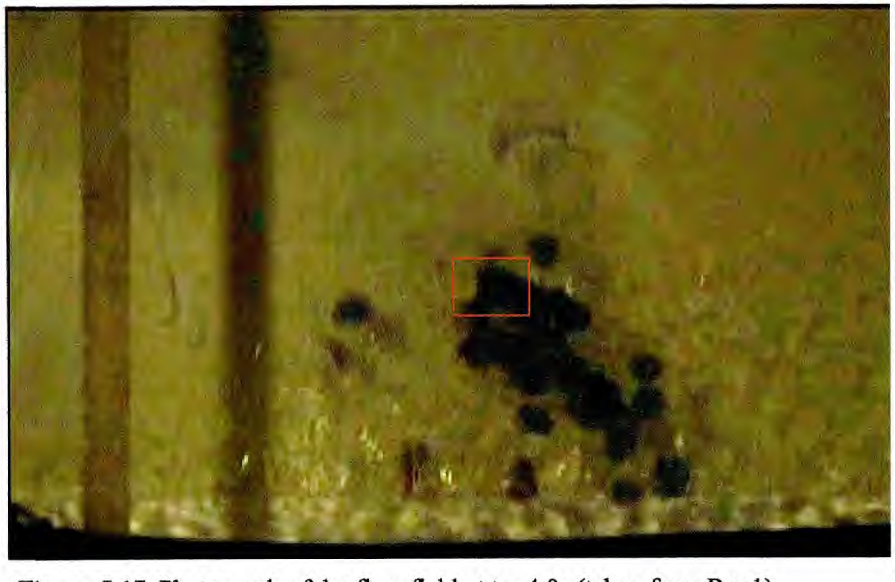


Figure 5.17. Photograph of the flow field at t = 4.0s (taken from Run1)



Figure 5.18. Photograph of the flow field at t = 6.0s (taken from Run1)

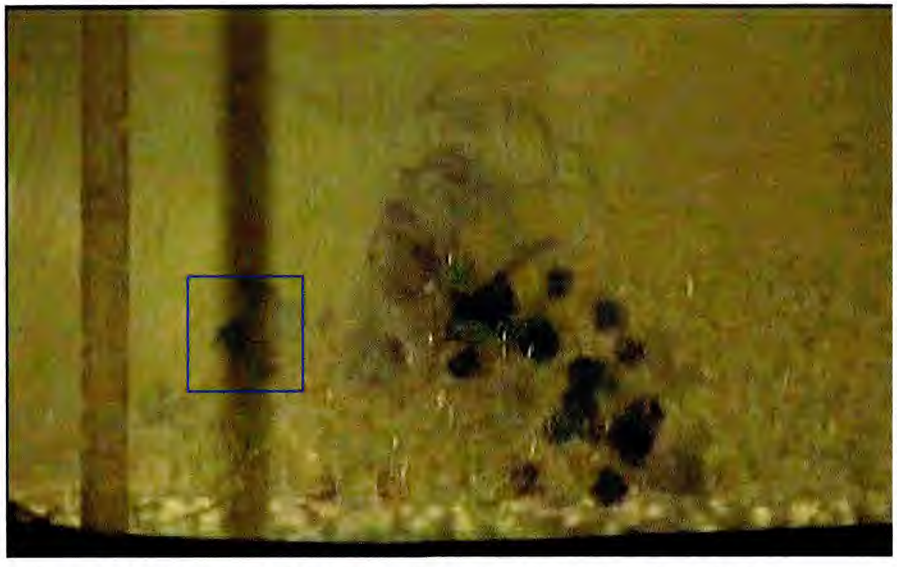


Figure 5.19. Photograph of the flow field at t = 8.0s (taken from Run1)

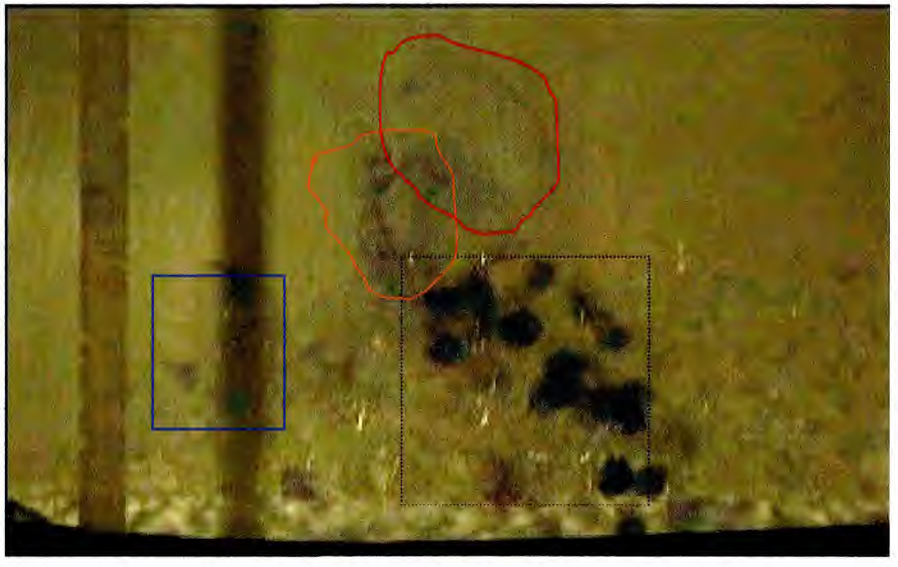


Figure 5.20. Photograph of the flow field at t = 10.0s (taken from Run1)

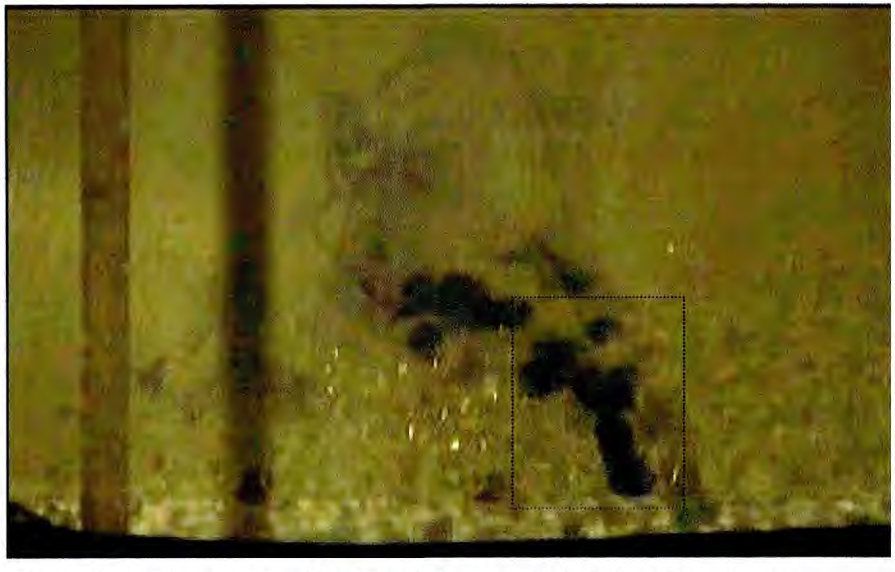


Figure 5.21. Photograph of the flow field at t = 12.0s (taken from Run1)

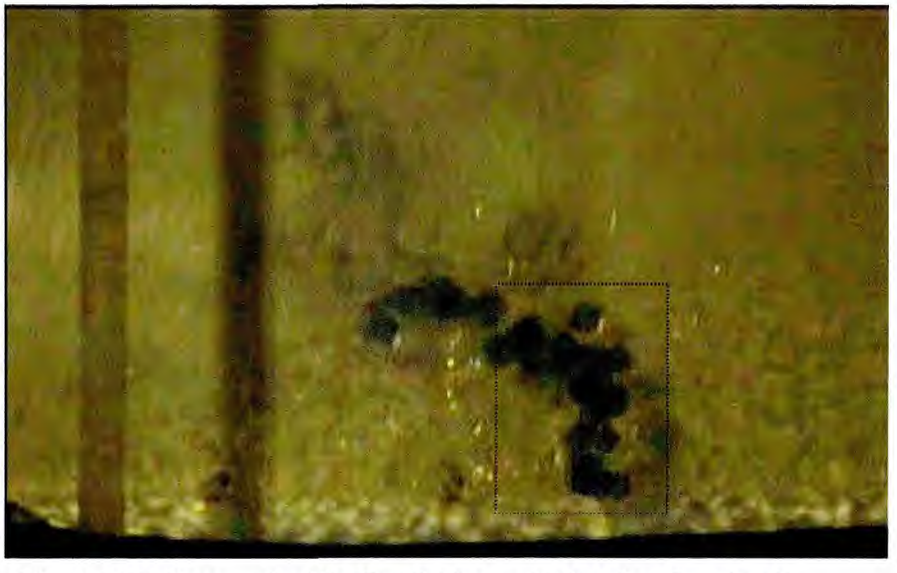


Figure 5.22. Photograph of the flow field at t = 14.0s (taken from Run1)

The other important objective of the full simulation was to visualise the froth-spray transition on a sieve tray and this was achieved in Runs 2, 3 and 6 (conditions shown in Table 5.4). A typical snapshot of a full simulation run is shown in Figure 5.23 below.

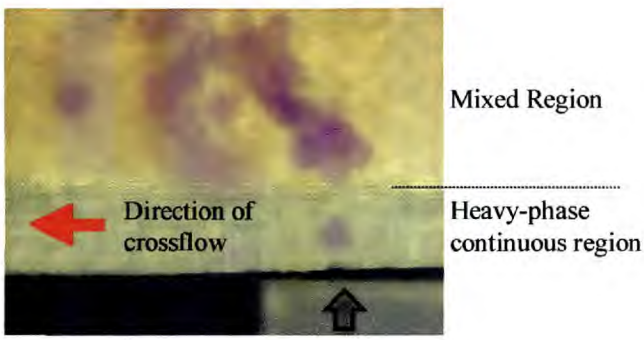


Figure 5.23. Typical snapshot of the flow field in full simulation experiment

Figures 5.24 (a)-(e) are results from Run 2 with lower kerosene flowrate (hole velocity of 0.32 m/s) showing the froth-like flow patterns. While keeping a constant flowrate of calcium chloride solution, an increase on the kerosene flowrate (Run 3) induces the jetting action from the holes. This is shown clearly in Figures 5.25 (a)-(e) and these represent the spray-like flow patterns.

In Run 6, where a larger flowrate of calcium chloride solution was used, a shear force provided by the strong crossflow acted on the jet body and this force tended to break the jet into a few bubbles within the heavy-phase continuous region. This phenomenon can be observed in Figures 5.26 (a)-(e).

Figure 5.24(a) to (e). Multiple-hole bubbling phenomenon (Run 2); kerosene hole velocity, u_h=0.32m/s, $CaCl_2$ flowrate Q_L=2.46lit/min

Figure 5.25(a) to (e). Multiple-hole bubbling phenomenon (Run 3); kerosene hole velocity, u_h=0.39m/s, $CaCl_2$ flowrate Q_L=2.46lit/min

Figure 5.26(a) to (e). Multiple-hole bubbling phenomenon (Run 6); kerosene hole velocity, u_h=0.39m/s, $CaCl_2$ flowrate Q_L=4.10lit/min

5.5.3. Liquid-Liquid System vs. Gas-Liquid System

The most obvious differences between a liquid-liquid system and a gas-liquid one are physical and surface (or interface) properties of the fluids. One major phenomenon of the experimental observations is the apparent delay of coalescence between kerosene drops. This may not be the case in the gas-liquid system. Important differences between the liquid-liquid and gas-liquid cases are as follows:

- **Density ratio**

The density ratio (kerosene / calcium chloride) of the present liquid-liquid system is about 0.57 which represents an extreme condition of very high-pressure vapour/liquid distillation (the usual value is in the order of 0.05, e.g. Porter and Jenkins, 1979). This means that the buoyancy forces in the liquid-liquid system are weak compared to those in a gas-liquid system.

- **Liquid viscosity**

The viscosity of the aqueous calcium chloride solution is high (compared to some common liquids) due to its high concentration. This slows down the drainage rate of the liquid film (of calcium chloride solution) between the kerosene drops and therefore slows the coalescence process.

- **Interfacial tension**

Surface tension of a gas-liquid system usually decreases with pressure. In a high-pressure distillation case, a typical value of surface tension is about 0.005 N/m (e.g. see Porter and Jenkins, 1979); the interfacial tension between the liquids in the present system is 0.019 which is relatively high.

For the above reasons, there are obvious limitations in applying the present results to gas-liquid systems. However, it should be stressed that there are no methods available for visualising the detailed phenomena in the gas-liquid case. This is why the present experiments were performed! The results presented show a number of previously undetected features of flow on a distillation tray, which are likely also to apply in the gas-liquid case.

5.6. Summary

The photochromic dye tracing technique applied to the present liquid-liquid crossflow system provides a non-intrusive visualisation of two phase flow above a sieve tray. The first part of the results, presented in still photographs, show good consistency with the single-hole bubbling mechanisms which have been identified in previous work. The full simulation results successfully reveal what to expect in the two-phase froth above a sieve tray. The complex transition between the froth and spray regimes has also been visualised.

Chapter 6

Application of Computational Fluid Dynamics to Distillation Hydrodynamics

6.1. Introduction

The next three chapters (6, 7 and 8) deal with applications of Computational Fluid Dynamics (CFD) to the prediction of flows on distillation trays. CFD studies have been a major focus of the work of the ASID (Advanced Studies In Distillation) Consortium, involving Bristol University, Aston University and Imperial College. The present work has been carried out under the aegis of this Consortium. The work of CFD started at Bristol University where Daly (1997) and Fischer (1999) carried out extensive calculations simulating both the rectangular configurations used in the CRODIS facility (see Chapter 2) and also full scale circular tray geometries. This work used the code CFX (supplied by *CFDS of AEA Technology Ltd*) and the calculation were performed using the so-called "heterogeneous" two-fluid model in which equations are written for the two phases, the equations being linked by interfacial transfer terms (in the form, for instance, of drag laws).

The work using the heterogeneous (two-fluid) approach was continued in the present study and a specific development was pursued, namely the applications of the MUSIG model in which the assumption of a uniform drop size (used by both Daly (1997) and Fischer (1999)) was relaxed with the flow being represented by groups of bubbles each with a characteristic size. Coalescence and break-up of bubbles (affecting the populations of the respective groups) are considered in their model.

A major problem with the heterogeneous model is the necessity to assume drag coefficients between the liquid and the gas which are clearly unphysical. There is, thus,

a significant element of "tuning" of the data to the experimental results. Despite this, however, the outcome gives extremely interesting, even if *qualitative*, physical insight into the flows occurring.

An urgent industrial need is for a *quantitative* methodology, taking reasonable account of the complex flow on the tray, by which tray efficiency can be calculated. To achieve this, the so-called "heterogeneous" model was used. In this model, the region froth on the tray was assumed to be well mixed and to have a density calculated from an available correlation. The froth was considered as one and vapour above it as a second region. However, from the computational point of view, the two regions are considered as being occupied a single fluid whose density and viscosity varies between the extremes of those of the froth and those of the vapour, depending on position within the computational domain. The physical properties were assumed to vary with the value of a scalar quantity (analogous to temperature) for which separate transport equations can be written. This method is, of course, the VOF (volume-of-fluid) method which is now used widely in tracking interface motion in gas-liquid systems, though it is referred to as the "homogeneous model" in the CFX code manual. The main difference here is that we consider a froth as one of the regions rather than a pure liquid.

The homogeneous model is introduced briefly in the present chapter but further details of how it may be used to predict tray efficiency are presented in Chapter 7. Finally, Chapter 8 presents the results of validations of the approach against a wide range of data and describes the applications of the approach to several specific cases. As will be seen, rather good results are obtained, through the need for more detailed calculation of tray behaviour still remains.

In section 6.2, the fundamental theory of CFD is briefly discussed for single-phase flows. The applications of the two-fluid ("heterogeneous") model is described in Section 6.3, with the new work on the MUSIG algorithm being presented in Section 6.3.3. Section 6.4 presents the "homogeneous" model, which forms the basic for the development discussed in Chapters 7 and 8.

6.2. CFD Fundamentals

Any fluid motion is caused by a force or forces which can be categorised into two types:

- **Surface forces**: forces which involves physical contact between, e.g. normal and shear stresses, surface tension, etc.
- **Body forces**: forces which acts at a distance away from a body, without any physical contact, e.g. gravity, centrifugal force, etc.

The first step in any fluid dynamics modelling is to provide an appropriate description of the flow field. There are two types of such descriptions given as follows:

- **Eulerian**: focus attention on the properties of the flow at a given point in space as a function of time
- **Lagrangian**: focus attention on the trajectories of fluid elements within the flow field

Both descriptions are useful for predicting the fluid motion, although the Eulerian approach (also known as the control volume approach) is always preferred by engineers for the simplicity and convenience. This approach is used in the present work.

6.2.1. Governing Equations

To describe a single-phase flow field within a Control Volume (CV), it is necessary to write down the conservation equations for mass, momentum and energy.

- Conservation of mass (also know as continuity):

Rate of accumulation of mass in CV	=	*Rate at which mass flows into CV*	-	*Rate at which mass flows out of CV*

Which in vector form becomes:

$$\frac{\partial \rho}{dt} + \bar{\nabla} \cdot (\rho \mathbf{u}) = 0 \tag{6.1}$$

- Conservation of momentum:

Sum of forces acting on the fluid in CV	=	*Rate of accumulation of momentum in CV*	+	*Rate at which momentum flows into CV*	-	*Rate at which momentum flows out of CV*

This principle leads to the *Navier-Stokes equations* which are written in vector form as follows:

$$\rho\frac{\partial \mathbf{u}}{\partial t}+\rho\,\mathbf{u}\cdot\bar{\nabla}\mathbf{u}=\rho\,\boldsymbol{g}-\bar{\nabla}p+\bar{\nabla}\cdot(\eta\bar{\nabla}\mathbf{u}) \tag{6.2}$$

- Conservation of energy:

Rate of accumulation of energy in CV	=	*Rate at which energy flows into CV*	-	*Rate at which energy flows out of CV*	+	*Rate of gain of energy due to surface stresses*

Which in vector form becomes:

$$\mathbf{u}\cdot\left(\rho\frac{\partial \mathbf{u}}{\partial t}\right)+\mathbf{u}\cdot(\rho\,\mathbf{u}\cdot\bar{\nabla}\mathbf{u})=\mathbf{u}\cdot(\rho\,\boldsymbol{g})-\mathbf{u}\cdot\bar{\nabla}p+\mathbf{u}\cdot(\bar{\nabla}\cdot(\eta\bar{\nabla}\mathbf{u})) \tag{6.3}$$

From Eq.(6.1) to Eq.(6.3), a generalised transport equation for a general variable, ϕ, (e.g. $\phi=1$ in Eq.(6.1), $\phi=\mathbf{u}$ in Eqs.(6.2) and (6.3) respectively), can be written as follows:

$$\frac{\partial(\rho\phi)}{\partial t}+\bar{\nabla}\cdot(\rho\phi\,\mathbf{u})=\bar{\nabla}\cdot(\Gamma\bar{\nabla}\phi)+S_{\phi} \tag{6.4}$$

where Γ is the appropriate coefficient for the diffusion of ϕ and S_{ϕ} represents a source term for the variable, ϕ.

6.2.2. Scalar Quantity

The generalised transport equation (Eq. 6.4) may also be applied to the transport of passive scalars and effectively trace their progress through the solution domain. However, it is the flow equations which are difficult to solve; the momentum equations have a non-linear inertial term which gives rise to mathematical and numerical difficulties. The pressure terms in the momentum equations also require special

treatment. In our specific case, the situation is even more difficult because the flow compressible (i.e. it has a variable density) and mass sources are distributed throughout the computational domain. However, once the flow distribution has been solved, then, it is relatively easy to impose any passive scalar field on to it and find how it is advected by the flow. The flow field determines how the passive scalar is advected within the computational domain, while being unaffected by it. Steady-state conservation of the scalar quantity is defined as:

$$\bar{\nabla}\cdot(\rho\psi)=0 \tag{6.5}$$

The distribution of a passive scalar, ψ, obeys Eq.(6.4), i.e.

$$\frac{\partial(\rho\psi)}{\partial t}+\bar{\nabla}\cdot(\rho\psi\mathbf{u})=\bar{\nabla}\cdot(\Gamma\bar{\nabla}\psi)+S_{\psi} \tag{6.6}$$

where S_{ψ} is a source term and Γ is a diffusivity coefficient, which accounts for both turbulent and molecular effects. For instance, the scalar, ψ, could be the temperature of the fluid, in which case, the above equation would describe the temperature distribution in the system.

6.2.3. Commercial CFD Code

In this work the commercial CFD code, CFX (developed by *AEA Technology*) version 4.3, is used to study the flow distribution over a distillation tray. There are other CFD codes similar to CFX available on the market, each code useing different algorithms to solve the conservation equations described earlier. CFX follows the finite volume method of solving the partial differential equations. Body fitted co-ordinate systems are adopted. Block-structured grid is used in CFX as a discrete representation of the geometry on which the problem is to be solved. A detailed description of the methods used in CFX can be found in the CFX manual.

6.3. Multiphase Modelling using the Heterogeneous Model

In theory, multiphase modelling is no different to that for single-phase flow. Conservation equations such as Eqs.(6.1) to (6.3) can be written for each phase involved in the flow field and the only additional information required is the relationships for the

interactions between the phases (e.g. interfacial friction factor, ...etc). In real life, such *closure* relationships are either unclear or unknown and this is what makes multiphase modelling difficult. Over the years, engineers have come up with various techniques to overcome these difficulties. It is understood that, although some of these techniques may not represent the physics in reality, the results are still considered to be very useful in giving insights into the phenomena. In what follows, Section 6.3.1 outlines the approaches which were undertaken by Daly (1997) and Fischer (1999) as part of the work under the ASID Consortium. The specific problem of determining the interfacial drag law is discussed in Section 6.3.2. Section 6.3.3 describes the new work performed in the present project, on the MUSIG algorithm.

6.3.1. Heterogeneous Model

The most comprehensive way of modelling the two-phase flows above a distillation tray is by describing the fluid motion for each phase separately. There are two adequate types of descriptions for such cases, i.e. the Eulerian-Lagrangian (liquid-gas) or the Eulerian-Eulerian description. In the former case, the great challenge would be the description of the trajectory of each bubble coming out of holes or slots from the tray floor. This would not only demand a huge computing power, but it could also give rise to other undesired problems such as instability or non-convergence of the solutions. Lapin and Lübbert (1994, 1996) argued that the inclusion of such detailed descriptions (of each bubble) in the model might be unnecessary. Therefore, the Eulerian-Eulerian approach was adopted by the ASID consortium research group to develop a heterogeneous model.

The Eulerian-Eulerian approach (known as the *two-fluid* model) considers each phase as an interpenetrating continuum. For the case of the gas-liquid flow on a tray deck, two sets of conservation equations (considering mass and momentum only) can be written as follows:

- **Gas phase:**

Mass: $$\frac{\partial(\rho_G \varepsilon_G)}{\partial t} + \bar{\nabla} \cdot (\rho_G \varepsilon_G \mathbf{u}) = 0 \qquad (6.7)$$

Momentum: $$\frac{\partial(\rho_G \varepsilon_G \mathbf{u})}{\partial t} + (\rho_G \varepsilon_G \mathbf{u}) \cdot \bar{\nabla}\mathbf{u} = \rho_G \varepsilon_G \mathbf{g} - \varepsilon_G \bar{\nabla} p + \bar{\nabla} \cdot (\eta \varepsilon_G \bar{\nabla}\mathbf{u}) + \mathbf{M}_{GL} \quad (6.8)$$

- **Liquid phase:**

Mass: $$\frac{\partial(\rho_L \varepsilon_L)}{\partial t} + \bar{\nabla} \cdot (\rho_L \varepsilon_L \mathbf{u}) = 0 \quad (6.9)$$

Momentum: $$\frac{\partial(\rho_L \varepsilon_L \mathbf{u})}{\partial t} + (\rho_L \varepsilon_L \mathbf{u}) \cdot \bar{\nabla}\mathbf{u} = \rho_L \varepsilon_L \mathbf{g} - \varepsilon_L \bar{\nabla} p + \bar{\nabla} \cdot (\eta \varepsilon_L \bar{\nabla}\mathbf{u}) - \mathbf{M}_{GL} \quad (6.10)$$

Eqs.(6.7) to (6.10) are similar to Eqs.(6.1) and (6.2); the differences are the inclusion of the volume fraction of each phase (ε_G and ε_L) and the momentum transfer between the two phases. The IPSA algorithm (Spalding, 1976) is used to couple the above equations for a stable solution within an appropriate convergence.

6.3.2. Interphase Drag Law

In the ASID consortium work by Daly (1997) and Fischer (1999), an interphase drag coefficient of 0.44 was applied as the closure relationship for the momentum transfer. An apparent average bubble size has to be specified in the code so that the interfacial drag force can be calculated. The κ-ε model is used to describe the liquid-phase flow while the laminar model is used for the gas phase.

The physical situation of gas flowing in a direction perpendicular to the liquid flow poses a typical problem to the CFD code. The resultant steady-state snapshot would be that nearly all the liquid would be lifted by the vapour momentum and this is clearly incorrect. To overcome these difficulties, the top surface, where the gas is about to enter the tray above, is defined as an impermeable but frictionless wall so that the liquid is restricted to leave from the outlet downcomer. Three Fortran subroutines have been used to modify the way of modelling the gas flow and thus to improve the simulation. These subroutines are briefly described below.

USRSRC: The gas flow is modelled as an internal source and sink within the geometric domain by this subroutine rather than specifying the flowrate in the main code (known as the "command file" in CFX). The gas inlet mass flowrate is

given in the USRTRN subroutine and all the gas is taken out at the defined outlet (at the top of the tray) by the DEGAS subroutine.

USRTRN: This subroutine stores the information of the locations for gas inlet where the mass flowrate (per cell of the grid) and injection velocity are also specified here.

DEGAS: All the gas at the top surface is to be taken off from the domain by this subroutine.

Figure 6.1 is a typical CFD result, obtained by Fischer (1999), of a simulation based on the geometry of the CRODIS facility (Chapter 3). The figure presents the liquid volume fraction profile above the tray with the gas phase velocity vectors shown in black arrows.

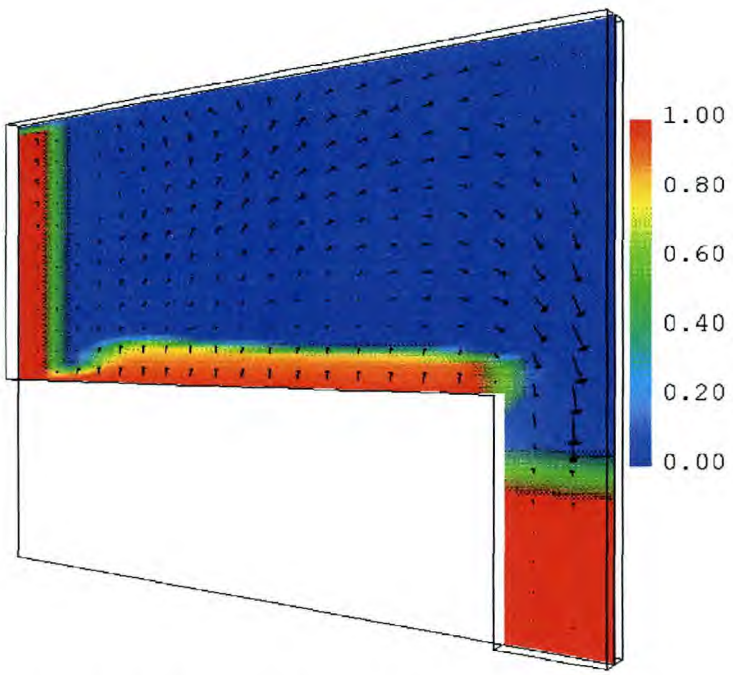


Figure 6.1. Liquid volume fraction profile of a heterogeneous model with arrows representing gas phase velocity; gas superficial velocity = 2 m/s and liquid volumetric flowrate = 1.35×10^{-4} m^3/s (Fischer, 1999)

Similar simulations were also performed for the 2.44m distillation simulator in Aston University and a typical set of results is shown in Figure 6.2.

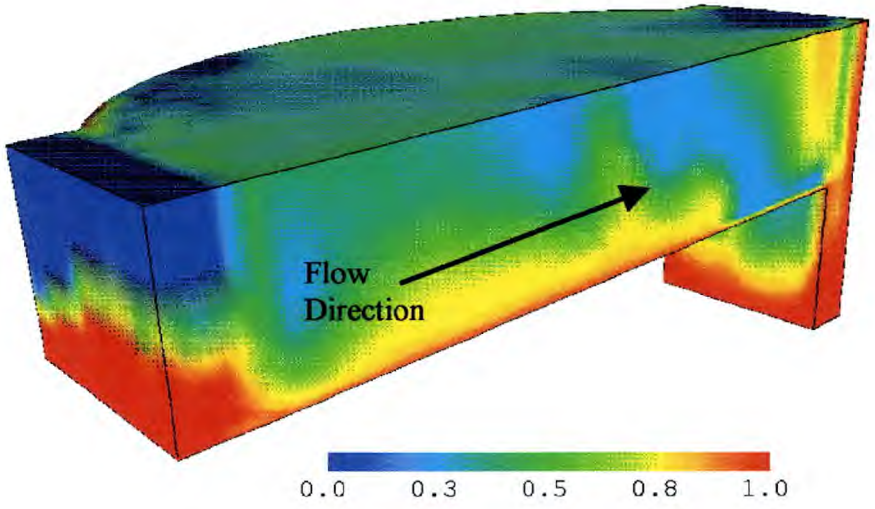


Figure 6.2. Heterogeneous modelling on the 2.44m rig at Aston University (taken from Fischer, 1999)

The results in Figures 6.1 and 6.2 show reasonable agreement with the experimental observations. However, there are still a few problems with these heterogeneous models:

1. The interphase drag law was developed for a single bubble phenomenon and it may not be appropriate for the case of a distillation tray. The drag force is usually over-estimated with normal sizes of bubble diameter.
2. It is necessary to reduce the mass flowrate of the gas phase by a certain factor (in the USRTRN file) so that the drag force is reduced.
3. In order to achieve sensible results for the above simulations, an exaggerated bubble size has to be defined. This is also due to the inappropriate drag law used in the code. The use of larger bubble sizes can reduce the interfacial area and therefore give a reduction in the drag force.

The search for a more appropriate constitutive relationship to replace the drag law used in the ASID consortium work seems to be the next step forward. Such an example can be found in Krishna *et al* (1999) where the authors adopted a slip velocity approach on determining a drag coefficient. The relationship is independent of bubble size, and it requires an empirical correlation for the liquid fraction (Bennett *et al*, 1983) in order to calculate the slip velocity. A drawback of the Krishna *et al* model is that the geometry is very over-detailed and therefore powerful computing hardware is required.

6.3.3. The MUSIG Model

As applied in the work summarised above, the heterogeneous model assumes that the dispersed phase has bubbles of similar size and shape (e.g. spherical bubble with a diameter specified by the user). In reality, especially for two-phase flow on a distillation tray, this is clearly incorrect. There will be a distribution of bubble sizes, and this distribution will develop with position. To overcome this problem, the MUltiple-SIze-Group (MUSIG) model developed by Lo (1996) may be used which allows, in principles, the possibility of describing a two-phase system with a wide spectrum of particle sizes in the dispersed phase. The model divides the dispersed phase particles (e.g. bubbles) into several size groups and the fraction of each group within the dispersed phase is treated as a scalar quantity in the CFD code. The number of bubbles in each group is subject to change due to the coalescence and break-up mechanisms provided in the model. A very important advantage of the MUSIG model is that it assumes that all bubble velocities are the same so that it is only necessary to solve one set of momentum equations for all the groups of bubbles. However, this also means that the interphase drag law is still of the type described in the last section, i.e. relating a mean bubble size to a drag coefficient.

For each size group-i within the gas phase, the continuity relationship is obeyed and Eq.(6.7) can be modified as follows:

$$\frac{\partial(\rho_G f_i \varepsilon_G)}{\partial t} + \bar{\nabla}\cdot(\rho_G f_i \varepsilon_G \mathbf{u}) = S_i \qquad (6.11)$$

where S_i is the additional source term for the size group-i and f_i is the fraction of the group-i within the gas phase.

In Eq.(6.11), the source term is just a simple population balance under the competition between two mechanisms: bubble coalescence and break-up.

- **Coalescence**: The action of bubble coalescence in turbulent gas-liquid dispersions is described in the model by Prince and Blanch (1990). The model states that the coalescence occurs when the liquid film between two bubbles drains until it reaches a critical thickness and then ruptures so that the two bubbles join together. The coalescence process is determined by a

collision rate and a collision efficiency. Three mechanisms for collisions are considered in the model and they are turbulence, buoyancy, and laminar shear.

- **Break-up**: A theoretical model developed by Luo and Svendsen (1996) is used to describe the drop and bubble break-up in turbulent dispersions. The theory is based on isotropic turbulence and the probability of breaking depends on the energy and the frequency of eddies hitting the surface of a bubble. The merit of the model is that it contains no unknown or adjustable parameters and no predefined daughter bubble size distributions are required (most of other models do need such distributions).

In both models, binary interactions are assumed, i.e. two bubbles coalescing into one larger one or one large bubble breaking-up into two smaller ones.

In the CFX version 4.3, the MUSIG model has been integrated into the standard code so that no additional subroutine is required. However, the user is able to "increase" or "decrease" the strength of any of these two mechanisms by giving either a coalescence or break-up coefficient (the default is unity for both coefficients).

The CFX code with the MUSIG model has been applied to simulate air-water system in the CRODIS facility and Figures 6.3 to 6.14 show the results at the centre of the channel. These have been obtained for an air superficial velocity of 0.1m/s and a water volumetric flowrate of 2.17×10^{-4} m^3/s. The air superficial velocity was purposely set to a low value to avoid the problem of gas lifting the liquid on the tray. The drag coefficient was set at 0.44 with a mean bubble diameter of 10mm. The main block (where the actual position of the tray is) has a grid of 20×6×25 cells to fit its geometry of 0.95×0.06×0.5m respectively and the outlet weir height is 0.038m. The MUSIG model was set to have 10 equally divided bubble size groups, from 0mm to 30mm. The coefficients for coalescence and break-up were left at their default values of unity. At the air inlet, the boundary condition was set so that all the bubbles were in Group 1 (0-3mm). The exercise was carried out purely to examine the applicability of the MUSIG model, therefore unlike the case described in the previous section, no additional user Fortran subroutine was used for this simulation.

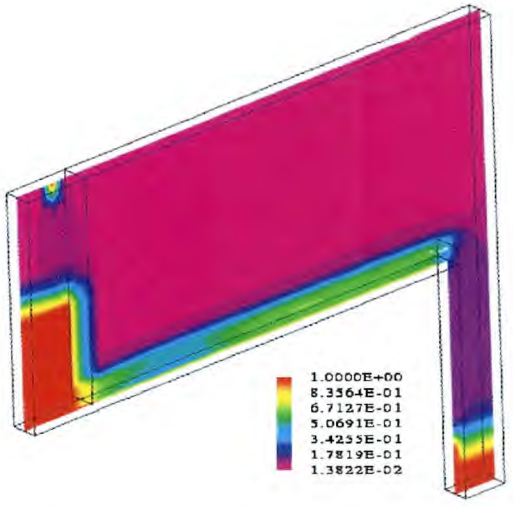


Figure 6.3. Liquid volume fraction profile of a heterogeneous model with the MUSIG model

A clear layer of froth above the tray floor is clearly shown in Figure 6.3 above and the boundary between the froth and the gas continuous region (shown in pink colour) can also be identified.

The bubble size distributions are shown in Figure 6.4 to 6.14. There is a lot of information in these figures, however, it is important to stress that the principle of the MUSIG model is to determine a size distribution within the dispersed phase. Thus, only the distribution within the froth area would be meaningful since everywhere outside the froth region, gas becomes the continuous phase. The results show that the majority of the bubbles in the froth region are of Group 1 regardless of the position, i.e. the initial bubble size specified as the boundary condition at the air inlet. This is because of the low air velocity used in the simulation where the system is operated in the bubble regime and generally, less bubble coalescence or break-up would occur. However, in the region near to the outlet weir, there seem to be larger bubbles, this is clearly shown in Figures 6.5 to 6.8 (Group 2 to Group 5 respectively). For a long single-pass tray, an hydraulic gradient between the inlet and outlet of the tray exists. The gas would preferentially pass through the tray at the locations near to the outlet weir due to the lower hydrostatic resistance. Thus, the local turbulence would promote the smallest bubbles (Group 1) to coalesce to form larger ones.

The sauter mean bubble size distribution is shown in Figure 6.14 to provide a general view of average bubble size on a tray. As expected, the gas continuous area (i.e. above

froth) contains mostly the largest bubbles and the froth body consists of smaller ones. It is also interesting to note that at the bottom of the outlet downcomber, some small bubbles are trapped inside the liquid which, in theory, is about to enter the tray below. This is similar to a physical situation occurred in the tray operation.

Some doubts may arise from the distribution information shown in some parts of the pictures (e.g. inlet downcomer and top left corner of the tray area). These are either due to the initial conditions specified or the nature of pressure boundary condition used for the gas outlet at the top of the surface. Once again, the main focus of the results lies in the froth body.

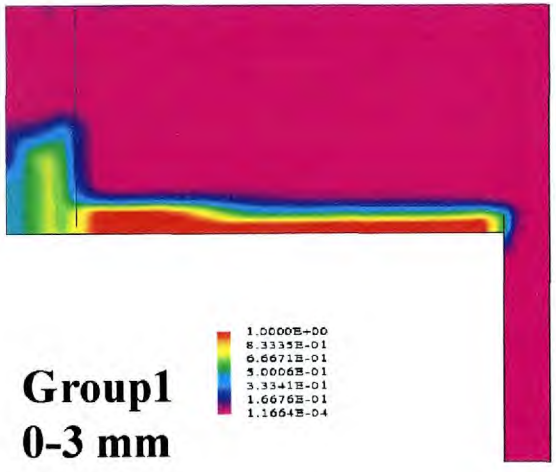


Figure 6.4. MUSIG group 1

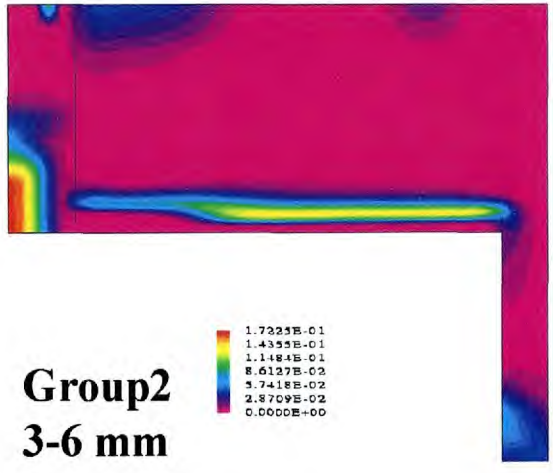


Figure 6.5. MUSIG group 2

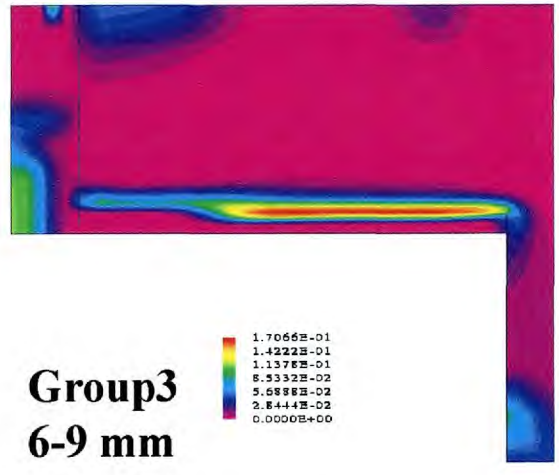


Figure 6.6. MUSIG group 3

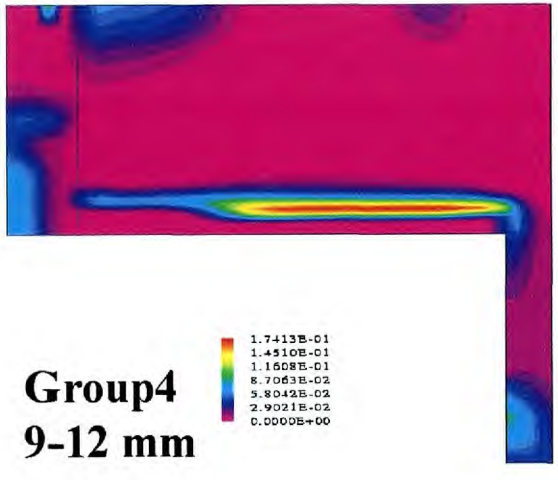


Figure 6.7. MUSIG group 4

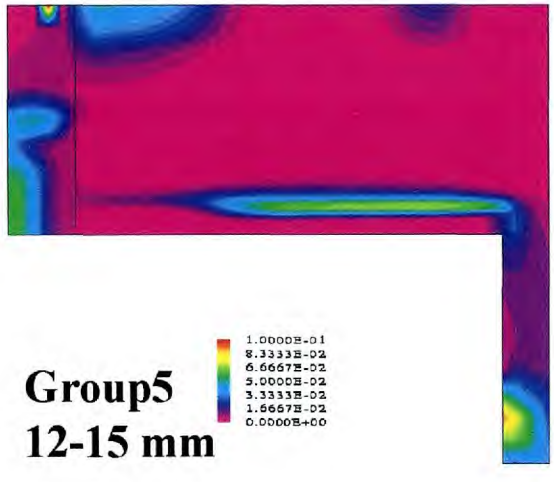


Figure 6.8. MUSIG group 5

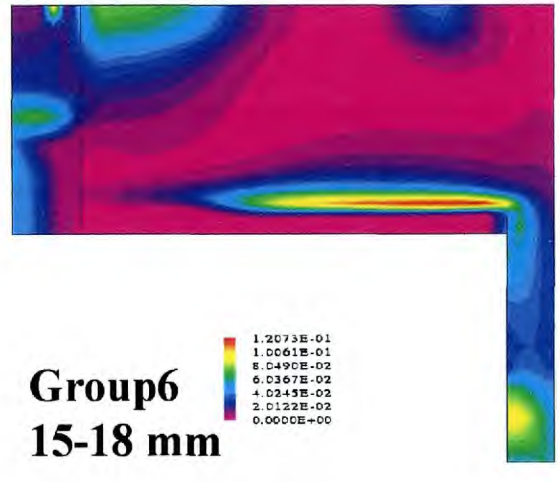


Figure 6.9. MUSIG group 6

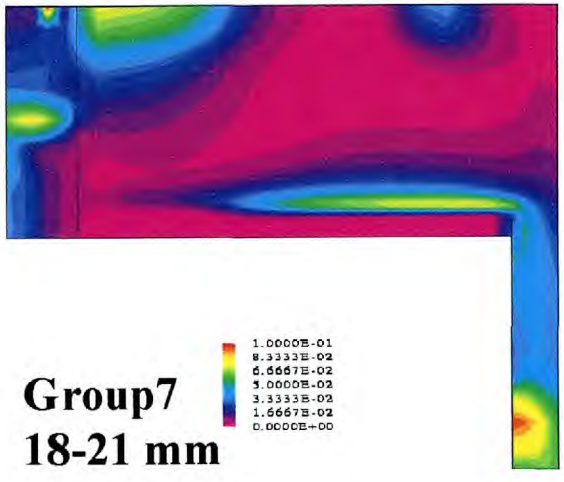


Figure 6.10. MUSIG group 7

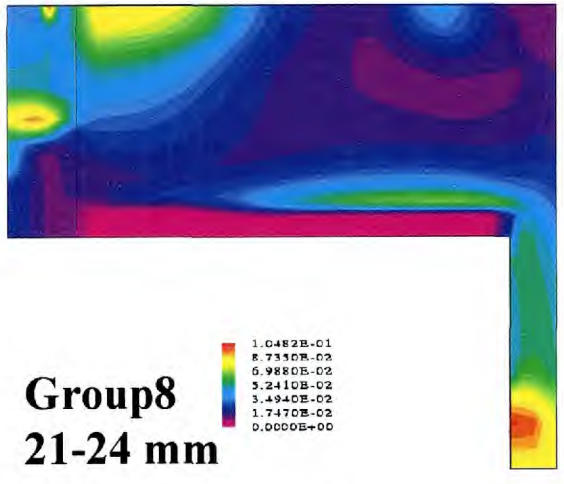


Figure 6.11. MUSIG group 8

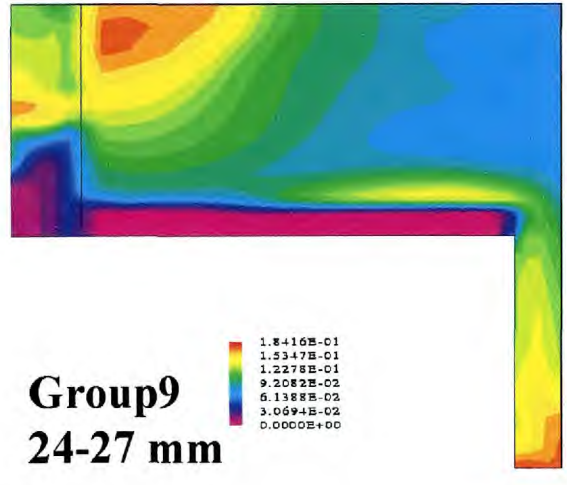


Figure 6.12. MUSIG group 9

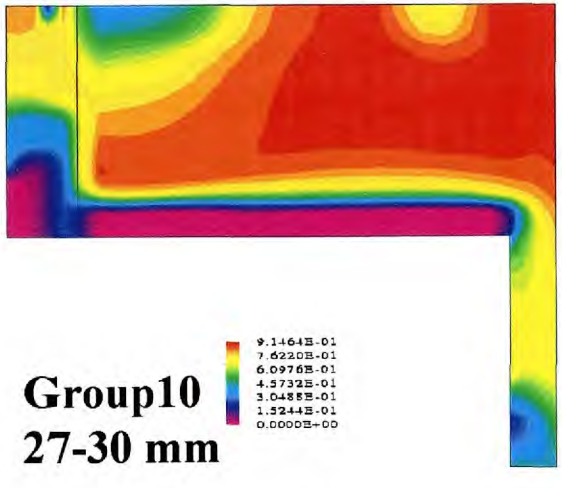


Figure 6.13. MUSIG group 10

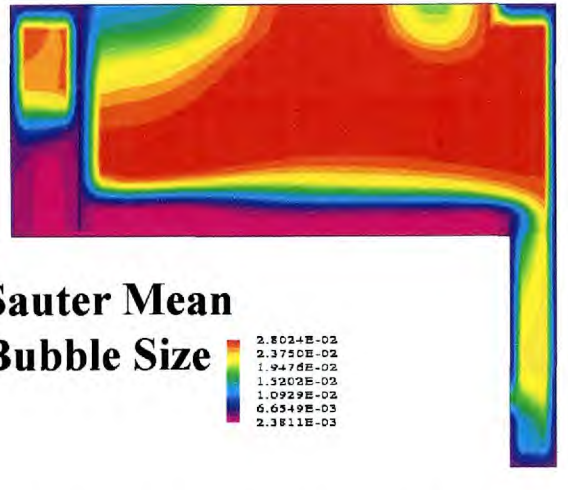


Figure 6.14. Sauter mean bubble size distribution

Max Diameter 30 mm
10 Equal Divisions

Coalescence Coeff. = 1.0
Break-up Coeff. = 1.0

6.4. Homogeneous Model

In the application of the homogeneous model, the computational domain was limited to the tray area because the nature of the model makes it unsuitable to simulate mechanisms such as mixing in the downcomer area. A simple illustration of the model is shown in Figure 6.15. Two "phases" (i.e. a froth of specified densities and a vapour) enter the computational domain in parallel, one above the other and both phases are given the same inlet velocity to the domain. The height at which the froth phase is introduced into the domain is decided by an empirical correlation for prediction of froth height (e.g. Stichlmair's correlation, 1978).

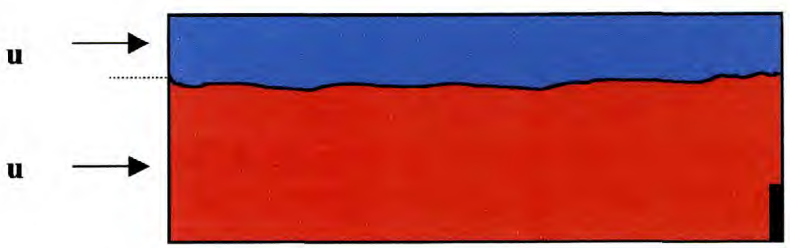


Figure 6.15. A simple side-view geometry of the homogeneous model

The free-surfaces between the liquid and vapour phases are deduced by computing volume fractions and the interface is placed at the location where the fraction of the froth "phase" changes from unity to zero. The froth properties are determined from the following equations:

$$\rho_m = \varepsilon_G \rho_G + \varepsilon_L \rho_L \tag{6.12}$$

$$\eta_m = \left(\varepsilon_G / \eta_G + \varepsilon_L / \eta_L \right)^{-1} \tag{6.13}$$

where ρ_m is the froth density and η_m is the froth viscosity.

Note that a number of alternative models are available for η_m; this one chosen here is based on reciprocal weighting on void fraction ε_G. The void fraction in the froth is given by a correlation (see Chapter 2).

The boundary between the two regions tends to be smeared because of the diffusive nature of the numerical schemes used. The CFX code has a "surface sharpening" algorithm which attempts to redress this effect. However, some smearing still occurs.

The homogeneous model approach was investigated by Fischer (1999). As stated above, the model does not give any variation of void fraction (mean density) within the froth. The froth is considered to be behaving as a single phase fluid with suitably averaged properties. Fischer (1999) attempted predictions of the void profile in the froth layer by combining the homogeneous model with an "algebraic slip model" which was used to account for the change of the liquid volume fraction due to the vertical gas flow. The slip velocity components are specified as scalar quantities in a user Fortran subroutine (USRSLP) in CFX and they are used to modify the froth velocity in the homogeneous model calculation. These modified velocity components (of the liquid) are then used in the volume fraction equations so that a more realistic volume fraction profile can be obtained. Such an example is shown in Figure 6.16. however, though these results are interesting, this combined approach was not used in the present work since it was considered too complex for regular practical application.

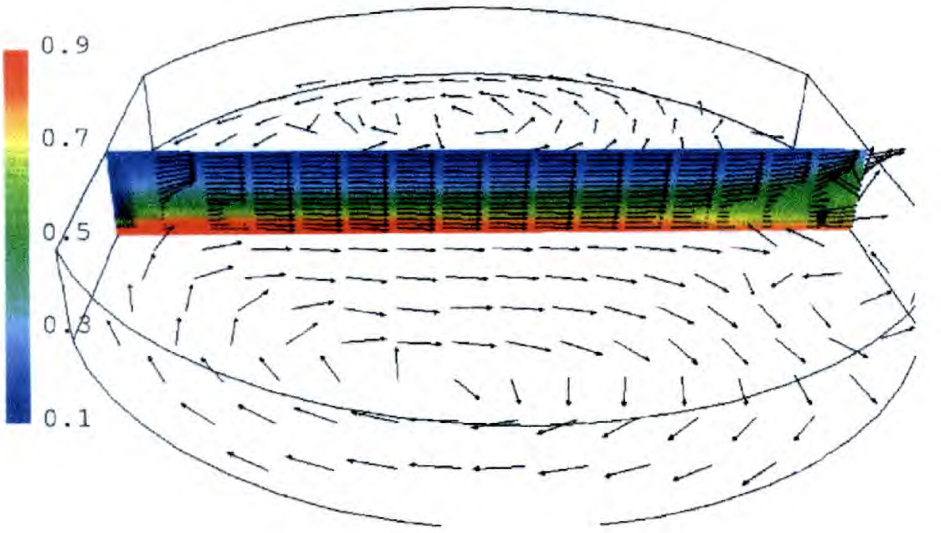


Figure 6.16. Homogeneous modelling of the 2.44m rig at Aston University: (1) liquid velocity vectors at the tray floor and central channel, (2) liquid volume fraction profile at the central channel. (results taken from Fischer, 1999)

6.5. CFD Application – Fluid Age Distribution

The ultimate goal of the CFD simulation on distillation trays is to understand how the flow distribution is and to relate such information to the performance of the tray in terms of mass transfer. A particularly useful concept for such a relationship is that of fluid age or residence time, which is a measure of the time that a fluid element has remained on the tray since it entered. In terms of CFD, the simplest way of considering the problem is to compute how old the fluid element is throughout the computational domain, if it had zero age when it entered the domain.

In the present work, the robust homogeneous framework is adopted for such a calculation. The distribution of this 'age of fluid', θ, can be computed by solving the scalar equation, Eq.(6.6), with the following assumptions:

- The *d/dt* term is set to zero, i.e. steady state.
- The diffusion coefficient is set to zero so that only the advection term remains in the equation.
- The source term at the right hand side of Eq.(6.6) is set to be equal to the fluid density so that the scalar quantity (i.e. θ) can be regarded as the fluid age. Thus, the "age of fluid" scalar equation becomes:

$$\bar{\nabla}\cdot(\rho\theta\mathbf{u}) = \rho \tag{6.14}$$

This equation effectively models the distribution of the age of the fluid within the computational domain. For example if the velocity is reduced to small values in a particular region, then the θ value increases rapidly, as might be expected in a recirculation or stagnation zone. Eq.(6.14) requires appropriate boundary conditions; these are:

$$\theta = 0 \text{ at all inlets}$$
$$\theta = 0 \text{ and } \bar{\nabla}\cdot\theta = 0 \text{ at the top outlet}$$

Fischer (1999) carried out a series of tests on the residence time distributions using the 2.44m tray of the Aston University distillation simulator. The liquid residence times were determined by the video images taken from the top of the column. The

corresponding CFD simulations were performed and the results showed some encouraging agreement with the experimental observations. Figure 6.17 shows a typical result of a CFD simulation where the liquid residence time distribution has been plotted just below the free surface (i.e. top of the froth).

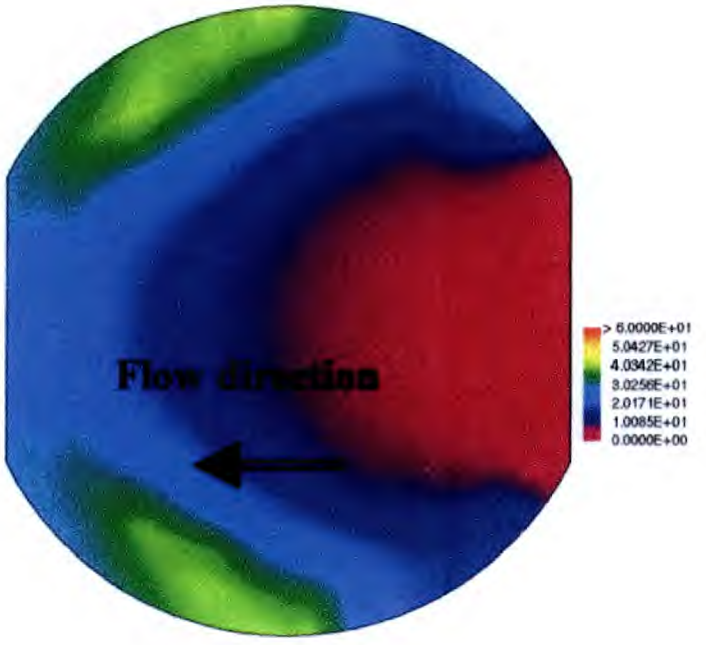


Figure 6.17. Residence time distribution for the 2.44m rig at Aston University (results taken from Fischer, 1999)

Figure 6.17 presents a snapshot of what could be observed in the experiment. Of course, such distribution picture would vary from tray floor to the top of the froth, and the advantage of a CFD simulation is to allow user to have such the view in all three dimensions. Thus, the liquid residence time distributions can also be plotted in the plane of the outlet weir (i.e. the exit of the computational domain).

6.6. Summary

The available methods for the CFD modelling of two-phase flows on distillation trays have been described in this chapter and a qualitative evaluation of these methods has been summarised from the work by Fischer (1999).

Although it is attractive to model the situation using the inter-penetrating heterogeneous approach, the current understanding of the physics of the two-phase flow makes it hard for this approach to be applied confidently. The other major drawback for this type of model is the difficulty on obtaining stable and convergent numerical solutions.

In contrast, the "homogeneous" (or VOF) approach with numerical techniques (e.g. coupled with some empirical correlations) lead, as we will see, to a reasonable approximation of the real physical situation and the numerical schemes tend to be easier. Thus, this methodology was chosen for further development in the present work.

An important step in the application of the homogeneous method to predicting tray efficiency is to establish the residence time of the liquid on the tray. CFD prediction of the distribution of the residence time has been obtained by the introduction of a scalar quantity, called the "age of fluid", in the transport equations of a homogeneous model.

Chapter 7

Prediction of Distillation Tray Performance

- A New Approach based on CFD Studies

7.1. Introduction

The basic elements of the applications of CFD methods to predict flow on distillation trays are presented in Chapter 6. In this present chapter, a method by which tray performance may be predicted using a simplified CFD approach is presented. The steps in this approach are as follows:

(1) The froth density and an initial value of the froth height are predicted using existing empirical correlations. The froth mixture is then treated as a single phase fluid having suitably averaged density and viscosity.

(2) The flow of the froth over the tray is predicted using the "homogeneous" model described in Section 6.4. This allows the flow velocity to be determined as a function of position on the tray. Most importantly, the distribution of the residence time of the liquid on the tray is obtained.

(3) Gas-liquid contact on the tray is assumed to occur in a "box" of froth bounded by the tray floor and the froth/vapour interface and leaving infinitesimal cross sectional area in the plane parallel to the tray. The liquid in this "box" is assumed to be well mixed in the vertical direction but mixing with adjacent boxes is neglected. The vapour phase passes vertically through the "box", exchanging mass with the liquid and escaping into the vapour space at the top of the "box". The liquid flow is visualised as the motion of successive "boxes" from the tray inlet to the tray outlet with a distribution of residence times corresponding to that calculated from the CFD analysis.

(4) The rates of mass transfer in the moving "boxes" are calculated using existing correlations. These correlations need values for interface area and the interface area is also determined from a correlation. This allows the calculation of the components concentration in the liquid in the box and the mean outlet concentrations can be obtained by summing over all the boxes (taking account residence time distribution).

The above procedure allows the calculation of mean compositions of the vapour and liquid leaving the tray, knowing the inlet values.

The data obtained can be expressed as tray efficiencies (see Chapter 2) or simply as outlet concentrations. Quarini (1999) criticises the use of efficiency values (point and tray efficiencies) stating that the heritage of efficiency is perhaps a bar to progress. In the present work, the results are expressed both in terms of efficiency and outlet concentrations.

This chapter is structured as follows:

(1) As a necessary input to the calculations of mass transfer rates, diffusion coefficients are required for both liquid and vapour phases. The approaches taken here in the calculation of diffusion coefficients are described briefly in Section 7.2.
(2) Another essential input in distillation calculations is, of course, vapour-liquid equilibrium data. The methods adopted here are presented in Section 7.3 which also reviews the physical property models (viscosity and surface tension).
(3) Section 7.4 presents the basic mass transfer methods starting with the selected relationships for mass transfer coefficient and interfacial area. The derivation of the expression for the variation of the liquid mole fraction with time in the "box" described above is also presented in this section.
(4) In Section 7.5, the bases of the CFD methodology are discussed covering input information, simulation results for residence time distribution and the method of relating this residence time distribution to the outlet composition of the vapour and liquid.

(5) Finally, Section 7.6 summarises the approach and gives a flow chart for the methodology.

7.2. Estimation of Diffusion Coefficients

Prediction methods for diffusion coefficients for binary gas and liquid mixtures are well established at conditions of low to moderate pressure. Most of the commonly used methods have been reviewed in Sections 2.5.2 and 2.5.3. This section outlines the prediction methods (with appropriate correction terms) which have seen used in the present methodology.

7.2.1. Diffusion Coefficients in Gas Mixtures

The correlation for predicting the gas phase diffusion coefficient by Fuller *et al* (1966) is based on a large databank covering extensive binary systems and it is the most widely recommended method in the literature. This makes it ideal to be the prediction method for the gas phase diffusion coefficient. The working equation of the correlation by Fuller *et al* (1966) is given below and the complete description of the method can be found in Section 2.5.2.1.

$$D_{AB} = \frac{0.00143\,T^{1.75}}{PM_{AB}^{1/2}\left[(\Sigma v)_A^{1/3} + (\Sigma v)_B^{1/3}\right]^2} \tag{2.83}$$

For high-pressure gas mixtures, the variation of diffusion coefficient with pressure is not well predicted by Eq.(2.83). The method suggested by Takahashi (1974) is chosen to provide a correction term to the predicted diffusion coefficient for high-pressure cases. This method is described in Section 2.5.2.3. Though the effect of temperature, predicted by Eq.(2.83), does not always fit the data precisely, no correlation has been introduced to take account of this. Also it is assumed that the diffusion coefficient is independent of concentration, though, again, variation may exist. The correction for temperature and concentration are, however, small compared to the correlation required for pressure.

7.2.2. Diffusion Coefficients in Liquid Mixtures

The empirical correlation by Wilke and Chang (1955) is chosen for the prediction of the liquid phase diffusion coefficients at infinite dilution. It is based on a wide range of data points and the equation retains a general form of the theoretical relationship derived by Stoke and Einstein (Eq.2.99) which makes it suitable for the purpose of the new methodology. The working equation of the Wilke-Chang (1955) correlation is given below and the complete description of the method can be found in Section 2.5.3.1.

$$D_{AB}^{\circ} = \frac{7.4\times10^{-8}(\phi M_B)^{1/2}T}{\eta_B V_A^{0.6}} \tag{2.100}$$

Unlike gas mixtures, the liquid phase diffusion coefficient depends very much on the concentration. The relationship by Vignes (1966) is chosen to account for the concentration effect in the present methodology and this method is described in Section 2.5.3.5.

Other effects such as temperature and pressure on liquid diffusion coefficients are not well studied. It is generally believed that these effects are already accounted for in the viscosity and temperature term in the equation of the Wilke-Chang correlation. Therefore, no additional corrections are added here.

7.3. Vapour-Liquid Equilibrium and Transport Property

The commercial process simulator, AspenMax™, which has a physical property databank built-in, was used as a tool for establishing the VLE relationships and estimating transport properties for a given system. Within AspenMax™, a standard flash calculation allows users to generate the VLE relationship according to the thermodynamic property models specified. The recommendations on choosing such a model is given in Section 7.3.1. Although AspenMax™ is used to predict the VLE relationship, validation against experimental data (under similar conditions to the system being investigated) is always recommended if such data is available.

Transport properties can also be estimated in AspenMax^{TM} and the available methods are given in Sections 7.3.2.

7.3.1. Recommendations on VLE Relationships

Given the large number of available models for predicting the VLE relationship (see Section 2.4.2), it is necessary to establish some general rules on choosing the appropriate ones. A brief summary is given below to form a recommended framework for the present methodology. However, a more detailed guideline is given in the AspenMax^{TM} user manual and this should be followed closely.

High pressure: (e.g. $P > 15$ bars)
Since all the activity coefficient models in AspenMax^{TM} are only applicable to a pressure of up to 10-15 bars, any high-pressure VLE relationship will need to be predicted by an equation of state (EOS) method with binary interaction parameters.

$\Rightarrow$ Peng-Robinson or Redlich-Kwong-Soave methods are recommended.

Low to moderate pressure: (e.g. $P < 15$ bars)
For non-polar or mildly polar components,

Vapour and liquid phases $\Rightarrow$ EOS with binary interaction parameters

For polar and non-ideal mixture,

Vapour $\Rightarrow$ EOS with binary interaction parameters

Liquid $\Rightarrow$ Activity coefficient models such as UNIFAC,...etc

7.3.2. Transport Property Models

The information used for the transport properties of a system is also very important. In the present methodology, three particularly important properties are diffusion coefficient, viscosity and surface tension and these can be predicted by various transport property models available in AspenMax^{TM}. These transport property methods are complementary to the thermodynamic models (described in Section 2.4.2) specified by users in an AspenMax^{TM} simulation. The information on the combinations of the thermodynamic and transport property models is given in the AspenMax^{TM} reference manual.

For gas phase diffusion coefficients, AspenMax™ adopts the method by Wilke and Lee (1955) for low-pressure conditions and Dawson-Khoury-Kobayashi's (1970) correction method for high pressure cases. For liquid phase, the Wilke-Chang (1955) method is used in AspenMax™. However, this method does not seem to account for the effect of concentration correctly (as described in Section 2.5.3.5). It is believed that methods summarised in Section 7.2.2 will provide more accurate results on diffusion coefficients for both phases and therefore they should be used instead of AspenMax™.

A number of methods are available in AspenMax™ for estimations of viscosity and surface tension and a full list of available methods are given as follows:

- **Vapour Viscosity**
  - Chapman-Enskog-Brokaw Model
  - DIPPR (Design Institute for Physical Property Data) Model
  - IAPS (International Association for Properties of Steam) Model

- **Liquid Viscosity**
  - Andrade Model
  - API (American Petroleum Institute) Model
  - Letsou-Stiel Model
  - DIPPR (Design Institute for Physical Property Data) Model
  - IAPS (International Association for Properties of Steam) Model

- **Surface tension**
  - API (American Petroleum Institute) Model
  - Hakim-Steinberg-Stiel Model
  - DIPPR (Design Institute for Physical Property Data) Model
  - IAPS (International Association for Properties of Steam) Model

As mentioned earlier, the choices on these transport property models depend entirely on the selected thermodynamic model. For example, the popular Peng-Robinson EOS model uses the following methods for predicting transport properties: Chapman-

Enskog-Brokaw Model for vapour viscosity, API Model for liquid viscosity and API Model for liquid surface tension

7.4. Recommendations on Mass Transfer Relationships

This section summarises the distillation tray mass transfer relationships used in the present methodology. The methods for calculating mass transfer coefficients and interfacial area are given in Section 7.4.1 and 7.4.2 respectively. These parameters are used to develop a bridging relationship between mass transfer and residence time of a single fluid element. This relationship is derived and discussed in Section 7.4.3. A key assumption here is the use of constant values for mass transfer coefficient and interfacial area throughout the entire froth.

7.4.1. Mass Transfer Coefficients

The treatment of mass transfer in the methodology presented here is based on the relationships proposed by Stichlmair (1978) which are related to Higbie's penetration theory. A complete description of the relationships is given in Section 2.5.1.4; the mass transfer coefficients can be calculated from

$$k'_G = 2\left(\frac{D_G u_s}{\pi h_f \varepsilon}\right)^{0.5} \quad \text{and} \quad k'_L = 2\left(\frac{D_L u_s}{\pi h_f \varepsilon}\right)^{0.5} \tag{2.73}$$

$$\frac{1}{K_{OG}} = \frac{1}{\rho'_G k'_G} + \frac{m}{\rho'_L k'_L} \qquad \text{(in molar units)}$$

where D_G, D_L are estimated from Section 7.2.

Information on froth height and gas void fraction is required for estimating the mass transfer coefficients and also for other steps in the methodology. The following relationships are used:

- Stichlmair correlation (1978) for ε:

$$\varepsilon_G = \left(\frac{F_s}{F_{s\max}}\right)^{0.28} \qquad \text{only valid for } 0.03 < \frac{F_s}{F_{s\max}} < 0.09 \tag{7.1}$$

- Colwell correlation (1981), is used for predicting ε when Eq.(7.1) is not valid:

$$\varepsilon = 1 - \left[1 + 12.6 \left(\frac{Fr \rho_G}{\rho_L - \rho_G} \right)^{0.4} A_f^{-0.25} \right]^{-1} \tag{7.2}$$

- Stichlmair correlation (1978) for h_f:

$$h_f = \left[h_w + \frac{1.45}{g^{1/3}} \left(\frac{Q_L}{(1-\varepsilon)W} \right)^{2/3} + \frac{125}{g(\rho_L - \rho_G)} \left(\frac{F - 0.2\sqrt{\rho_G}}{\varepsilon} \right)^2 \right] \tag{7.3}$$

where the last term is ignored when $F - 0.2\sqrt{\rho_G} < 0$

More details of the above hydrodynamic correlations can be found in Chapter 2.

7.4.2. Interfacial Area

The Stichlmair's correlation (1978) is used for estimating the interfacial area in the present methodology. The working equations are given below and the complete description of this method can be found in Section 2.5.4.1.

- When $F_s / F_{s\,max} \leq 0.7$:

$$a = a_B - \left(\frac{F_s / F_{s\,max}}{0.7} \right) \left(a_B^* - a_T^* \right) \tag{2.116}$$

- When $F_s / F_{s\,max} > 0.7$:

$$a = \frac{F_s^2}{2\sigma A_f^2} \left[1 - \left(F_s / F_{s\,max} \right)^{0.28} \right] \tag{2.120}$$

7.4.3. Mass Transfer in a Fluid Element

Imagine a "box" of froth containing liquid and vapour as shown in Figure 7.1. The "box" is bounded by the tray surface at the bottom and by the froth-vapour interface at

the top. The sides of the "box" are in contact with other froth "boxes". The cross sectional area of the box in a direction parallel to the tray floor (A) is small and thus only a small element of liquid phase is contained in the "box". It is assumed that the flow of the liquid across the tray can be considered as a flow of a succession of such "boxes" on the tray. The distribution of residence time of the "boxes" is determined from the CFD calculation. The liquid element in the "box" is assumed to remain in the same "box" for the whole of their "box"'s residence time on the tray. There is a continuous flow of vapour into the "box" through the froth – vapour interface. It is assumed that the superficial velocity and inlet concentration of the vapour are constant across the tray.

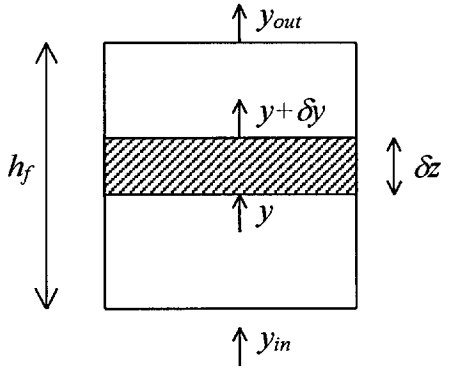


Figure 7.1.
Shaded area represents a small packet of fluid (two-phase), y being the mole fraction of the more volatile component.

We now calculate the concentration of liquid in the "box" as a function of the "box"'s residence time on the tray. We can write an expression as follows for the change of vapour phase concentration δy resulting from the vapour phase flow traversing a distance δz up the box:

$$\begin{aligned} Au_s\rho'_G\delta y &= -K_{OG}A\delta z\, a\left(y-y^*\right) \\ &= -K_{OG}A\delta z\, a\left(y-mx-b\right) \end{aligned} \tag{7.4}$$

Eq.(7.4) can be rearranged to obtain a differential equation for the change of gas phase composition with distance up the "box":

$$\frac{dy}{dz} = -\frac{-K_{OG}\,a}{u_s\rho'_G}\left(y-mx-b\right) \tag{7.5}$$

The change in gas phase concentration from the tray floor to the froth-vapour surface is given by integration of Eq.(7.5) as follows:

$$\int_{y_{in}}^{y_{out}} \frac{dy}{y-mx-b} = \int_{0}^{h_f} -\frac{K_{OG}\,a}{u_s \rho'_G} dz \tag{7.6}$$

Several important assumptions are used in integrating Eq.(7.6):

- The overall mass transfer coefficient, K_{OG}, is assumed to be constant along the vertical direction
- The interfacial area per unit volume, a, remains constant along the vertical direction
- The molar density of the gas mixture, ρ'_G, also remains constant along the vertical direction

With these assumptions, the gas composition at the outlet of the "box" can be obtained:

$$y_{out} - mx - b = (y_{in} - mx - b)e^{-\frac{K_{OG}\,a\,h_f}{u_s \rho'_G}} \tag{7.7}$$

For the liquid phase, the rate of change of liquid concentration with time can be written as:

$$\begin{aligned} \frac{dx}{dt} &= \frac{\text{Rate of absorption of the more volatile component (kmol/s)}}{\text{Total number of moles of liquid in the element (kmol)}} \\ &= \frac{(y_{in} - y_{out})u_s A \rho'_G}{\alpha h_f A \rho'_L} \end{aligned} \tag{7.8}$$

To simplify the algebra in the following equations, let $Z = e^{-\frac{K_{OG}\,a\,h_f}{u_s \rho'_G}}$, so that Eq.(7.7) becomes $y_{in} - y_{out} = (1-Z)(y_{in} - mx - b)$ and this is fed into Eq.(7.8) to obtain a differential equation for the liquid side:

$$\frac{dx}{dt} = \frac{(1-Z)(y_{in} - mx - b)u_s \rho'_G}{\alpha h_f \rho'_L} \tag{7.9}$$

Eq.(7.9) is integrated over the duration time over which the "box" travels on the tray:

$$\int_{x_{in}}^{x_{out}} \frac{dx}{y_{in} - mx - b} = \int_0^t \frac{(1-Z)u_s \rho'_G}{\alpha h_f \rho'_L} dt \tag{7.10}$$

Several further important assumptions are used in integrating Eq.(7.10):

- The assumptions used in integrating Eq.(7.6) are also applied here, i.e. constant values assumed over the whole liquid flow domain
- The molar density of the liquid mixture, ρ'_L, remains constant across the liquid flow domain
- The froth height and liquid fraction of the two-phase froth are assumed to be constant over the tray cross section

The last assumption is, of course, somewhat inconsistent with the CFD calculation in that h_f needs to vary with position to provide a driving force and transport the liquid across the tray. However, the assumption is used to provide a considerable simplification of the mass transfer calculation. The variations of h_f are relatively small and, within the expected accuracy of the method, the assumption has only a small impact.

With these assumptions, the integration of Eq.(7.10) leads to the expression:

$$ln\left(\frac{mx_{in} + b - y_{in}}{mx_{out} + b - y_{in}}\right) = \frac{m(1-Z)u_s \rho'_G}{\alpha h_f \rho'_L} t \tag{7.11}$$

Eq.(7.11) may be rearranged to obtain the outlet liquid composition as a function of its residence time, i.e. the residence time of the "box", counting the element of liquid, on the tray:

$$x_{out} = \left(x_{in} + \frac{b}{m} - \frac{y_{in}}{m}\right) e^{-\frac{m(1-Z)u_s \rho'_G}{\alpha h_f \rho'_L} t} + \left(\frac{y_{in}}{m} - \frac{b}{m}\right) \tag{7.12}$$

The limiting conditions for Eq.(7.12) can be checked by substituting $t = 0$ and $t \to \infty$ into the equation.

- The initial condition: when $t = 0$, $\left[e^{-\frac{m(1-Z)u_s \rho'_G}{\alpha h_f \rho'_L} t}\right] \to 1$, and $x_{out} = x_{in}$

- At the other limiting condition: when $t \to \infty$, $\left[e^{-\frac{m(1-Z)u_s\rho'_G}{\alpha h_f \rho'_L} t} \right] \to 0$, and

$$x_{out} \to \left(\frac{y_{in}}{m} - \frac{b}{m} \right) \qquad \text{i.e.} \qquad y_{in} = mx_{out} + b$$

This result indicates that the outlet liquid reaches equilibrium with the inlet vapour when the liquid remains an infinite period of time on the tray.

Figure 7.2 is an example of calculation done using Eq.(7.12) for a distillation case. As it can be seen clearly, the exit liquid mole fraction of the more volatile component decreases as the liquid stays longer on the tray. Conditions close to equilibrium are reached after about 100 seconds on the tray. More examples of this type of graph are shown in Chapter 8.

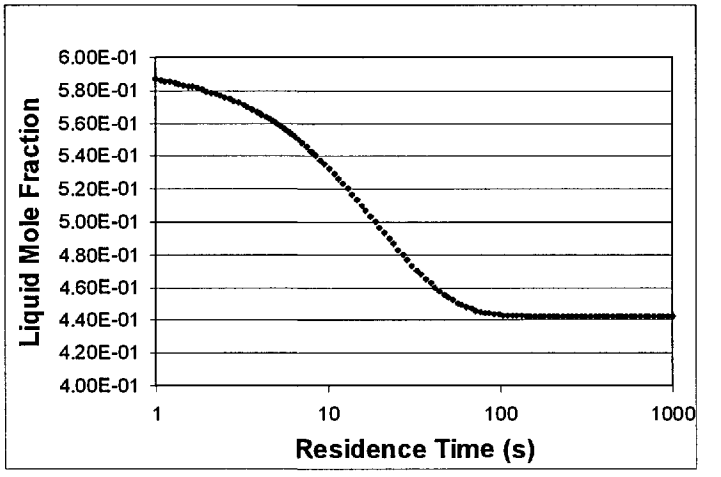


Figure 7.2. Liquid mole fraction profile v.s. residence time for a distillation case

7.5. CFD Studies: Flow Distribution and Residence Time

As described in Chapter 6, a CFD model has been specifically developed for the present methodology. It involves the prediction of flow distribution over a distillation tray in terms of liquid residence time. The relationship between residence time and mass transfer has been established in Section 7.4.3 (Eq.7.12).

For simplicity and robustness, the homogeneous model has been adopted in the present methodology to determine the flow distribution.

7.5.1. Model Input Information

As discussed previously in Chapter 6, the homogeneous model requires "mixing rules" to calculate the density and viscosity of the hypothetical single-phase fluid. The most commonly used relationships for density and viscosity are given by Eqs.(6.14) and (6.15):

$$\rho_m = \varepsilon_G \rho_G + \varepsilon_L \rho_L \tag{6.14}$$

$$\eta_m = \left(\varepsilon_G / \eta_G + \varepsilon_L / \eta_L \right)^{-1} \tag{6.15}$$

where ρ_m and η_m are the density and viscosity of the hypothetical single-phase fuid, α is the liquid holdup above the distillation tray.

These equations require knowledge of the void fraction, ε_G. This is predicted from the correlations given in Section 7.4.1.

7.5.2. Simulation Results

Figure 7.3 shows a typical liquid residence time distribution result from a CFD simulation.

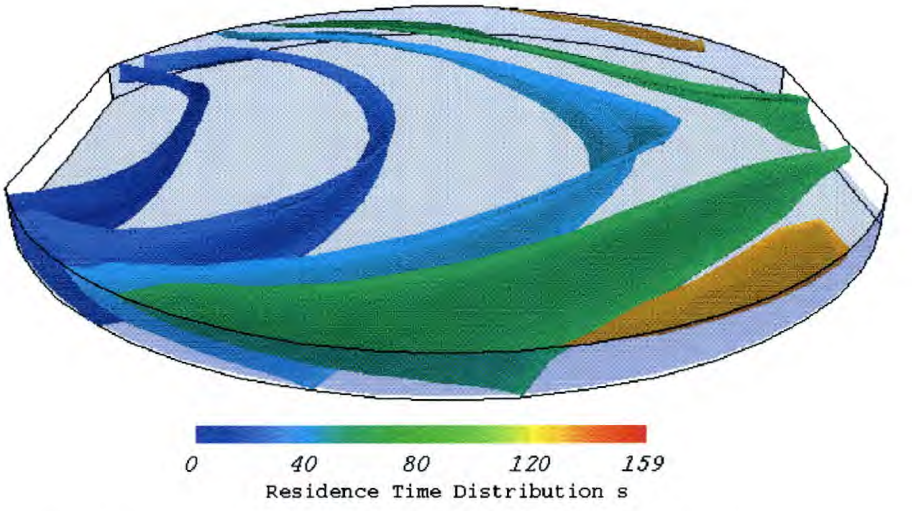


Figure 7.3. Three-dimensional distribution of liquid residence time over the tray

The residence time distribution has been integrated out in the vertical direction, to obtain the height averaged age of the liquid at any point over the tray. This effectively reduces the inherent three dimensional problem to a two dimensional one. The result of this vertical averaging procedure is shown in Figure 7.4.

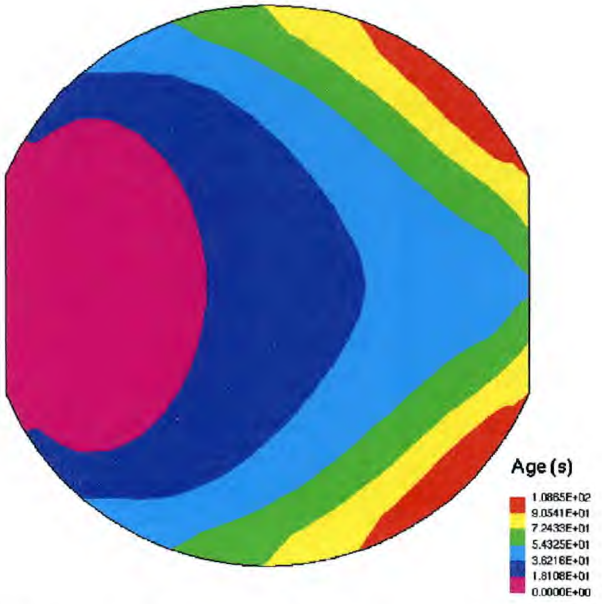


Figure 7.4. Vertically averaged fluid age distribution (top view)

Figures 7.3 and 7.4 clearly show a rapid flow in the central portion of the tray and a slow flow region in the outer regions of the tray. The amount of information can be reduced further by just considering the residence time distribution from the outlet weir. This is done by summarising the fluid elements passing over the outlet weir in different groups of residence time (e.g. 5-second intervals between groups). Typical results are shown graphically in Figure 7.5 below where the liquid mass flowrate is plotted against residence time.

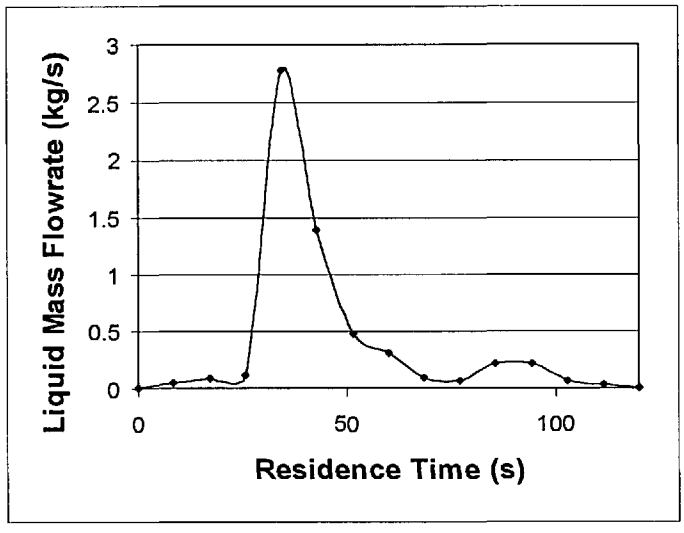


Figure 7.5. Liquid residence time and corresponding mass flowrate

It is interesting to note that the numerical evaluation of outlet residence time distribution tends to erode the so called distribution tails. This is due to the fact that the CFD computation discretises the age of the fluid to finite values at each mesh point. Thus, if fluid from a grid cell with old fluid and fluid from one with young fluid flow into a third cell, the age of the fluid in this third cell is the mass flow weighted age average of the two feeder cells and the 'tail' of the age distributiuon is effectively integrated or smeared out.

7.5.3. Relationships between CFD Results and Outlet Composition

Using the information from Figure 7.5, the average exit liquid mole fraction can be calculated from

$$\bar{x}_{out} = \frac{\sum_i \left(L_i x_{out,i}\right)}{\sum_i L_i} \tag{7.13}$$

where L_i is the flowrate of liquid having the ith residence time for which the liquid composition is $x_{out,i}$, $x_{out,i}$ being obtained from Eq.(7.12). The outlet mole fraction of the gas phase ($\bar{y}_{out}$) is given by the mass balance:

$$G\left(\bar{y}_{out} - \bar{y}_{in}\right) = L\left(\bar{x}_{in} - \bar{x}_{out}\right)$$

$$\text{i.e. } \bar{y}_{out} = \frac{L}{G}(\bar{x}_{in} - \bar{x}_{out}) + \bar{y}_{in} \tag{7.14}$$

Once the outlet compositions for both vapour and liquid are obtained, they can be converted (if necessary) into the Murphree tray efficiency from the following relationship:

$$E_{MV} = \frac{\bar{y}_{out} - \bar{y}_{in}}{y^* - \bar{y}_{in}}$$

7.6. Summary

A novel methodology has been developed for the prediction of distillation tray performance. Compared to the traditional empirical correlation of Murphree point and tray efficiency for assessing tray performance, it has firmer basis in that account is taken of the residence time distribution on the tray. The flow chart for the complete algorithm is shown in Figure 7.6 where each colour of box represents specific information described as follows:

- Green Boxes: properties and conditions of a given system
- Orange Boxes: calculations of required parameters
- Red Boxes: mass transfer calculations
- Blue Boxes: CFD flow simulations
- Yellow Box: combination of results to obtain final answers

The algorithm is basically solving the problems in each of the boxes in the colour order given above (i.e. from green down to yellow). Using this algorithm, extensive comparisons have been made against existing tray data and these are described in Chapter 8.

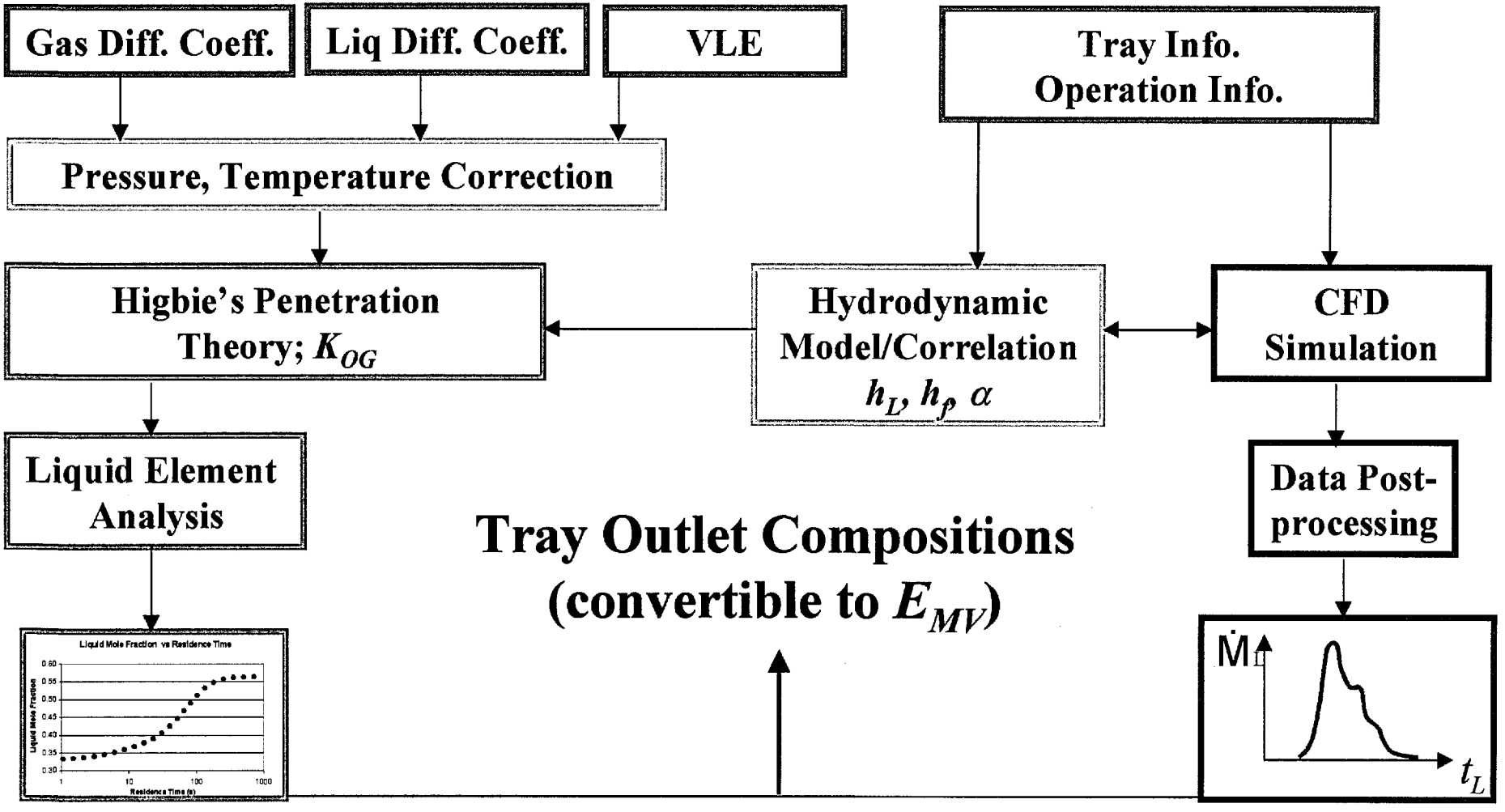


Figure 7.6. The new methodology for tray efficiency prediction

Chapter 8

Validation and Application

of the New Methodology

8.1. Introduction

Previously, Chapter 6 introduced the role of CFD in calculating flow on distillation trays. One of the approaches (the so-called "homogeneous" model) can be used to calculate a residence time distribution for the liquid on the tray and, as is discussed in Chapter 7, this residence time distribution can be combined with relationships for inter-phase mass transfer to calculate the average composition of the liquid leaving the tray. The average exit vapour composition can then be calculated by a mass balance and the performance of the tray can be estimated. This performance can be expressed directly in terms of the changes of compositions or, alternatively, in terms of tray efficiency.

In the past, the practice has been to develope point efficiency correlations which were developed (and then validated) from experimental databases. The original data were usually given in tray efficiency or overall column efficiency (although outlet compositions for each tray are also available). In order to make the data useful, the tray or column efficiencies were converted into point efficiencies using appropriate models. The conversion models between these three types of efficiencies can be numerically complex (as described previously in Section 2.6.3) and the choice of model may vary significantly in each case due to the different assumptions used. For example, the popular Chan and Fair's correlation (1984) used a simple backmixing model (Section 2.6.3.1) and assumed well-mixed vapour between trays. However, Katayama and Imoto (1972) gave a totally opposite comment and suggested that the vapour between trays was unmixed. In the latest point efficiency correlation by Bennett *et al* (1997), the mixing effects of both phases are taken account for (see Section 2.6.3.2) and the authors

also included the effect of entrainment when converting the data into point efficiency. These contradictions indicate that the development and validation processes for point efficiency correlations have been inconsistent.

Unlike the traditional point efficiency correlations, the residence time based methodology, described in Chapter 7, has a logical basis and, therefore, the experimental data is only used for the validation purpose, not for its development. The simulation results (in terms of the outlet compositions for both phases) from this methodology offer direct comparisons to experimental data without any complex transformations.

In this present chapter, the residence time based methodology is compared with a wide range of available data. Section 8.2 gives the actual compositions and Section 8.3 investigates the sensitivity of the method to various input assumptions. As will be seen, the method's general performance is rather good! Also (in Section 8.4), results obtained from the applications of the new methodology in the investigation of geometrical effects (effect of size of plate and effect of flow directors) are presented.

8.2. Methodology Validation

Most of the recent commercial tray efficiency data are not available in the public domain, mainly due to the cost of performing such experiments. However, there are two sets of data available from the late 1950's, which have been frequently used for the development of point efficiency correlations. In 1957, the *Fractionation Research Inc.* (FRI) of USA carried out a series of sieve tray distillation experiments in a 1.2m diameter column. Its extensive databank includes distillation data from three different binary systems at various pressure conditions. In 1958, the *American Institute of Chemical Engineer* (AIChE) performed experiments on some 0.6m diameter bubble cap trays. It includes absorption and desorption experiments as well as distillation experiments and different types of trays were also investigated. The residence time methodology presented in the present work has been tested against these two databanks and the procedures of the validation process are as follows:

(1) Investigate the vapour-liquid equilibrium relationship of the given system using AspenMax^{TM} and compare the prediction with available experimental data (if possible).
(2) Quantify the extent of mass transfer as a function of the liquid residence time using Eq.(7.12).
(3) Perform a CFD simulation to obtain residence time distributions on the tray.
(4) Calculate the outlet compositions using the results obtained from Steps (1) to (3) and compare to the experimental results.

The FRI data only became available in public domain in the late 1970's, therefore, the validation results for the AIChE are first presented in Section 8.2.1 followed by the FRI data in Section 8.2.2.

8.2.1. AIChE Data

All the tests were carried out on various types of 24-in. diameter bubble cap trays installed in two experimental rigs. A single tray test facility was used to collect absorption and desorption data and a distillation unit was used which was specially designed for the separation of an acetone-benzene system at various pressures. The cross-sectional dimensions of the test tray are shown in Figure 8.1 below (a more detailed description of the experimental rig may be found in the AIChE report, 1958).

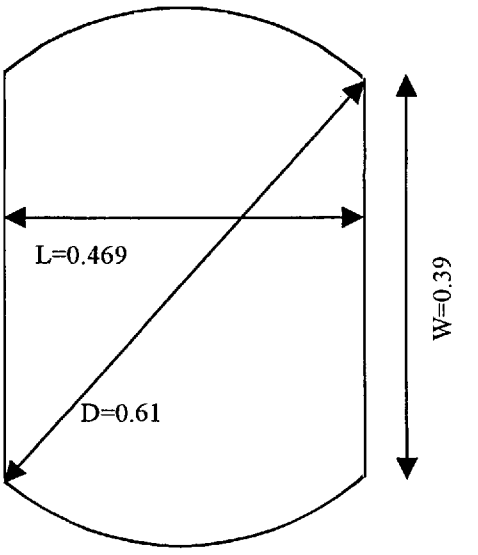


Figure 8.1. Cross-sectional dimensions of the AIChE column (dimensions in metres)

Data from four types of the bubble cap trays were chosen here for this validation work and their open fractions are given in Table 8.1 below. More detailed specifications and operating conditions for the absorption–desorption data (Section 8.2.1.1) and distillation data (Section 8.2.1.2).

Tray Type Number	Open Fraction	Tray Type Number	Open Fraction
AIChE Type I	0.187	AIChE Type II	0.164
AIChE Type IV	0.082	AIChE Type V	0.288

Table 8.1. Open fraction for the bubble cap trays used for validation work

8.2.1.1. Absorption and Desorption Data

This is the non-distillation data used in the present validation work and it contains two types of experimental data: ammonia-air-water absorption data and oxygen-air-water desorption data. These are described as follows.

- **Ammonia-Air-Water Absorption Experiment**

In this experiment, the gas supplied to the single tray test facility consisted of air from a blower and contained about 2 mole % of ammonia vapour. Water was supplied to the tray as the absorbing fluid. The outlet concentration of ammonia in water was measured so that the tray efficiency could be obtained. The equilibrium relationship follows

Henry's Law and the Henry's constant could be calculated using Eq.(8.1) provided in the AIChE report (1958).

$$m = \frac{y^*}{x} = \frac{\left(10^{-1665/T+6.695}\right)}{760 \times 0.018} \tag{8.1}$$

where T is the absolute temperature of the system (K).

The Henry's constant has also been predicted using the API Sour Water model in AspenMax™ and excellent agreement is shown with the results given by Eq.(8.1) for a temperature range of 287-300K, as presented in Figure 8.2.

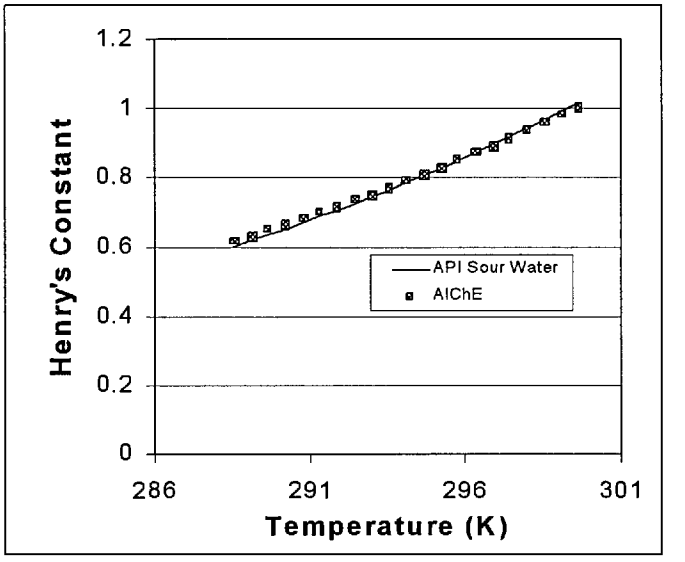


Figure 8.2. Henry's constant for the ammonia-air-water system calculated with the API Sour Water model and the AIChE model (Eq.8.1)

From the analysis given in Section 7.4.3, the estimation of the extent of mass transfer as a function residence time is given by Eq.(7.12) and this has been applied to Run-11 with a "Type I" tray and is shown graphically in Figure 8.3. As it can be seen clearly, the liquid begins to reach equilibrium with the inlet gas if it stays over 300 seconds on the tray.

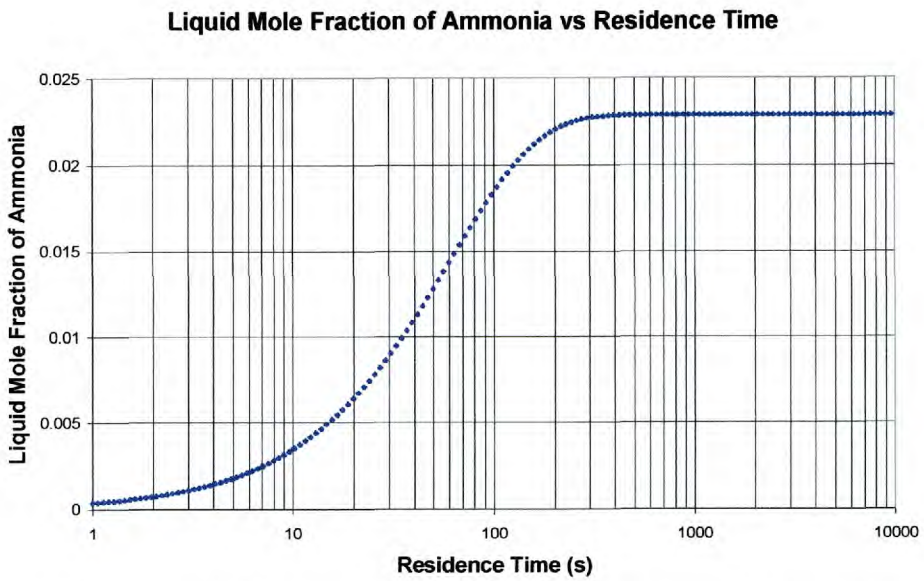


Figure 8.3. Liquid mole fraction vs. Residence time for an ammonia absorption case (results taken from Run-11)

Figure 8.4 presents the CFD simulation results of the average residence time (in the vertical direction) distribution on the tray. Two patches of old fluid age are clearly seen at both sides of the tray active area and these correspond with the re-circulation zones commonly observed in industrial operation.

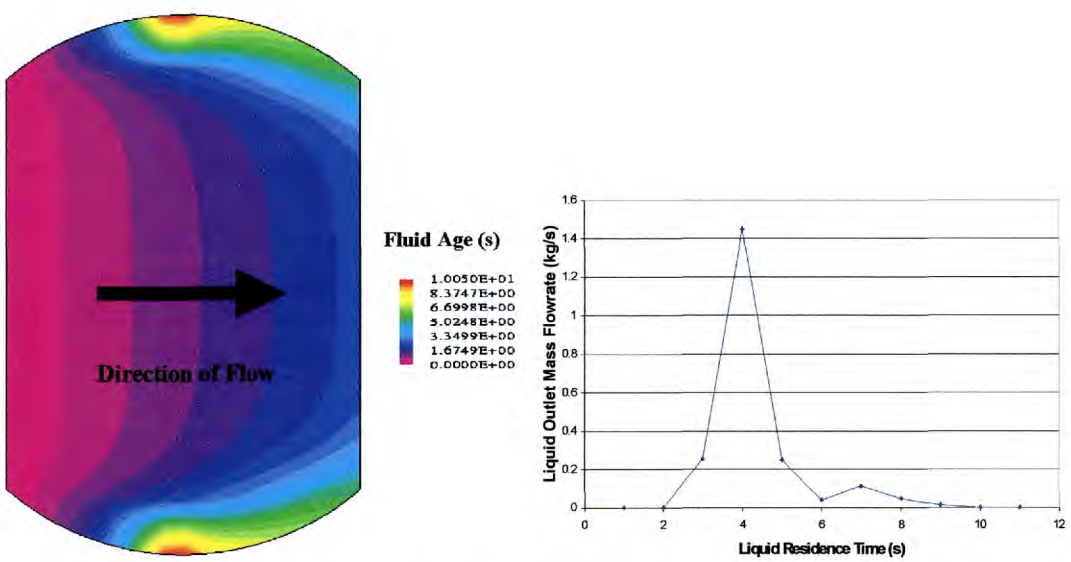


Figure 8.4. CFD results on residence time distribution for an ammonia absorption case (results taken from Run-11)

Following the same treatment in Section 7.5.2, the mean ammonia concentration in the outlet liquid flow was determined by summing the individual liquid element

concentration according to their residence time group. The graph below divides the residence time into 11 groups and the interval between each group is 1 second. The results shown on the graph indicates that a large part of the outlet fluid has an averaged age of 4 seconds.

A total of 27 sets of ammonia absorption experiments were simulated and the results for each test are summarised in Table 8.2. In this set of runs, the outlet compositions were used to calculate tray efficiency, which had also been calculated from the experimental data. The maximum deviation between the efficiency calculated by the present method and that measured was about -14% (Run 6B) while the average error was -3.3% and the absolute average error was 4.8%.

Tray Type	Run	u_s (m/s)	Q_L (lit/s)	h_w (m)	Expt E_{MV}	CFD E_{MV}	% error
I	6B	1.890	4.164	0.076	0.85	0.731	-14.00
I	20	1.018	2.398	0.127	0.921	0.831	-9.77
I	7A	1.018	2.397	0.076	0.881	0.795	-9.76
I	3A	1.890	0.631	0.076	0.754	0.711	-5.70
I	31A	1.018	0.631	0.025	0.669	0.639	-4.48
I	12	1.890	0.631	0.025	0.666	0.638	-4.20
I	11	1.890	2.398	0.025	0.696	0.692	-0.57
I	17A	1.018	2.397	0.025	0.763	0.766	0.39
I	34B	0.146	4.164	0.025	0.859	0.911	6.05
II	13B	2.591	2.398	0.076	0.685	0.607	-11.39
II	7A	1.859	2.398	0.076	0.768	0.684	-10.94
II	12A	1.859	2.398	0.025	0.692	0.641	-7.37
II	6A	0.972	2.398	0.127	0.868	0.829	-4.49
II	8A	1.859	0.631	0.076	0.729	0.716	-1.78
II	1A	0.972	2.398	0.076	0.791	0.785	-0.76
II	3A	0.972	2.398	0.025	0.725	0.728	0.41
II	16A	0.573	2.398	0.076	0.85	0.855	0.59
II	4A	0.972	0.631	0.025	0.636	0.649	2.04
IV	22A	0.972	2.398	0.127	0.916	0.854	-6.77
IV	18A	1.859	2.398	0.127	0.855	0.822	-3.86
IV	17A	1.859	2.398	0.076	0.794	0.789	-0.63
IV	19A	1.859	2.398	0.025	0.712	0.724	1.69
IV	25A	0.570	2.398	0.025	0.784	0.818	4.34
V	5A	1.945	2.398	0.076	0.738	0.673	-8.81
V	7A	1.079	2.398	0.076	0.802	0.772	-3.74
V	6A	1.975	0.631	0.076	0.711	0.728	2.39
V	8	1.067	0.631	0.076	0.736	0.754	2.45
						Average error	-3.30
						Absolute average error	4.80

Table 8.2. CFD simulation results of ammonia absorption experiments

- **Oxygen-Air-Water Desorption Experiment**

In this experiment, oxygen was brought in contact with the water at a location about 40ft. upstream from the column inlet. The amount of oxygen added did not exceed its solubility in water which is about 25p.p.m. at room temperature. The oxygen was completely dissolved in the water by the time it entered the tray where the oxygen was partially desorbed by the air passing through it. The outlet concentration of oxygen in the water was measured so that the tray efficiency could be obtained. As in the ammonia absorption case, the equilibrium relationship for the oxygen-air-water system followed Henry's Law and the Henry's constant can be predicted from:

$$m = \frac{y^*}{x} = \frac{(0.05565T + 1.9285)\times 10^7}{760} \tag{8.2}$$

where T is the temperature of the system (°C).

The Henry's law constant has also been predicted using the Ideal gas law in AspenMax™ and the comparison of results with Eq.(8.2) are shown in Figure 8.5 below. Again, excellent agreement between the predictions and Eq.(8.2) is observed in the temperature range under investigation (i.e. 285-295K).

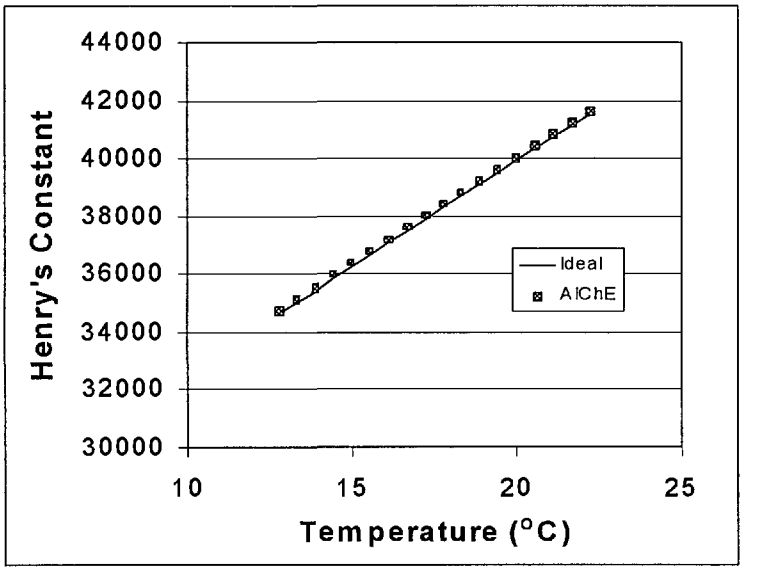


Figure 8.5. Henry's constant for the ammonia-air-water system (pink dots represent results from Eq.(8.2) above)

Following Eq.(7.12), the change in concentration in a fluid element flowing on a tray can be obtained as a function of its residence time and the results taken from Run-

KO19A of the "Type II" tray are shown in Figure 8.6 below. As it can be seen clearly, concentration of oxygen in the liquid becomes close to equilibrium with the inlet gas if the element of liquid stays over 10 seconds on the tray.

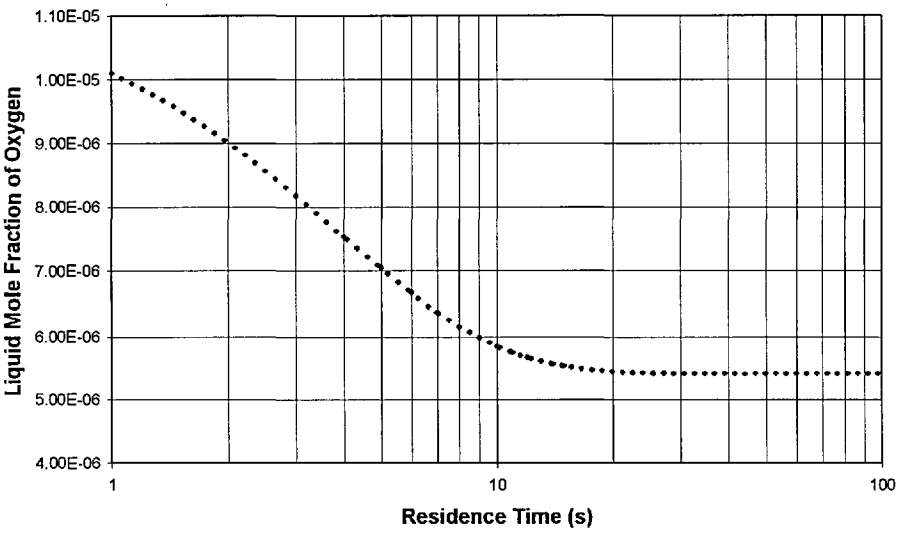


Figure 8.6. Liquid mole fraction vs. Residence time for an oxygen desorption case (results taken from Run-KO19A)

Figure 8.7 presents the CFD simulation results of the average residence time (in vertical direction) distribution on the tray. The two re-circulation zones are again observed in this case and the average age of fluid at these locations are well over 10 seconds. From the information given in Figure 8.6, the liquid at these locations has reached equilibrium with the inlet air and therefore no more mass transfer could take place (i.e. the equilibrium solubility of oxygen in water under the system temperature and pressure is reached).

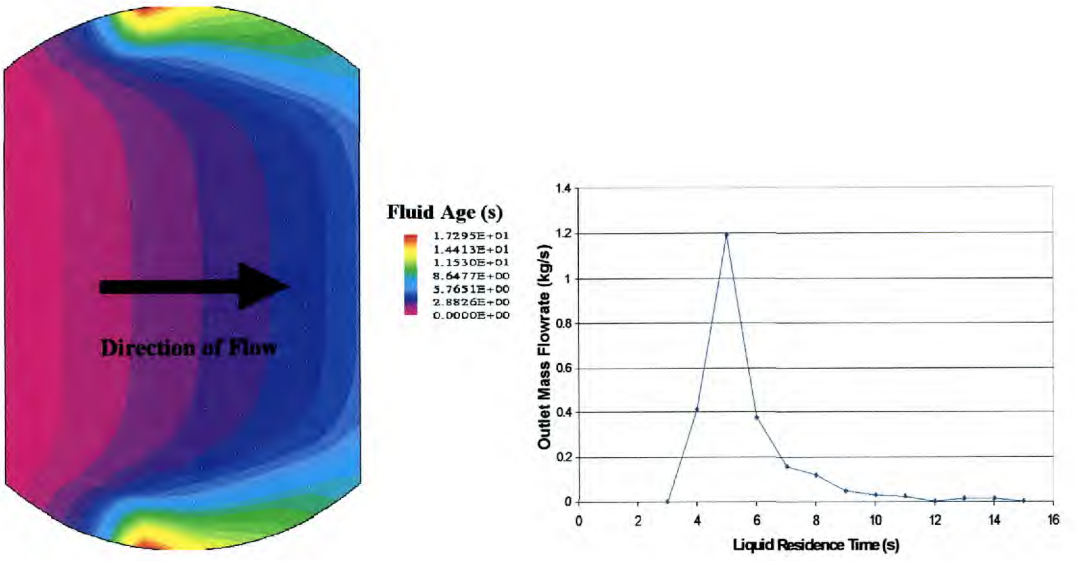


Figure 8.7. CFD results on residence time distribution for an oxygen desorption case (results taken from Run-KO19A)

A total of 14 sets of oxygen desorption experiments were simulated and the results for each test are summarised in Table 8.3. The results are shown in tray efficiency again for the convenience of comparisons. The agreement between the predictions and the data is reasonable here with the maximum deviation of just below -20% (Run LO14). The average error is -1.3% and the absolute average error is 8.3%.

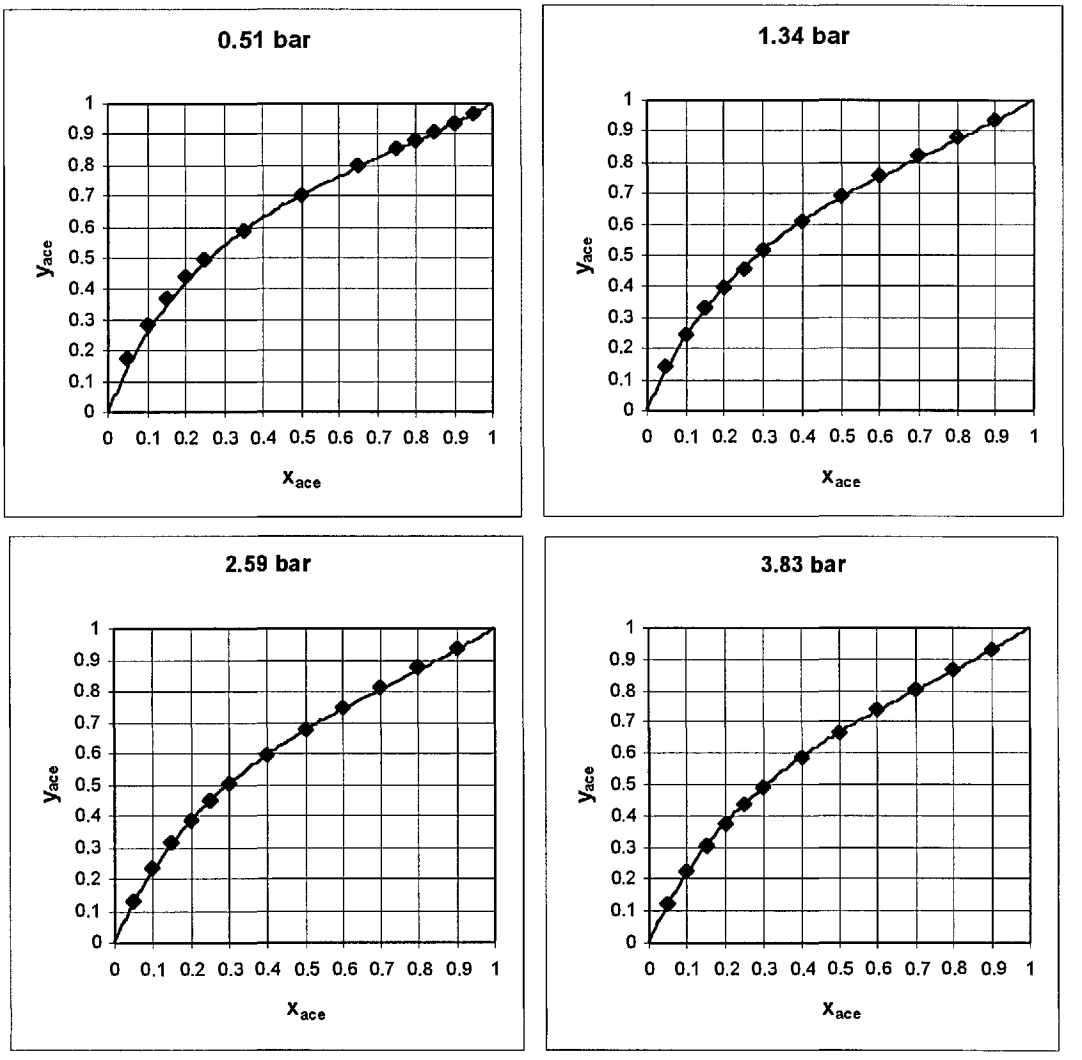
Tray Type	Run	u_s (m/s)	Q_L (lit/s)	h_w (m)	Expt E_{MV}	CFD E_{MV}	% error
I	LO14	1.018	2.398	0.076	0.893	0.718	-19.60
I	LO23	1.018	2.398	0.127	0.924	0.781	-15.48
I	LO2	0.146	2.398	0.025	0.311	0.269	-13.50
I	LO5	1.018	2.398	0.025	0.727	0.673	-7.43
I	LO13	1.018	0.631	0.076	0.967	0.977	1.03
I	LO8	1.890	2.398	0.025	0.702	0.797	13.53
II	KO14B	1.061	2.524	0.051	0.737	0.711	-3.53
II	KO24A	1.082	1.893	0.051	0.817	0.796	-2.57
II	KO19A	1.082	2.524	0.076	0.754	0.756	0.27
II	KO22A	1.951	1.893	0.051	0.858	0.91	6.06
II	KO17A	1.951	2.524	0.076	0.788	0.847	7.49
II	KO12B	1.938	2.524	0.051	0.78	0.842	7.95
II	KO11B	2.460	2.524	0.051	0.785	0.856	9.04
						Average error	-1.30
						Absolute average error	8.30

Table 8.3. CFD simulation results of oxygen desorption experiments

8.2.1.2. AIChE Distillation Data

In this section, distillation data for the binary system acetone/benzene at a total column pressure varying from 1 to 6 atm are evaluated and compared with the residence time distribution methodology. The experiments were performed in a 0.6m internal diameter distillation column with 5 bubble cap trays installed inside and the data presented here were collected from Tray 3.

The VLE data at various pressures are given in the AIChE report (1958) and VLE predictions were obtained from AspenMax™ using the UNIFAC activity coefficient model (for liquid phase) with the Redlich-Kwong equations of state method (for gas phase). The results are in good agreement with experimental data and these are shown in Figure 8.8. The predictions agree well with the experimental over a wide range of pressures.



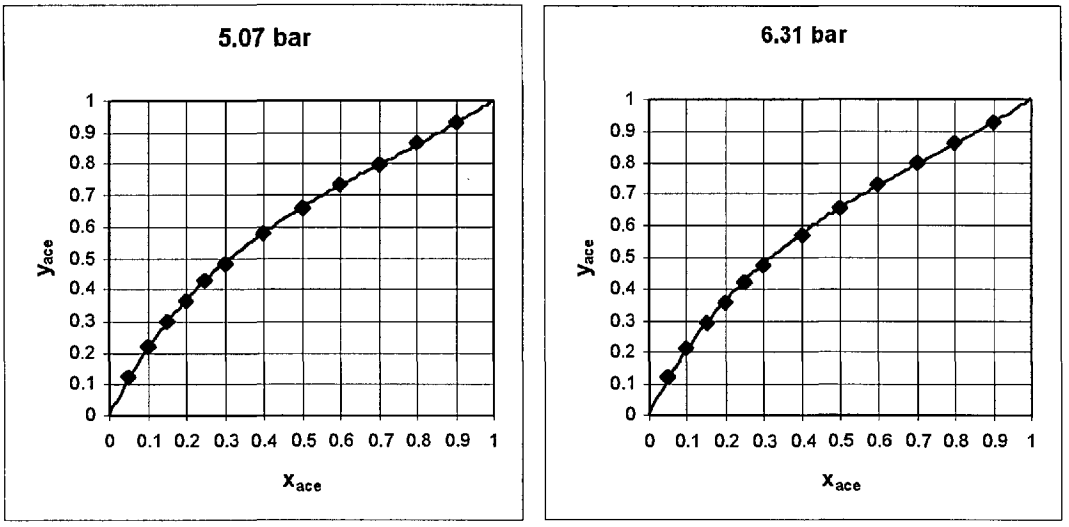


Figure 8.8. VLE for Acetone/Benzene system at different pressure conditions (the lines represent Aspen Max results and the dots represent data provided in the AIChE report, 1958)

Standard methods already discussed in Chapter 7 are used for the estimation of diffusion coefficients (i.e. Fuller *et al* (1966) for the gas phase, Wilke-Chang (1955) for the liquid phase). In the absorption/desorption experiments, where the liquid mole fraction of the absorbed or desorbed component is very small, the liquid phase diffusion coefficient can be estimated at infinite dilution. In the present distillation case, the liquid phase binary diffusion coefficient is no longer independent of concentration therefore a different correlation needs to be used such as the one by Vignes (Eq.2.113). The thermodynamic correction term required in Eq.(2.113) can be calculated from the VLE data at different pressures. The results are shown in Table 8.4 below.

Pressure (bar)	$\left[\frac{\partial \ln a_A}{\partial \ln x_A}\right]_{T,P}$
6.31	0.6927
5.07	0.6872
3.83	0.6756
2.59	0.6584
1.34	0.6377
0.51	0.5945

Table 8.4. Thermodynamic correction term at various system pressures

The relationship between the mass transfer and residence time following Eq.(7.12) is shown graphically in Figure 8.9 below (results taken from Run-T13 of the "Type I"

tray). In this particular case, any liquid staying over 50 seconds on the tray will reach equilibrium with the inlet vapour.

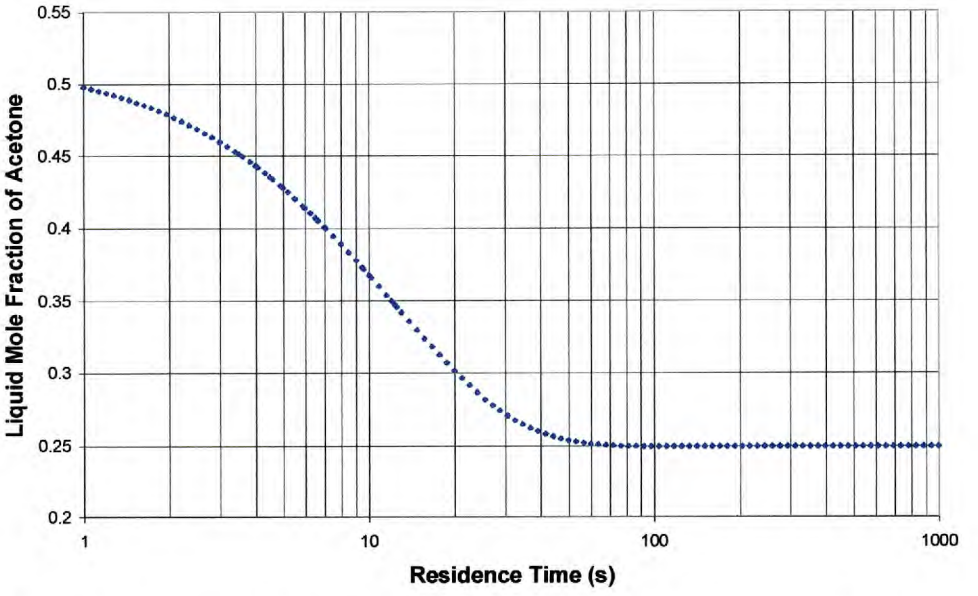


Figure 8.9. Liquid mole fraction vs. Residence time for acetone/benzene distillation case (results taken from Run-T13)

Figure 8.10 presents the CFD simulation result of vertically averaged residence time distributions on the tray. The pattern of the residence time distribution is similar to the previous experiments and this is not surprising since similar trays were used.

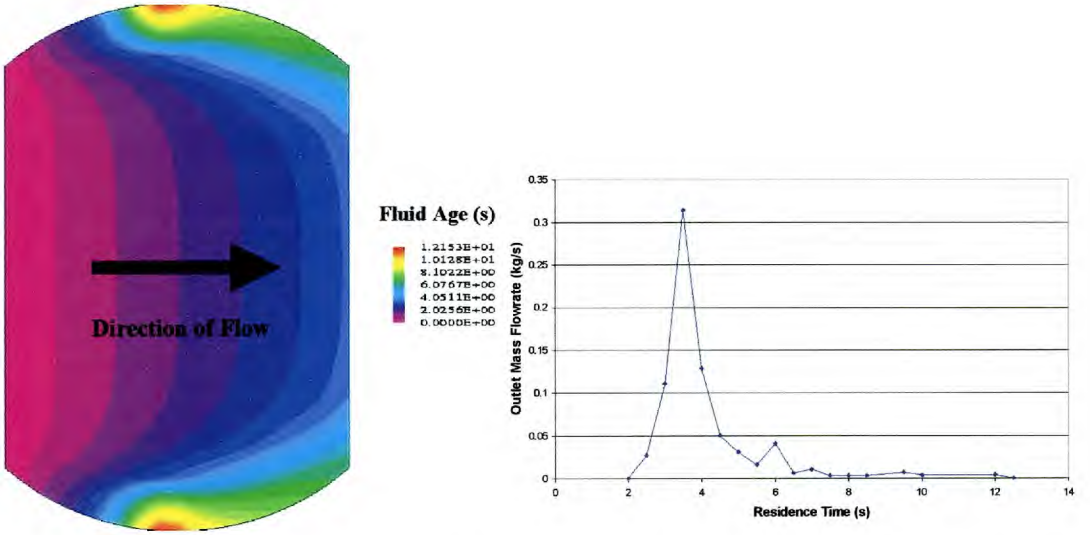


Figure 8.10. CFD results on residence time distribution for acetone/benzene distillation case (results taken from Run-T13)

A total of 19 sets of acetone/benzene distillation experiments were simulated and the results for each test are summarised in Table 8.8. The predictions are shown in outlet compositions because the data were given in the same form. The maximum deviation is 9.5% for the outlet vapour composition less than -13.5% for the liquid one.

Tray Type	Run	P (bar)	u_s (m/s)	Q_L (lit/s)	h_w (m)	y_{in}	x_{in}	y_{out} (Expt)	x_{out} (Expt)	y_{out} (CFD)	x_{out} (CFD)	% error (y)	% error (x)
I	T11	6.32	0.49	2.032	0.0635	0.639	0.741	0.734	0.649	0.685	0.69	-6.68	6.32
I	T17	4.99	0.57	1.325	0.0635	0.548	0.538	0.609	0.457	0.581	0.485	-4.60	6.13
I	T14	6.36	0.72	2.341	0.0635	0.628	0.654	0.684	0.58	0.674	0.585	-1.46	0.86
I	T22	5.23	0.95	1.905	0.0635	0.638	0.629	0.69	0.578	0.681	0.545	-1.30	-5.71
I	T7A	4.18	0.96	1.155	0.0635	0.64	0.549	0.657	0.518	0.658	0.502	0.15	-3.09
I	T1	1.43	0.98	1.344	0.0635	0.649	0.594	0.69	0.546	0.698	0.557	1.16	2.01
I	T2A	3.83	1.07	2.675	0.0635	0.497	0.653	0.631	0.519	0.61	0.528	-3.33	1.73
I	T13	2.66	1.07	1.218	0.0635	0.551	0.519	0.595	0.443	0.595	0.444	0.00	0.23
I	T5	2.63	1.35	2.360	0.0635	0.541	0.701	0.684	0.606	0.687	0.545	0.44	-10.07
I	T3	1.41	2.04	1.666	0.0635	0.636	0.68	0.674	0.605	0.738	0.554	9.50	-8.43
II	108	5.08	0.680	2.397	0.0635	0.58	0.697	0.682	0.589	0.632	0.642	-7.33	9.00
II	V3	0.51	1.554	1.009	0.108	0.061	0.098	N/A	0.049	0.152	0.0424	N/A	-13.47
II	203	2.60	1.204	1.476	0.108	0.511	0.503	0.565	0.416	0.546	0.449	-3.36	7.93
II	V1	0.51	1.186	0.738	0.108	0.314	0.313	N/A	0.241	0.471	0.211	N/A	-12.45
II	205	2.66	0.594	1.886	0.108	0.474	0.381	N/A	0.358	0.517	0.354	N/A	-1.12
II	206	2.60	0.777	1.136	0.108	0.283	0.308	N/A	0.201	0.349	0.219	N/A	8.96
II	119	5.50	0.984	2.454	0.0635	0.602	0.602	N/A	0.532	0.659	0.508	N/A	-4.51
II	123	1.70	1.475	1.142	0.0635	0.538	0.531	0.565	0.447	0.579	0.465	2.48	4.03
II	113	1.70	0.789	1.356	0.0635	0.116	0.149	0.204	0.092	0.19	0.092	-6.86	0.00

Table 8.5. CFD simulation results of acetone/benzene distillation experiments

8.2.2. FRI Distillation Data

The FRI distillation column was used to collect a wide range of distillation data, mainly on the studies of flooding, efficiency and pressure drop. There were 9 sieve trays installed in this unit at 610mm tray spacing. The cross-sectional dimensions of the column are shown in Figure 8.11 below.

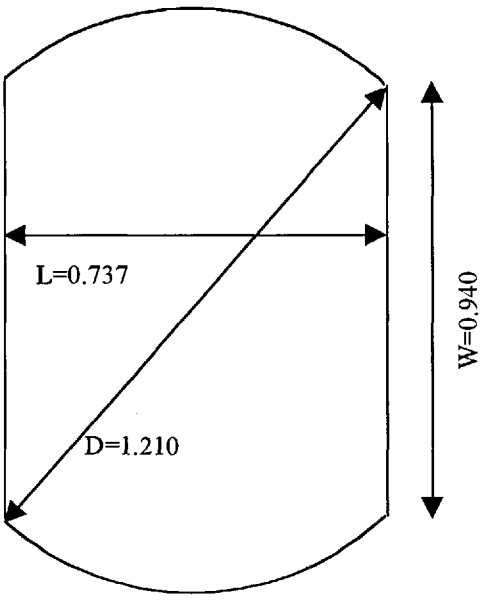


Figure 8.11. Cross-sectional dimensions of the FRI column

The data used in the present validation work was obtaned for sieve trays with 12.7mm hole diameter, 30mm triangular pitch and 16% open fraction and the outlet weir height was fixed at 51mm. The column was operated at total reflux condition for all the efficiency experiments. More detailed descriptions of the experimental rig may be found in the FRI progress report (October, 1955). The data used in the work has been taken from the FRI progress report dated February, 1957, for the three different systems: cyclohexane/n-heptane, isobutane/n-butane and isopropanol/water.

8.2.2.1. Cyclohexane / n-Heptane system

The VLE relationship for the cyclohexane/n-heptane system was calculated using the Peng-Robinson equations of state for both phases in AspenMax^{TM}. Although no direct experimental data (under the same pressure as the present system) is available to verify the accuracy, the AspenMax^{TM} user manual suggests that Peng-Robinson works well with hydrocarbon mixtures similar to this case. Some experimental data at atmospheric pressure are available and these data fall within the envelop bounded by the two curves in Figures 8.12 (1.66 bar) and 8.13 (0.28 bar).

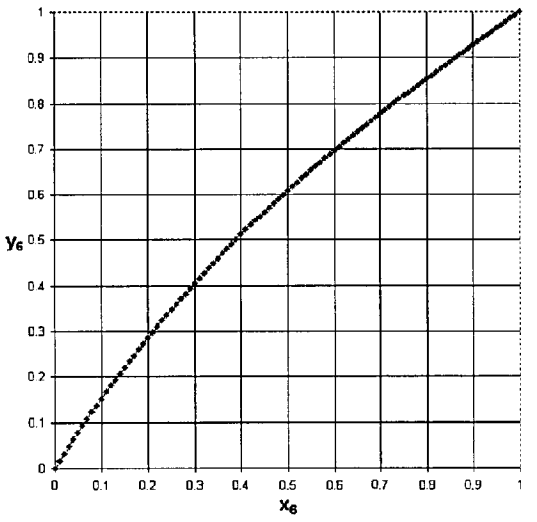


Figure 8.12.
VLE for C6/C7 system at 1.66bar (24psia)

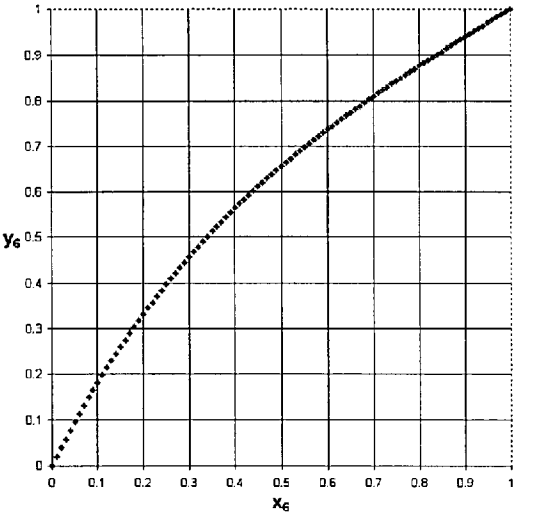


Figure 8.13.
VLE for C6/C7 system at 0.28bar (4psia)

Figure 8.14 below illustrates the relationship between the liquid composition and residence time according to Eq.(7.12), (taken from the results of Run-1328), where it is shown that the liquid becomes saturated with the inlet vapour when it remains on the tray for about 60 seconds.

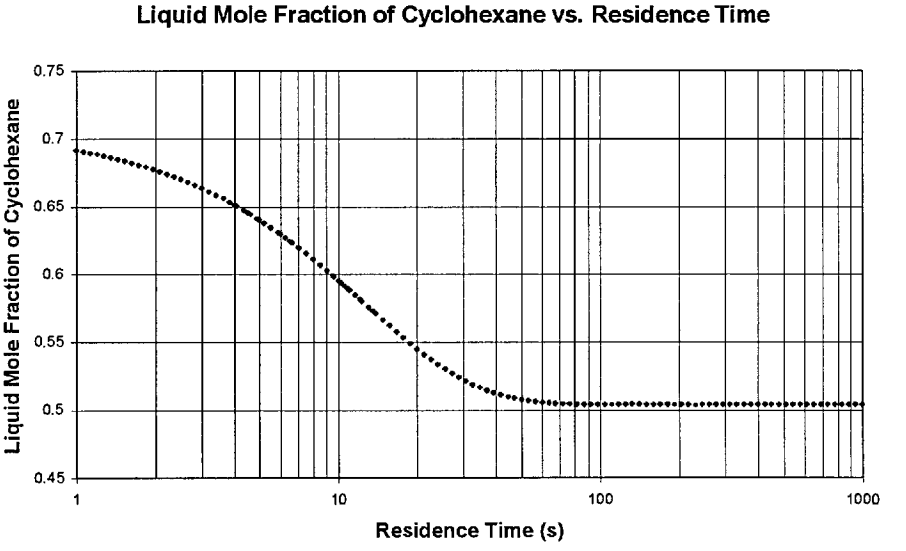


Figure 8.14. Liquid mole fraction profile v.s. residence time for the C6/C7 distillation case (results taken from Run-1328)

The CFD simulation result on the flow distribution of Run-1328 is shown in Figure 8.15 below. The stagnant zones at both sides of the tray are not present in this case; instead, there two slow flowing stripes at both corners near the tray outlet.

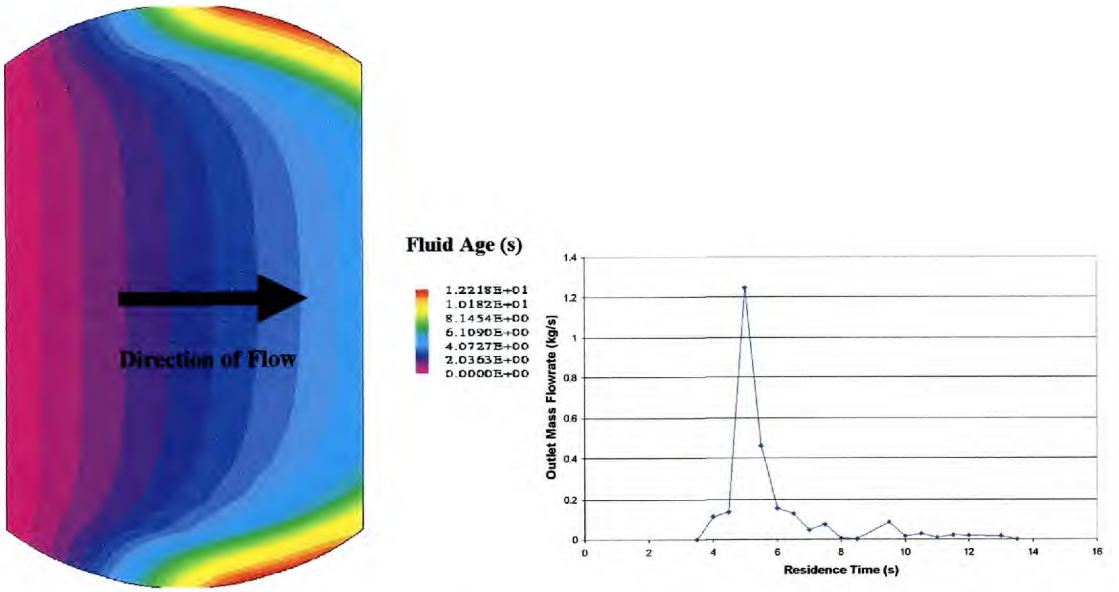


Figure 8.15. CFD results on residence time distribution for a 1.66bar (24psi) C6/C7 distillation case (results taken from Run-1328)

A total of 8 sets of cyclohexane/n-heptane distillation data (include the ones at sub-atmospheric pressure condition) have seen simulated and the results for each test are summarised in Table 8.6. The maximum deviation for the outlet compositions of both phases is less than ±10%.

Ref	Run	u_S (m/s)	Q_L (m3/s)	y_{in}	x_{in}	y_{out} (Expt)	x_{out} (Expt)	y_{out} (CFD)	x_{out} (CFD)	% error (y)	% error (x)
FRI_C6/C7_24psi	1324	1.822	9.72E-03	0.594	0.674	0.674	0.594	0.711	0.561	5.48961	-5.55556
FRI_C6/C7_24psi	1325	1.761	9.21E-03	0.596	0.6785	0.6785	0.596	0.712	0.563	4.93736	-5.53691
FRI_C6/C7_24psi	1326	1.634	8.01E-03	0.6135	0.6975	0.6975	0.6135	0.722	0.586	3.51254	-4.48248
FRI_C6/C7_24psi	1327	1.179	6.15E-03	0.6255	0.709	0.709	0.6255	0.68	0.655	-4.09027	4.71623
FRI_C6/C7_24psi	1328	0.787	4.07E-03	0.6165	0.707	0.707	0.6165	0.692	0.633	-2.12164	2.6764
FRI_C6/C7_24psi	1329	0.417	2.21E-03	0.5595	0.5855	0.5855	0.5595	0.625	0.518	6.74637	-7.41734
FRI_C6/C7_4psi	1343	3.931	3.82E-03	0.639	0.727	0.727	0.639	0.788	0.577	8.39065	-9.70266
FRI_C6/C7_4psi	1344	4.04	3.34E-03	0.498	0.86	0.86	0.498	0.816	0.505	-5.11628	1.40562

Table 8.6. CFD simulation results of C6/C7 distillation experiments

8.2.2.2. Isobutane / n-Butane system

The VLE relationship for the isobutane/n-butane system was calculated using the Peng-Robinson equations of state for both phases in AspenMax™. This was again based on the recommendations from the AspenMax™ user manual for light hydrocarbon mixtures. Attempts were made to find experimental data under similar conditions to this system, however there were none available in the common VLE databooks. Therefore, only the Aspen results are shown in Figure 8.16 below.

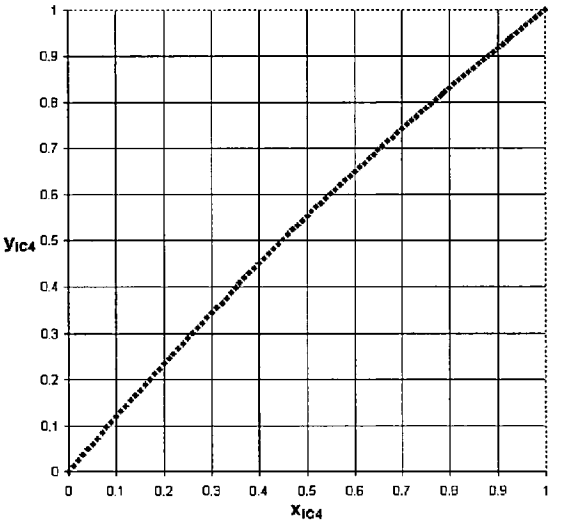


Figure 8.16. VLE for iC4/nC4 system at 11.4 bar

Figure 8.17 shows the extent of mass transfer as a function of its residence time (results taken from Run-1313). In this case, any liquid staying beyond 40 seconds on the tray becomes in equilibrium with the inlet vapour.

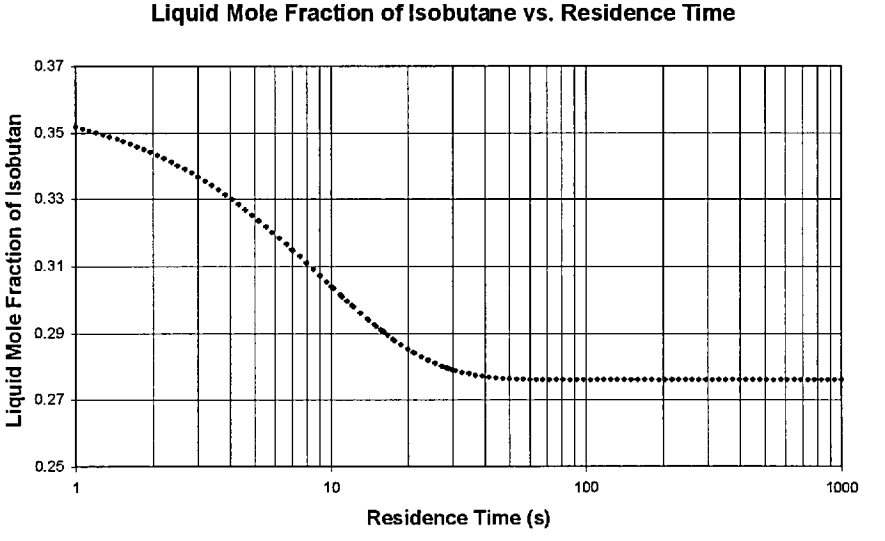


Figure 8.17. Liquid mole fraction profile v.s. residence time for the iC4/nC4 distillation case (results taken from Run-1313)

The CFD simulation results on flow distributions for Run-1313 are shown in Figure 8.16 below. The general pattern is not much different from the previous ones, however it is worth mentioning that (in this case) the slow moving patches at the sides of the tray

represent a residence time of more than 20 seconds. Looking back to Figure 8.17, the outlet liquid concentration after 20 seconds will be very close to its ultimate value (i.e. equilibrium with inlet vapour).

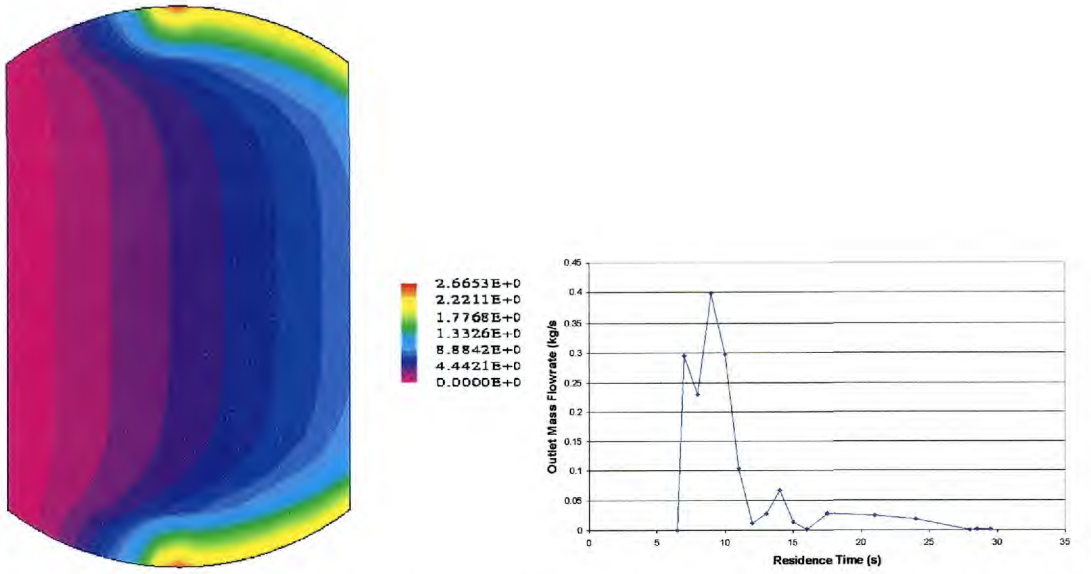


Figure 8.18. CFD results on residence time distribution for 165psi (11.4bar) iC4/nC4 distillation case (results taken from Run-1313)

A total of 12 sets of isobutane/n-butane distillation experiment were simulated and the results for each test are summarised in Table 8.7. Two consecutive trays (4 & 5) were simulated and the results are generally in good agreement here.

Ref	Run	u_s (m/s)	Q_L (m3/s)	y_{in}	x_{in}	y_{out} (Expt)	x_{out} (Expt)	y_{out} (CFD)	x_{out} (CFD)	% error (y)	% error (x)
FRI_IC4/NC4_165psi	1306-5	0.4493	0.01893	0.32	0.366	0.366	N/A	0.382	0.302	4.37	
FRI_IC4/NC4_165psi	1306-4	0.4493	0.01893	0.272	0.302	N/A	0.272	0.32	0.252		-7.35
FRI_IC4/NC4_165psi	1310-5	0.3671	0.01508	0.336	0.403	0.403	N/A	0.408	0.327	1.24	
FRI_IC4/NC4_165psi	1310-4	0.3671	0.01508	0.281	0.327	N/A	0.281	0.336	0.268		-4.63
FRI_IC4/NC4_165psi	1311-5	0.245	0.01028	0.353	0.402	0.402	N/A	0.404	0.349	0.50	
FRI_IC4/NC4_165psi	1311-4	0.245	0.01028	0.308	0.349	N/A	0.308	0.353	0.302		-1.95
FRI_IC4/NC4_165psi	1312-5	0.1716	7.13E-03	0.337	0.393	0.393	N/A	0.393	0.334	0.00	
FRI_IC4/NC4_165psi	1312-4	0.1716	7.13E-03	0.289	0.334	N/A	0.289	0.337	0.283		-2.08
FRI_IC4/NC4_165psi	1355-5	0.1508	6.12E-03	0.314	0.345	0.345	N/A	0.355	0.3	2.90	
FRI_IC4/NC4_165psi	1355-4	0.1508	6.12E-03	0.28	0.3	N/A	0.28	0.314	0.264		-5.71
FRI_IC4/NC4_165psi	1313-5	0.0806	3.34E-03	0.37	0.425	0.425	N/A	0.431	0.36	1.41	
FRI_IC4/NC4_165psi	1313-4	0.0806	3.34E-03	0.318	0.36	N/A	0.318	0.37	0.306		-3.77

Table 8.7. CFD simulation results of iC4/nC4 distillation experiments

8.2.2.3. Isopropanol / Water system

It is well-known that any alcohol/water binary mixture will exhibit non-ideal behaviour due to the strong molecular interactions. Therefore, the VLE relationship for the

isopropanol/water system was calculated using the combination of the Redlich-Kwong equations of state (for the gas phase) and the UNIFAC activity coefficient model (for the liquid phase) in AspenMax^{TM}. Experimental data at atmospheric pressure are available and the predictions from AspenMax^{TM} are in good agreements with these data. The VLE results at the two pressure levels at which comparisons were made with the present methodology are shown in Figure 8.19 (1atm) and 8.20 (0.28bar) below.

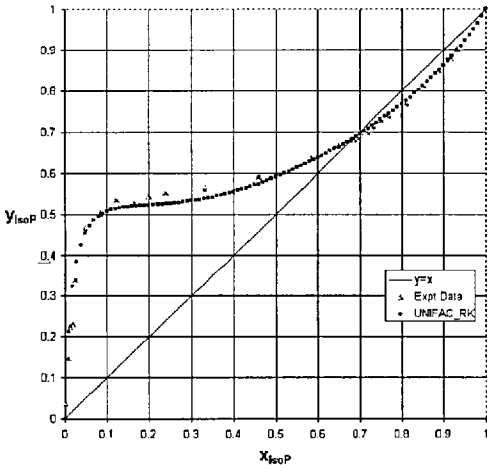


Figure 8.19.
VLE for Isopropanol/Water system at 1atm

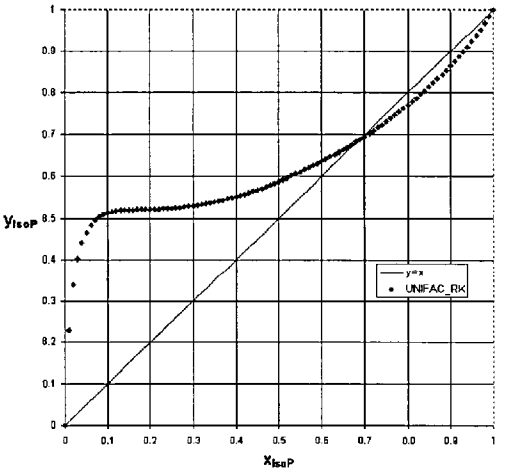


Figure 8.20.
VLE for Isopropanol/Water system at 0.28bar

Figure 8.21 shows the extent of mass transfer as a function of residence time (results taken from Run-1381) and the 80-second mark seems to be the point where further mass transfer becomes negligible.

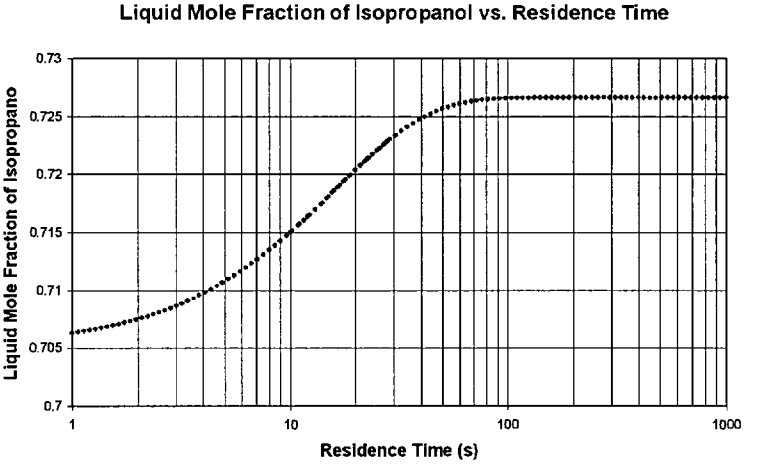


Figure 8.21. Liquid mole fraction vs. Residence time for an Isopropanol/Water distillation case (results taken from Run-1381)

The CFD simulation results on flow distribution for Run-1381 are shown in Figure 8.22. There are two slow moving stripes at both sides of the tray near the outlet, representing about 23 seconds of average fluid age.

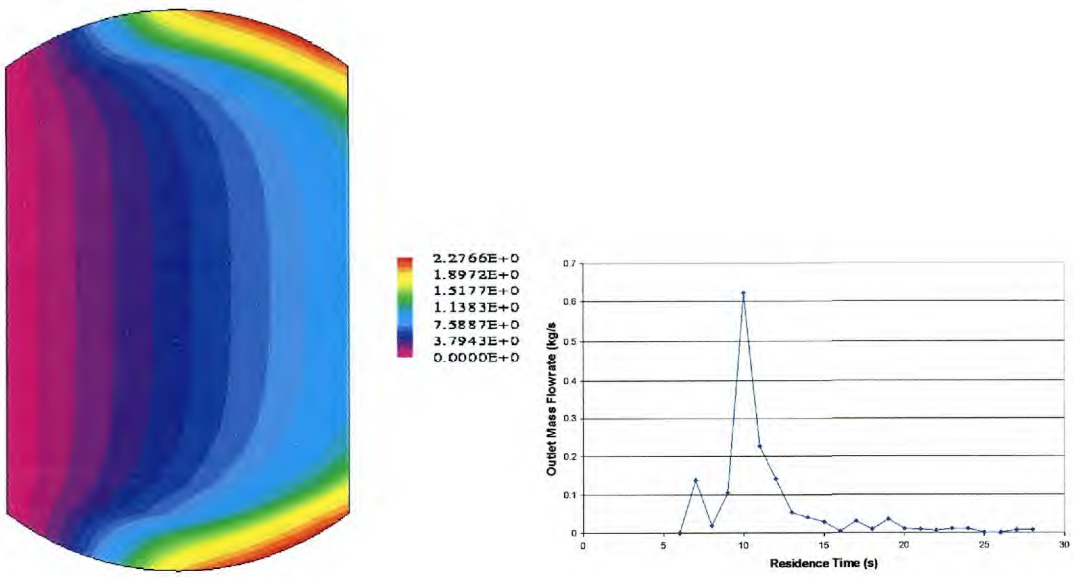


Figure 8.22. CFD results on residence time distribution for 1atm Isopropanol/Water distillation case (results taken from Run-1381)

A total of 10 sets of isopropanol/water distillation experiment (include the ones at sub-atmospheric pressure condition) were simulated and the results for each test are summarised in Table 8.8. The predicted results are in excellent agreement with the experimental data where the maximum error is just over 1%.

Ref	Run	u_s (m/s)	Q_L (m3/s)	y_{in}	x_{in}	y_{out} (Expt)	x_{out} (Expt)	y_{out} (CFD)	x_{out} (CFD)	% error (y)	% error (x)
FRI_IsoP/Water_1atm	1378	3.695	4.80E-03	0.723	0.713	0.713	0.723	0.709	0.731	-0.56	1.11
FRI_IsoP/Water_1atm	1379	3.402	4.14E-03	0.713	0.705	0.705	0.713	0.703	0.719	-0.28	0.84
FRI_IsoP/Water_1atm	1380	2.602	3.10E-03	0.713	0.702	0.702	0.713	0.703	0.718	0.14	0.70
FRI_IsoP/Water_1atm	1381	1.786	2.11E-03	0.713	0.705	0.705	0.713	0.705	0.716	0.00	0.42
FRI_IsoP/Water_1atm	1382	1.355	1.57E-03	0.715	0.705	0.705	0.715	0.705	0.716	0.00	0.14
FRI_IsoP/Water_4psi	1370	7.12	2.35E-03	0.737	0.721	0.721	0.737	0.718	0.747	-0.42	1.36
FRI_IsoP/Water_4psi	1373	5.476	1.45E-03	0.709	0.702	0.702	0.709	0.701	0.715	-0.14	0.85
FRI_IsoP/Water_4psi	1374	3.777	9.59E-04	0.71	0.7	0.7	0.71	0.704	0.71	0.57	0.00
FRI_IsoP/Water_4psi	1375	2.787	7.13E-04	0.709	0.69	0.69	0.709	0.698	0.71	1.16	0.14
FRI_IsoP/Water_4psi	1376	1.95	4.64E-04	0.695	0.698	0.698	0.695	0.694	0.699	-0.57	0.58

Table 8.8. CFD simulation results of isopropanol/water distillation experiments

8.3. Sensitivity Studies and Discussion

As it can be seen clearly from the algorithm flowchart in Figure 7.6, the accuracy of the final results (i.e. outlet compositions or tray efficiency) obtained using the residence time distribution methodology depends on how good the intermediate predictions are. In general, such intermediate predictions cause variations on the final results in two main areas: (1) mass transfer analysis (i.e. the red boxes in Figure 7.6); (2) CFD simulation method (i.e. the blue boxes in Figure 7.6).

This sensitivity study is to examine how the methodology behaves with different values of physical properties and hydrodynamic parameters. The study is based on the results of Run-17A from the ammonia absorption case (Section 8.2.1.1) and the conditions for each test are listed in Table 8.9.

Test	Ref	ε	h_f (m)	m	k_G (kmol/sm^2)	k_L (kmol/sm^2)	K_{OG} (kmol/sm^2)
1	Control	0.6365	0.091	0.7522	9.14×10^{-4}	1.17×10^{-2}	8.63×10^{-4}
2	$m\times2$	0.6365	0.091	1.5044	9.14×10^{-4}	1.17×10^{-2}	8.18×10^{-4}
3	$m\times0.5$	0.6365	0.091	0.3761	9.14×10^{-4}	1.17×10^{-2}	8.88×10^{-4}
4	$D_G\times2$	0.6365	0.091	0.3761	1.29×10^{-3}	1.17×10^{-2}	1.19×10^{-3}
5	$D_G\times0.5$	0.6365	0.091	0.3761	6.46×10^{-4}	1.17×10^{-2}	6.20×10^{-4}
6	Expt h_f	0.7116	0.132	0.7522	7.15×10^{-4}	9.13×10^{-3}	7.15×10^{-4}

Table 8.9. Conditions for the sensitivity study

Eq.(7.12) has been applied on each of these cases and the results are shown in Figure 8.23 below. The blue line represents the control study (Test 1) where results were obtained by following every step specified in the methodology. The pink and green lines show the results based on double and half of the Henry's constant used in the control study respectively. The yellow and brown lines show the results obtained using double and half of the predicted gas phase diffusion coefficient used in the control study. The red line represents the results using experimental values of froth height and gas void fraction instead of those predicted from the Stichlmair's correlation (1978).

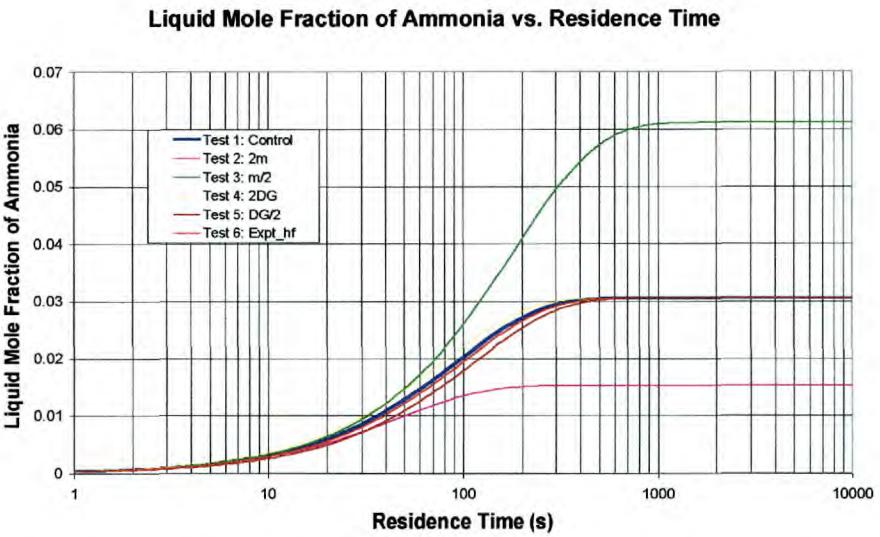


Figure 8.23. Liquid mole fraction vs. Residence time for an ammonia absorption case under different conditions.

As it can be seen clearly from Figure 8.23 (Test 1 to 3), the Henry's constant controls both the ultimate liquid composition and the rate of change in the liquid composition. The lower the Henry's constant, the steeper the rate of change in liquid composition becomes and the higher the ultimate liquid composition would occur. The ammonia-air-water absorption is a gas-phase-controlled process and this is also normally the case in distillation. Thus, the prediction of the gas phase diffusion coefficient becomes important so that the mass transfer coefficients can be calculated more accurately. In Figure 8.23 (Test 1, 4 and 5), the curve shifts from the right to the left as the value of gas phase diffusion coefficient increases. i.e. the diffusion coefficients only affect the rate of mass transfer! Although differences are easily observed for the curves in Figure 8.23, these only become significant after 10 seconds of residence time.

When comparing Tests 1 and 6 (i.e. blue and red lines Figure 8.23), the effects of the hydrodynamic parameters on mass transfer seem to be much less significant than the other physical properties described above. However, in the homogeneous CFD model presented, they are the primary input parameters. Therefore, they play much more important roles in the CFD simulation and directly affect the residence time distribution. Figures 8.24 and 8.25 below are the CFD results on residence time distribution for Tests 1 and Test 6 respectively. Both figures show nearly identical patterns of distribution but

the results from Test 6 (i.e. higher froth height) show a longer average residence time along the flow path.

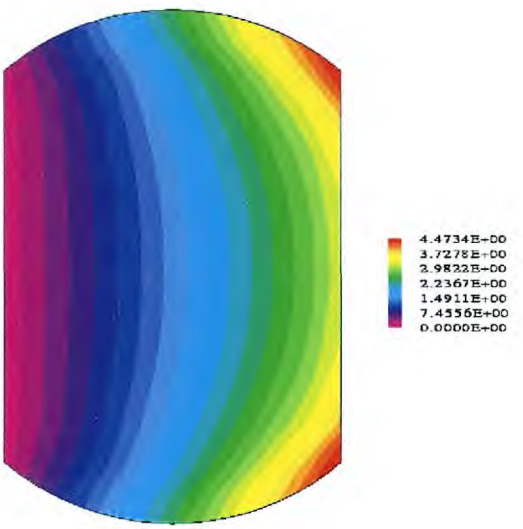


Figure 8.24. CFD simulation results for Test 1

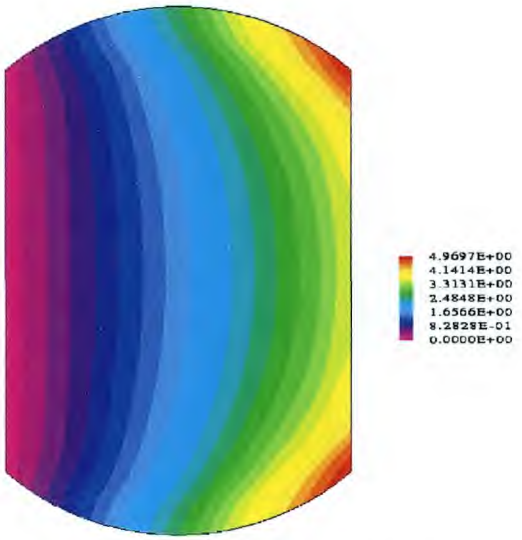


Figure 8.25. CFD simulation results for Test 6

The final results for all the tests, with the comparisons to the experimental data, are shown in Table 8.10 below.

Test	Ref	x_{in}	x_{out}	E_{MV}
1	Control	0	0.00128	0.766
2	m×2	0	0.00121	0.756
3	m×0.5	0	0.00131	0.771
4	D_G ×2	0	0.00151	0.914
5	D_G×0.5	0	0.00104	0.617
6	Expt_h_f	0	0.00133	0.766
	Experiment	0	0.00125	0.763

Table 8.10. Outlet liquid composition results and conversion to Murphree tray efficiency for each test in the sensitivity study

Observations on the net effect of the various changes in input variables are as follows:

- **Equilibrium constant**

Only small differences are seen between the final results (i.e. outlet compositions) for Tests 1 to 3 despite the large change in equilibrium constant (÷ and ×2). This is due to the fact that the maximum residence time predicted from the CFD simulation (Figure

8.24) is less than 5 seconds and within this period of time, all three curves (blue, pink and green) in Figure 8.23 fall on nearly the same path. For the system investigated, therefore, there is no large effect of equilibrium constant, though this would not be the case for trays with larger residence times.

- **Gas phase diffusion coefficient**

The gas-phase-controlled nature of the ammonia absorption process means the prediction on the gas phase diffusion coefficient will directly impact the final prediction. This is shown clearly in Table 8.10.

- **Hydrodynamic parameters**

The prediction of the hydrodynamic parameters relies on the empirical correlations of Stichlmair (1978). In the case where the predictions deviate from the real values, different mass transfer relationships and residence time distributions are expected. This is illustrated in Test 6, where the froth height is higher than the one used in the control study and as a result, this slightly decreases the rate of mass transfer (red curve in Figure 8.23). However, the final result shows no difference to the control study, because the slower mass transfer process is compensated by the prolonged average residence time (Figure 8.25).

8.4. Applications of the Residence Time Methodology

From the previous sections, it has been demonstrated that the methodology is able to provide both quantitative and qualitative information on the tray performance. The generality of the methodology makes it possible to provide a more reliable design tool than do, say, efficiency correlations based on limited data. Potential applications may include re-designs and optimisation of existing columns as well as development of new equipment. However, it has two major drawbacks:

(1) The use of Stichlmair's correlation (1978) limits the methodology to sieve trays and bubble cap trays.

(2) The CFD model only simulates the behaviour on the tray active area, treating the froth as homogeneous and assuming that the flowrate and composition of vapour entering the tray are uniform. No account is taken of vapour concentration variations introduced by the tray below nor of any effects arising from the downcomer.

In both the above cases, there seems to be scope for further development in achieving more general correlation and carrying out more detailed CFD calculation. However, the methodology does seem to present a straightforward attack on the prediction problem which already offers a useful tool when data is not available. There are two particular areas where the methodology may be useful and examples of these two applications are discussed in the following sections:

- Estimations of tray scale-up operations (Section 8.4.1)
- Improvement of flow distribution (Section 8.4.2)

8.4.1. Tray Scale-up

In an existing chemical plant, it may sometimes be desirable to increase production in order to meet the demands of the market. In such cases, one may require additional distillation columns of a larger size to cope with the higher throughputs and the new methodology may be used here to investigate the feasibility of different tray sizes under the same system. For this purpose, simulation tests were carried out from one of the FRI experiments (Run1328 from the C6/C7 distillation case) where the original tray was simulated together with two other tray sizes: twice and three times the original tray size. Simulations of the original size tray are described in Section 8.2.2.1. All other operating variables, such as temperature and pressure, were kept constant throughout the three simulations and the volumetric flowrates were scaled up appropriately so that the vapour superficial velocity and liquid loading were also kept at the same value as the original test. The conditions are given in Table 8.11. Further relevant information is given in Section 8.2.2.1.

Test	Ref	D (m)	A_f	h_w (m)	u_s (m/s)	Q_L/W (m3/sm)	ε	h_f (m)
1	Run 1328	1.21	0.16	0.0508	0.787	4.33×10^{-3}	0.846	0.156
2	Double Size	2.42						
3	Triple Size	3.63						

Table 8.11. Operating variables of each test under different tray size (original results taken from Run1328 of the FRI C6/C7 distillation case)

The results of CFD residence time distributions of the double and triple sized trays are given in Figures 8.26 and 8.27. The result of CFD simulation on the original tray was given earlier in Figure 8.15.

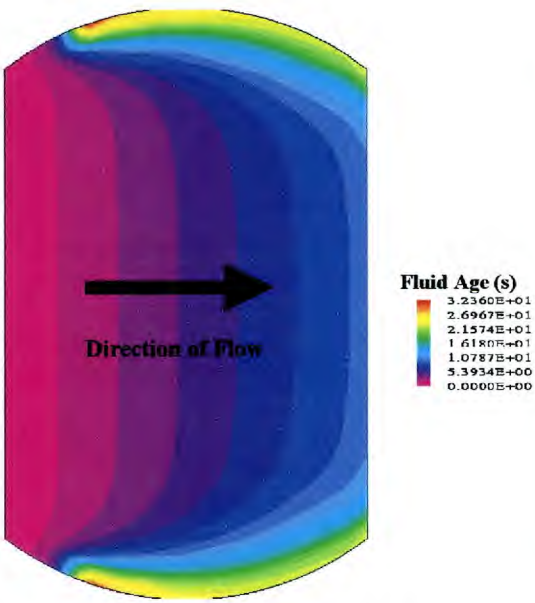


Figure 8.26. CFD residence time distributions for double sized tray

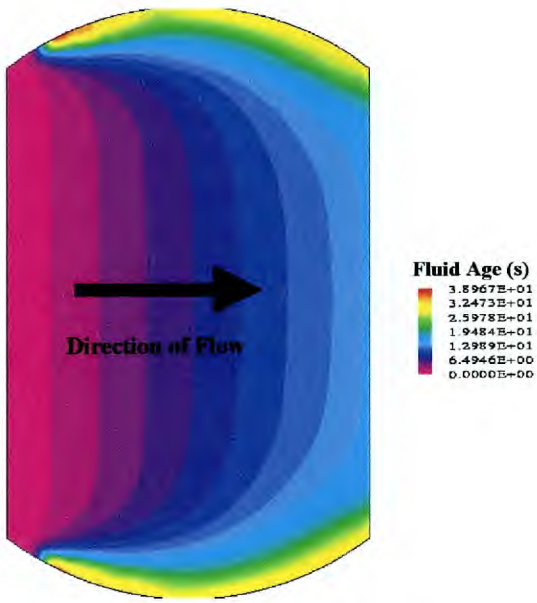


Figure 8.27. CFD residence time distributions for triple sized tray

From Figure 8.15, there is a peak of outlet flow with 5 seconds of residence time. Visual observations from Figures 8.26 and 8.27 reveals that the peak flowrate (i.e. the colour which occupies the most area near the outlet) for each case has roughly 10 and 15 seconds of fluid age respectively. This is not surprising since the tray sizes were double and triple to the original one. An interesting point to note from the three figures are the positions of "old" fluids. In the original tray (Figure8.15), there are two stripes of the old fluids (in red colour) at each side of the tray near to the outlet. When the tray is enlarged (Figures 8.26 and 8.27), the slow moving stripes extend further towards the inlet of the tray, i.e. the positions of the oldest fluids move against the direction of the

flow. The larger the tray becomes, the closer the two patches of old fluids are to the tray inlet. Other useful information obtained from this study is that a tray more than 3 times larger than the original one is probably undesirable. This is because the two "dead zones" (i.e. areas of old fluids) in Figure 8.26 represent fluids of nearly 40 seconds old and re-examing Figure 8.14, it is seen that little mass transfer takes place after such a time interval (although equilibrium is not quite yet reached)! Table 8.12 shows a comparison of the outlet compositions of cyclohexane. The results show, as expected, that the larger the tray is, the longer the liquid remains on the tray and therefore the more mass transfer takes place.

Test	Ref	y_{in}	x_{in}	y_{out}	x_{out}
1	Run 1328	0.6165	0.707	0.692	0.633
2	Double Size			0.740	0.586
3	Triple Size			0.770	0.557

Table 8.12. Outlet compositions of cyclohexane for the three different sizes of trays

8.4.2. Improved Flow Distribution

The ideal flow distribution is plug flow but the reality is never close to this situation. It has been shown in this chapter that re-circulation zones exist on a distillation tray and there are many possible factors responsible for their occurrence. When these zones lower the tray performance to a significant extent (e.g. Figure 8.7 for the Oxygen desorption case), it is desirable to provide some mixing mechanism (with some younger age fluids) to remove the slow moving patches of liquid. The usual practice is to introduce some flow directors, which are normally thin metal plates like weirs attached on the tray floor, so that the flow can be better distributed. Recently, the use of flow directors has been studied experimentally in detail by Kahn (1998). The work by Fischer (1999) showed that CFD models could adequately predict the effects of flow directors on the flow distributions.

Two examples of such exercise are chosen from the FRI data: (1) Run 1313 of the isobutane/n-butane distillation case; (2) Run 1381 of the isopropanol/water distillation case. In each run, a thin-plate (40cm wide, 3cm high) flow director is placed centrally on the channel and it is 7cm away from the inlet. The size and position of this flow

director is purely arbitrary and it may not give optimal results. The CFD simulation results of these two cases given in Figures 8.28 and 8.29 below.

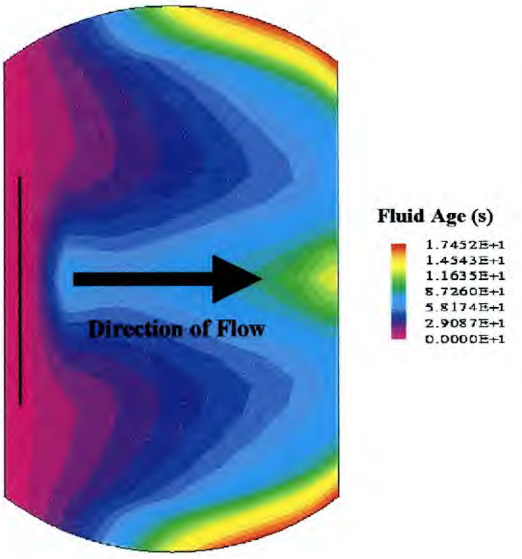


Figure 8.28. Modified flow distributions for Run 1313 of iC4/nC4 distillation case (Figure 8.18)

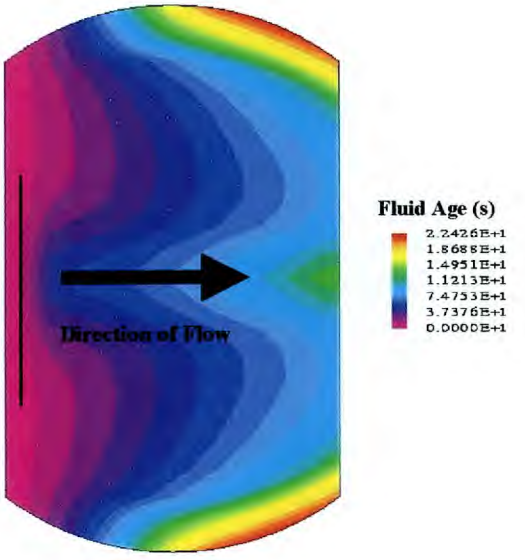


Figure 8.29. Modified flow distributions for Run 1381 of isopropanol/water distillation case (Figure 8.22)

When comparing the above two figures to their original results (i.e. Figures 8.18 and 8.22), the flow director seems to have stronger effect on reducing the dead zones in the isobutane/n-butane case than the isopropanol/water one. i.e. in Figure 8.28, the maximum residence time has been reduced to about 17.5 seconds from 26.5 seconds originally observed in Figure 8.18.

To make best use of flow diversion devices, the system would need to be fully optimised in term of the height, position and shape of the devices. No attempt has been made to do this in the work described here but the example calculation illustrates the potential use of the residence time methodology in performing such calculation.

8.5. Summary

This chapter describes the validation of the residence time methodology presented in Chapter 7 against two sets of experimental data which cover wide ranges of conditions of tray operation. The agreement between the present model and the data is generally good. Some examples of the application of the new methodology as a tool for optimising existing equipment are also included and the predicted outcomes are also in line with general expectations. The generality of the new methodology makes it easy to adapt any future improvements on the intermediate steps (for instance in the mass transfer correlation) and therefore it is potentially more applicable in new situation than the traditional efficiency correlations/models.

Chapter 9

Conclusions and Recommendations

9.1. General

The ultimate goal of the ASID research on distillation trays is to establish a scientific basis for predicting the (two-phase) tray flows and the associated mass transfer processes. The work described in this thesis covers both experimental and computational studies. The experiments were carried out using the CRODIS air-water facility and a liquid-liquid simulation facility. In CRODIS, new data were obtained for froth characteristics using both established methods and a new technique (the 'flying optical probe'). The liquid-liquid simulation facility provided new insights into the behaviour of the froth layer. In the computational work, a new algorithm, combining the hydrodynamics (CFD) and mass transfer aspects of distillation tray, has been developed to predict tray performance and it has been successfully validated against experimental data.

9.2. Conclusions

9.2.1. General Distillation Hydrodynamics

(a) The experimental facility, CRODIS, has been modified to ensure the conditions of the two-phase flow simulation experiments are closer to those occurring on a real distillation tray. The modifications (described in Chapter 3) also help to avoid damage to the equipment (as occurred in the previous setup) and increase the rig safety.

(b) The γ-ray densitometry system and the laser light scattering technique previously used both by Tezock (1994) and Tahmasbi (1997) have been used to generate extensive new data on the two-phase hydrodynamic properties on the CRODIS tray. Re-calibrations of these measuring techniques were carried out and experiments were successfully completed for trays having a variety of hole sizes and outlet weir heights. The influence of calming zones was also investigated.

(c) The results for froth density obtained from the CRODIS test trays showed trends consistent with those published in the literature and the clear liquid heights were generally in good agreements with the predictions from some available correlations. The algorithm of predicting the total tray pressure loss by Tahmasbi (1997) was modified by the present author to incorporate Stichlmair's correlation (1978) for calculating the value of clear liquid height. The experimental results showed that the modified algorithm could successfully predict the total tray pressure drop within an acceptable accuracy.

(d) The measurements of the apparent Sauter mean bubble and droplet diameter profile for the new tray configurations showed consistent trends, with bubble size growing with the vertical distance above the tray floor. The initial bubble sizes depend slightly on the gas flowrate but not on the liquid one. The results provided excellent qualitative assessments of the complex tray flows.

(e) The profiles of froth density and Sauter mean bubble diameter for the CRODIS test trays were used as a basis for the validation of the CFD simulation of flows over distillation trays (carried out by Dr. C. Fischer at Bristol). This is a part of the collaboration work with Bristol University under the sponsorship of the ASID consortium.

(f) A simple theory has been established for the phenomenon of partial bubbling on distillation trays. Experimental observations were used to confirm the condition of its occurrence and to establish the speed at which the patch of bubbles travelled.

9.2.2. Results from Flying Optical Probe Measurements

(a) A new experimental measurement technique (the "flying optical probe system") has been developed for the CRODIS facility. The system consists of five moving optical fibre probes which can effectively determine the local phase when immersed into the two-phase froth. This system has been successfully employed in the measurement of the complex two-phase flow above the test tray in the CRODIS facility.

(b) In the actual experiments, the optical probes are pushed in a direction against the flow in order to penetrate through the froth. The obtained electrical signals are interpreted into gas-phase and liquid-phase chord length distributions. Assuming that the froth consists of spherical bubbles and spherical droplets of different sizes, the results of chord length distributions can be fed into a conversion algorithm to calculate the distributions of diameters for both bubbles and droplets. The conversion algorithm used was a modified form of that developed by Turton and Clark (1998). The data can be averaged to give Sauter mean values of bubble/drops diameters in the regions covered. This is the first time, to the author's knowledge, that experimental results are able to directly reveal the structure of the froth body.

(c) The results on the Sauter mean diameter distributions obtained from the probes are very encouraging and inline with expectations. The effects of tray configuration and flowrates on these distributions have been investigated and the results are able to reflect the changes on the froth structure from one condition to another (e.g. from a froth regime to a spray one).

9.2.3 Liquid-liquid Simulation Rig

(a) Previous attempts by Tezock (1994) and Tahmasbi (1997) to visualise the two-phase flows on a distillation tray using a liquid-liquid simulation rig were not fully successful. In the present work, the rig was successfully revamped with an additional heavy-duty gear pump in place. This enabled the system to produce a full range of flow conditions.

(b) A digital high-speed video camera was employed in the liquid-liquid simulation experiment to improve the quality of the images. The detailed behaviours of the flows were captured and the complex transition between the froth and spray regimes was also observed. The results provide excellent qualitative description and analysis to the two-phase flows on a distillation tray.

9.2.4 Computational Fluid Dynamics Predictions

(a) The MUSIG algorithm (Lo, 1999) was adapted as a possible CFD model on predicting the hydrodynamic behaviour of the tray flow. The model was able to describe the variation on the sizes of the dispersed phase (a scalar quantity), however, the lack of appropriate closure relationships still made the heterogeneous approach difficult to reach satisfactory results when solving vector equations.

(b) A CFD model was developed at a simpler level. In this model, the froth was considered as an equivalent single phase fluid where density and viscosity were determined from appropriate correlation and mixing rules. The flow of the froth and the vapour above it were then predicted using the "VOF" (Volume Of Fluid) or "homogeneous" CFD method in which the whole fluid field is considered as a continuum in which the fluid properties vary from those of the froth to those of the vapour over a small range of values of an arbitrary non-diffusing scalar where local value is tracked in order to determine the local position of the froth/vapour interface. The flow field in the (assumed uniform) froth is then determined and this allows the residence time distribution of the liquid on the tray to be estimated. The steps in the overall methodology were thus as follows:

(1) Obtain the fluid residence time distribution from the CFD simulation.
(2) Calculate appropriate mass transfer coefficients.
(3) Choose a suitable VLE relationship and determine the equilibrium constant using the process simulator, AspenMax^{TM}.
(4) Post-process the fluid residence time results in order to determine the compositions of the streams leaving the tray.

(c) The residence time distribution methodology was tested against two well-known tray efficiency databases, covering a reasonably wide range of binary distillation and absorption processes under different pressures. The agreement is encouragingly good!

(d) One of the many advantages of the new methodology is that it can provide a quick solution to any modification on an existing tray. This has been demonstrated by two important applications: variation of tray sizes and improvement on flow distribution.

9.3. Recommendations to Future Work

(a) To extend the current database of CRODIS trays by including more experimental results from different specifications of trays (hole sizes, open area fractions), different heights of inlet and outlet weirs. The results will continuously serve as the validation data for any future CFD models.

(b) The flying optical probes system worked well in the present study, however, the success of the technique depends not only on the quality of the hardware, it also requires a good treatment on the raw data obtained from each probe, e.g. the assumption of the froth structure and the conversion algorithm (for bubble/droplet diameter distribution). In order to further improve on the technique, some suggestions for the future modifications are as follows:

Hardware:

(1) Cosidering at the possibility of using thinner optical fibres and therefore smaller size of probe tip. It may also be useful to investigate the effect of the shape of probe tip on the overall results. These can help to detect smaller bubbles and droplets and have less intrusive effect during measurements.

(2) Increase the speed at which the probes are travelling. This can be done by changing the size of pinion attached on the gear motor.

(3) In the attempt of increasing the speed of the system, it is necessary to increase the frequency of data collection. The data acquisition card is capable of acquiring data up to 55kHz per channel (i.e. for each probe) although only 5kHz is used in the present study.

Signal Processing:

(1) The assumption of the two-phase froth structure (consists of only spherical bubbles and droplets) worked well in the present work. It is possible to modify this assumption slightly and carry out similar treatment on the signals, e.g. the froth containing only "elliptical" bubbles and "spherical" droplets.

(2) Since the conversion algorithm by Clark and Turton (1988), there have been a few numbers of alternative methods developed (e.g. Clark *et al*, 1996 and Cartellier, 1999). They are generally more complex and may only become useful when better hardware (e.g. the size of the probe tip) is installed.

Experiment:

(1) As mentioned in Section 9.2.1.(a), it is important to collect more experimental data from different tray configurations, weirs,...etc using the flying optical probes system.

(2) The results obtained from the flying optical probe system provide statistical information on the froth structure. It is useful to double or triple the number of runs for each experimental condition (currently 20 runs per condition). This will help to achieve better convergence of the conversion algorithm (Turton and Clark, 1988) and also produce a closer-to-reality distribution.

(3) The multiple region experiment mentioned in Section 4.5.4. is perhaps an interesting area of future work. The approach of analysing the froth structure in zones may help to better understand the behaviour of the flows. In order to carry out the multiple region experiment, it is necessary to increase the number of runs per experimental condition as described above in (2).

(c) The current design of the liquid-liquid simulation rig has reached its maximum capacity but the full potential of the technique has yet to be explored. With the current setup, it is only possible to achieve the jetting regime under one condition (see Chapter 5 for details). Re-design of the experimental equipment would seem desirable in order to simulate more jetting-regime conditions: a more rigid but robust design of the rig is required so that it can cope with higher kerosene flowrates in the jetting regime. The new design should take the following potential problems into considerations: kerosene leakage due to excessive pressure, deterioration of rubber tubes, efficient separation method for the two liquids, the feasibility of replacing the perspex with alternative materials on non-viewing parts of the rig.

(d) With the continuing development on the CFD modelling of the tray flows, the prediction of mass transfer behaviour could be built into the code so that local mass transfer rates can be estimated and summed over the tray. Validation of the present methodology still requires further attention and data from industrial size columns will be the most valuable on providing such information.

Nomenclature

All parameters are in S.I. units, unless specified elsewhere.

A_f Fractional free area of a sieve tray

A_s Active (or bubbling) area of a sieve tray, m^2

a Constant defined in Jet Penetration model by Lockett (1981), Eq.(2.6)

a Interfacial area per unit volume of two-phase dispersion, $m^2 m^{-3}$

$\bar{a}$ Interfacial area per unit volume of liquid, $m^2 m^{-3}$

a_1 Constant defined in Biddulph's correlation (1995), Eq.(2.56)

a_2 Constant defined in Biddulph's correlation (1995), Eq.(2.56)

a_3 Constant defined in Biddulph's correlation (1995), Eq.(2.56)

Bo Bond number, $\frac{(\rho_L - \rho_G)gd_h^2}{\sigma}$

b Intercept of equilibrium line (binary)

C Constant defined in Bennett's correlation (1983), Eq.(2.27)

C_d Constant defined in Francis equation (1983), Eq.(2.21)

CF Capacity factor based on A_s, $u_s\left(\frac{\rho_G}{\rho_L - \rho_G}\right)^{0.5}$, $m\ s^{-1}$

C_v Discharge coefficient for an orifice

c Concentration

D_B Diameter of a rising bubble defined in Bennett's correlation (1983), Figure 2.19, m

D_{Bmax} Maximum diameter of a rising bubble defined in Bennett's correlation (1983), Eq.(2.50), m

D_G Diffusion coefficient in vapour phase, $m^2 s^{-1}$

D_L Diffusion coefficient in liquid phase, $m^2 s^{-1}$

d Diameter (general), m

d_b Bubble diameter, m

d_G Parameter defined in Bekassy-Molnar & Mustafa (1991), Eq.(2.33), m

d_h Hole diameter, m

d_p Droplet diameter, m

E_0 Section / overall efficiency

E_m liquid entrainment rate, $kg\ s^{-1}$

E_{ML} Murphree liquid phase tray efficiency

E_{MV} Murphree vapour phase tray efficiency

E_{OG} Murphree vapour phase point efficiency

e Liquid entrainment rate ÷ vapour rate (molar flowrate)

e_m Liquid entrainment rate ÷ vapour rate (mass flowrate)

$\mathcal{F}_i$ Poynting Factor

F_0 Parameter to be found for h_σ prediction, Eq.(2.57)

F_h Hole F-factor, $u_h \rho_G^{0.5}$, $kg^{0.5} m^{-0.5} s^{-1}$

FP Flow parameter, $\frac{M_L}{M_G}\left(\frac{\rho_G}{\rho_L}\right)^{0.5}$

Fr Froude number, u_s^2 / gh_L

Fr^* Modified Froude number, $\left[\rho_G u_h^2 / (\rho_L - \rho_G) g d_h\right]^{0.5}$

F_s Superficial F-factor, $u_s \rho_G^{0.5}$, $kg^{0.5}m^{-0.5}s^{-1}$

f Fanning friction factor, Eq.(2.42)

f Fugacity (in Section 2.4)

G Vapour flowrate, kg-mol s^{-1}

G' Vapour flowrate per unit bubbling area, kg-mol s^{-1} m^{-2}

g Acceleration due to gravity, m s^{-2}

h_D Dry tray pressure drop (equivalent height of liquid), m

h_f Froth height above tray, m

h_{fl} Clear liquid layer thickness on the tray, m

h_{hg} Hydraulic gradient on the tray, m

h_L Clear liquid height, m

$h_{L,ow}$ Clear liquid height over weir, Eq.(2.24), m

h'_L Pressure loss defined in Eq.(2.35), m

h_{ow} Height of froth flowing over the weir, m

h_T Total pressure drop across a wet tray (equivalent height of liquid), m

h_σ Residual pressure drop (equivalent height of liquid), m

h_w Weir height, m

J Flux

K Vapourisation equilibrium ratio

K_{OG} Overall mass transfer coefficient based on vapour, kg-mol s^{-1} m^{-2}

K'_{OG} Overall mass transfer coefficient based on vapour, m s^{-1}

K_{OL} Overall mass transfer coefficient based on liquid, kg-mol s^{-1} m^{-2}

K_w Constant defined in Smith and Van Winkle (1958), Eq.(2.43)

k Dry-plate coefficient defined in McAllister (1958), Eq.(2.42)

k_B Boltzman constant

k_G, k_L Vapour and liquid phase mass transfer coefficient, kg-mol s^{-1} m^{-2}

k'_G, k'_G Vapour and liquid phase mass transfer coefficient, m s^{-1}

L Liquid flowrate, kg-mol s^{-1}

L' Liquid flowrate per unit tray area, kg-mol s^{-1} m^{-2}

L'_w Weeping rate per unit tray area, kg-mol s^{-1} m^{-2}

M_G Gas mass flowrate, kg s^{-1}

M_L Liquid mass flowrate, kg s^{-1}

m Slope of equilibrium line (binary)

N Number of completely mixed liquid pools

N_A Molar flux of component A, kg-mol s^{-1} m^{-2}

N_{Actual} Number of actual trays

N_G Number of binary vapour phase transfer units

N_L, N'_L Number of binary liquid phase transfer units (different definitions!)
N_{OG} Number of overall binary vapour phase transfer units
N_p Number of liquid passes per tray
N_{Theo} Number of theoretical trays
n Constant defined in Jet Penetration model by Lockett (1981), Eq.(2.6)
Pe Peclet number
p Hole pitch of a sieve tray, m
ΔP_0 Pressure drop defined in Bekassy-Molnar & Mustafa (1991), N m^{-2}
ΔP_{dry} Dry tray pressure drop, N m^{-2}
Q_h Gas volumetric flowrate through hole, m^3s^{-1}
Q_G Gas volumetric flowrate, m^3s^{-1}
Q_L Liquid volumetric flowrate, m^3s^{-1}
r Separation ditance for L-J potential, Eq.(2.77)
r_0 Orifice radius, m
r_b Bubble departure radius, m
Re_h Hole Reynolds number
T_s Tray spacing, m
t Tray thickness, m
t_c Contact time of the interface, s
t_G Vapour residence time, s
t_L Liquid residence time, s
u_b Velocity defined in Stichlmair's correlation (1978), m s^{-1}
u_h Hole velocity, m s^{-1}
u_L Average liquid velocity on the tray, m s^{-1}
u_s Superficial velocity, m s^{-1}
u_t Large drop terminal velocity, Eq.(2.4), m s^{-1}
V_0 Volume of a bubble with the orifice diameter, Eq.(2.55), m^3
W Weir length, m
w Distance from centre line measured parallel to weir, m
x_n Liquid mole fraction leaving elemental strip n
$\bar{x}_n$ Mean mole fraction in liquid leaving tray n via downcomer
x'_n Mole fraction in liquid weeping or entrained from a point on tray n
x^*_n Mole fraction of liquid in equilibrium with mean vapour concentration leaving tray n
y Vertical position, m
y_0 Inlet vapour mole fraction
y_n Mole fraction in vapour at a point on tray n ; vapour mole fraction leaving elemental strip n
$\bar{y}_n$ Mean mole fraction in vapour leaving tray n
y^*_n Mole fraction of vapour in equilibrium with mean liquid concentration leaving tray n via downcomer ; vapour mole fraction in equilibrium with mean liquid concentration leaving elemental strip n
Z Liquid flow path length, m
z Distance from inlet weir, m

z' position on the tray; z' changes from unity to zero as the liquid flows from the inlet weir to the outlet weir

Greek Symbols

α Liquid holdup fraction
α' Constant defined in Eq.(2.34)
α_p A parameter defined in Eq.(2.1)
α_r Residual volume ratio in Eq.(2.55)
β Aeration factor, Eq.(2.36)
β' Constant defined in Eq.(2.34)
γ Activity coefficient
γ' Constant defined in Eq.(2.34)
δ' Constant defined in Eq.(2.34)
ε Gas holdup fraction
ε Characteristic L-J energy, Eq.(2.77)
ε_s Value of ε in the spray body
ε_w Value of ε in the froth flowing over outlet wier
θ Contact angle
λ Stripping factor or ratio of slope of equilibrium line to slope of operating line, mG/L
ξ Orifice coefficient
ξ_0 Parameter defined in Stichlmair & Mersmann's correlation (1978), Eq.(2.44)
σ Surface tension, kg m^{-3}
σ Characteristic L-J length, Eq.(2.77)
ρ_L, ρ_G Liquid and vapour density, kg m^{-3}
ρ'_L, ρ'_G Liquid and vapour density, kg-mol m^{-3}
τ $1 \div$ (bubbling frequency), Eq.(2.55), s^{-1}
ϕ Fugacity coefficient
ϕ_e Parameter defined in Bennett's correlation (1983), Eq.(2.27)
ψ Defined by Hofhuis & Zuiderweg (1979), Eq.(2.24), m
ψ Intermolecular potential, Eq.(2.77)
Ω_D Dimensionless collision intergral, Eq.(2.75)

Subscripts

i Interface
j Leaving elemental strip j
n Leaving tray n
G In vapour or gas phase
L In liquid phase

Superscripts

0 Local value at the exit weir
- Mean value

References

1. Abuaf, N., Jones, O.C., Zimmer, G.A. (1978). Optical probe for local void fraction and interface velocity measurements, *Rev. Sci. Instrum.*, vol.49, no.8, pp.1090
2. AIChE (1958). *Bubble Tray Design Manual*, AIChE, New York
3. AID (1983). Grenoble-Meylan, France
4. Al Taweel, A.M., Divakarla, R. and Gomaa, H.G. (1984). Measurement of large gas-liquid interfacial areas, *Can. J. Chem. Engng.* **62**, (Feb), 73
5. Assael M. J., Trusler J. P. M. and Tsolakis T. F. *Thermophysical Properties of Fluids.* Imperial College Press, London, 1996.
6. Azbel, D.S. (1963). The hydrodynamics of bubbler processes, *Int. Chem Eng*, vol.3, no.3, pp.319
7. Barber, A.D., Wijn, E.F. (1979). Foaming in crude distillation units, *IChemE Symposium series*, no.56, pp.3.1
8. Barker, P.E., Self, M.F. (1962). The evaluation of liquid mixing effects on a sieve plate using unsteady and steady state tracer techniques, *Chem Eng Sci*, vol.17, pp.541
9. Bekassy-Molnar, E., Mustafa, H. (1991). Clear liquid height on sieve plates in the froth, mixed and spray regimes, *Trans IChemE*, vol.69, part.A, pp.14
10. Bekassy-Molnar, E., Mustafa, H. (1991). Influence of surface tension on pressure drop of sieve plates, *Trans IChemE*, vol.69, part.A, pp.287
11. Benedict, M., Webb, G.B. and Rubin, L.C. (1940). *J. Chem. Phys.* **8** : 334
12. Bennett, D.L., Agrawal, R., Cook, P.J. (1983). New pressure drop correlation for sieve tray distillation columns, *AIChE Journal.* vol.29, no.3, pp.434
13. Bennett, D.L., Kovak, K., Zak, D. (1997). Optimisation of sieve-type distillation trays, *AIChE meeting*, paper 25f, November 1997
14. Bennett, D.L., Ludwig, K.A. (1994). Understand the limitations of air/water testing of distillation equipment, *Chem Eng Progress*, no.4, pp.72
15. Bennett, D.L., Watson, D.N., Wiescinski, M.A. (1997). New correlation for sieve-tray point efficiency, entrainment, and section efficiency, *AIChE Journal.* vol.43, no.6, pp.1611
16. Biddulph, M.W., Thomas, C.P. (1995). Effect of liquid surface tension on small hole distillation sieve tray pressure drop, *AIChE Journal.* vol.41, no.4, pp.819
17. Brambilla, A., Nardini, G., Nencetti, G.F., Zanelli, S. (1969). Hydrodynamic behaviour of distillation columns: pressure drop in plate distillation columns, *IChemE Symposium series*, no.32, pp.2.63
18. Bravo, J.L. (1997). Select structured packings or trays?, *Chem Eng Progress*, no.7, pp.36
19. Brokaw, R. S.: *Ind. Eng. Chem. Process Design Develop.*, **8:** 240 (1969).
20. Brown, G.H. (1971). Photochromism. Techniques of Chemistry Vol. III, John Wiley & Sons, New York
21. Burgess, R.G., Robinson, K. (1969). Transition from spray to bubbling on a large sieve plate with cross-flow of the liquid, *IChemE Symposium series*, no.32, pp.2.34

22. Burgess, J.M., Calderbank, P.H. (1975). Measurement of bubble parameters in two-phase dispersions-II The structure of sieve tray froths, *Chem. Eng. Sci.* vol.30, pp.1107-1121
23. Calderbank, P.H. (1959). Physical rate processes in industrial fermentation – Part II, *Trans. Inst. Chem. Engrs.* **37**, 173
24. Calderbank, P.H., Pereira, J. (1977). The prediction of distillation plate efficiencies from froth properties, *Chem Eng Sci*, vol.32, pp.1427
25. Carrica, P.M., Masson, V., Marco, P.D. (1997), Application of a low cost true-monofiber local phase detection probe to void fraction measurements in pool boiling, *Expt. Heat Transfer, Fluid Mechs, Thermodynamics...*, pp.293
26. Cartellier, A. (1990). Optical probes for local void fraction measurements: characterisation of performance, *Rev. Sci. Instrum.* Vol.61, no.2, pp.874
27. Cartellier, A., Achard, J.L. (1991). Local phase detection probes in fluid/fluid two-phase flows, *Rev. Sci. Instrum*, vol.62, no.2, pp.279
28. Castillejos, A.H., Brimacombe, J.K. (1987). Measurement of physical characteristics of bubbles in gas-liquid plumes: Part I. An improved electroresistivity probe technique, *Metallurgical Transactions B*, vol.18B, pp.649
29. Cervenka, J., Kolar, V. (1973). The structure and height of the gaseous-liquid mixture on sieve plates without downcomers, *Chem Eng Journal*, vol.6, pp.45
30. CFDS (1992) *Flow3D User Guide, Release 3.2*, AEA Technology.
31. CFX (1997) *CFX User Guide, Release 4.4*, AEA Technology.
32. Chan, H. and Fair, J.R. (1984). *Ind. Eng. Chem. Pros. Des. Dev.*, **23**: 814 & 820
33. Chapman S. and Cowling T.G. (1970). *The mathematical theory of non-uniform gases : an account of the kinetic theory of viscosity, thermal conduction and diffusion in gases*
34. Chen, G., Y. Hou and H. Knapp: *J. Chem. Eng. Data*, **40:** 1005 (1995)
35. Chen, J.J.J. (1985) Correpondence, *Chem Eng Res Des*, vol.63,pp.206
36. Chen, J.J.J. (1987) Comments on "clear liquid height and froth density on sieve trays by Colwell (1981)", *Ind Eng Chem Res*, vol.26,pp.638
37. Chen, J.J.J., Wong, P.F.Y., Kwan, W.K. (1982) Spray-bubbling transition on sieve trays, *Int. J. Multiphase Flow*, vol.8, no.5, pp.565
38. Chen, N.H. and Othmer, D.P. (1962). *J. Chem. Eng. Data.* 7: 37
39. Clark, N.N. and Turton, R. (1988). *Int. J. Multiphase Flow*, vol.14, no.4., pp.413
40. Clift, R., Grace, J.R., Weber, M.E. (1978). *Bubbles, drops, and particles.* Academic Press, New York
41. Colwell, C.J. (1981). Clear water height and froth density on sieve trays, *Ind Eng Chem Pro Des Dev*, vol.20, no.2, pp.298
42. Coulson, J.M., Richardson J.F. (1983). *Chemical Engineering.* Vol. 6, An introduction to chemical engineering design. Oxford: Pergamon
43. Crabtree, J.R., Bridgwater, J. (1971). Bubble coalescence in viscous liquids, *Chem Eng Sci*, vol.26, pp.839
44. Cussler, E. L. (1984) *Diffusion : Mass transfer in fluid systems.* Cambridge University Press.
45. Daly, B. (1997). PhD Thesis, University of Bristol.
46. Daily, J.W. and Harleman, D.R.F. (1966). *Fluid Dynamics.* Addison-Wesley: Reading, Mass.
47. Danel, D. and Delhaye, J.M. (1971). *Mesures Regulation Automatisme* 36, 8/9:99-101
48. Darken, L.S. (1948). *Trans. Am. Inst. Mining Metall. Eng.*, **175**: 184

49. Davidson, J.F., Schuler, B.O.G. (1960) Bubble formation at an orifice in a viscous liquid, *Trans Instn Chem Engrs*, no.38, pp.144
50. Davidson, J.F., Schuler, B.O.G. (1960) Bubble formation at an orifice in an inviscid liquid, *Trans Instn Chem Engrs*, no.38, pp.335
51. Davidson, L., Amick, E.H. (1956). Formation of gas bubbles at horizontal orifices, *AIChE Journal*, vol.2, no.3, pp.337
52. Delhaye, J.M. and Galup, J.P. (1974). *European Two-Phase Flow Meeting*, Harwell
53. Dhulesia, H. (1984). Clear liquid height on sieve and valve trays, *Chem Eng Res Des.* vol.62, no.5, pp.321
54. Easteal, A. J.: *AiChE J.*, **30:** 641 (1984).
55. Fair, J.R. (1961). How to predict sieve tray entrainment and flooding, *Petro/Chem. Engineer*, vol.33, (10), 45
56. Fair, J.R. (1997). Tres bien! Trays are still "in"!, *AIChE meeting*, paper 25a, November 1997
57. Fair, J.R., Seibert, A.F. (1996). Understand distillation-column debottlenecking options, *Chem Eng Progress*, no.6, pp.42
58. Fairbanks, D.F. and Wilke, C.R. (1950). *Ind. Eng. Chem.* vol.42, no.3, pp471
59. Fane, A.G. (1962). PhD Thesis, Imperial College
60. Finch, R.N., Van Winkle, M. (1964). Statistical correlation of the efficiency of perforated trays, *Ind Eng Chem Pro Des Dev*, vol.3, no.2, pp.106
61. Fischer, C.H. (1997). Numerical modelling of distillation tray hydraulics, First Year Report
62. Fischer, C.H., Quarini, G.L. (1998). Three-dimensional heterogeneous modelling of distillation tray hydraulics, *AIChE meeting*, November 1998, unpublished
63. Fischer, C.H., Quarini, G.L., Yang, H.M., Hewitt, G.F. (1998). The formation of partial bubbling zones on distillation trays and their periodic translation, *AIChE meeting*, November 1998, unpublished
64. Fischer, C.H. (1999). PhD Thesis, University of Bristol
65. Fogwell, T.W. and Hope, C.B. (1987). Thermal Hydraulics Division, Harwell Laboratory, Ref: AERE R 12652
66. Fuller, E. N., K. Ensley, and J.C. Giddings: *J. Phys. Chem.*, **75:** 3679 (1969).
67. Fuller, E.N., P. D. Schettler, and J. C. Giddings: *Ind. Eng. Chem.*, **58**(5), 18 (1966).
68. Galup, J.P. and Delhaye, J.M. (1976). La Houille Blanche 1
69. Gardner, R.G., McLean A.Y. (1969). Effect of system properties on sieve-plate froths, *IChemE Symposium Series*, no.32, pp.2:39
70. Gilliland, E.R. (1934). *Ind. Eng. Chem.* **26**: 681
71. Habibullah, A., Gong, J. (1997) Trends in column internals for refinery revamp projects, *AIChE meeting*, paper 25g, November 1997
72. Hamad, F.A., Imberton, F., Bruun, H.H. (1997). An optical probe for measurements in liquid-liquid two-phase flow, *Meas. Sci. Technol.*, no.8, 1997
73. Harris, I.J., Roper, G.H. (1962). Performance characteristics of a 12in. diameter sieve plate, *Can. J. of Chem Eng*, vol.40, no.6, pp.245
74. Hayduk, W. and Laudie, H. (1974). *AIChE J.*, **19**: 698
75. Hayduk, W. and Minhas, B.S. (1982). *Can. J. Chem. Eng.*, **60**: 295
76. Hewitt G. F., Shires G. L. and Bott T.R. *Process Heat Transfer*. (1994) CRC Press, Begell House. ISBN 0-8493-9918-1
77. Higbie, R. (1935). *Trans. Am. Inst. Chem. Engrs.* **31**: 365

78. Ho, G.E., Muller, R.L., Prince, R.G.H. (1969). Characterisation of two-phase flow pattern in plate columns, *IChemE Symposium Series*, no.32, pp.2:10
79. Hofhuis, P.A.M., Zuiderweg, F.J. (1979). Sieve plates: dispersion density and flow regimes, *IChemE Symposium series*, no.56, pp.2.2/12
80. Hofhuis, P.A.M., Zuiderweg, F.J., Kuzniar, J. (1984). Flow regimes on sieve trays: the significance of the emulsion flow regime, *Chem Eng Res Des.* vol.62, pp.39
81. Hong J. H., Malone P. V., Jett M. D. and Kobayashi R., *Fluid Phase Equil.* **38** 83 (1987).
82. Hughes, R.R., Handlos, A.E., Evans, H.D., Maycock, R.L. (1955). The formation of bubbles at simple orifices, *Chem Eng Progress*, vol.51, no.12, pp.557
83. Humphrey, J.A.C. (1977). *Can. J. Chem. Eng.*, **55**: 126
84. Jeronimo, M.A.S., Sawistowski, H. (1973). Phase inversion correlation for sieve trays, *Trans Instn Chem Engrs*, vol.51, pp.265
85. Johnson, P.A., Babb, A.L.: *Chem. Rev.*, **56:**387 (1956)
86. Katayamo, H. and Imoto, T. (1972). *J. Chem. Soc. Japan.*, **9**: 1745
87. Kawagoe, K., Inoue, T., Nakao, K., Otake, T. (1976). Flow-pattern and gas-holdup conditions in gas-sparged contactors, *Int. Chem Eng*, vol.16, no.1, pp.176
88. Khalfaoui B., Meniai A. H. and Borja R., *Fluid Phase Equil.* **127**, 181 (1997).
89. Kim, S.K. (1966). Theoretical study of vapour-liquid holdup on a perforated plate, *Int. Chem Eng*, vol.6, no.4, pp.634
90. King, C.J. (1980). *Separation Processes.* McGraw-Hill
91. Kister, H.Z. (1997). Are column malfunctions becoming extinct-or will they persist in the 21st century?, *Trans IChemE*, vol.75., part A, pp.563
92. Kister, H.Z., Larson, K.F., Madsen, P.E. (1992). Vapour cross-flow channelling on sieve trays fact or myth?, *Chem Eng Progress*, no.11, pp.86
93. Kister, H.Z. (1992). *Distillation Design.* McGraw-Hill.
94. Kister, H.Z. (1990). *Distillation Operation.* McGraw-Hill.
95. Kolar, V. (1969). The structure of gas-liquid mixtures on sieve trays of separation columns, *Chem Eng Sci*, vol.24, pp.1285
96. Koneripalli, N., Z. Tekie and B. I. Morsi: *Chem. Eng. J.*, **54:** 63 (1994).
97. Krishna, R., Van Baten, J.M., Ellenberger, J., Higler, A.P. and Taylor, R. (1999). *Trans IChemE*, vol.77, part A, Oct 1999, pp.639
98. Kumar, A. and Kuloor, N.R. (1970), The formation of bubbles and drops, *Advances in Chem Engng.* **8**, pp.256
99. Kunesh, J.G., Kister, H.Z., Lockett, M.J., Fair, J.R. (1995). Distillation: still towering over other options, *Chem Eng Progress*, no.10, pp.43
100. Kupferberg, A., Jameson, G.J. (1969). Bubble formation at a submerged orifice above a gas chamber of finite volume, *Tran Instn Chem Engrs*, vol.47, pp.T241
101. Kurihara K., Minoura T., Takda K. and Kojima K., *J. Chem. Eng. Data* **40**, 679 (1995).
102. Kwan, W.K., Ng, R.K.F., So, L.W.M., Wong, P.F.Y. (1992). Effect of spray structure on the spray froth transition on sieve trays, *IChemE Symposium series*, no.128, pp.A385
103. Lappin, A. and Lubbert, A. (1994). *Chem. Eng. Sci.*, vol.49, no.21, pp.3661
104. Lee, B.I. and Kesler, M.G. (1975). *AIChE J.* **21**: 510
105. Lee, Y. E. and S. F. Y. Li: *J. Chem. Eng. Data*, **36:** 240 (1991).
106. Lehner, M. and Mewes, D. (1999). *Applied Optical Measurements*, Springer-Verlag Berlin Heidelberg

107. Leibson, I., Holcomb, E.G., Cacoso, A.G. and Jacmic, J.J. (1957) Rate of flow and mechanics of bubble formation from single submerged orifices, *AIChE J.* **2**, (3), 296
108. Lewis, W.K. (1936). *Ind. Eng. Chem.*, **28**: (1), 399
109. Lo, S. (1996). Application of the MUSIG model to bubbly flows, AEAT-1096, AEA Technology, June 1996.
110. Lockett, M.J. (1981). Froth to spray transition on sieve trays, *Trans IChemE*, vol.59, pp.26
111. Lockett, M.J. (1986). *Distillation tray fundamentals*. Cambridge University Press.
112. Loon, R.E., Pinczewski, W.V., (1973). Dependence of the froth-to-spray transition on sieve tray design parameters, *Trans Instn Chem Engrs*, vol.51, pp.374
113. Luo, H. and Svendsen, H.F. (1996). Theoretical model for drop and bubble breakup in turbulent dispersions, AIChE J., May 1996, Vol 42, No 5, pp 1225-1233.
114. Marrero, T.R. and Mason, E.A. (1972). *J. Phys. Chem. Ref. Data.*, **1**: 3
115. Marshall, S.H., Chudacek, M.W., Bagster, D.F. (1993). A model for bubble formation from an orifice with liquid cross-flow, *Chem Eng Sci*, vol.48, no.11, pp.2049
116. Matthews, M. A., J. B. Rodden and A. Akgerman: *J. Chem. Eng. Data*, **32:** 319 (1987).
117. Matthews, M. A. and A. Akgerman: *J. Chem. Eng. Data*, **33:** 123 (1988).
118. McAdams, W. H., Woods, W. K. and Heroman, L.C. (1942), Vapourization inside horizontal tubes. II: Benzene-oil mixtures, *Trans. ASME*, 64, 193
119. McAllister, R.A., McGinnis, P.H., Plank, C.A. (1958). Perforated plate performance, *Chem Eng Sci*, vol.9, pp.25
120. McCabe, W.L., Smith, J.C., Harriott, P. (1993). *Unit Operations of Chemical Engineering*. 5th Edition, McGraw-Hill.
121. McCann, D.J., Prince, R.G.H. (1969). Bubble formation and weeping at a submerged orifice, *Chem Eng Sci*, vol.24, pp.801
122. McCann, D.J., Prince, R.G.H. (1971). Regimes of bubbling at a sumberged orifice, *Chem Eng Sci*, vol.26, pp.1505
123. McFarland, S.A., Sigmund, P.M. and Van Winkle, M. (1972). *Hydrocarbon Processing*, **51**: (July), 111
124. McGlashan M. L. and Wiliamson A. G., *J. Chem. Eng. Data* **21**, 196 (1976).
125. McKetta, J.J., Cunningham, W.A. (1982) *Encyclopedia of Chemical Processing and Design.* Vol. 16. McGraw-Hill.
126. Miller, N. and Mitchie, R.E. (1969). *Two-Phase Flow Instrumentation ASME 82-88*
127. Miller, N. and Mitchie, R.E. (1970). *J. Br. Nucl. Energy Soc.*, **9**, 2: 94-100
128. Miyahara, T., Takahashi, T. (1984). Transition from froth to spray on perforated plates, *J. of Chem Eng of Japan*, vol.17,no.2,pp.221
129. Miyahara, T., Terakado, H., Takahashi, T. (1983) Transition from bubbling to jetting at single orifices, *J. of Chem Eng of Japan*, vol.16, no.6, pp.454
130. Morris, D., Teyssedou, A., Lapierre, J., Tapucu, A. (1987). Optical fiber probe to measure local void fraction profiles, *Applied optics*, vol.26, no.21, pp.4660
131. Muller, R.L., Prince, R.G.H. (1972). Regimes of bubbling and jetting from submerged orifices, *Chem Eng Sci*, vol.27, pp.1583
132. Murphree, E.V. (1925). *Ind. Eng. Chem.*, **17**, (7), 747
133. Neuburg, H.J. and Chuang, K.T. (1982). *Can. J. Chem. Eng.*, **60**: Aug, 504 & 510

134. Payne, G.J., Prince, R.G.H. (1977). Relationship between the froth and spray regimes, and the orifice processes occurring on perforated distillation plates, *Trans IChemE*, vol.55,pp266
135. Peng D. Y. and Robinson D. B., *Ind. Eng. Chem. Fundam.* **15**, 59 (1976).
136. Perkins, L.R. and Geankoplis, C.J. (1969). *Chem. Eng. Sci.*, **24**: 1035
137. Perry, R.H., Green, D.W. (1997). *Perry's Chemical Engineers' Handbook.* 7th Edition, McGraw-Hill
138. Pertler, M., Blass, E. and Stevens, G.W. (1996). *AIChE J.*, vol.42, no.4, pp910
139. Pierotti G. J., Deal C. H. and Derr E. L., *Ind. Eng. Chem.* **51**, 95 (1959).
140. Pinczewski, W.V., Yeo, H.K. and Fell, C.J.D. (1973). Transition behaviour at submerged orifices, *Chem Eng Sci*, vol.28, pp.2261
141. Pinczewski, W.V. (1981). The formation and growth of bubbles at a submerged orifice, *Chem Eng Sci*, vol.36, pp.405
142. Pinczewski, W.V., Fell, C.J.D. (1972). Transition from froth-to-spray regime on commercially loaded sieve trays, *Trans Instn Chem Engrs*, vol.50, pp.102
143. Pinczewski, W.V., Fell, C.J.D. (1982). Froth to spray transition on sieve trays, *Ind Eng Chem Pro Des Dev*, vol.21, pp.774
144. Pitzer, K.S., Lippmann, R.F. Curl, Huggins, C.M. and Petersen, D.E. (1955). *J. Am. Chem. Soc.* **77**: 3433
145. Plöcker, U., Knapp, H. and Prausnitz, J.M. (1978). *Ind. Eng. Chem. Process Design Develop* **17**: 324
146. Pohorecki, R., Kruszewski, J., Duczmal, B. (1992). The influence of surface phenomena on the interfacial area during absorption/desorption on a sieve plate, *IChemE Symposium Series*, no.128, pp.A69
147. Ponter, A.B., Surati, A.I. (1997). Bubble emissions from submerged orifices-a critical review, *Chem Eng Tech*, vol.20, pp.85
148. Porter, K.E., Davis, B.T. and Wong, P.F.Y. (1967). Mass transfer and bubble sizes in cellular foams and froths, *Trans. Inst. Chem. Engrs.* **50**, 91
149. Porter, K.E. (1995). Why research in needed in distillation, *Trans IChemE*, vol.73, part A, pp.358
150. Porter, K.E., Wong, P.F.Y. (1969). Transition from spray to bubbling on sieve plates, *IChemE Symposium series*, no.32, pp.2.22
151. Porter, K.E. and Jenkins, J.D. (1979). *Inst. Chem. Eng. Symp. Series No.56*, Discussion Volume, pp.75
152. Porter, K. E., Lockett, M. J. and Lim, C. T. (1972). The effect of liquid Channelling on Distillation Plate Efficiency, *Trans. Instn. Chem. Engrs.*, 50, pp 190 195.
153. Prince, M.J. and Blanch, H.W. (1990). Bubble coalescence and break-up in air-sparged bubble columns, AIChE J., Oct 1990, Vol 36, No 10, pp 1485-1499.
154. Prince, R.G.H., Jones, A.P., Panic, R.J. (1979). Froth spray transition, *IChemE Symposium series*, no.56, pp.2.2
155. Quarini, G. L., Chang Y. C., Tierney M. J. and Poulter R. Characteristics and Figure of Merits for the value of the ventilation in clean room. (1997) *Trans IChemE* Part A pp 672-675.
156. Raper, J.A., Burgess, J.M. and Fell, C.J.D. (1977a). *Inst. Chem. Eng.*, 4th annual research meeting, Swansea.
157. Raper, J.A., Phuong, T.V. and Fell, C.J.D. (1977b). Chemeca 77, 14-16, Sept, Canberra.
158. Raper, J.A., Dixon, D.C., Fell, C.J.D. and Burgess, J.M. (1978). *Chem. Eng. Sci.*, **33**: 1405

159. Raper, J.A., Kearney, M.S., Burgess, J.M. and Fell, C.J.D. (1982). The structure of industrial sieve tray froths, *Chem. Eng. Sci.* **37**, 501
160. Redlich, O. and Kwong, J.N.S. (1949). *Chem. Rev.* **44**: 233
161. Reid, R.C., Prausnitz, J.M., Poling, B.E. (1987). *The Properties of Gases & Liquids*. McGraw-Hill. 4th Edition
162. Reid, R.C., Prausnitz, J.M., Sherwood, T.K. (1977). *The Properties of Gases & Liquids*. McGraw-Hill. 3rd Edition
163. Rigby, G.D., Evans, G.M., Jameson, G.J. (1995). Modelling of gas flow from a submerged orifice in liquid cross-flow, *Trans IChemE*, vol.73, part A, pp.234
164. Rose, L.M. (1985). *Distillation Design in Practice*. Amsterdam Oxford: Elsevier.
165. Rousseau, R.W. (1987). *Handbook of Separation Process Technology*. Chapter 5.7. John Wiley & Sons.
166. Ruzicka, M.C., Drahos, J., Zahradnik, J., Thomas, N.H. (1997). Intermittent transition from bubbling to jetting regime in gas liquid two phase flows, *Int. J. Multiphase Flow*, vol.23, vol.4, pp.671
167. Saville, G. and Szczepanski, R. (1982). Methane-based equations of state for a corresponding state reference substance. *Chem. Eng. Sci.* **37**: 719
168. Schweitzer, P.A. (1979). *Handbook of Separation Techniques for Chemical Engineers*. McGraw-Hill.
169. Serizawa (1975). *Int. J. Multiphase Flow.*, vol.1
170. Siddiqi, M. A. and K. Lucas: *Can. J. Chem. Eng.*, **64:** 839 (1986).
171. Skelland, A.H.P. *Diffusional Mass Transfer* (1985).
172. Slattery, J.C., and R.B. Bird: *AIChE J.*, **4**:137 (1958)
173. Smith, B.D. (1963). *Design of Equilibrium Stage Processes*. Chapter 15, McGraw-Hill.
174. Soave, G. (1972). *Chem. Eng. Sci.* **27**: 1197
175. Sorel, (1893). "La rectification de l'alcool"
176. Spell, K.E. (1954). Bubble formation by rapid air flow through slots submerged in water, *Trans Instn Chem Engrs*, vol.32, pp.167
177. Steiner, L., Ballmer, J.F., Hartland, S. (1975). The structure of gas-liquid dispersions on perforated plates, *Chem Eng Journal*, vol.10, pp.35
178. Stichlmair J.G. and Fair, J.R. (1998). *Distillation: principles and practices*. Wiley-Liss Publication.
179. Stichlmair, J., Mersmann, A. (1978) Dimensioning plate columns for absorption and rectification, *Int. Chem Eng*, vol.18, no.2, pp.223
180. Tahmasbi, K. (1997) Two phase hydrodynamics in crossflow distillation, PhD Thesis, Imperial College, University of London
181. Takahashi, T., Mathuno, R., Miyahara, T. (1973). Theoretical consideration of gas void fraction and froth height on a perforated plate, *J. Chem. Eng. Japan,* vol.6, no.1, pp.38
182. Takahashi, S.: *J. Chem. Eng. Japan,* **7:** 417 (1974).
183. Takahashi, T., Matsuno, R., Miyahara, T. (1979). Theoretical consideration of gas void fraction and froth height on a perforate plate: low clear liquid height under liquid stagnant, *J. of Chem Eng of Japan*, vol.6,no.1,pp.38
184. Takahashi, T., Miyahara, T. (1979). Gas void fraction on a perforated plate: gas-liquid crosscurrent flow, *J. of Chem Eng of Japan*, vol.12,no.4,pp.269
185. Taylor, R., Krishna, R. (1993) *Multicomponent Mass Transfer*. John Wiley & Sons, Inc.
186. Tezock, M.C. (1993) Some Aspects of crossflow hydrodynamics on distillation trays, PhD Thesis, Imperial College, University of London

187. Thomas, W.J., Campbell, M. (1967). Hydraulic studies in a sieve plate downcomer system, *Trans Instn Chem Engrs*, vol.45, pp.T53
188. Thomas, W.J., Haq, M.A. (1976). Studies of the performance of a sieve tray with 3/8-in diameter perforations, *Ind Eng Chem Pro Des Dev*, vol.15, no.4, pp.509
189. Treybal, R. E. (1980) Mass-transfer operations. 3rd Edition.
190. Turton, R. and Clark, N.N. (1989). *Powder Technology*, **59**: 117-123
191. Tyn, M. T. and W. F. Calus: *J. Chem. Eng. Data*, **20:** 106 (1975).
192. Unno, H., Inoue, I. (1976). Froth density profiles and froth height on perforated plate, *J. of Chem Eng of Japan*, vol.9,no.2,pp.92
193. Van de Ven-Lucassen, I. M. J. J., F. G. Kieviet and P. J. A. M. Kerkhof: *J. Chem. Eng. Data*, **40:** 407 (1995).
194. Versteeg, H. K. and Malalasekera, W. (1995). *An introduction to Computational Fluid Dynamics, The finite volume method.* Longman Scientific and Technical
195. Vignes, A. (1966). *Ind. Eng. Chem. Fundam.*, **5**:189
196. Wijn, E.F., (2000). Website literature "http://www.euronet.nl/~wijnef/"
197. Wilke, C. R., and P. Chang: *AIChE J.*, **1:** 264 (1955).
198. Wilke, C. R., and C.Y. Lee: *Ind. Eng. Chem*, **47:** 1253 (1955).
199. Wong, C. F. and W. Hayduk: *Can. J. Chem. Eng.*, **68:** 849 (1990).
200. Wong, P.F.Y., Kwan, W.K. (1979). Generalised method for predicting the spray-bubbling transition on sieve plates, *Trans IChemE*, vol.57, pp.205
201. Yang, H.M., Hewitt, G.F., Mendes-Tatsis, M.A. (1998). Literature Review: Sieve Tray Hydrodynamics, MPS/113, ASID/05
202. Yang, H.M., Hewitt, G.F., Mendes-Tatsis, M.A. (1999). Literature Review: Sieve Tray Efficiency
203. Zuiderweg, F.J. (1982). Sieve trays: A view on the state of the art, *Chem Eng Sci*, vol.37, no.10, pp.1441
204. Zuiderweg, F.J. (1983). *Chem. Eng. Res. Des.*, **61**: Nov, 388
205. Zuiderweg, F.J., Hofhuis, P.A.M., Kuzniar, J. (1984). Flow regimes on sieve trays: the siginificance of the emulsion flow regime, *Chem Eng Res Des*, vol.62, pp.39

Appendix A. Le Bas (1915) Additive Volumes Method

This is a method used to estimate molar volume at normal boiling temperature (1 bar).

	Volume Increment, cm^3/mol
Carbon	14.8
Hydrogen	3.7
Oxygen (except as noted below)	7.4
In methyl esters and ethers	9.1
In ethyl esters and ethers	9.9
In higher esters and ethers	11.0
In acids	12.0
Joined to S, P, or N	8.3
Nitrogen: Doubly bonded	15.6
Nitrogen: In primary amines	10.5
Nitrogen: In secondary amines	12.0
Bromine	27.0
Chlorine	24.6
Fluorine	8.7
Iodine	37.0
Sulphur	25.6
Ring, three-membered	-6.0
Ring, four-membered	-8.5
Ring, five-membered	-11.5
Ring, six-membered	-15.0
Ring, Naphthalene	-30.0
Ring, Anthracene	-47.5

e.g. for methanol (CH_3OH)

$V_b = 14.8\times1+3.7\times4+7.4\times1 = 37.0$ cm^3/mol

Experimental data (from Chemistry handbook): 41.9 cm^3/mol

Percentage error = -11.7%

Appendix B. Dispersion Density Profile

The froth density profile above a tray is obtained by using the gamma densitometer described in Section 3.3.1. Six different tray geometries have been investigated in the present work and the results displayed below represent an average liquid fraction over 30 seconds and across the width of the column. Some of these results have been used to validate the CFD studies of sieve trays carried out at Bristol University.

B1. 1.8mm Tray, 8mm inlet and outlet weir, 940mm active/bubbling length

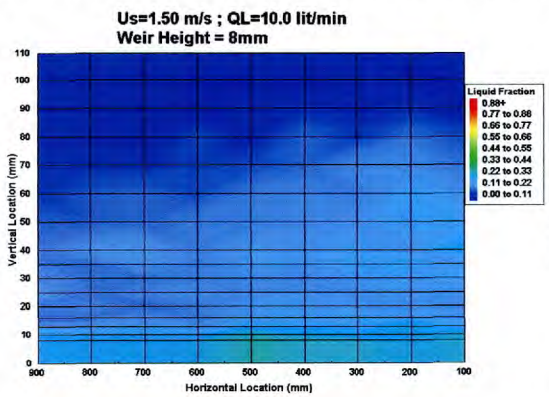


Figure B1.1

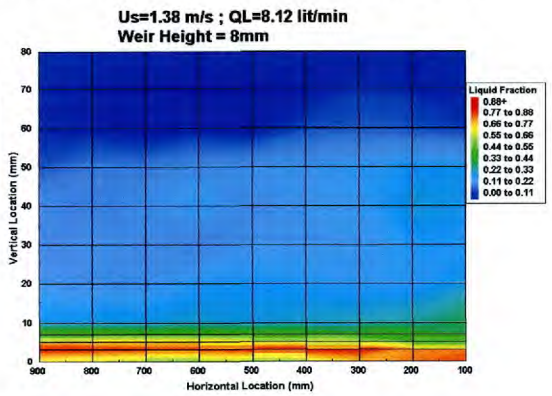
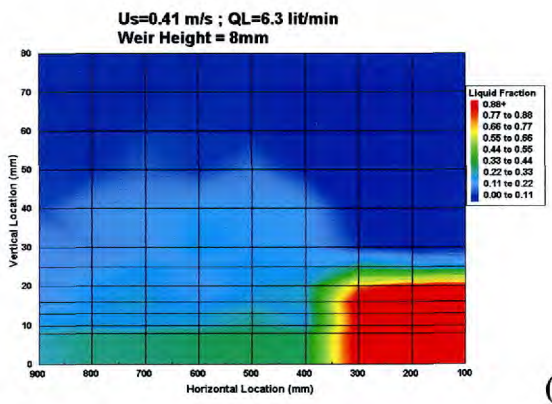


Figure B1.2



(Partial bubbling case)

Figure B1.3

The first two figures reflect typical results from sieve tray operations. The froth height is higher at the inlet of the tray (i.e. right hand side of the figure) and decreases slowly towards the outlet. The partial bubbling case (Figure B1.3) occurs at a much lower gas velocity where gas tends to pass through the tray via area with lower resistance (i.e. near the outlet where the clear liquid height is lower).

B2. 1.8mm Tray, 8mm inlet and outlet weir, calming zones

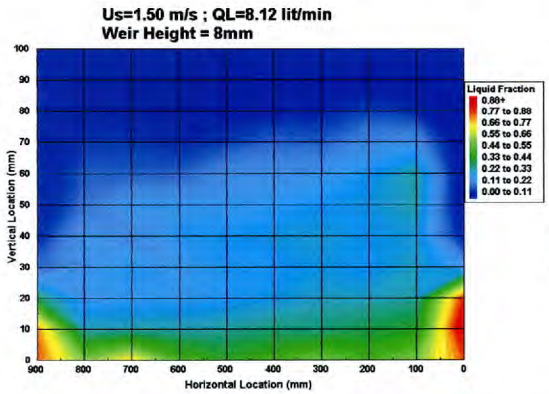


Figure B2.1

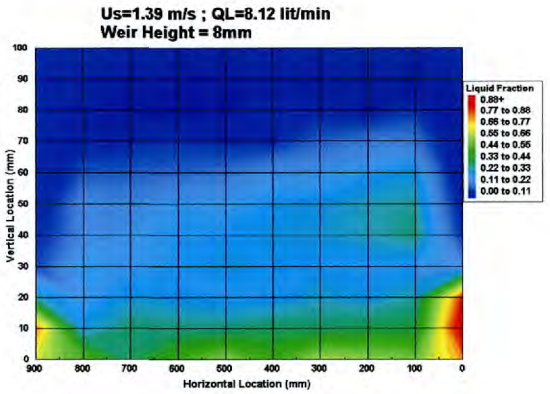


Figure B2.2

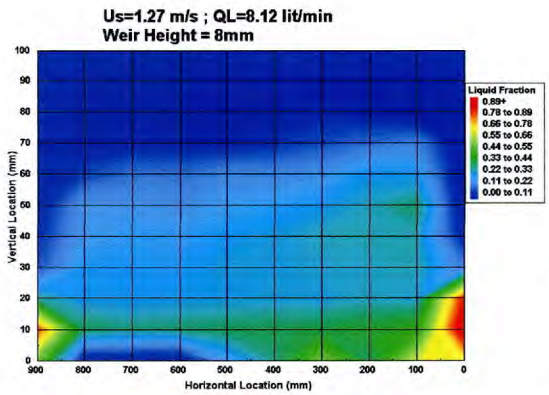


Figure B2.3

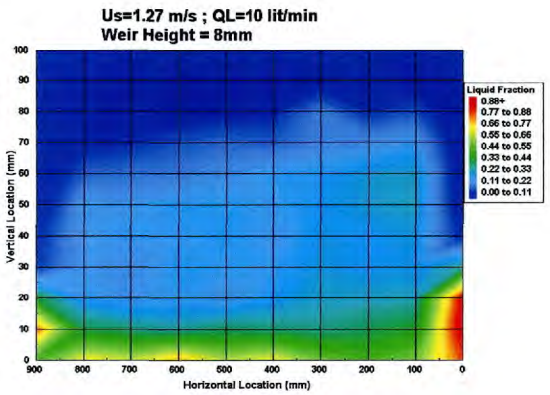


Figure B2.4

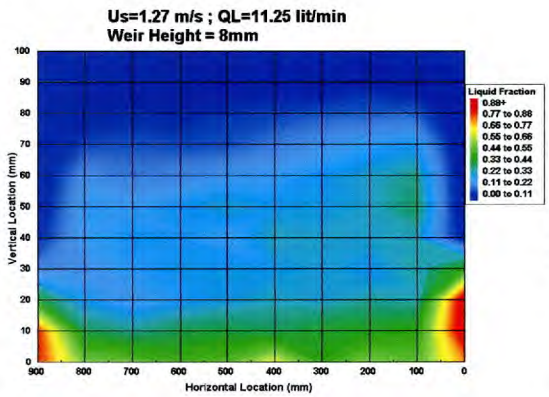


Figure B2.5

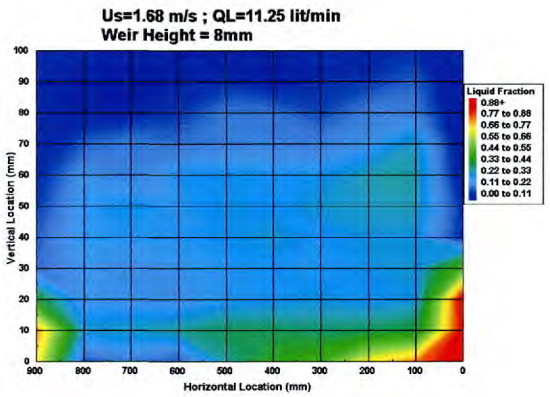


Figure B2.6

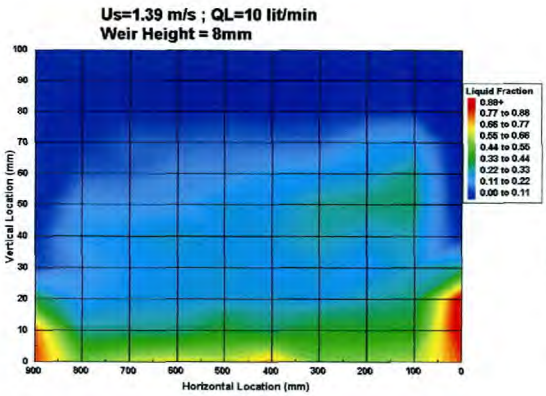


Figure B2.7

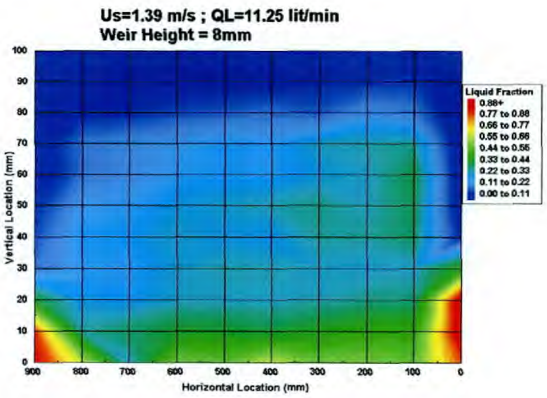


Figure B2.8

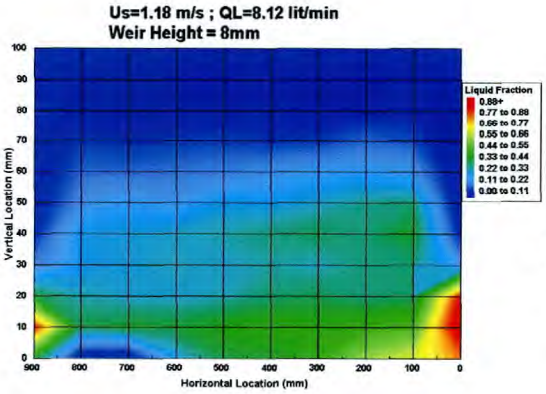


Figure B2.9

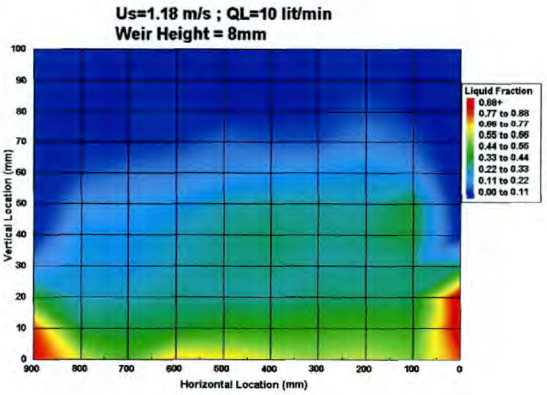


Figure B2.10

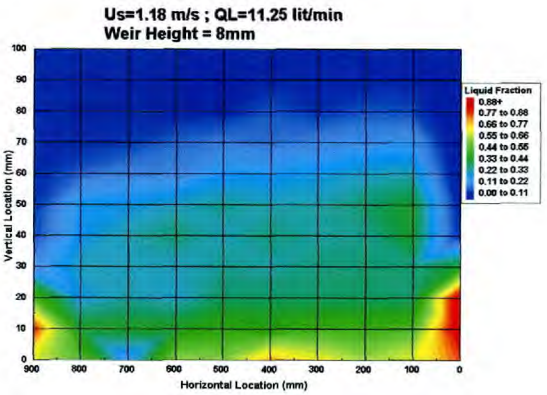


Figure B2.11

In this set of results, the effect of calming zones can be observed clearly from the two red colour patches at both ends of the tray floor (i.e. high fraction of liquid). An important point to note is that every profile looks similar to its neighbouring ones. This is because the effect of varying flowrates on the profile is a gradual process. However, obvious differences can be seen between Figures B2.6 and B2.11 where spray and froth were the observed flow patterns respectively. In Figure B2.6, the froth height can be as

high as 90mm above the tray floor and the froth body is mainly filled with blue colour (i.e. liquid fraction from 0.11 to 0.33 roughly). In Figure B2.11, the froth height is just over 70mm and the majority part of the froth is filled with green colour (i.e. liquid fraction from 0.22 to 0.44 roughly). Finally, regardless of flow conditions, the froth height decreases from the inlet to the outlet of the tray in all the cases above.

B3. 1.8mm Tray, 8mm inlet weir, 38mm outlet weir, calming zones

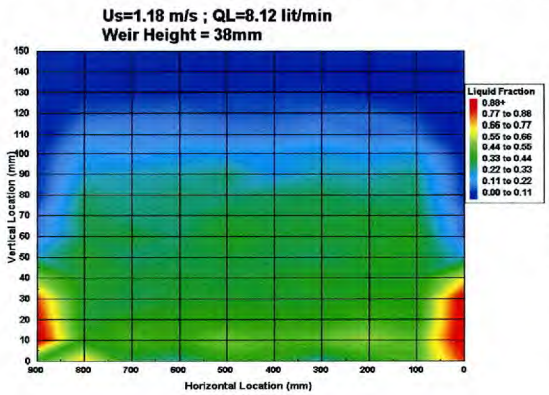


Figure B3.1

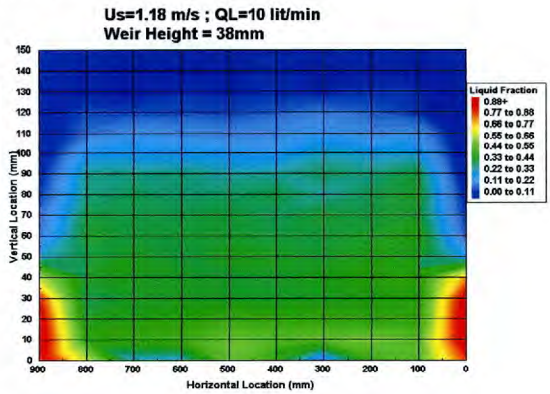


Figure B3.2

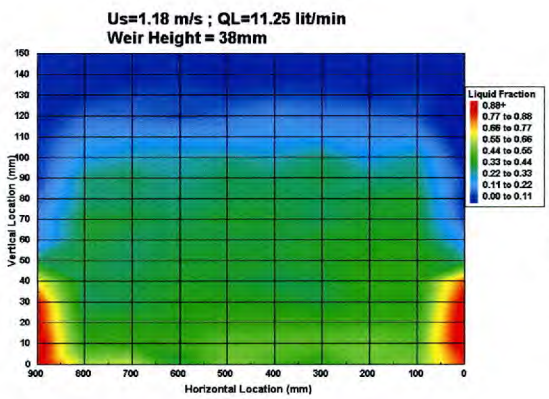


Figure B3.3

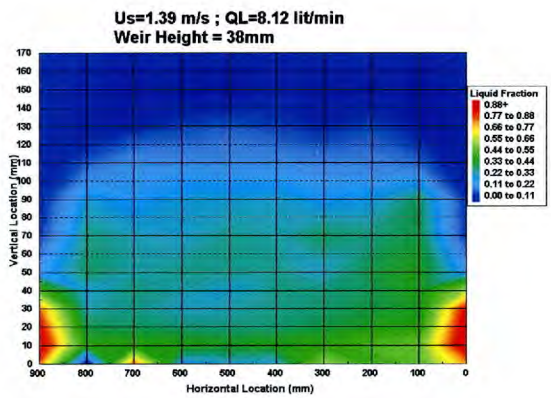


Figure B3.4

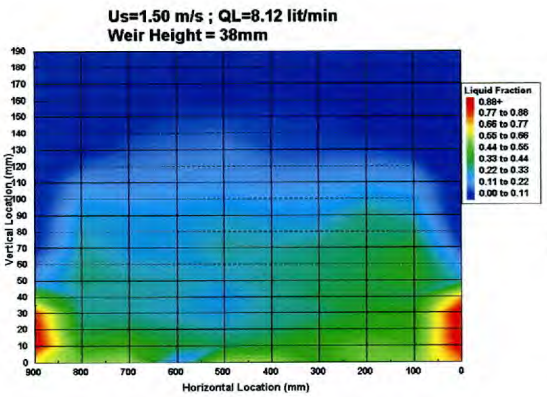


Figure B3.5

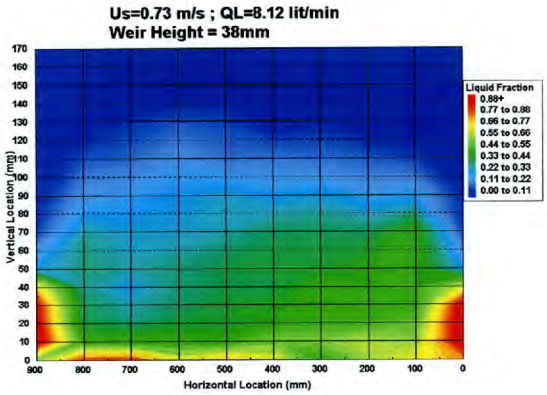


Figure B3.6

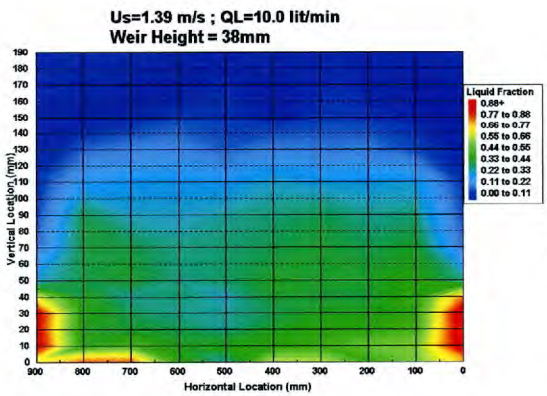


Figure B3.7

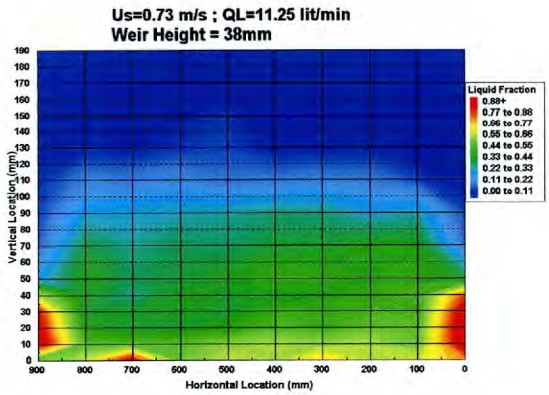


Figure B3.8

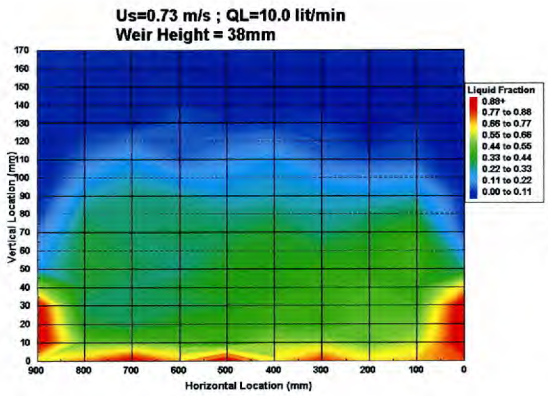


Figure B3.9

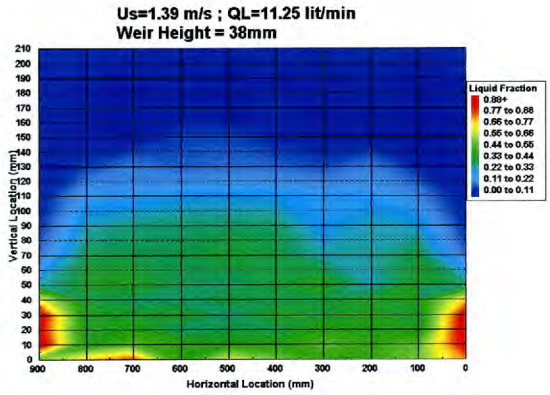


Figure B3.10

The increase on the outlet weir height increases the froth height in the present set of experiments (compared to the figures in Section B2). It is also noted that the drop of froth height level from the inlet to the outlet of the tray seems to disappear with the higher outlet weir used.

B4. 1.8mm Tray, no inlet weir, 38mm outlet weir, calming zones

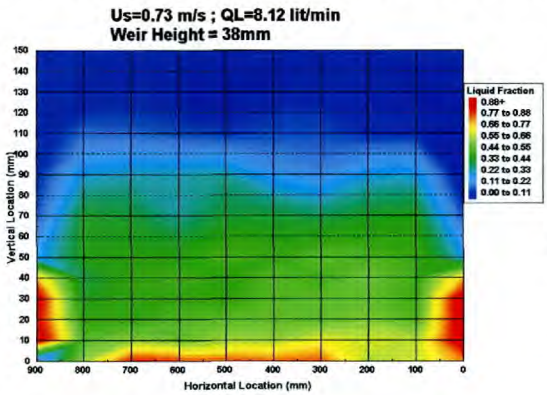


Figure B4.1

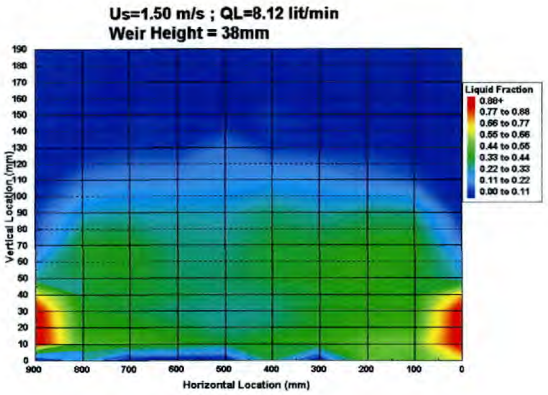


Figure B4.2

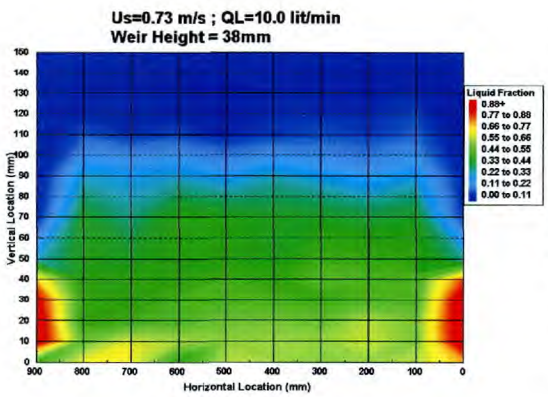


Figure B4.3

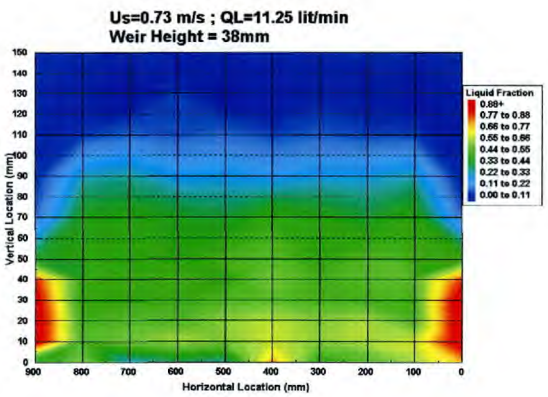


Figure B4.4

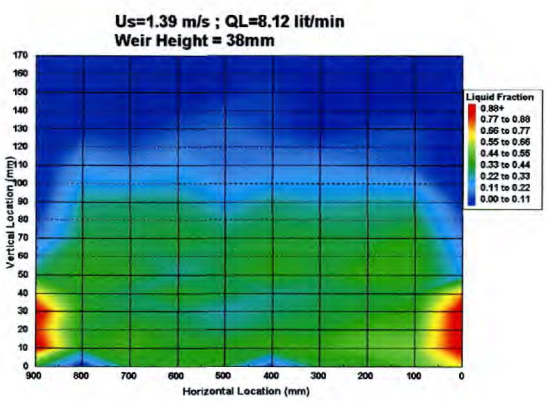


Figure B4.1

The above results show that the effect of inlet weir on the dispersion density profile is negligible.

B5. 6mm Tray, no inlet weir, 38mm outlet weir, calming zones

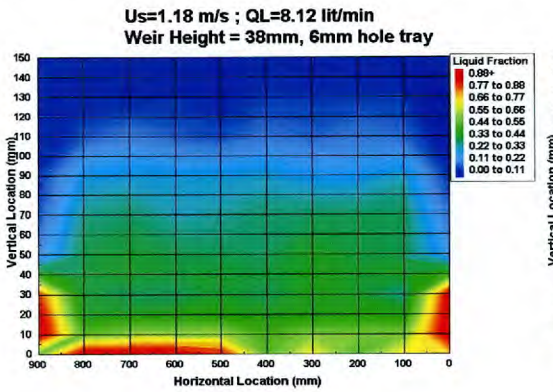


Figure B5.1

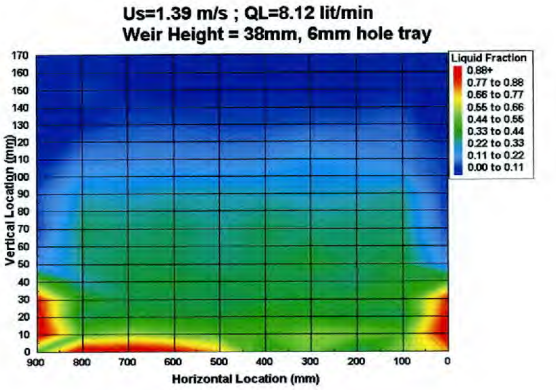


Figure B5.2

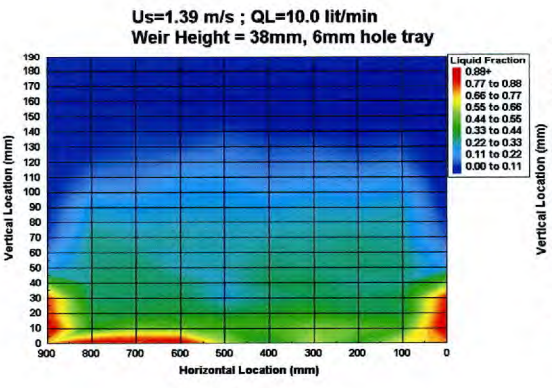


Figure B5.3

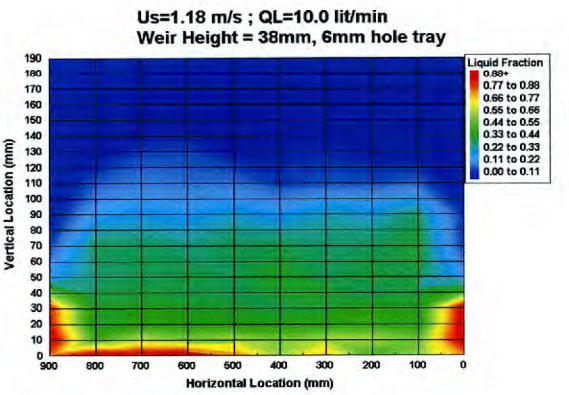


Figure B5.4

B6. 6mm Tray, no inlet weir, 8mm outlet weir, calming zones

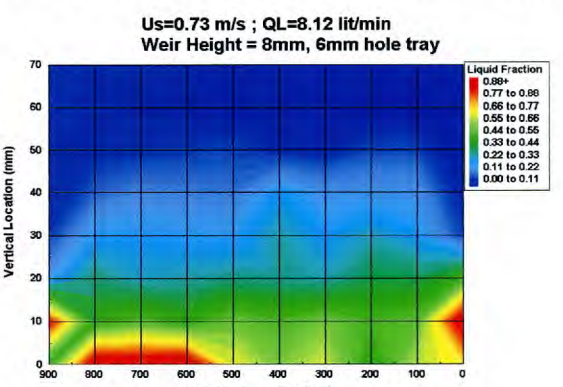


Figure B6.1

Appendix C. Sauter Mean Bubble/Droplet Diameter Profile

The figures below are the experimental results on the Sauter mean bubble/droplet diameter profile of different flowrates under five geometries of trays. The blue and pink lines represent the bubble and droplet respectively. These profiles generally look reasonable although sometimes the Sauter mean diameters at lower positions (e.g. at 0mm or 10mm) are a little in doubt due to the weak laser signal coming out of the froth.

C1. 1.8mm Tray, 8mm outlet weir, 940mm active/bubbling length

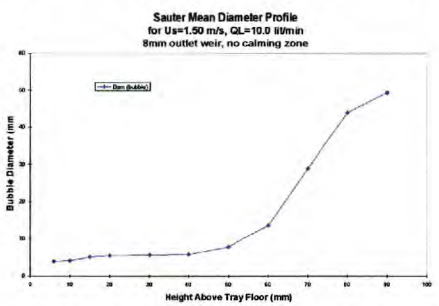


Figure C1.1

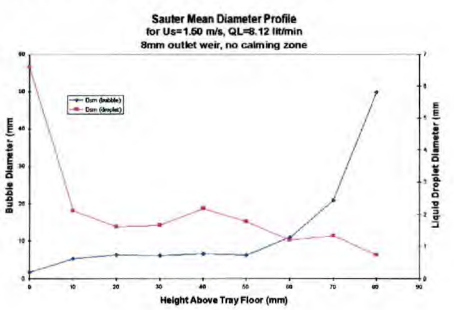


Figure C1.2

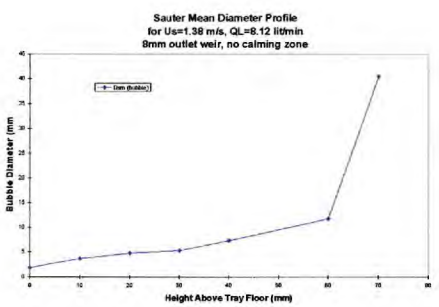


Figure C1.3

C2. 1.8mm Tray, 8mm outlet weir, calming zones

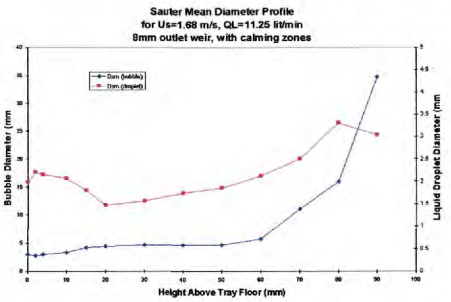


Figure C2.1

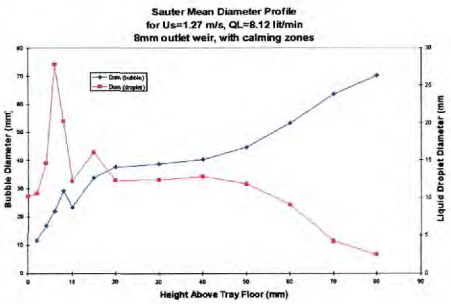


Figure C2.2

C3. 1.8mm Tray, 38mm outlet weir, calming zones

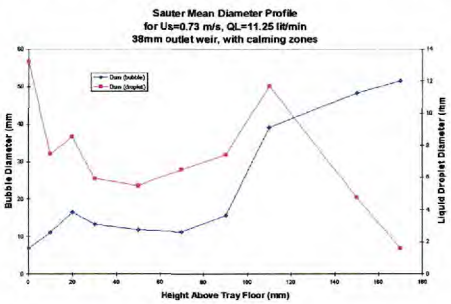


Figure C3.1

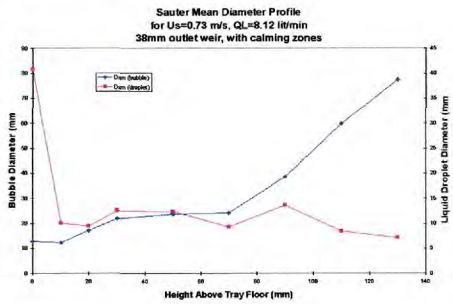


Figure C3.2

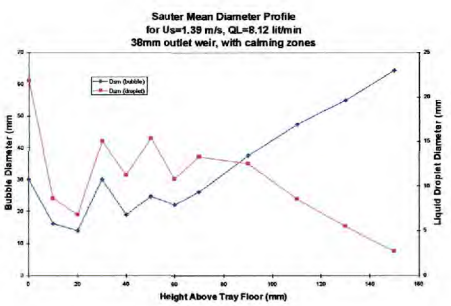


Figure C3.3

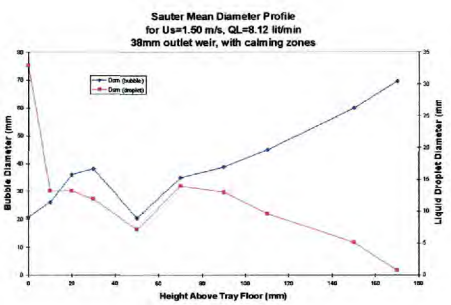


Figure C3.4

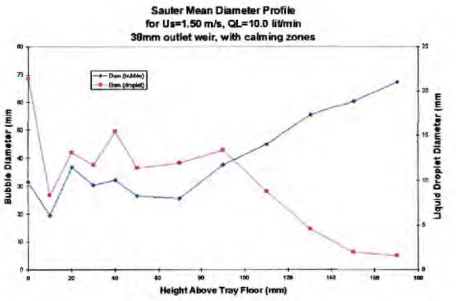


Figure C3.5

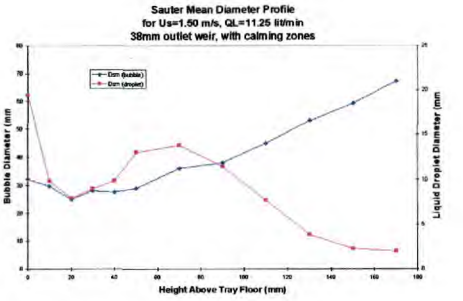


Figure C3.6

C4. 6mm Tray, 38mm outlet weir, calming zones

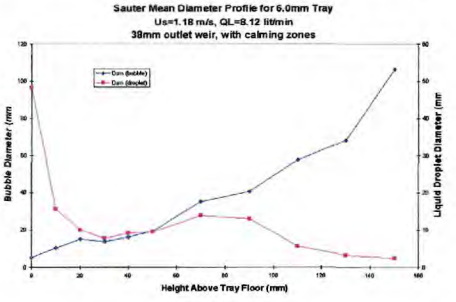


Figure C4.1

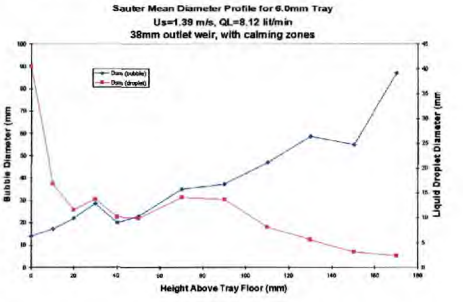


Figure C4.2

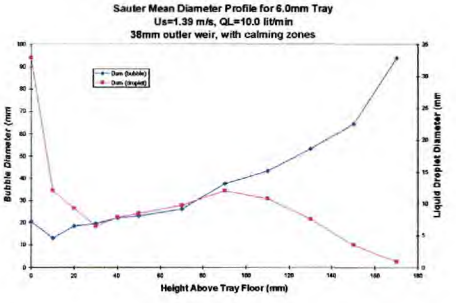


Figure C4.3

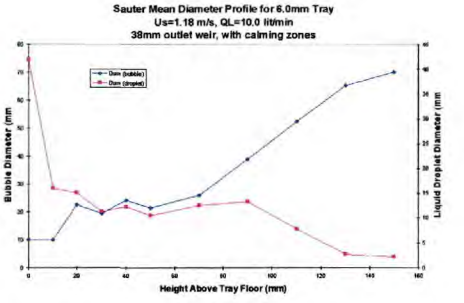


Figure C4.4

C5. 6mm Tray, 8mm outlet weir, calming zones

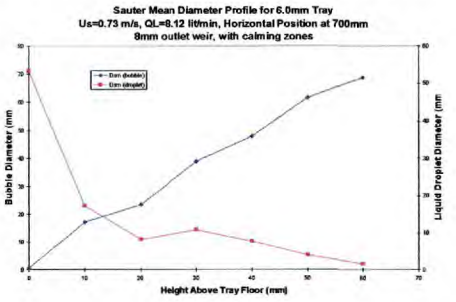


Figure C5.1

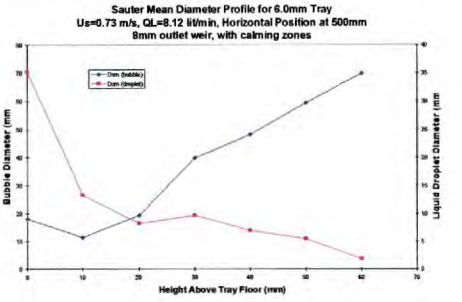


Figure C5.2

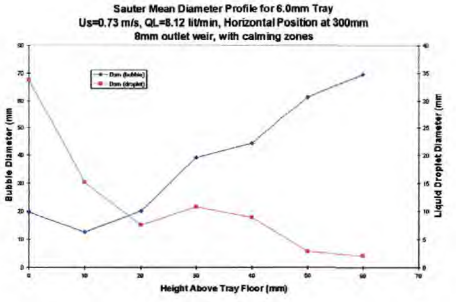


Figure C5.3

This set of results shows that the Sauter mean diameter profiles for both bubbles and droplets are not very much affected by the horizontal position.

Appendix D. Computer Codes

Computer codes are used in various part of the present work. Most of these are either written in Visual Basic or Fortran language for different purposes. The full list of the program is given in the sections below. Some of these codes are also included in the CD-ROMs attached to this thesis.

D1. Visual Basic Programs (in Microsoft Excel) for tray pressure drop prediction

```
**************************************************************************

'**************************************************************************
Sub PressureDrop()

' Variables Dictionary:
' am*    -    An arbitary constant relating hT to hL; "amlow", "ammid",and "amhigh" were
used in
'           the bisection iteration method
' Af     -   Free area fraction of the tray
' Asuf   -   Surface area of the tray (m^2)
' At     -   Total cross-sectional area of all the holes on the tray (m^2)
' Ah     -   Single hole area (m^2)
' alfa   -    Fraction of residual volume at the orifice, an arbitary constant, between 0
and 0.5
' dh     -   Hole diameter (m)
' delt   -   A small time interval during a bubble formation process
' em     -   (entrained liquid flow rate) / (vapour flow rate)
' f      -   Bubble frequency (1/s)
' g      -   Accelaration due to gravity (m/s^2)
' hT     -   Total pressure drop (N/m^2)
' hL     -   Head loss due to the liquid head, or clear liquid height (N/m^2)
' hsig   -   Residual pressure drop head (N/m^2)
' hdry   -   Dry tray pressure drop head (N/m^2)
' hno    -   Number of holes on the tray
' i      -   Loop counter
' k      -   A constant for dry tray pressure drop correlation
' n      -   Number of iterations
' Qh     -   Volumetric flowrate through a single hole (m^3/s)
' r*     -    Radius of curvature for the growing bubble; "rlow", "rmid",and "rhigh" were
used in
'           the bisection iteration method
' rh     -   Tray hole radius (m)
' Rhog   -   Gas density (kg/m^3)
' ratiol-   A ration between "vr" and "vb"
' sig    -   Gas liquid interfacial tension (N/m)
' sum*   -     Sum of "hsig", "hdry" and "Us" over all the time intervals in a bubble
formation
' Us     -   Air superficial veloity (m/s)
' Uh     -   Vapour velocity through each hole (m/s)
' vr     -   Mean release volume of bubbles (m^3)
'  vol*    -      Volume of the growing bubble (m^3), used in interation; "vollow",
"volmid",and
'           "volhigh" were used in the bisection iteration method
' vo     -   Volume of sphere with a diameter same as the hole diameter (m^3)
' valfa -    Residual bubble volume, i.e. the volume of the bubble immediately after the
release
'           of the previous bubble (m^3)
' vb     -   Volume of the growing bubble; it is time dependent (m^3)
' vrate -   Volumetric fowrate of gas at an interval delt
' x      -   A constant for dry tray pressure drop correlation
```

```
'   Reading in all the required values

    n = Cells(5, 1).Value
    Af = Cells(2, 1).Value
    Asuf = Cells(2, 2).Value
    dh = Cells(2, 3).Value
    Us = Cells(2, 4).Value
    f = Cells(2, 5).Value
    k = Cells(2, 7).Value
    x = Cells(2, 8).Value
    hL = Cells(5, 2).Value
    rh = Cells(2, 6).Value
    alfa = Cells(5, 3).Value

'   Physical constants

    g = 9.81
    RhoG = 1.205
    Pi = 3.141592654
    sig = 0.07325

'   Unit of the hL read was in mmH2O, this must be changed to N/m2, multiplied by "g"

    hL = hL * g

'   Calculate other important parameters

    At = Af * Asuf
    Ah = (Pi / 4) * (dh ^ 2)
    hno = At / Ah
    Uh = (Us * Asuf) / (hno * Ah)
    Qh = Uh * Ah
    vr = Qh / f
    v0 = (4 / 3) * Pi * (rh ^ 3)
    valfa = alfa * v0

'   Start main program calculation

    Call ra(hL, ammid, vb, vr, hdry, valfa, f, k, x, rh, hT, n, Asuf, hno, Ah, sig, g)

    End Sub

'*****************************************************************************************

Sub ra(hL, ammid, vb, vr, hdry, valfa, f, k, x, rh, hT, n, Asuf, hno, Ah, sig, g)

    amlow = 0.1
    amhigh = 30

'   Starting iteration for calculating "am" (bisection method)

50  ammid = (amlow + amhigh) / 2

'   Relating hT to hL by multiplying a constant, "ammid"

    hT = ammid * hL

'   Speficying a time step within a single bubble formation cycle

    delt = 1 / (n * f)

'   Assume the initial bubble volume is equal to the residual bubble volume

    vb = valfa

'    Summing up the values of "hsig", "hdry" and "Us" at each interval of the bubble
formation
'   process in order to calculate average values for them later on

    sumhsig = 0
    sumhdry = 0
    sumUs = 0

'   At beginning of a new bubble formation cycle, "Us" is zero
```

```
    Us = 0

'   Starting the loop

    i = 0
99  i = i + 1


'   A subroutine will calculate the radius of curvature during the bubble growth

        Call Cal(rh, vb, rmid)

'   Once the radius of curvature of the bubble was obtained, calculate "hsig" at this
value

        hsig = (3 * sig) / rmid
        sumhsig = sumhsig + hsig

'   Calculate "hdry" by subtracting all other components if pressure drop from total
pressure
'   loss. If it is less than zero, then the arbitary constant "am" is too small. Adjust
the
'   value of "am" using bisection method until a feasible value was obtained.

        hdry = hT - hL - hsig
        If (hdry <= 0) Then
            amlow = ammid
            GoTo 50
        End If
        sumhdry = sumhdry + hdry

'   There exists a relationship between "hdry" and "Us", and this was previously
established
'   At each different time interval of the bubble formation cycle, there will be a
different
'   value of "Us", the equation below is used to find its value.

        Us = (hdry / 9.81 / k) ^ (1 / x)
        sumUs = sumUs + Us

'   Print out the results for one complete bubble formation cycle

        Cells(i + 10, 1).Value = i
        Cells(i + 10, 2).Value = rmid
        Cells(i + 10, 3).Value = hsig / 9.81
        Cells(i + 10, 4).Value = hdry / 9.81
        Cells(i + 10, 5).Value = Us

'   Calculate volumetric flowrate through a single hole within one time interval "delt"

        Uh = Us * Asuf / hno / Ah
        vrate = (Uh) * (rh ^ 2) * 3.14159
        vi = vrate * delt

'   Updating the bubble volume after the current interval. i.e. adding up the volume
'   contributed in this interval

        vb = vb + vi

'   Ending the loop

    If (i < n) Then
        GoTo 99
    End If

'   Checking whether "vb" is close enough to "vr". If not, adjust the value of "am" and
'   start the above procedure again.

    ratio1 = vr / vb

    If (ratio1 < 0.9999) Then
        amhigh = ammid
        GoTo 50
    ElseIf (ratio1 > 1.0001) Then
        amlow = ammid
        GoTo 50
```

```
    End If

'    em = 0.19

'   Converting pressure drop values from N/m2 into mmH2O

    meanhsig = sumhsig / (n * 9.81)
    meanhdry = sumhdry / (n * 9.81)
'    meanhdry = meanhdry * (1 + em)
    meanUs = sumUs / n

    deltpUs = k * (meanUs) ^ x * g

    Cells(n + 12, 2).Value = meanhsig
    Cells(n + 13, 2).Value = meanhdry
    Cells(n + 14, 2).Value = meanUs
    Cells(n + 15, 2).Value = deltpUs / 9.81

    hT = (hL / 9.81) + meanhdry + meanhsig
    Cells(n + 16, 2).Value = hT

    End Sub

'*****************************************************************************************

Sub Cal(rh, vb, rmid)

'     This part of the program works out the radius of curvature of
'     various bubble volumes for bubbles exiting a hole in a sieve plate
'     from the moment of initiation to the point of detachment using an
'     interval bisection method to solve an equation for radius


'     Set up starting values for the interval bisection method

    Pi = 3.141592654
    rlow = rh + 0.000001
    rhigh = 1000

'     Calculate hemispherical volume

    hemi = (2 / 3) * Pi * rh ^ 3

'     Starting iteration for calculating the radius of curvature (bisection method)

10  rmid = (rlow + rhigh) / 2

'     Calculate the volume for these radii

    If (vb < hemi) Then

        vollow = Pi * (rlow * (rlow - (rlow ^ 2 - rh ^ 2) ^ 0.5) ^ 2 - (rlow - (rlow ^ 2
- rh ^ 2) ^ 0.5) ^ 3 / 3)
        volhigh = Pi * (rhigh * (rhigh - (rhigh ^ 2 - rh ^ 2) ^ 0.5) ^ 2 - (rhigh -
(rhigh ^ 2 - rh ^ 2) ^ 0.5) ^ 3 / 3)
        volmid = Pi * (rmid * (rmid - (rmid ^ 2 - rh ^ 2) ^ 0.5) ^ 2 - (rmid - (rmid ^ 2
- rh ^ 2) ^ 0.5) ^ 3 / 3)

    Else

        vollow = Pi * ((rlow - (rlow ^ 2 - rh ^ 2) ^ 0.5) ^ 3 / 3 - rlow * (rlow - (rlow
^ 2 - rh ^ 2) ^ 0.5) ^ 2 + 4 / 3 * rlow ^ 3)
        volhigh = Pi * ((rhigh - (rhigh ^ 2 - rh ^ 2) ^ 0.5) ^ 3 / 3 - rhigh * (rhigh -
(rhigh ^ 2 - rh ^ 2) ^ 0.5) ^ 2 + 4 / 3 * rhigh ^ 3)
        volmid = Pi * ((rmid - (rmid ^ 2 - rh ^ 2) ^ 0.5) ^ 3 / 3 - rmid * (rmid - (rmid
^ 2 - rh ^ 2) ^ 0.5) ^ 2 + 4 / 3 * rmid ^ 3)

    End If

'     Update interval bisection

    If ((rhigh - rlow) > 0.000001) Then

        If (vb < hemi) Then
            If (volmid <= vb) Then
```

```
            rhigh = rmid
            Else
            rlow = rmid
        End If
    Else
        If (volmid <= vb) Then
            rlow = rmid
            Else
            rhigh = rmid
        End If
    End If

    GoTo 10

End If


End Sub
'*******************************************************************************

**********************************************************************
```

The output screen which the Visual Basic program generates is given in Figure D1 below.

Free Area Fraction of the Tray	Tray Surface Area	Tray Hole Diameter	Superficial Velocity	Bubble Formation Frequency	Hole Radius	k	x
0.08	0.0504	0.0018	1.27	500	0.0009	13.173	2

Number of Iteration	h_L	α
100	14	0.1

Pressure Drop

Iteration	rmid	hsig	hdry	Us
1	0.001843032	12.15421784	21.45172089	1.276111795
2	0.000921955	24.29686694	9.309071779	0.840641534
3	0.000901466	24.84910141	8.756837315	0.815326006
4	0.000921955	24.29686694	9.309071779	0.840641534
5	0.000954551	23.46717108	10.13876764	0.877304262
6	0.000992735	22.56453869	11.04140003	0.915523985
7	0.001030919	21.72877143	11.87716729	0.949541807
8	0.001070035	20.93446833	12.67147039	0.980779005
9	0.00110915	20.19618932	13.4097494	1.008946144
10	0.001146403	19.53990543	14.06603329	1.033340556

meanhsig	12.27824613
meanhdry	21.32769259
meanUs	1.265248203
deltpUs	21.08803677
h_T (mmH2O)	47.60593872
h_T (mm paraffin)	59.5074234

Figure D1.
Output screen of the Visual Basic program for the tray pressure drop prediction

D2. Visual Basic Programs (in Microsoft Excel) for Flying Optical Probes System

```
**************************************************************************

'*************************************************************************
Sub Program()

' **********************
'   IMPORTANT!!!!!!!!!
' **********************
'
'   Make sure the directory information is correct in all subroutines
'   before starting this program!!!
'   ( i.e. Module 1 to Module 5 )

    Call Preparation1
    Call Preparation2
    Call Preparation3
    Call Preparation4
    Call Preparation5
    Call Preparation6
    Call Preparation7
    Call Preparation8
    Call Preparation9
    Call Preparation10
    Call Preparation11
    Call Preparation12

    Call Summary1
    Call Summary2
    Call Summary3
    Call Summary4
    Call Summary5
    Call Summary6
    Call Summary7
    Call Summary8
    Call Summary9
    Call Summary10
    Call Summary11
    Call Summary12

    Call Conversion1
    Call Conversion2
    Call Conversion3
    Call Conversion4
    Call Conversion5
    Call Conversion6
    Call Conversion7
    Call Conversion8
    Call Conversion9
    Call Conversion10
    Call Conversion11
    Call Conversion12

End Sub

'*************************************************************************

Sub Preparation1()
'
' 1. NEED TO CHANGE "test260900"
'
'
'*************************************************************************
'#########################################################################
'*************************************************************************
    Workbooks.OpenText FileName:="D:\Optical Probe Expt\test260900\test1\run1", _
        Origin:=xlWindows, StartRow:=1, DataType:=xlDelimited, TextQualifier:= _
        xlDoubleQuote, ConsecutiveDelimiter:=False, Tab:=True, Semicolon:=False, _
        Comma:=True, Space:=False, Other:=False, FieldInfo:=Array(Array(1, 1), _
        Array(2, 1), Array(3, 1), Array(4, 1), Array(5, 1), Array(6, 1))
```

```
    Columns("A:A").Select
    Selection.Insert Shift:=xlToRight
    Selection.Insert Shift:=xlToRight
    Range("B2").Select
    ActiveCell.FormulaR1C1 = "0"
    Range("B3").Select
    ActiveCell.FormulaR1C1 = "=R[-1]C+1/5000"
    Range("B3").Select
    Selection.Copy
    Range("C3").Select
    Selection.End(xlDown).Select
    Range("B3:B10001").Select
    Range("B10001").Activate
    ActiveSheet.Paste
    Selection.End(xlUp).Select
    Range("A2").Select
    Application.CutCopyMode = False
    ActiveCell.FormulaR1C1 = "1"
    Range("A3").Select
    ActiveCell.FormulaR1C1 = "=1+R[-1]C"
    Range("A3").Select
    Selection.Copy
    Range("B3").Select
    Selection.End(xlDown).Select
    Range("A3:A10001").Select
    Range("A10001").Activate
    ActiveSheet.Paste
    Range("A1").Select
    ActiveWindow.Zoom = 75

    Call New_code

    Application.CutCopyMode = False
    ActiveWorkbook.SaveAs FileName:=
        "D:\Optical Probe Expt\test260900\test1\run1.xls", FileFormat:=xlNormal, _
        Password:="", WriteResPassword:="", ReadOnlyRecommended:=False, _
        CreateBackup:=False
    Windows("run1.xls").Activate
    ActiveWindow.Close

'*******************************************************************************

Sub New_code()

'   Instruction:
'   User is required to input value for p1 and p2
'       for hw=8mm experiments, p1=0.9 and p2=3.0
'       for hw=38mm experiments, p1=1.2 and p2=2.8

'*************************************************************************
' Step 1: Determination of Starting and Endging points
'*************************************************************************

'   Symbol definitions in Section1
'   p       Position (in terms of voltage signal)
'   p1      Starting position (in terms of voltage signal) of measurement
'   p2      End position (in terms of voltage signal) of measurement
'   i       Counter (as in row number)
'   i1      Row number for position "p1"
'   i2      Row number for position "p2"
'   t1      Time for position "p1"
'   t2      Time for position "p2"

Cells(1, 1).Value = "Point #"
Cells(1, 2).Value = "Time"
Cells(1, 3).Value = "Probe 1"
Cells(1, 4).Value = "Probe 2"
Cells(1, 5).Value = "Probe 3"
Cells(1, 6).Value = "Probe 4"
Cells(1, 7).Value = "Probe 5"
Cells(1, 8).Value = "Position"


p1 = 0.9
p2 = 3#
```

```
i1 = 0
i2 = 0
i = 2
t1 = 0
t2 = 0

10  P = Cells(i, 8).Value

If P = p1 Then
    t1 = Cells(i, 2).Value
    i1 = i
End If

11  P = Cells(i, 8).Value

If P = p2 Then
    t2 = Cells(i, 2).Value
    i2 = i
End If

If t1 > 0 And t2 > 0 Then
    GoTo 20
'   Goto Step 2
ElseIf t1 = 0 And t2 = 0 Then
    i = i + 1
    GoTo 10
ElseIf t1 > 0 And t2 = 0 Then
    i = i + 1
    GoTo 11
End If


'************************************************************************
' Step 2: Corrections on voltage signal
'************************************************************************

'   Symbol definitions for Section2
'   x           Counter (as in column number)
'   y           Counter (as in row number)
'   signal      Voltage Signal


20

Cells(1, 10).Value = "Time"
Cells(1, 11).Value = "Probe 1"
Cells(1, 12).Value = "Probe 2"
Cells(1, 13).Value = "Probe 3"
Cells(1, 14).Value = "Probe 4"
Cells(1, 15).Value = "Probe 5"
'   <<added 30/12/00>> Addition of Column "Position"
Cells(1, 16).Value = "Real Position"

For x = 3 To 7

For y = i1 To i2

    signal = Cells(y, x).Value

    If signal > 0 Then
        signal = 5#
    Else
        signal = -5#
    End If

'   Write "time" for each point
    Cells(y - i1 + 2, 10).Value = Cells(y, 2).Value
'   Write "corrected signal" for each point
    Cells(y - i1 + 2, x + 8).Value = signal
'   <<added 30/12/00>> Write "position" for each point
'   <<added 30/12/00>> Real position 200, 500mm = Signal position 2.8, 1.62
'   <<added 30/12/00>> Signal position 0.29 = Real Position 842.5mm, scale = 257.5 mm/V
(see below)
    Cells(y - i1 + 2, 16).Value = 842.5 - (Cells(y, 8).Value - 0.29) * 257.5

Next y
```

```
Next x

'*************************************************************************
' Step 3: Bubble/Droplet sizes calculations
'*************************************************************************

'   Symbol definition for Section3
'   x       Counter (as in column number)
'   y       Counter (as in row number)
'   a       Signal at a particular cell (y,x)
'   b       Signal at a particular cell (y+1,x)
'   tb1     Time at the beginning of a bubble signal
'   tb2     Time at the end of a bubble signal
'   td1     Time at the beginning of a droplet signal
'   td2     Time at the end of a droplet signal
'   nb      Number of bubbles
'   nd      Number of droplets
'   Db      Bubble chord length, mm
'   Dd      Droplet chord length, mm
'   speed   Actuation speed, mm/s



'   The scale of actual travelling distance
'   Signal = 0.29 - 3.09V   ;   Distance = 720mm
'   Signal = 0.57 - 3.09V   ;   Distance = 650mm
'   Taking average      Scale = 257.5 mm/V


speed = (p2 - p1) * 257.5 / (t2 - t1)

'   <<added 30/12/00>> Corrections on locations due to the new column of "Position"
Cells(1, 18).Value = "B_Pos_P1"
Cells(1, 19).Value = "B_Chord_P1"
Cells(1, 20).Value = "D_Pos_P1"
Cells(1, 21).Value = "D_Chord_P1"
Cells(1, 22).Value = "B_Pos_P2"
Cells(1, 23).Value = "B_Chord_P2"
Cells(1, 24).Value = "D_Pos_P2"
Cells(1, 25).Value = "D_Chord_P2"
Cells(1, 26).Value = "B_Pos_P3"
Cells(1, 27).Value = "B_Chord_P3"
Cells(1, 28).Value = "D_Pos_P3"
Cells(1, 29).Value = "D_Chord_P3"
Cells(1, 30).Value = "B_Pos_P4"
Cells(1, 31).Value = "B_Chord_P4"
Cells(1, 32).Value = "D_Pos_P4"
Cells(1, 33).Value = "D_Chord_P4"
Cells(1, 34).Value = "B_Pos_P5"
Cells(1, 35).Value = "B_Chord_P5"
Cells(1, 36).Value = "D_Pos_P5"
Cells(1, 37).Value = "D_Chord_P5"


For x = 11 To 15

'   Initialisation for each parameters

    tb1 = 0
    tb2 = 0
    td1 = 0
    td2 = 0
    nb = 0
    nd = 0
    Db = 0
    Dd = 0

    For y = 2 To (i2 - i1 + 1)

        a = Cells(y, x).Value
        b = Cells(y + 1, x).Value
        ta = Cells(y, 10).Value
        tb = Cells(y + 1, 10).Value

        If a > 0 And b > 0 Then
```

```
            GoTo 31
        ElseIf a < 0 And b < 0 Then
            GoTo 31
        ElseIf a > 0 And b < 0 Then
            td1 = (ta + tb) / 2
            td2 = (ta + tb) / 2
        Else
            tb1 = (ta + tb) / 2
            td2 = (ta + tb) / 2
        End If

        If tb2 = 0 Or td2 = 0 Then
            GoTo 31
        ElseIf tb2 > tb1 Then
            tb = tb2 - tb1
            nb = nb + 1
            Db = speed * tb
'   <<added 30/12/00>> add position for each bubble detected
            Cells(nb + 1, 4 * x - 25).Value = Db
            Cells(nb + 1, 4 * x - 26).Value = Cells(y, 16) - Db
        ElseIf td2 > td1 Then
            td = td2 - td1
            nd = nd + 1
            Dd = speed * td
'   <<added 30/12/00>> add position for each droplet detected
            Cells(nd + 1, 4 * x - 23).Value = Dd
            Cells(nd + 1, 4 * x - 24).Value = Cells(y, 16) - Dd
        End If

31

    Next y

'   <<added 17/01/01>> add total number of bubbles/droplets
            Cells(nb + 2, 4 * x - 26).Value = nb
            Cells(nd + 2, 4 * x - 24).Value = nd

Next x


Range("AK1").Select

End Sub

'*************************************************************************************

Sub Summary1()
'
' 1. NEED TO CHANGE "test260900"
' 2. NEED TO CHANGE "h6_w8"
'
'
'*************************************************************************************
'   Required to change to the appropriate directory
'   This macro is only applicable for 20 runs within a test
'*************************************************************************************

    ChDir "D:\Optical Probe Expt\test260900\test1"
    Workbooks.Open FileName:="D:\Optical Probe Expt\test260900\test1\run1.xls"

    Workbooks.Add
    ActiveWorkbook.SaveAs FileName:= _
        "D:\Optical            Probe            Expt\test260900\summary_test1_h6_w8.xls",
FileFormat:=xlNormal, _
        Password:="", WriteResPassword:="", ReadOnlyRecommended:=False, _
        CreateBackup:=False

    Windows("run1.xls").Activate

    Dim TNP(10) As Double

    For i = 1 To 10
        Cells(1, 16 + 2 * i).Select
        Selection.End(xlDown).Select
        TNP(i) = Selection
    Next i
```

```
    For ii = 1 To 10
        Windows("run1.xls").Activate
        Range(Cells(1, 16 + 2 * ii), Cells(TNP(ii) + 2, 17 + 2 * ii)).Select
        Selection.Copy
        Windows("summary_test1_h6_w8.xls").Activate
        Cells(1, 2 * ii - 1).Select
        ActiveSheet.Paste
    Next ii
' @@@@

    Workbooks.Open FileName:="D:\Optical Probe Expt\test260900\test1\run2.xls"
    For i = 1 To 10
        Cells(1, 16 + 2 * i).Select
        Selection.End(xlDown).Select
        TNP(i) = Selection
    Next i

    For ii = 1 To 10
        Windows("run2.xls").Activate
        Range(Cells(2, 16 + 2 * ii), Cells(TNP(ii) + 2, 17 + 2 * ii)).Select
        Selection.Copy
        Windows("summary_test1_h6_w8.xls").Activate
        Cells(1, 2 * ii - 1).Select
        Selection.End(xlDown).Select
        ActiveSheet.Paste
    Next ii
' @@@@

    Workbooks.Open FileName:="D:\Optical Probe Expt\test260900\test1\run3.xls"
    For i = 1 To 10
        Cells(1, 16 + 2 * i).Select
        Selection.End(xlDown).Select
        TNP(i) = Selection
    Next i

    For ii = 1 To 10
        Windows("run3.xls").Activate
        Range(Cells(2, 16 + 2 * ii), Cells(TNP(ii) + 2, 17 + 2 * ii)).Select
        Selection.Copy
        Windows("summary_test1_h6_w8.xls").Activate
        Cells(1, 2 * ii - 1).Select
        Selection.End(xlDown).Select
        ActiveSheet.Paste
    Next ii
' @@@@

    Workbooks.Open FileName:="D:\Optical Probe Expt\test260900\test1\run4.xls"
    For i = 1 To 10
        Cells(1, 16 + 2 * i).Select
        Selection.End(xlDown).Select
        TNP(i) = Selection
    Next i

    For ii = 1 To 10
        Windows("run4.xls").Activate
        Range(Cells(2, 16 + 2 * ii), Cells(TNP(ii) + 2, 17 + 2 * ii)).Select
        Selection.Copy
        Windows("summary_test1_h6_w8.xls").Activate
        Cells(1, 2 * ii - 1).Select
        Selection.End(xlDown).Select
        ActiveSheet.Paste
    Next ii
' @@@@

    Workbooks.Open FileName:="D:\Optical Probe Expt\test260900\test1\run5.xls"
    For i = 1 To 10
        Cells(1, 16 + 2 * i).Select
        Selection.End(xlDown).Select
        TNP(i) = Selection
    Next i

    For ii = 1 To 10
        Windows("run5.xls").Activate
        Range(Cells(2, 16 + 2 * ii), Cells(TNP(ii) + 2, 17 + 2 * ii)).Select
        Selection.Copy
```

```
        Windows("summary_test1_h6_w8.xls").Activate
        Cells(1, 2 * ii - 1).Select
        Selection.End(xlDown).Select
        ActiveSheet.Paste
    Next ii
' @@@@

    Workbooks.Open FileName:="D:\Optical Probe Expt\test260900\test1\run6.xls"
    For i = 1 To 10
        Cells(1, 16 + 2 * i).Select
        Selection.End(xlDown).Select
        TNP(i) = Selection
    Next i

    For ii = 1 To 10
        Windows("run6.xls").Activate
        Range(Cells(2, 16 + 2 * ii), Cells(TNP(ii) + 2, 17 + 2 * ii)).Select
        Selection.Copy
        Windows("summary_test1_h6_w8.xls").Activate
        Cells(1, 2 * ii - 1).Select
        Selection.End(xlDown).Select
        ActiveSheet.Paste
    Next ii
' @@@@

    Workbooks.Open FileName:="D:\Optical Probe Expt\test260900\test1\run7.xls"
    For i = 1 To 10
        Cells(1, 16 + 2 * i).Select
        Selection.End(xlDown).Select
        TNP(i) = Selection
    Next i

    For ii = 1 To 10
        Windows("run7.xls").Activate
        Range(Cells(2, 16 + 2 * ii), Cells(TNP(ii) + 2, 17 + 2 * ii)).Select
        Selection.Copy
        Windows("summary_test1_h6_w8.xls").Activate
        Cells(1, 2 * ii - 1).Select
        Selection.End(xlDown).Select
        ActiveSheet.Paste
    Next ii
' @@@@

    Workbooks.Open FileName:="D:\Optical Probe Expt\test260900\test1\run8.xls"
    For i = 1 To 10
        Cells(1, 16 + 2 * i).Select
        Selection.End(xlDown).Select
        TNP(i) = Selection
    Next i

    For ii = 1 To 10
        Windows("run8.xls").Activate
        Range(Cells(2, 16 + 2 * ii), Cells(TNP(ii) + 2, 17 + 2 * ii)).Select
        Selection.Copy
        Windows("summary_test1_h6_w8.xls").Activate
        Cells(1, 2 * ii - 1).Select
        Selection.End(xlDown).Select
        ActiveSheet.Paste
    Next ii
' @@@@

    Workbooks.Open FileName:="D:\Optical Probe Expt\test260900\test1\run9.xls"
    For i = 1 To 10
        Cells(1, 16 + 2 * i).Select
        Selection.End(xlDown).Select
        TNP(i) = Selection
    Next i

    For ii = 1 To 10
        Windows("run9.xls").Activate
        Range(Cells(2, 16 + 2 * ii), Cells(TNP(ii) + 2, 17 + 2 * ii)).Select
        Selection.Copy
        Windows("summary_test1_h6_w8.xls").Activate
        Cells(1, 2 * ii - 1).Select
        Selection.End(xlDown).Select
        ActiveSheet.Paste
```

```
    Next ii
' @@@@

    Workbooks.Open FileName:="D:\Optical Probe Expt\test260900\test1\run10.xls"
    For i = 1 To 10
        Cells(1, 16 + 2 * i).Select
        Selection.End(xlDown).Select
        TNP(i) = Selection
    Next i

    For ii = 1 To 10
        Windows("run10.xls").Activate
        Range(Cells(2, 16 + 2 * ii), Cells(TNP(ii) + 2, 17 + 2 * ii)).Select
        Selection.Copy
        Windows("summary_test1_h6_w8.xls").Activate
        Cells(1, 2 * ii - 1).Select
        Selection.End(xlDown).Select
        ActiveSheet.Paste
    Next ii
' @@@@

    Workbooks.Open FileName:="D:\Optical Probe Expt\test260900\test1\run11.xls"
    For i = 1 To 10
        Cells(1, 16 + 2 * i).Select
        Selection.End(xlDown).Select
        TNP(i) = Selection
    Next i

    For ii = 1 To 10
        Windows("run11.xls").Activate
        Range(Cells(2, 16 + 2 * ii), Cells(TNP(ii) + 2, 17 + 2 * ii)).Select
        Selection.Copy
        Windows("summary_test1_h6_w8.xls").Activate
        Cells(1, 2 * ii - 1).Select
        Selection.End(xlDown).Select
        ActiveSheet.Paste
    Next ii
' @@@@

    Workbooks.Open FileName:="D:\Optical Probe Expt\test260900\test1\run12.xls"
    For i = 1 To 10
        Cells(1, 16 + 2 * i).Select
        Selection.End(xlDown).Select
        TNP(i) = Selection
    Next i

    For ii = 1 To 10
        Windows("run12.xls").Activate
        Range(Cells(2, 16 + 2 * ii), Cells(TNP(ii) + 2, 17 + 2 * ii)).Select
        Selection.Copy
        Windows("summary_test1_h6_w8.xls").Activate
        Cells(1, 2 * ii - 1).Select
        Selection.End(xlDown).Select
        ActiveSheet.Paste
    Next ii
' @@@@

    Workbooks.Open FileName:="D:\Optical Probe Expt\test260900\test1\run13.xls"
    For i = 1 To 10
        Cells(1, 16 + 2 * i).Select
        Selection.End(xlDown).Select
        TNP(i) = Selection
    Next i

    For ii = 1 To 10
        Windows("run13.xls").Activate
        Range(Cells(2, 16 + 2 * ii), Cells(TNP(ii) + 2, 17 + 2 * ii)).Select
        Selection.Copy
        Windows("summary_test1_h6_w8.xls").Activate
        Cells(1, 2 * ii - 1).Select
        Selection.End(xlDown).Select
        ActiveSheet.Paste
    Next ii
' @@@@

    Workbooks.Open FileName:="D:\Optical Probe Expt\test260900\test1\run14.xls"
```

```
    For i = 1 To 10
        Cells(1, 16 + 2 * i).Select
        Selection.End(xlDown).Select
        TNP(i) = Selection
    Next i

    For ii = 1 To 10
        Windows("run14.xls").Activate
        Range(Cells(2, 16 + 2 * ii), Cells(TNP(ii) + 2, 17 + 2 * ii)).Select
        Selection.Copy
        Windows("summary_test1_h6_w8.xls").Activate
        Cells(1, 2 * ii - 1).Select
        Selection.End(xlDown).Select
        ActiveSheet.Paste
    Next ii
' @@@@

    Workbooks.Open FileName:="D:\Optical Probe Expt\test260900\test1\run15.xls"
    For i = 1 To 10
        Cells(1, 16 + 2 * i).Select
        Selection.End(xlDown).Select
        TNP(i) = Selection
    Next i

    For ii = 1 To 10
        Windows("run15.xls").Activate
        Range(Cells(2, 16 + 2 * ii), Cells(TNP(ii) + 2, 17 + 2 * ii)).Select
        Selection.Copy
        Windows("summary_test1_h6_w8.xls").Activate
        Cells(1, 2 * ii - 1).Select
        Selection.End(xlDown).Select
        ActiveSheet.Paste
    Next ii
' @@@@

    Workbooks.Open FileName:="D:\Optical Probe Expt\test260900\test1\run16.xls"
    For i = 1 To 10
        Cells(1, 16 + 2 * i).Select
        Selection.End(xlDown).Select
        TNP(i) = Selection
    Next i

    For ii = 1 To 10
        Windows("run16.xls").Activate
        Range(Cells(2, 16 + 2 * ii), Cells(TNP(ii) + 2, 17 + 2 * ii)).Select
        Selection.Copy
        Windows("summary_test1_h6_w8.xls").Activate
        Cells(1, 2 * ii - 1).Select
        Selection.End(xlDown).Select
        ActiveSheet.Paste
    Next ii
' @@@@

    Workbooks.Open FileName:="D:\Optical Probe Expt\test260900\test1\run17.xls"
    For i = 1 To 10
        Cells(1, 16 + 2 * i).Select
        Selection.End(xlDown).Select
        TNP(i) = Selection
    Next i

    For ii = 1 To 10
        Windows("run17.xls").Activate
        Range(Cells(2, 16 + 2 * ii), Cells(TNP(ii) + 2, 17 + 2 * ii)).Select
        Selection.Copy
        Windows("summary_test1_h6_w8.xls").Activate
        Cells(1, 2 * ii - 1).Select
        Selection.End(xlDown).Select
        ActiveSheet.Paste
    Next ii
' @@@@

    Workbooks.Open FileName:="D:\Optical Probe Expt\test260900\test1\run18.xls"
    For i = 1 To 10
        Cells(1, 16 + 2 * i).Select
        Selection.End(xlDown).Select
        TNP(i) = Selection
```

```
    Next i

    For ii = 1 To 10
        Windows("run18.xls").Activate
        Range(Cells(2, 16 + 2 * ii), Cells(TNP(ii) + 2, 17 + 2 * ii)).Select
        Selection.Copy
        Windows("summary_test1_h6_w8.xls").Activate
        Cells(1, 2 * ii - 1).Select
        Selection.End(xlDown).Select
        ActiveSheet.Paste
    Next ii
' @@@@

    Workbooks.Open FileName:="D:\Optical Probe Expt\test260900\test1\run19.xls"
    For i = 1 To 10
        Cells(1, 16 + 2 * i).Select
        Selection.End(xlDown).Select
        TNP(i) = Selection
    Next i

    For ii = 1 To 10
        Windows("run19.xls").Activate
        Range(Cells(2, 16 + 2 * ii), Cells(TNP(ii) + 2, 17 + 2 * ii)).Select
        Selection.Copy
        Windows("summary_test1_h6_w8.xls").Activate
        Cells(1, 2 * ii - 1).Select
        Selection.End(xlDown).Select
        ActiveSheet.Paste
    Next ii
' @@@@

    Workbooks.Open FileName:="D:\Optical Probe Expt\test260900\test1\run20.xls"
    For i = 1 To 10
        Cells(1, 16 + 2 * i).Select
        Selection.End(xlDown).Select
        TNP(i) = Selection
    Next i

    For ii = 1 To 10
        Windows("run20.xls").Activate
        Range(Cells(2, 16 + 2 * ii), Cells(TNP(ii) + 1, 17 + 2 * ii)).Select
        Selection.Copy
        Windows("summary_test1_h6_w8.xls").Activate
        Cells(1, 2 * ii - 1).Select
        Selection.End(xlDown).Select
        ActiveSheet.Paste
    Next ii
' @@@@

    Windows("summary_test1_h6_w8.xls").Activate
    ActiveWorkbook.Save
    ActiveWindow.Close

    Windows("run1.xls").Activate
    ActiveWindow.Close
    Windows("run2.xls").Activate
    ActiveWindow.Close
    Windows("run3.xls").Activate
    ActiveWindow.Close
    Windows("run4.xls").Activate
    ActiveWindow.Close
    Windows("run5.xls").Activate
    ActiveWindow.Close
    Windows("run6.xls").Activate
    ActiveWindow.Close
    Windows("run7.xls").Activate
    ActiveWindow.Close
    Windows("run8.xls").Activate
    ActiveWindow.Close
    Windows("run9.xls").Activate
    ActiveWindow.Close
    Windows("run10.xls").Activate
    ActiveWindow.Close
    Windows("run11.xls").Activate
    ActiveWindow.Close
    Windows("run12.xls").Activate
```

```
    ActiveWindow.Close
    Windows("run13.xls").Activate
    ActiveWindow.Close
    Windows("run14.xls").Activate
    ActiveWindow.Close
    Windows("run15.xls").Activate
    ActiveWindow.Close
    Windows("run16.xls").Activate
    ActiveWindow.Close
    Windows("run17.xls").Activate
    ActiveWindow.Close
    Windows("run18.xls").Activate
    ActiveWindow.Close
    Windows("run19.xls").Activate
    ActiveWindow.Close
    Windows("run20.xls").Activate
    ActiveWindow.Close

End Sub

'*******************************************************************************************

Sub Conversion1()
'
' 1. NEED TO CHANGE "test260900"
' 2. NEED TO CHANGE "h6_w8"
'
    Workbooks.Open FileName:="D:\Optical Probe Expt\test260900\summary_test1_h6_w8.xls"

    Call size

    Sheets("Sheet2").Select
    Range("B6:F13").Select
    Sheets("Sheet2").Select
    Charts.Add
    ActiveChart.ChartType = xlColumnClustered
    ActiveChart.SetSourceData Source:=Sheets("Sheet2").Range("B6:F13")
    ActiveChart.Location Where:=xlLocationAsNewSheet
    ActiveChart.PlotArea.Select
    With Selection.Border
        .ColorIndex = 16
        .Weight = xlThin
        .LineStyle = xlContinuous
    End With
    Selection.Interior.ColorIndex = xlNone
    With ActiveChart
        .HasTitle = True
        .ChartTitle.Characters.Text = "Gas Chord Length Distribution (h6_w8_test1)"
        .Axes(xlCategory, xlPrimary).HasTitle = True
        .Axes(xlCategory, xlPrimary).AxisTitle.Characters.Text = _
        "Gas Chord Length Groups (2mm to 25mm, equal division)"
        .Axes(xlValue, xlPrimary).HasTitle = True
        .Axes(xlValue, xlPrimary).AxisTitle.Characters.Text = "Probability"
    End With
    Sheets("Chart1").Select
    Sheets("Chart1").Name = "Gas Chord"
    Sheets("Sheet2").Select
    Range("I6:M12").Select
    Sheets("Sheet2").Select
    Charts.Add
    ActiveChart.ChartType = xlColumnClustered
    ActiveChart.SetSourceData Source:=Sheets("Sheet2").Range("I6:M12")
    ActiveChart.Location Where:=xlLocationAsNewSheet
    ActiveChart.PlotArea.Select
    With Selection.Border
        .ColorIndex = 16
        .Weight = xlThin
        .LineStyle = xlContinuous
    End With
    Selection.Interior.ColorIndex = xlNone
    With ActiveChart
        .HasTitle = True
        .ChartTitle.Characters.Text = _
        "Liquid Chord Length Distribution (h6_w8_test1)"
        .Axes(xlCategory, xlPrimary).HasTitle = True
        .Axes(xlCategory, xlPrimary).AxisTitle.Characters.Text = _
```

```
        "Liquid Chord Length Groups (3mm to 20mm, equal division)"
        .Axes(xlValue, xlPrimary).HasTitle = True
        .Axes(xlValue, xlPrimary).AxisTitle.Characters.Text = "Probability"
    End With
    Sheets("Chart2").Select
    Sheets("Chart2").Name = "Liquid Chord"
    Sheets("Sheet3").Select
    Range("B6:F13").Select
    Sheets("Sheet3").Select
    Charts.Add
    ActiveChart.ChartType = xlColumnClustered
    ActiveChart.SetSourceData Source:=Sheets("Sheet3").Range("B6:F13")
    ActiveChart.Location Where:=xlLocationAsNewSheet
    ActiveChart.PlotArea.Select
    With Selection.Border
        .ColorIndex = 16
        .Weight = xlThin
        .LineStyle = xlContinuous
    End With
    Selection.Interior.ColorIndex = xlNone
    With ActiveChart
        .HasTitle = True
        .ChartTitle.Characters.Text = "Bubble Size Distribution (h6_w8_test1)"
        .Axes(xlCategory, xlPrimary).HasTitle = True
        .Axes(xlCategory, xlPrimary).AxisTitle.Characters.Text = _
        "Bubble Diameter Groups (2mm to 25mm, equal division)"
        .Axes(xlValue, xlPrimary).HasTitle = True
        .Axes(xlValue, xlPrimary).AxisTitle.Characters.Text = "Probability"
    End With
    Sheets("Chart3").Select
    Sheets("Chart3").Name = "Bubble Diameter"
    Sheets("Sheet3").Select
    Range("I6:M12").Select
    Sheets("Sheet3").Select
    Charts.Add
    ActiveChart.ChartType = xlColumnClustered
    ActiveChart.SetSourceData Source:=Sheets("Sheet3").Range("I6:M12"), PlotBy _
        :=xlColumns
    ActiveChart.Location Where:=xlLocationAsNewSheet
    ActiveChart.PlotArea.Select
    With Selection.Border
        .ColorIndex = 16
        .Weight = xlThin
        .LineStyle = xlContinuous
    End With
    Selection.Interior.ColorIndex = xlNone
    With ActiveChart
        .HasTitle = True
        .ChartTitle.Characters.Text = "Droplet Size Distribution (h6_w8_test1)"
        .Axes(xlCategory, xlPrimary).HasTitle = True
        .Axes(xlCategory, xlPrimary).AxisTitle.Characters.Text = _
        "Droplet Diameter Groups (3mm to 20mm, equal division)"
        .Axes(xlValue, xlPrimary).HasTitle = True
        .Axes(xlValue, xlPrimary).AxisTitle.Characters.Text = "Probability"
    End With
    Sheets("Chart4").Select
    Sheets("Chart4").Name = "Droplet Diameter"
    Sheets("Sheet3").Select
    Range("A1").Select
    ActiveWorkbook.Save
    ActiveWindow.Close

End Sub

'*******************************************************************************

Sub size()

'*********************************************************************
' Step 1: Chord length distribution
'*********************************************************************
'   Symbol definitions for current section
'   <<added 30/12/00>> corrections added throughout here according to previous steps


Const maxposn = 700
```

```
Const minposn = 100
Const region = 1
Const maxb = 25
Const minb = 2
Const groupb = 7
Const maxd = 20
Const mind = 3
Const groupd = 6
Const probe = 5

Dim chord_b(groupb + 1) As Double
Dim chord_d(groupd + 1) As Double
Dim count_b(groupb, region, probe) As Double
Dim count_d(groupd, region, probe) As Double
Dim posn(region + 1) As Double
Dim total_b(region, probe) As Double
Dim total_d(region, probe) As Double

'   Initialise all values
'
    Sheets("Sheet1").Select

    chord_b(1) = minb
    For i = 2 To groupb + 1
        chord_b(i) = chord_b(i - 1) + (maxb - minb) / groupb
    Next i

    chord_d(1) = mind
    For i = 2 To groupd + 1
        chord_d(i) = chord_d(i - 1) + (maxd - mind) / groupd
    Next i

    posn(1) = minposn
    For i = 2 To region + 1
       posn(i) = posn(i - 1) + (maxposn - minposn) / region
    Next i

'   Begin bubble chord length grouping
'
    For x = 1 To probe
        counter = 2
9       If Cells(counter, 4 * x - 2).Value = 0 Then
            GoTo 11
        End If

        For i = 1 To groupb
        For j = 1 To region
            If chord_b(i) < Cells(counter, 4 * x - 2).Value And Cells(counter, 4 * x -
2).Value < chord_b(i + 1) And posn(j) < Cells(counter, 4 * x - 3).Value And
Cells(counter, 4 * x - 3).Value < posn(j + 1) Then
                count_b(i, j, x) = count_b(i, j, x) + 1
            End If
        Next j
        Next i

        counter = counter + 1
        GoTo 9
11  Next x


'   Begin liquid chord length grouping
'
    For x = 1 To probe
        counter = 2
19      If Cells(counter, 4 * x).Value = "" Then
            GoTo 21
        End If

        For i = 1 To groupd
        For j = 1 To region
            If chord_d(i) < Cells(counter, 4 * x).Value And Cells(counter, 4 * x).Value
< chord_d(i + 1) And posn(j) < Cells(counter, 4 * x - 1).Value And Cells(counter, 4 * x
- 1).Value < posn(j + 1) Then
                count_d(i, j, x) = count_d(i, j, x) + 1
            End If
        Next j
```

```
        Next i

        counter = counter + 1
        GoTo 19
21  Next x


'   Results Display
'
    Sheets("Sheet2").Select

    Cells(1, 1).Value = "Region"
    Cells(2, 1).Value = "from"
    Cells(3, 1).Value = "to"
    For i = 1 To region
        Cells(1, i + 1).Value = i
        Cells(2, i + 1).Value = posn(i)
        Cells(3, i + 1).Value = posn(i + 1)
    Next i


    For i = 1 To region
        For j = 1 To probe
            For kb = 1 To groupb
                total_b(i, j) = total_b(i, j) + count_b(kb, i, j)
            Next kb
            For kd = 1 To groupd
                total_d(i, j) = total_d(i, j) + count_d(kd, i, j)
            Next kd
        Next j
    Next i

    If groupb > groupd Then
        group = groupb
    Else
        group = groupd
    End If

    For i = 1 To region
        For j = 1 To probe
            For kb = 1 To groupb
'               Cells(kb + 6 + (i - 1) * (group + 3), j + 1).Value = count_b(kb, i, j)
                Cells(kb + 6 + (i - 1) * (group + 3), j + 1).Value = count_b(kb, i, j) /
total_b(i, j)
            Next kb
            For kd = 1 To groupd
'               Cells(kd + 6 + (i - 1) * (group + 3), j + 8).Value = count_d(kd, i, j)
                Cells(kd + 6 + (i - 1) * (group + 3), j + 8).Value = count_d(kd, i, j) /
total_d(i, j)
            Next kd
        Next j

        For kb = 1 To groupb
            Cells(6 + kb + (i - 1) * (group + 3), 1).Value = chord_b(kb + 1)
        Next kb
        For kd = 1 To groupd
            Cells(6 + kd + (i - 1) * (group + 3), 8).Value = chord_d(kd + 1)
        Next kd

        Cells(5 + (i - 1) * (group + 3), 5).Value = "Region"
        Cells(5 + (i - 1) * (group + 3), 12).Value = "Region"
        Cells(5 + (i - 1) * (group + 3), 6).Value = i
        Cells(5 + (i - 1) * (group + 3), 13).Value = i
        Cells(5 + (i - 1) * (group + 3), 1).Value = "Gas Chord Length"
        Cells(5 + (i - 1) * (group + 3), 8).Value = "Liquid Chord Length"
        Cells(6 + (i - 1) * (group + 3), 1).Value = "(mm)"
        Cells(6 + (i - 1) * (group + 3), 2).Value = "Probe 1"
        Cells(6 + (i - 1) * (group + 3), 3).Value = "Probe 2"
        Cells(6 + (i - 1) * (group + 3), 4).Value = "Probe 3"
        Cells(6 + (i - 1) * (group + 3), 5).Value = "Probe 4"
        Cells(6 + (i - 1) * (group + 3), 6).Value = "Probe 5"
        Cells(6 + (i - 1) * (group + 3), 8).Value = "(mm)"
        Cells(6 + (i - 1) * (group + 3), 9).Value = "Probe 1"
        Cells(6 + (i - 1) * (group + 3), 10).Value = "Probe 2"
        Cells(6 + (i - 1) * (group + 3), 11).Value = "Probe 3"
        Cells(6 + (i - 1) * (group + 3), 12).Value = "Probe 4"
```

```
        Cells(6 + (i - 1) * (group + 3), 13).Value = "Probe 5"
    Next i


'*************************************************************************
' Step 2: Bubble/Droplet size group distribution
'*************************************************************************
'   Symbol definitions for current section
'   Transformation of chord length distribution into bubble size distribution
'   <<added 02/01/01>>

Dim y(groupb + 1) As Double
Dim yd(groupd + 1) As Double
Dim R(groupb + 1) As Double
Dim Rd(groupd + 1) As Double
Dim W(groupb, region, probe) As Double
Dim Wd(groupd, region, probe) As Double
Dim C(groupb, region, groupb) As Double
Dim Cd(groupd, region, groupd) As Double
' Dim CC(15) As Double
Dim P(groupb, region, probe) As Double
Dim Pd(groupd, region, probe) As Double

'@@@@@@@@@@
'   Bubble
'@@@@@@@@@@
y(1) = maxb
R(1) = y(1) / 2

For i = 2 To groupb + 1
    y(i) = chord_b(groupb + 2 - i)
    R(i) = y(i) / 2
Next i

dR = R(1) - R(2)

For k = 1 To probe
    For j = 1 To region
        For i = 1 To groupb
            W(i, j, k) = count_b(groupb + 1 - i, j, k) / total_b(j, k)
        Next i
    Next j
Next k

For k = 1 To region
    For j = 1 To groupb
        For i = 1 To groupb
            If i < j Then
                C(i, k, j) = 0
            Else
                C(i, k, j) = (y(i) ^ 2 - y(i + 1) ^ 2) / 4 / R(j) ^ 2
            End If
        Next i
    Next j
Next k

For k = 1 To probe
    For j = 1 To region
        P(1, j, k) = W(1, j, k) / C(1, j, 1) / dR
        P(2, j, k) = (W(2, j, k) - C(2, j, 1) * P(1, j, k) * dR) / C(2, j, 2) / dR

        For i = 3 To groupb

            CC = 0

            For jj = 1 To i - 1
                CC = CC + C(i, j, jj) * P(jj, j, k) * dR
            Next jj

            P(i, j, k) = (W(i, j, k) - CC) / C(i, j, i) / dR
        Next i
    Next j
Next k

    Sheets("Sheet3").Select
```

```
    Cells(1, 1).Value = "Region"
    Cells(2, 1).Value = "from"
    Cells(3, 1).Value = "to"
    For i = 1 To region
        Cells(1, i + 1).Value = i
        Cells(2, i + 1).Value = posn(i)
        Cells(3, i + 1).Value = posn(i + 1)
    Next i


For i = 1 To region
        For j = 1 To probe
            Pbsum = 0
            For kb = 1 To groupb
                Pbsum = Pbsum + P(groupb + 1 - kb, i, j) * dR
            Next kb
            For kb = 1 To groupb
                Cells(kb + 6 + (i - 1) * (group + 3), j + 1).Value = P(groupb + 1 - kb,
i, j) * dR / Pbsum
            Next kb
        Next j
        Cells(5 + (i - 1) * (group + 3), 5).Value = "Region"
        Cells(5 + (i - 1) * (group + 3), 6).Value = i
        Cells(5 + (i - 1) * (group + 3), 1).Value = "Bubble Diameter"
        Cells(6 + (i - 1) * (group + 3), 1).Value = "(mm)"
        Cells(6 + (i - 1) * (group + 3), 2).Value = "Probe 1"
        Cells(6 + (i - 1) * (group + 3), 3).Value = "Probe 2"
        Cells(6 + (i - 1) * (group + 3), 4).Value = "Probe 3"
        Cells(6 + (i - 1) * (group + 3), 5).Value = "Probe 4"
        Cells(6 + (i - 1) * (group + 3), 6).Value = "Probe 5"

        For kb = 1 To groupb
            Cells(6 + kb + (i - 1) * (group + 3), 1).Value = R(groupb + 1 - kb) * 2
        Next kb

Next i

'@@@@@@@@@@
'   droplet
'@@@@@@@@@@
yd(1) = maxd
Rd(1) = yd(1) / 2

For i = 2 To groupd + 1
    yd(i) = chord_d(groupd + 2 - i)
    Rd(i) = yd(i) / 2
Next i

dRd = Rd(1) - Rd(2)

For k = 1 To probe
    For j = 1 To region
        For i = 1 To groupd
            Wd(i, j, k) = count_d(groupd + 1 - i, j, k) / total_d(j, k)
        Next i
    Next j
Next k

For k = 1 To region
    For j = 1 To groupd
        For i = 1 To groupd
            If i < j Then
                Cd(i, k, j) = 0
            Else
                Cd(i, k, j) = (yd(i) ^ 2 - yd(i + 1) ^ 2) / 4 / Rd(j) ^ 2
            End If
        Next i
    Next j
Next k

For k = 1 To probe
    For j = 1 To region
        Pd(1, j, k) = Wd(1, j, k) / Cd(1, j, 1) / dRd
        Pd(2, j, k) = (Wd(2, j, k) - Cd(2, j, 1) * Pd(1, j, k) * dRd) / Cd(2, j, 2) /
dRd
```

```
        For i = 3 To groupd

            CC = 0

            For jj = 1 To i - 1
                CC = CC + Cd(i, j, jj) * Pd(jj, j, k) * dRd
            Next jj

            Pd(i, j, k) = (Wd(i, j, k) - CC) / Cd(i, j, i) / dRd
        Next i
    Next j
Next k

For i = 1 To region
        For j = 1 To probe
            Pdsum = 0
            For kd = 1 To groupd
                Pdsum = Pdsum + Pd(groupd + 1 - kd, i, j) * dRd
            Next kd
            For kd = 1 To groupd
                Cells(kd + 6 + (i - 1) * (group + 3), j + 8).Value = Pd(groupd + 1 - kd,
i, j) * dRd / Pdsum
            Next kd
        Next j
        Cells(5 + (i - 1) * (group + 3), 12).Value = "Region"
        Cells(5 + (i - 1) * (group + 3), 13).Value = i
        Cells(5 + (i - 1) * (group + 3), 8).Value = "Droplet Diameter"
        Cells(6 + (i - 1) * (group + 3), 8).Value = "(mm)"
        Cells(6 + (i - 1) * (group + 3), 9).Value = "Probe 1"
        Cells(6 + (i - 1) * (group + 3), 10).Value = "Probe 2"
        Cells(6 + (i - 1) * (group + 3), 11).Value = "Probe 3"
        Cells(6 + (i - 1) * (group + 3), 12).Value = "Probe 4"
        Cells(6 + (i - 1) * (group + 3), 13).Value = "Probe 5"

        For kd = 1 To groupd
            Cells(6 + kd + (i - 1) * (group + 3), 8).Value = Rd(groupd + 1 - kd) * 2
        Next kd

Next i

End Sub

'*****************************************************************************

*****************************************************************************
```

D3. CFX Command File for the MUSIG model

```
**************************************************************************

/*********************************************************          */
/* IMPIPSA WITH MASS FLOW BOUNDARIES AND AIRFLOW IN                  */
/* OUT SPEDCIFIED VIA USER FORTRANS/ ONE BLOC                        */
/*********************************************************          */

>>CFX4
  >>SET LIMITS
    TOTAL INTEGER WORK SPACE 5000000
    TOTAL CHARACTER WORK SPACE 5000
    TOTAL REAL WORK SPACE 9000000
    MAXIMUM NUMBER OF BLOCKS 10
    MAXIMUM NUMBER OF PATCHES 100
    MAXIMUM NUMBER OF INTER BLOCK BOUNDARIES 50
  >>OPTIONS
    THREE DIMENSIONS
    RECTANGULAR GRID
    CARTESIAN COORDINATES
    TURBULENT FLOW
    ISOTHERMAL FLOW
    INCOMPRESSIBLE FLOW
    BUOYANT FLOW
    STEADY STATE
    NUMBER OF PHASES 2
    NUMBER OF MUSIG SIZE GROUPS 10
>>MODEL TOPOLOGY
  >>INPUT TOPOLOGY
    READ GEOMETRY FILE
  >>CREATE PATCH
    PATCH NAME 'DOWNCOMER INLET'
    BLOCK NAME 'BLOCK-NUMBER-1'
    PATCH TYPE 'THIN SURFACE'
    PATCH LOCATION 5 5 1 6 4 25
    HIGH I
  >>CREATE PATCH
    PATCH NAME 'WEIR'
    BLOCK NAME 'BLOCK-NUMBER-2'
    PATCH TYPE 'THIN SURFACE'
    PATCH LOCATION 20 20 1 6 1 6
    HIGH I
  >>CREATE PATCH
    PATCH NAME 'TOP'
    BLOCK NAME 'BLOCK-NUMBER-2'
    PATCH TYPE 'PRESSURE BOUNDARY'
    PATCH LOCATION 1 20 1 6 25 25
    HIGH K
  >>CREATE PATCH
    PATCH NAME 'ENTRANCE'
    BLOCK NAME 'BLOCK-NUMBER-1'
    PATCH TYPE 'INLET'
    PATCH LOCATION 3 4 1 6 25 25
    HIGH K
  >>CREATE PATCH
    PATCH NAME 'DOUTLET'
    BLOCK NAME 'BLOCK-NUMBER-4'
    PATCH TYPE 'MASS FLOW BOUNDARY'
    PATCH LOCATION 1 1 1 6 7 8
    LOW I
  >>CREATE PATCH
    PATCH NAME 'AENTRANCE'
    BLOCK NAME 'BLOCK-NUMBER-2'
    PATCH TYPE 'INLET'
    PATCH LOCATION 1 20 1 6 1 1
    LOW K
>>MODEL DATA
/*  >>SET INITIAL GUESS
    >>INPUT FROM FILE
      READ DUMP FILE */
  >>RHIE CHOW SWITCH
    MULTIPHASE DAMPING
  >>TITLE
```

```
    PROBLEM TITLE +
    'MUSIG Algorithm Test Run'
  >>PHYSICAL PROPERTIES
    >>BUOYANCY PARAMETERS
      GRAVITY VECTOR 0.000000E+00 0.000000E+00 -9.810000E+00
      BUOYANCY REFERENCE DENSITY 1.0000E+03
    >>FLUID PARAMETERS
      PHASE NAME 'PHASE1'
      VISCOSITY 1.0000E-03
      DENSITY 1.0000E+03
    >>FLUID PARAMETERS
      PHASE NAME 'PHASE2'
      VISCOSITY 1.8000E-05
      DENSITY 1.2000E+00
    >>MULTIPHASE PARAMETERS
      >>PHASE DESCRIPTION
        PHASE NAME 'PHASE1'
        LIQUID
        CONTINUOUS
        MODIFY EMPTY CELL VELOCITY 0.0000E+00
      >>PHASE DESCRIPTION
        PHASE NAME 'PHASE2'
        GAS
        DISPERSE
        MEAN DIAMETER 3.0000E-02
        MINIMUM VOLUME FRACTION 1.0000E-08
        MODIFY EMPTY CELL VELOCITY 0.0000E+00
      >>MULTIPHASE MODELS
        >>MOMENTUM
          INTER PHASE TRANSFER
          SINCE
        >>TURBULENCE
          INTER PHASE TRANSFER
          SINCE
      >>INTER PHASE TRANSFER MODELS
        >>MOMENTUM
          FIRST PHASE NAME 'PHASE1'
          SECOND PHASE NAME 'PHASE2'
          SURFACE TENSION COEFFICIENT 7.3250E-02
          >>PARTICLE DRAG MODEL
            FLOW REGIME 'NEWTON'
            NEWTON COEFFICIENT 4.4000E-01
          >>NON DRAG FORCES
            TURBULENT DISPERSION FORCE
            DISPERSION COEFFICIENT 1.0000E-01
      >>MUSIG MODEL
        PHASE NAME 'PHASE2'
        MAXIMUM DIAMETER 3.0000E-02
        MINIMUM DIAMETER 0.0000E+00
        EQUAL DIAMETER DIVISION
/*        ITERATIONS BETWEEN MUSIG MODEL UPDATES 50 */
        >>BREAKUP MODEL
          LUO SVENDSEN
          BREAKUP COEFFICIENT 1.0000E+00
        >>COALESCENCE MODEL
          PRINCE BLANCH
          COALESCENCE COEFFICIENT 2.0000E+00
          INITIAL FILM THICKNESS 1.0000E-04
          CRITICAL FILM THICKNESS 1.0000E-08
    >>TURBULENCE PARAMETERS
      >>TURBULENCE MODEL
        PHASE NAME 'PHASE1'
        TURBULENCE MODEL 'K-EPSILON'
        PARTICLE INDUCED TURBULENCE 'SATO'
      >>TURBULENCE MODEL
        PHASE NAME 'PHASE2'
        TURBULENCE MODEL 'LAMINAR'
        PARTICLE INDUCED TURBULENCE 'SATO'
>>SOLVER DATA
  >>PROGRAM CONTROL
    MAXIMUM NUMBER OF ITERATIONS 2500
    MASS SOURCE TOLERANCE 1.0000E-06
  >>FALSE TIMESTEPS
    U VELOCITY 1.0000E-05
    V VELOCITY 1.0000E-05
    W VELOCITY 1.0000E-05
```

```
  >>UNDER RELAXATION FACTORS
    U VELOCITY 3.0000E-01
    V VELOCITY 3.0000E-01
    W VELOCITY 3.0000E-01
    VOLUME FRACTION 5.0000E-01
    K 3.0000E-01
    EPSILON 3.0000E-01
    ALL MUSIG VOL FRACTIONS 8.0000E-01
  >>PRESSURE CORRECTION
    SIMPLE
>>CREATE GRID
  >>INPUT GRID
    READ GRID FILE
>>MODEL BOUNDARY CONDITIONS
  >>INLET BOUNDARIES
    PHASE NAME 'PHASE2'
    PATCH NAME 'AENTRANCE'
    W VELOCITY 3.0
    VOLUME FRACTION 0.1
    MUSIG VOL FRACTION1 1.0
  >>PRESSURE BOUNDARIES
    PHASE NAME 'PHASE2'
    PATCH NAME 'TOP'
    PRESSURE 0.0000E+00
    VOLUME FRACTION 0.95
  >>SET VARIABLES
    PHASE NAME 'PHASE1'
    PATCH NAME 'ENTRANCE'
    W VELOCITY -6.0148E-02
    VOLUME FRACTION 1.0
    K 1.0000E-03
    EPSILON 2.6870E-07
  >>SET VARIABLES
    PHASE NAME 'PHASE2'
    PATCH NAME 'ENTRANCE'
    W VELOCITY 0.0
    VOLUME FRACTION 0.0
  >>SET VARIABLES
    PHASE NAME 'PHASE1'
    PATCH NAME 'DOUTLET'
    U VELOCITY -3.6089E-02
    VOLUME FRACTION 1.0
  >>SET VARIABLES
    PHASE NAME 'PHASE2'
    PATCH NAME 'DOUTLET'
    U VELOCITY 0.0
    VOLUME FRACTION 0.0
  >>SET VARIABLES
    PHASE NAME 'PHASE1'
    PATCH NAME 'AENTRANCE'
    W VELOCITY 0.0
    VOLUME FRACTION 0.9
  >>SET VARIABLES
    PHASE NAME 'PHASE1'
    PATCH NAME 'TOP'
    PRESSURE 0.0000E+00
    VOLUME FRACTION 0.05
>>OUTPUT OPTIONS
  >>FRONTEND PRINTING
    NO TOPOLOGY STRUCTURE
  >>PRINT OPTIONS
    >>WHAT
      NO VARIABLES
      NO GEOMETRIC INFORMATION
      NO WALL PRINTING
    >>WHERE
      I PLANES 18 19 20
      BLOCK NAME 'BLOCK-NUMBER-2'
    >>WHEN
      INITIAL GUESS
      FINAL SOLUTION
      EACH ITERATION
  >>LINE GRAPH DATA
    PHASE NAME 'PHASE1'
    BLOCK NAME 'BLOCK-NUMBER-2'
    IJK 10 3 5
```

```
    EACH ITERATION
    DYNAMIC PLOT
    U VELOCITY
    PRESSURE
    VOLUME FRACTION
>>STOP
```

****

D4. CFX Command File for the residence time methodology

```
**********************************************************************

/*******************************************************          */
/* Residence Time Methodology Imperial HM                          */
/*                      TWO PHASE                                  */
/*******************************************************          */


/* Run Number 11 Stichlmair */
/* Input Flow conditions */

    #CALC
     GASVID=0.7573;
     HF=0.15;
     MLIQ=2.3975;
     DENGAS =1.2;
     DENLIQ=1000.0;
     VISCL=1.0E-3;
     VISCG=1.8E-5;
     VISCH=1.0/((1-GASVID)/VISCL+GASVID/VISCG);
     DENLIH=GASVID*DENGAS+(1-GASVID)*DENLIQ;
     UINL=MLIQ/DENLIH/HF/0.463;
     TEINL=0.002*UINL*UINL;
     DE=0.05;
     EPSINL=TEINL**1.5/(0.3*DE);
    #ENDCALC

>>CFX4
  >>SET LIMITS
    TOTAL INTEGER WORK SPACE 5000000
    TOTAL CHARACTER WORK SPACE 5000
    TOTAL REAL WORK SPACE 8000000
    MAXIMUM NUMBER OF BLOCKS 20
    MAXIMUM NUMBER OF PATCHES 900
    MAXIMUM NUMBER OF INTER BLOCK BOUNDARIES 80
  >>OPTIONS
    THREE DIMENSIONS
    BODY FITTED GRID
    CARTESIAN COORDINATES
    TURBULENT FLOW
    ISOTHERMAL FLOW
    INCOMPRESSIBLE FLOW
    BUOYANT FLOW
    STEADY STATE
    USER SCALAR EQUATIONS 4
    NUMBER OF PHASES 2
  >>USER FORTRAN
    USRSRC
  >>VARIABLE NAMES
    USER SCALAR1 'FLUID AGE'
    USER SCALAR2 'SMIX'
    USER SCALAR3 'AGED'
    USER SCALAR4 'FRANK'
>>MODEL TOPOLOGY
  >>INPUT TOPOLOGY
    READ GEOMETRY FILE
  >>CREATE PATCH
    PATCH NAME 'INLETV1'
    BLOCK NAME 'BLOCK-NUMBER-1'
    PATCH TYPE 'INLET'
    PATCH LOCATION 1 1 1 20 1 15
    LOW I
  >>CREATE PATCH
    PATCH NAME 'INLETV2'
    BLOCK NAME 'BLOCK-NUMBER-1'
    PATCH TYPE 'INLET'
    PATCH LOCATION 1 1 1 20 16 17
    LOW I
  >>CREATE PATCH
    PATCH NAME 'OUTLETP'
    BLOCK NAME 'BLOCK-NUMBER-1'
    PATCH TYPE 'PRESSURE BOUNDARY'
```

```
    PATCH LOCATION 20 20 1 20 4 17
    HIGH I
  >>CREATE PATCH
    PATCH NAME 'TOP'
    BLOCK NAME 'BLOCK-NUMBER-1'
    PATCH TYPE 'THIN SURFACE'
    PATCH LOCATION 1 20 1 20 17 17
    HIGH K

>>MODEL DATA
  >>PHYSICAL PROPERTIES
    >>BUOYANCY PARAMETERS
      GRAVITY VECTOR 0.0 0.0 -9.8
    >>FLUID PARAMETERS
      PHASE NAME 'PHASE1'
      VISCOSITY #VISCH
      DENSITY #DENLIH
    >>FLUID PARAMETERS
      PHASE NAME 'PHASE2'
      VISCOSITY #VISCG
      DENSITY #DENGAS
    >>MULTIPHASE PARAMETERS
      >>PHASE DESCRIPTION
        PHASE NAME 'PHASE1'
        LIQUID
        CONTINUOUS
      >>PHASE DESCRIPTION
        PHASE NAME 'PHASE2'
        GAS
        CONTINUOUS
      >>MULTIPHASE MODELS
        >>MOMENTUM
          HOMOGENEOUS
          SURFACE SHARPENING ALGORITHM
        >>TURBULENCE
          HOMOGENEOUS
        >>HOMOGENEOUS
          SINCE
          SURFACE SHARPENING ALGORITHM
    >>SCALAR PARAMETERS
      >>DIFFUSIVITIES
        FLUID AGE 1.0000E-10
        SMIX 1.0000E-03
        AGED 1.0000E-03
        FRANK 1.0000E-10
    >>TURBULENCE PARAMETERS
      >>TURBULENT PRANDTL NUMBER
        FLUID AGE 1.0000E+10
        SMIX 1.0000E+00
        AGED 1.0000E+00
        FRANK 1.0000E+10
      >>LOGLAYER CONSTANT
        FLUID AGE 1.0000E+00
        FRANK 1.0000E+00
>>SOLVER DATA
  >>PROGRAM CONTROL
    MAXIMUM NUMBER OF ITERATIONS 500
    MINIMUM NUMBER OF ITERATIONS 5
    OUTPUT MONITOR POINT 10 10 5
    MASS SOURCE TOLERANCE 1.0000E-16
  >>DEFERRED CORRECTION
    K START 300
    K END 301
    EPSILON START 300
    EPSILON END 301
  >>EQUATION SOLVERS
    ALL PHASES
    VOLUME FRACTION 'STONE'
  >>FALSE TIMESTEPS
    U VELOCITY 1.0000E-02
    V VELOCITY 1.0000E-02
    W VELOCITY 1.0000E-02
  >>UNDER RELAXATION FACTORS
    U VELOCITY 5.0000E-01
    V VELOCITY 5.0000E-01
    W VELOCITY 5.0000E-01
```

```
>>CREATE GRID
  >>INPUT GRID
    READ GRID FILE
>>MODEL BOUNDARY CONDITIONS
  >>SET VARIABLES
    PATCH NAME 'INLETV1'
    PHASE NAME 'PHASE1'
    U VELOCITY #UINL
    K #TEINL
    EPSILON #EPSINL
    VOLUME FRACTION 1.0
    FLUID AGE 0.0
    AGED 0.0
    SMIX 0.0

  >>SET VARIABLES
    PATCH NAME 'INLETV2'
    PHASE NAME 'PHASE2'
    U VELOCITY #UINL
    K #TEINL
    EPSILON #EPSINL
    VOLUME FRACTION 1.0
    FLUID AGE 0.0
    AGED 0.0

  >>SET VARIABLES
    PATCH NAME 'INLETV2'
    PHASE NAME 'PHASE1'
    U VELOCITY #UINL
    K #TEINL
    EPSILON #EPSINL
    VOLUME FRACTION 0.0
    FLUID AGE 0.0
    AGED 0.0

  >>SET VARIABLES
    PATCH NAME 'INLETV1'
    PHASE NAME 'PHASE2'
    U VELOCITY #UINL
    K #TEINL
    EPSILON #EPSINL
    VOLUME FRACTION 0.0
    FLUID AGE 0.0
    AGED 0.0

  >>SET VARIABLES
    PATCH NAME 'OUTLETP'
    PHASE NAME 'PHASE1'
    PRESSURE 0.0

  >>SET VARIABLES
    PATCH NAME 'OUTLETP'
    PHASE NAME 'PHASE2'
    PRESSURE 0.0

>>STOP

**********************************************************************
```

D5. CFX User Fortran File for the residence time methodology

```
**********************************************************************

      SUBROUTINE USRSRC(IEQN,ICALL,CNAME,CALIAS,AM,SP,SU,CONV
     +                 ,U,V,W,P,VFRAC,DEN,VIS,TE,ED,RS,T,H,RF,SCAL
     +                 ,XP,YP,ZP,VOL,AREA,VPOR,ARPOR,WFACT,IPT
     +                 ,IBLK,IPVERT,IPNODN,IPFACN,IPNODF,IPNODB,IPFACB
     +                 ,WORK,IWORK,CWORK)
C
C**********************************************************************
C
C   UTILITY SUBROUTINE FOR USER-SUPPLIED SOURCES
C
C   >>> IMPORTANT                                                    <<<
C   >>>                                                             <<<
C   >>> USERS MAY ONLY ADD OR ALTER PARTS OF THE SUBROUTINE WITHIN  <<<
C   >>> THE DESIGNATED USER AREAS                                   <<<
C
C**********************************************************************
C
C   THIS SUBROUTINE IS CALLED BY THE FOLLOWING SUBROUTINES
C      CUSR  SCDF  SCDS  SCED  SCENRG  SCHF  SCMOM  SCPCE  SCSCAL
C      SCTE  SCVF
C
C**********************************************************************
C   CREATED
C      08/03/90  ADB
C   MODIFIED
C      04/03/91  ADB  ALTERED ARGUMENT LIST.
C      28/08/91  IRH  NEW STRUCTURE
C      28/09/91  IRH  CHANGE EXAMPLE + ADD COMMON BLOCKS
C      10/02/92  PHA  UPDATE CALLED BY COMMENT, ADD RF ARGUMENT,
C                     CHANGE LAST DIMENSION OF RS TO 6 AND IVERS TO 2
C      03/06/92  PHA  ADD PRECISION FLAG AND CHANGE IVERS TO 3
C      23/11/93  CSH  EXPLICITLY DIMENSION IPVERT ETC.
C      07/12/93  NSW  INCLUDE CONV IN ARGUMENT LIST AND CHANGE IVERS
C                     TO 4
C      03/02/94  PHA  CHANGE FLOW3D TO CFDS-FLOW3D
C      03/03/94  PHW  CORRECTION OF SPELLING MISTAKE
C      08/03/94  NSW  CORRECT SPELLING
C
C**********************************************************************
C
C   SUBROUTINE ARGUMENTS
C
C     IEQN   - EQUATION NUMBER
C     ICALL  - SUBROUTINE CALL
C     CNAME  - EQUATION NAME
C     CALIAS - ALIAS OF EQUATION NAME
C     AM     - OFF DIAGONAL MATRIX COEFFICIENTS
C     SU     - SU IN LINEARISATION OF SOURCE TERM
C     SP     - SP IN LINEARISATION OF SOURCE TERM
C     CONV   - CONVECTION COEFFICIENTS
C     U      - U COMPONENT OF VELOCITY
C     V      - V COMPONENT OF VELOCITY
C     W      - W COMPONENT OF VELOCITY
C     P      - PRESSURE
C     VFRAC  - VOLUME FRACTION
C     DEN    - DENSITY OF FLUID
C     VIS    - VISCOSITY OF FLUID
C     TE     - TURBULENT KINETIC ENERGY
C     ED     - EPSILON
C     RS     - REYNOLD STRESSES
C     T      - TEMPERATURE
C     H      - ENTHALPY
C     RF     - REYNOLD FLUXES
C     SCAL   - SCALARS (THE FIRST 'NCONC' OF THESE ARE MASS FRACTIONS)
C     XP     - X COORDINATES OF CELL CENTRES
C     YP     - Y COORDINATES OF CELL CENTRES
C     ZP     - Z COORDINATES OF CELL CENTRES
C     VOL    - VOLUME OF CELLS
C     AREA   - AREA OF CELLS
C     VPOR   - POROUS VOLUME
```

```
C      ARPOR  - POROUS AREA
C      WFACT  - WEIGHT FACTORS
C
C      IPT    - 1D POINTER ARRAY
C      IBLK   - BLOCK SIZE INFORMATION
C      IPVERT - POINTER FROM CELL CENTERS TO 8 NEIGHBOURING VERTICES
C      IPNODN - POINTER FROM CELL CENTERS TO 6 NEIGHBOURING CELLS
C      IPFACN - POINTER FROM CELL CENTERS TO 6 NEIGHBOURING FACES
C      IPNODF - POINTER FROM CELL FACES TO 2 NEIGHBOURING CELL CENTERS
C      IPNODB - POINTER FROM BOUNDARY CENTERS TO CELL CENTERS
C      IPFACB - POINTER FROM BOUNDARY CENTERS TO BOUNDARY FACESS
C
C      WORK   - REAL WORKSPACE ARRAY
C      IWORK  - INTEGER WORKSPACE ARRAY
C      CWORK  - CHARACTER WORKSPACE ARRAY
C
C    SUBROUTINE ARGUMENTS PRECEDED WITH A '*' ARE ARGUMENTS THAT MUST
C    BE SET  BY THE USER IN THIS ROUTINE.
C
C    NOTE THAT OTHER DATA MAY BE OBTAINED FROM CFDS-FLOW3D USING THE
C    ROUTINE GETADD, FOR FURTHER DETAILS SEE THE RELEASE 3
C    USER MANUAL.
C
C*********************************************************************
C
       LOGICAL LDEN,LVIS,LTURB,LTEMP,LBUOY,LSCAL,LCOMP
      +       ,LRECT,LCYN,LAXIS,LPOROS,LTRANS
C
       CHARACTER*(*) CWORK
       CHARACTER     CNAME*6, CALIAS*24
C
C+++++++++++++++++ USER AREA 1 ++++++++++++++++++++++++++++++++++++++++
C---- AREA FOR USERS EXPLICITLY DECLARED VARIABLES
C
C+++++++++++++++++ END OF USER AREA 1 ++++++++++++++++++++++++++++++++++
C
       COMMON
      + /ALL/     NBLOCK,NCELL,NBDRY,NNODE,NFACE,NVERT,NDIM
      + /ALLWRK/ NRWS,NIWS,NCWS,IWRFRE,IWIFRE,IWCFRE
      + /ADDIMS/ NPHASE,NSCAL,NVAR,NPROP
      +          ,NDVAR,NDPROP,NDXNN,NDGEOM,NDCOEF,NILIST,NRLIST,NTOPOL
      + /CHKUSR/ IVERS,IUCALL,IUSED
      + /DEVICE/ NREAD,NWRITE,NRDISK,NWDISK
      + /IDUM/   ILEN,JLEN
      + /LOGIC/  LDEN,LVIS,LTURB,LTEMP,LBUOY,LSCAL,LCOMP
      +          ,LRECT,LCYN,LAXIS,LPOROS,LTRANS
      + /MLTGRD/ MLEVEL,NLEVEL,ILEVEL
      + /SGLDBL/ IFLGPR,ICHKPR
      + /SPARM/  SMALL,SORMAX,NITER,INDPRI,MAXIT,NODREF,NODMON
      + /TRANSI/ NSTEP,KSTEP,MF,INCORE
      + /TRANSR/ TIME,DT,DTINVF,TPARM
C
C+++++++++++++++++ USER AREA 2 ++++++++++++++++++++++++++++++++++++++++
C---- AREA FOR USERS TO DECLARE THEIR OWN COMMON BLOCKS
C     THESE SHOULD START WITH THE CHARACTERS 'UC' TO ENSURE
C     NO CONFLICT WITH NON-USER COMMON BLOCKS
C
C+++++++++++++++++ END OF USER AREA 2 ++++++++++++++++++++++++++++++++++
C
       DIMENSION AM(NCELL,6,NPHASE),SP(NCELL,NPHASE),SU(NCELL,NPHASE)
      +,CONV(NFACE,NPHASE)
C
       DIMENSION
      + U(NNODE,NPHASE),V(NNODE,NPHASE),W(NNODE,NPHASE),P(NNODE,NPHASE)
      +,VFRAC(NNODE,NPHASE),DEN(NNODE,NPHASE),VIS(NNODE,NPHASE)
      +,TE(NNODE,NPHASE),ED(NNODE,NPHASE),RS(NNODE,NPHASE,6)
      +,T(NNODE,NPHASE),H(NNODE,NPHASE),RF(NNODE,NPHASE,4)
      +,SCAL(NNODE,NPHASE,NSCAL)
C
       DIMENSION
      + XP(NNODE),YP(NNODE),ZP(NNODE)
      +,VOL(NCELL),AREA(NFACE,3),VPOR(NCELL),ARPOR(NFACE,3)
      +,WFACT(NFACE)
      +,IPT(*),IBLK(5,NBLOCK)
      +,IPVERT(NCELL,8),IPNODN(NCELL,6),IPFACN(NCELL,6),IPNODF(NFACE,4)
      +,IPNODB(NBDRY,4),IPFACB(NBDRY)
```

```
     +,IWORK(*),WORK(*),CWORK(*)
C
      DIMENSION
     +RANGE(100),PRO(100)
C
C+++++++++++++++++ USER AREA 3 ++++++++++++++++++++++++++++++++++++++++++
C---- AREA FOR USERS TO DIMENSION THEIR ARRAYS
C
C---- AREA FOR USERS TO DEFINE DATA STATEMENTS
C
C+++++++++++++++++ END OF USER AREA 3 ++++++++++++++++++++++++++++++++++
C
C---- STATEMENT FUNCTION FOR ADRESSING
      IP(I,J,K)=IPT((K-1)*ILEN*JLEN+(J-1)*ILEN+I)
C
C----VERSION NUMBER OF USER ROUTINE AND PRECISION FLAG
C
      IVERS=4
      ICHKPR = 1
C
C+++++++++++++++++ USER AREA 4 ++++++++++++++++++++++++++++++++++++++++++
C---- TO USE THIS USER ROUTINE FIRST SET IUSED=1
C
       IUSED=1
       IF (IUSED.EQ.0) RETURN
C
C+++++++++++++++++ END OF USER AREA 4 ++++++++++++++++++++++++++++++++++
C
C---- FRONTEND CHECKING OF USER ROUTINE
       IF (IUCALL.EQ.0) RETURN
C
C---- ADD TO SOURCE TERMS
      IF (ICALL.EQ.1) THEN
C
C+++++++++++++++++ USER AREA 5 ++++++++++++++++++++++++++++++++++++++++++
C
C     Test on variable name.
      IF(CALIAS.EQ.'FLUID AGE') THEN
C       Use IPALL to get addresses of all cells in all blocks.
        CALL IPALL('*','*','BLOCK','CENTRES',IPT,NPT,CWORK,IWORK)
C
C       Loop over all cells.
        DO 100 I=1,NPT
          INODE = IPT(I)
C
C         Add source term rho*vol.
          SU(INODE,1) = SU(INODE,1) + DEN(INODE,1)*VOL(INODE)
     C                              *VFRAC(INODE,1)
C
  100   CONTINUE
C
      ENDIF
C      GO TO 365
      SMGLQ = 1.0
      IF(CALIAS.EQ.'AGED  ') THEN
C
      CALL IPREC('BLOCK-NUMBER-1','BLOCK','CENTRES',IPT,ILEN,JLEN,KLEN,
     +           CWORK,IWORK)
C  LOOP OVER PATCH
           AGEAR = 0.0
           AREAT = 0.0
      DO 11103 J = 1, JLEN
        DO 11102 I = 1, ILEN
          SDUMMY = 0.0
          VDUMMY = 0.0
          DO 11101 K = 1, KLEN
           INODE = IP(I,J,K)
          AM(INODE,1,1) = 0.0
          AM(INODE,2,1) = 0.0
          AM(INODE,3,1) = 0.0
          AM(INODE,4,1) = 0.0
          AM(INODE,5,1) = 0.0
          AM(INODE,6,1) = 0.0
          SP(INODE,1) = -SMGLQ
          SU(INODE,1)= SMGLQ *SCAL(INODE,1,1)*1.0*
     C         VOL(INODE)
```

```
          SDUMMY = SDUMMY + SU(INODE,1)
          VDUMMY = VDUMMY + VOL(INODE)
11101     CONTINUE
          AGEARR = SDUMMY/VDUMMY
          SU(INODE,1) = AGEARR
          AGEAR = AGEAR + AGEARR*VOL(INODE)
          AREAT = VOL(INODE) + AREAT
11102   CONTINUE
C
11103  CONTINUE
          IF (NITER.EQ.MAXIT) THEN
          AGEAR = AGEAR/AREAT
          WRITE(6,*) ' AREA = ', AREAT, 'AGEAR =  ', AGEAR
      CALL IPREC('BLOCK-NUMBER-1','BLOCK','CENTRES',IPT,ILEN,JLEN,KLEN,
     +           CWORK,IWORK)
C  LOOP OVER PATCH
           AGEAR = 0.0
           AREAT = 0.0
           SDUMMY = 0.0
           VDUMMY = 0.0
           ILENM1 = ILEN - 1
           RANGE(1) = -0.001
           IITOP = 40
        DO 21105 II = 1, IITOP
        PRO(II) = 0.0
        RANGE(II+1) = RANGE(II) + 1.
21105   CONTINUE
        RANGE(IITOP+1) = RANGE(IITOP) + 100.
      DO 21103 K = 1, KLEN
        DO 21102 J = 1, JLEN
          DO 21101 I = ILEN, ILEN
           INODE = IP(I,J,K)
          SAGE = SCAL(INODE,1,1)
          SDUMMY = SDUMMY + SAGE*VOL(INODE)
          VDUMMY = VDUMMY + VOL(INODE)
          VRHOD = VRHOD + VOL(INODE)*DEN(INODE,1)
            DO 21104 II = 1, IITOP
         IF(SAGE.LT.RANGE(II+1).AND.SAGE.GT.RANGE(II)) THEN
             PRO(II) = PRO(II)+ U(INODE,1)*1000.0*VOL(INODE)
     C                               *VFRAC(INODE,1)*0.2427/0.0198577
           ENDIF
21104       CONTINUE
21101     CONTINUE
21102   CONTINUE
21103  CONTINUE
          AGEAR = SDUMMY/VDUMMY
          WRITE(6,*) ' AREAOUT = ', AREAT, 'AGEAROUT =  ', AGEAR
         WRITE(6,*) 'II    RANGE(II+1)     PRO(II)'
         DO 21106 II = 1, IITOP
         WRITE(6,*) II, RANGE(II+1), PRO(II)
21106 CONTINUE
          ENDIF
C
      ENDIF
 365  CONTINUE
      IF(CALIAS.EQ.'SMIX  ') THEN
         CKOG = 3.064E-5
         CM = 5.3E-5
C       Use IPALL to get addresses of all cells in all blocks.
        CALL IPALL('*','*','BLOCK','CENTRES',IPT,NPT,CWORK,IWORK)
C
C       Loop over all cells.
        DO 101 I=1,NPT
          INODE = IPT(I)
C
C         Add source term rho*vol.
          SU(INODE,1) = SU(INODE,1) -
     C      CKOG*(CM*SCAL(INODE,1,2)-SCAL(INODE,2,2))*VFRAC(INODE,1)
     C     *DEN(INODE,1)*VOL(INODE)
C
          SU(INODE,2) = SU(INODE,2) -
     C      CKOG*(SCAL(INODE,2,2)-CM*SCAL(INODE,1,2))*VFRAC(INODE,2)
     C     *DEN(INODE,2)*VOL(INODE)
C
  101   CONTINUE
      ENDIF
```

```
C
C
      IF(CALIAS.EQ.'FRANK ') THEN
C
      CALL IPREC('BLOCK-NUMBER-1','BLOCK','CENTRES',IPT,ILEN,JLEN,KLEN,
     +           CWORK,IWORK)
C  LOOP OVER PATCH
           AGEAR = 0.0
           AREAT = 0.0
        FRV = -1./JLEN*1000./JLEN
      DO 11113 J = 1, JLEN
        FRV = FRV + (J/JLEN)*1000./JLEN
        DO 11112 I = 1, 1
          SDUMMY = 0.0
          VDUMMY = 0.0
          DO 11111 K = 1, KLEN
           INODE = IP(I,J,K)
          AM(INODE,1,1) = 0.0
          AM(INODE,2,1) = 0.0
          AM(INODE,3,1) = 0.0
          AM(INODE,4,1) = 0.0
          AM(INODE,5,1) = 0.0
          AM(INODE,6,1) = 0.0
          SP(INODE,1) = -FRV
          SU(INODE,1)= FRV * 1.0*
     C         0.0
          SDUMMY = SDUMMY + SU(INODE,1)
          VDUMMY = VDUMMY + VOL(INODE)
11111     CONTINUE
          AGEARR = SDUMMY/VDUMMY
          SU(INODE,1) = AGEARR
          AGEAR = AGEAR + AGEARR*VOL(INODE)
          AREAT = VOL(INODE) + AREAT
11112    CONTINUE
C
11113  CONTINUE
      ENDIF
C
C+++++++++++++++++ END OF USER AREA 5 ++++++++++++++++++++++++
      ENDIF
      RETURN
      END

**********************************************************************
```

List of Figures

Figure 2.1. Sieve tray pitch layout: (a) triangular (b) square
Figure 2.2. Tray dynamics schematic diagram (Smith, 1963)
Figure 2.3. Idealised stages in bubble formation (Kupferberg and Jameson, 1969)
Figure 2.4. Bubbling and jetting from single holes. d_h=6.4mm (Muller and Prince, 1972), modified by Pinczewski *et al*, 1973; picture extracted from Lockett, 1986)
Figure 2.5. Common flow regimes on distillation trays (Kister, 1992)
Figure 2.6. Capacity factor (based on bubbling area) vs. flow parameter showing flow regimes. (Lockett, 1986)
Figure 2.7. Flow regime map: capacity factor vs. flow parameter (Hofhuis and Zuiderweg, 1979)
Figure 2.8. Flooding correlation for columns with crossflow trays (Fair, 1961)
Figure 2.9. (a) Gas jet penetrating the froth; (b) bridging of gas jet by liquid (Lockett, 1981)
Figure 2.10. Measurement of clear liquid height by floor mounted manometer (Lockett, 1986)
Figure 2.11. Positions for local dispersion density measurement above a sieve tray. The dots represent measuring positions.
Figure 2.12. Dependence of dispersion density profile on regime (Lockett, 1986)
Figure 2.13. Aeration factor for pressure drop calculation (Perry's Chemical Engineers' Handbook, 1992)
Figure 2.14. Discharge coefficients for gas flow (Leibson et al 1957)
Figure 2.15. Dry-plate coefficient k as a function of *t/dh* (McAllister et al 1958)
Figure 2.16. Correlation of Smith and Van Winkle (1958) for orifice coefficient, K_w (Lockett, 1986)
Figure 2.17. Orifice coefficient correlation due to Stichlmair & Mersmann (1978)
Figure 2.18. Pressure loss through an orifice
Figure 2.19. Bubble formation model
Figure 2.20. Photograph of froth (taken from Fane, 1962)
Figure 2.21. Sauter mean bubble size distribution (results from Raper et al, 1982)
Figure 2.22. McCabe-Thiele graphical method for operating and VLE relationships
Figure 2.23. Concentration profile of the more volatile component near the interface in a binary mixture
Figure 2.24. Exponent of temperature for diffusion coefficient in gases (adapted from Marrero and Mason, 1972, with the approximation that $\varepsilon/k_B \approx 0.75T_c$)
Figure 2.25. Slattery-Bird generalised chart for gas self-diffusion coefficient at high pressure
Figure 2.26. Takahashi correlation (1974) for the effect of pressure and temperature on the binary gas diffusion coefficient
Figure 2.27. Simple vapour-liquid relationship of a binary mixture system in a column
Figure 2.28. Elemental strips used to define transfer units (Lockett, 1986)
Figure 2.29. Concentration profile for more volatile component in the vapour leaving a tray (Lockett, 1986)
Figure 2.30. Geometry of a tray
Figure 2.31. Mass balance over dispersion on a differential control volume
Figure 2.32. Assumed liquid flow profile for the SRM

Figure 2.33. Sequence of steps for the prediction of tray efficiency (modified from Kister, 1992)
Figure 2.34. CFD predictions of velocity profile on Aston's rig
Figure 2.35. CFD predictions of dispersion density on CRODIS
Figure 2.36. CFD predictions of dispersion density on Aston's rig

Figure 3.1. The flowsheet of CRODIS
Figure 3.3. The detailed dimensions (in mm) of CRODIS test section
Figure 3.5. Calibration results for the anemometer in a 4-inch duct
Figure 3.6. Impact-plate air-water separator used by Tahmasbi (1997)
Figure 3.7. Conventional design of a cyclone separator (pictures taken from the Perry's Chemical Engineers' Handbook, 7th Edition)
Figure 3.8. Old inlet downcomer arrangement
Figure 3.9. New inlet downcomer arrangement (Tahmasbi, 1997) (present work)
Figure 3.10. Measuring locations above the test tray
Figure 3.11. Calibration cell for gamma densitometer
Figure 3.12. Special near-tray floor calibration
Figure 3.13. The four mechanisms of light attenuation through particles
Figure 3.14. Schematic presentation of the optical set-up for the Sauter mean bubble size measurement
Figure 3.15. CRODIS test tray in operation
Figure 3.16. Bubbling on the tray (1)
Figure 3.17. Bubbling on the tray (2)
Figure 3.18. Outlet calming zone
Figure 3.19. Inlet calming zone
Figure 3.20. Froth regime operation
Figure 3.21. Spray regime operation
Figure 3.22. Dependence of froth density profile on flow regime, taken from Lockett (1986)
Figure 3.23. Local clear liquid height distribution for 1.8mm tray, 8mm outlet weir
Figure 3.24. Local clear liquid height distribution for 1.8mm tray, 38mm outlet weir
Figure 3.25. Local clear liquid height distribution for 6mm tray, 38mm outlet weir
Figure 3.26. Dispersion density profile
Figure 3.27. Dispersion density profile at outlet calming zone and inlet calming zone
Figure 3.28. Discharge coefficient for gas flow (Leibson *et al* 1957)
Figure 3.29. Prediction of dry tray pressure drop using various correlations
Figure 3.30. CRODIS results: comparisons with correlations (8mm weir)
Figure 3.31. CRODIS results: comparisons with correlations (38mm weir)
Figure 3.32. Sauter mean bubble/droplet diameter profile
Figure 3.33. Schematic of partial bubbling phenomenon
Figure 3.34. Hydraulic jump at liquid inlet region

Figure 4.1. The principle of the optical fibre probe
Figure 4.2. Various types of optical fibre probe
Figure 4.3. Instantaneous image of the froth structure (left) and at 0.5 second later (right)
Figure 4.4. The Calderbank bubble probe
Figure 4.5. Proposed design of the new probes measuring system
Figure 4.6. 200μm optical fibre used in the present work
Figure 4.7. The tip of the optical probe

Figure 4.8. Five pairs of optical fibres with/without external protection jacket
Figure 4.9. High power emitter with bulkhead SMA
Figure 4.10. Experimental setup for probe testing and signal response (scale: 200mV, 5ms)
Figure 4.11. Experimental setup for optical probe testing on bubble (a) and droplet (b) signals
Figure 4.12. Sequential pictures of an elliptical bubble passing through a probe
Figure 4.13. Signal profile of a bubble passing through a probe (corresponds to Figure 4.12.)
Figure 4.14. Motion of a bubble before in contact with a probe
Figure 4.15. Sequential pictures of a large bubble passing through a probe
Figure 4.16. Change of the shape of a rising bubble before in contact with a probe
Figure 4.17. Signal profile of a bubble passing through a probe (corresponds to Figure 4.10.)
Figure 4.18. Motion of a bubble before in contact with a probe
Figure 4.19. Sequential pictures of a droplet passing through a probe
Figure 4.20. Signal profile of a droplet passing through a probe (corresponds to Figure 4.14.) The red box represents the actual penetration period for the droplet
Figure 4.21. Signal profile of several droplets continuously passing through a probe. The arrow represents the actual penetration periods for each droplet
Figure 4.22. Sequential pictures of the first droplet passing through a probe
Figure 4.23. Sequential pictures of the second droplet passing through a probe
Figure 4.24. Sequential pictures of the third droplet passing through a probe
Figure 4.25. Mechanical structure of the actuation mechanism
Figure 4.26. Geometry of the probes inside CRODIS facility
Figure 4.27. Five probes with the stainless steel plate clamped by an aluminium box
Figure 4.28. Special flange design for the moving stainless steel tube
Figure 4.29. Pre-drilled linear shaft used for support system
Figure 4.30. Support rail for the linear shaft
Figure 4.31. Waterproof linear bush and the assembly with the linear shaft and support rail
Figure 4.32. "Pinion and rack" motor-driven actuation mechanism
Figure 4.33. Front view (left) and side view (right) of the driving mechanism
Figure 4.34. Forward control switch (left) and decelerating pads (right)
Figure 4.35. The Complete Flying Optical Probes System
Figure 4.36. Electronic circuit for the optical probes
Figure 4.37. Signal profiles for Probe 1 and position (one scan), taken from Run1 of "h1.8_w8_test1"
Figure 4.38. The "useful" part of the full signal profile (red box in Figure 4.37)
Figure 4.39. Gas chord length distribution for the condition of "h6_w8_test1"
Figure 4.40. Liquid chord length distribution for the condition of "h6_w8_test1"
Figure 4.41. Pre-assumed froth structure for data interpretation (grey represents gas, blue represents liquid and imagine the white areas filled up by smaller gas and liquid elements).
Figure 4.42. A probe penetrates a spherical bubble
Figure 4.43. "Actual" vs. "Apparent" penetration path
Figure 4.44. A probe intersecting a bubble
Figure 4.45. Conversion from Figure 4.39 into bubble size distribution (h6_w8_test1)
Figure 4.46. Conversion from Figure 4.40 into droplet size distribution (h6_w8_test1)

Figure 4.47. Gas chord length and bubble size distribution for "h6_w38_test9" experiment
Figure 4.48. Gas chord length and bubble size distribution for "h1.8_w8_test8" experiment
Figure 4.49. Liquid chord length and droplet size distribution for "h6_w38_test9" experiment
Figure 4.50. Liquid chord length and droplet size distribution for "h1.8_w8_test8" experiment
Figure 4.51. Sauter mean bubble diameter for Test 8
Figure 4.52. Sauter mean droplet diameter for Test 8
Figure 4.53. Sauter mean bubble diameter for Test 9
Figure 4.54. Sauter mean droplet diameter for Test 9
Figure 4.55. A "two-region" signal processing example with the gas phase results
Figure 4.56. A "two-region" signal processing example with the liquid phase results

Figure 5.1. Behaviour of a photochromic substance (after Brown, 1971)
Figure 5.2. Reversible photochromic reaction of the dye, TNSB
Figure 5.3. Fading rate of the photochromic dye TNSB (Tezock, 1993)
Figure 5.4. Refractive index of aqueous calcium chloride solution under different concentrations
Figure 5.5. Diagram of the liquid-liquid crossflow experiment
Figure 5.6. Test section of the liquid-liquid crossflow experiment
Figure 5.7. Dimension of the 1.8mm hole size sieve tray (top view)
Figure 5.8. Original quartz capillary used by Tezock (1993) and Tahmasbi (1997)
Figure 5.9. New design of activation chamber in the present work
Figure 5.10. Typical snapshot of the flow field in single hole bubbling experiment
Figure 5.11. Single bubbling phenomenon (Run 5); kerosene hole velocity, u_h=0.50m/s, $CaCl_2$ flowrate Q_L=2.46lit/min
Figure 5.12. Single bubbling phenomenon (Run 6); kerosene hole velocity, u_h=0.57m/s, $CaCl_2$ flowrate Q_L =2.46lit/min
Figure 5.13. Single bubbling phenomenon (Run 7); kerosene hole velocity, u_h=0.62m/s, $CaCl_2$ flowrate Q_L =2.46lit/min
Figure 5.14. A typical snapshot of the flow field (taken from Run 1)
Figure 5.15. Photograph of the flow field at t = 0.0s (taken from Run1)
Figure 5.16. Photograph of the flow field at t = 2.0s (taken from Run1)
Figure 5.17. Photograph of the flow field at t = 4.0s (taken from Run1)
Figure 5.18. Photograph of the flow field at t = 6.0s (taken from Run1)
Figure 5.19. Photograph of the flow field at t = 8.0s (taken from Run1)
Figure 5.20. Photograph of the flow field at t = 10.0s (taken from Run1)
Figure 5.21. Photograph of the flow field at t = 12.0s (taken from Run1)
Figure 5.22. Photograph of the flow field at t = 14.0s (taken from Run1)
Figure 5.23. Typical snapshot of the flow field in full simulation experiment
Figure 5.24. Multiple-hole bubbling phenomenon (Run 2); kerosene hole velocity, u_h=0.32m/s, $CaCl_2$ flowrate Q_L=2.46lit/min
Figure 5.25. Multiple-hole bubbling phenomenon (Run 3); kerosene hole velocity, u_h=0.39m/s, $CaCl_2$ flowrate Q_L=2.46lit/min
Figure 5.26. Multiple-hole bubbling phenomenon (Run 6); kerosene hole velocity, u_h=0.39m/s, $CaCl_2$ flowrate Q_L=4.10lit/min

Figure 6.1. Liquid volume fraction profile of a heterogeneous model with arrows representing gas phase velocity; gas superficial velocity = 2 m/s and liquid volumetric flowrate = 1.35×10^{-4} m3/s (Fischer, 1999)
Figure 6.2. Heterogeneous modelling on the 2.44m rig at Aston University (taken from Fischer, 1999)
Figure 6.3. Liquid volume fraction profile of a heterogeneous model with the MUSIG model
Figure 6.4. MUSIG group 1
Figure 6.5. MUSIG group 2
Figure 6.6. MUSIG group 3
Figure 6.7. MUSIG group 4
Figure 6.8. MUSIG group 5
Figure 6.9. MUSIG group 6
Figure 6.10. MUSIG group 7
Figure 6.11. MUSIG group 8
Figure 6.12. MUSIG group 9
Figure 6.13. MUSIG group 10
Figure 6.14. Sauter mean bubble size distribution
Figure 6.15. A simple side-view geometry of the homogeneous model
Figure 6.16. Homogeneous modelling of the 2.44m rig at Aston University: (1) liquid velocity vectors at the tray floor and central channel, (2) liquid volume fraction profile at the central channel. (results taken from Fischer, 1999)
Figure 6.17. Residence time distribution for the 2.44m rig at Aston University (results taken from Fischer, 1999)

Figure 7.1. Shaded area represents a small packet of fluid (two-phase), y being the mole fraction of the more volatile component.
Figure 7.2. Liquid mole fraction profile v.s. residence time for a distillation case
Figure 7.3. Three-dimensional distribution of liquid residence time over the tray
Figure 7.4. Vertically averaged fluid age distribution (top view)
Figure 7.5. Liquid residence time and corresponding mass flowrate
Figure 7.6. The new methodology for tray efficiency prediction

Figure 8.1. Cross-sectional dimensions of the AIChE column (dimensions in metres)
Figure 8.2. Henry's constant for the ammonia-air-water system calculated with the API Sour Water model and the AIChE model (Eq.8.1)
Figure 8.3. Liquid mole fraction vs. Residence time for an ammonia absorption case (results taken from Run-11)
Figure 8.4. CFD results on residence time distribution for an ammonia absorption case (results taken from Run-11)
Figure 8.5. Henry's constant for the ammonia-air-water system (pink dots represent results from Eq.(8.2) above)
Figure 8.6. Liquid mole fraction vs. Residence time for an oxygen desorption case (results taken from Run-KO19A)
Figure 8.7. CFD results on residence time distribution for an oxygen desorption case (results taken from Run-KO19A)
Figure 8.8. VLE for Acetone/Benzene system at different pressure conditions (the lines represent Aspen Max results and the dots represent data provided in the AIChE report, 1958)

Figure 8.9. Liquid mole fraction vs. Residence time for acetone/benzene distillation case (results taken from Run-T13)
Figure 8.10. CFD results on residence time distribution for acetone/benzene distillation case (results taken from Run-T13)
Figure 8.11. Cross-sectional dimensions of the FRI column
Figure 8.12. VLE for C6/C7 system at 1.66bar (24psia)
Figure 8.13. VLE for C6/C7 system at 0.28bar (4psia)
Figure 8.14. Liquid mole fraction profile v.s. residence time for the C6/C7 distillation case (results taken from Run-1328)
Figure 8.15. CFD results on residence time distribution for a 1.66bar (24psi) C6/C7 distillation case (results taken from Run-1328)
Figure 8.16. VLE for iC4/nC4 system at 11.4 bar
Figure 8.17. Liquid mole fraction profile v.s. residence time for the iC4/nC4 distillation case (results taken from Run-1313)
Figure 8.18. CFD results on residence time distribution for 165psi (11.4bar) iC4/nC4 distillation case (results taken from Run-1313)
Figure 8.19. VLE for Isopropanol/Water system at 1atm
Figure 8.20. VLE for Isopropanol/Water system at 0.28bar
Figure 8.21. Liquid mole fraction vs. Residence time for an Isopropanol/Water distillation case (results taken from Run-1381)
Figure 8.22. CFD results on residence time distribution for 1atm Isopropanol/Water distillation case (results taken from Run-1381)
Figure 8.23. Liquid mole fraction vs. Residence time for an ammonia absorption case under different conditions.
Figure 8.24. CFD simulation results for Test 1
Figure 8.25. CFD simulation results for Test 6
Figure 8.26. CFD residence time distributions
Figure 8.27. CFD residence time distributions for double sized tray for triple sized tray
Figure 8.28. Modified flow distributions for Run 1313 of iC4/nC4 distillation case (Figure 8.18)
Figure 8.29. Modified flow distributions for Run 1381 of isopropanol/water distillation case (Figure 8.22)

List of Tables

Table 2.1. Theoretical relationships for liquid holdup
Table 2.2. Commonly used correlations for the calculation of liquid holdup
Table 2.3. Other empirical correaltions for clear liquid height
Table 2.4. Conditions for the empirical correlations in Table 2.3
Table 2.5. Values of coefficients found by experiment (Biddulph et al, 1995)
Table 2.6. Coefficient for F_0
Table 2.7. Atomic Diffusion Volumes for different components (Fuller et al 1966)
Table 2.8. Diffusion volumes for simple molecules (Fuller et al 1966)
Table 2.9. Constants defined in Eq.(2.95) by Takahashi (1974)
Table 2.10. Molecular volumes for some common substances

Table 3.1. Dimensions of the cyclone separator
Table 3.2. Calibration data for gamma densitometer system

Table 4.1. Technical specifications of the high power emitter
Table 4.2. Technical specifications of the receiver
Table 4.3. Combinations of gas and liquid flowrates in the experiments
Table 4.4. Information on group sizes used in the data interpretation

Table 5.1. Applications of photochromic dyes on fluid flow visualisation experiments
Table 5.2. Other physical properties of kerosene and aqueous calcium chloride solution
Table 5.3. Flowrates of each experimental run
Table 5.4. Flowrates of each experimental run

Table 8.1. Open fraction for the bubble cap trays used for validation work
Table 8.2. CFD simulation results of ammonia absorption experiments
Table 8.3. CFD simulation results of oxygen desorption experiments
Table 8.4. Thermodynamic correction term at various system pressures
Table 8.5. CFD simulation results of acetone/benzene distillation experiments
Table 8.6. CFD simulation results of C6/C7 distillation experiments
Table 8.7. CFD simulation results of iC4/nC4 distillation experiments
Table 8.8. CFD simulation results of isopropanol/water distillation experiments
Table 8.9. Conditions for the sensitivity study
Table 8.10. Outlet liquid composition results and conversion to Murphree tray efficiency for each test in the sensitivity study
Table 8.11. Operating variables of each test under different tray size (original results taken from Run1328 of the FRI C6/C7 distillation case)
Table 8.12. Outlet compositions of cyclohexane for the three different sizes of trays